Breaking Quantum Limits with Collective Cavity-QED: Generation of Spin Squeezed States via Quantum Non-Demolition Measurements

by

Zilong Chen

B.S., Massachusetts Institute of Technology, 2004

M.S., University of Colorado at Boulder, 2009

A thesis submitted to the

Faculty of the Graduate School of the

University of Colorado in partial fulfillment

of the requirements for the degree of

Doctor of Philosophy

Department of Physics

2013

ProQuest LLC.
789 East Eisenhower Parkway
P.O. Box 1346
Ann Arbor, MI 48106 - 1346

This thesis entitled:
Breaking Quantum Limits with Collective Cavity-QED: Generation of Spin Squeezed States via Quantum Non-Demolition Measurements
written by Zilong Chen
has been approved for the Department of Physics

James K. Thompson

Jun Ye

Date

The final copy of this thesis has been examined by the signatories, and we find that both the content and the form meet acceptable presentation standards of scholarly work in the above mentioned discipline.

Chen, Zilong (Ph.D., Physics)

Breaking Quantum Limits with Collective Cavity-QED: Generation of Spin Squeezed States via Quantum Non-Demolition Measurements

Thesis directed by Prof. James K. Thompson

Large ensembles of uncorrelated atoms are extensively used as precise sensors of time, rotation, and gravity, and for tests of fundamental physics. The quantum nature of the sensors imposes a limit on their ultimate precision. Larger ensembles of N atoms can be used to average the quantum noise as $1/\sqrt{N}$, a scaling known as the standard quantum limit. However, the ensemble size may be limited by technical constraints and/or atom-atom collisions – a fundamental distinction from photon-based sensors. Learning to prepare entangled states of large ensembles with noise properties below the standard quantum limit will be key to extending both the precision and/or bandwidth of atomic sensors. More broadly, the generation and application of entanglement to solve problems is a core goal of quantum information science being pursued in both atomic and solid state systems.

In this thesis, we utilize the tools of cavity-QED to prepare entangled spin-squeezed states with 3.4(6) dB improvement in spectroscopic sensitivity over the standard quantum limit. The collective atomic spin is composed of the two-level clock states of ^{87}Rb confined in a medium finesse $F = 710$ optical cavity. We employ cavity-aided quantum non-demolition measurements of the vacuum Rabi splitting to measure and subtract out the quantum projection noise of the collective spin state, preparing states with collective atomic spin projection noise 4.9(6) dB below the projection noise level. The conditionally reduced spin noise combined with the measured 1.5(3) dB reduction in the mean spin length implies a net 3.4(6) dB spectroscopic enhancement or conditional squeezing as defined by the Wineland criterion. Our method does not require single particle addressability and is applied to a spectroscopically large ensemble of $N = 7 \times 10^5$ atoms using two collective population measurements, with the whole squeezing operation taking $\sim 150\ \mu$s.

The gain in sensitivity is spectroscopically equivalent to the enhancement obtained had we created $> 10^5$ pairs of maximally entangled qubits, demonstrating the power of a top-down approach for entangling large ensembles. The nondemolition probing of atomic populations via the vacuum Rabi splitting is also of broad interest for non-destructively reading out a wide variety of both atomic and solid state qubits.

Contents

Chapter

Appendix

Tables

Table

Figures

Figure

Chapter 1

Introduction and Motivation

The idea of using quantum entanglement as a resource to overcome classical and quantum constraints has become a paradigm in modern physics. Entanglement is a concept that arises naturally when the superposition principle is applied to composite quantum systems. Two quantum systems are entangled if the total wavefunction for the composite system is in a *non-factorizable* superposition of joint-system wavefunctions. This means that the two systems are no longer independent of each other, and possess correlations stronger than classical correlations could create. Measuring one system necessarily disturbs the other system instantaneously regardless of their physical separation. This notion of non-locality — that the two sub-systems still remain a single quantum system no matter how far apart — presented a conundrum for Einstein, Poldosky and Rosen [1], who famously called entanglement "spooky action at a distance".

Whereas Einstein and co-workers viewed entanglement as a problematic feature of quantum mechanics, others saw entanglement as a fertile land of opportunity on which they sowed the seeds of quantum-enabled strategies that could surpass classical strategies. With constant nurturing by generations of scientists, these seeds have grown into large healthy trees today — quantum communication [2], quantum computation [3], quantum simulation [4] and, last but not least, quantum metrology [5] — with interconnecting branches and cross fertilization resulting in some utilitarian fruits already. For instance, quantum key distribution was commercialized in 2004, providing a provably secure method for sharing information [6]. In quantum computation, the celebrated Shor's factoring algorithm [7] provides an exponential speed-up over the best classical algorithms — a problem with practical applications to cryptography. Quantum simulators of strongly correlated entangled many-body systems are within reach of current ultracold atom and trapped ion technology [8–11]. Quantum metrology aims to achieve measurement precision below quantum limits using entanglement, and atomic spin squeezing is one way to achieve this. My contribution in this landscape is a leaf on the spin squeezing branch of the quantum metrology tree.

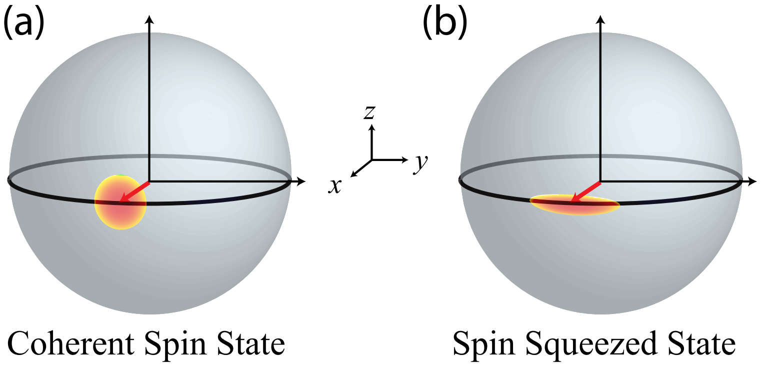

Figure 1.1: (a) A coherent spin state (CSS) features isotropic pointing fluctuations indicated by the noise blob perpendicular to the mean spin (red arrow). (b) A spin squeezed state possesses entanglement that reduce fluctuations in one direction. As a consequence of Heisenberg uncertainty relations, fluctuations in another direction are increased.

This leaf tells the story of using collective cavity quantum nondemolition measurements to prepare entangled spin squeezed states of atoms that have spectroscopic sensitivities below the standard quantum limit [12]. As will be explained in more detail in Chapter 2, coherent spin states are collective spins of N identical but otherwise independent spins. Coherent spin states are used, *de facto*, in quantum phase estimation — a central problem in quantum metrology. Unlike a classical spin that has no noise in its pointing direction, quantum mechanics imposes pointing uncertainty in a coherent spin state (CSS), as depicted by the noise blob at the tip of the mean spin direction in Fig. 1.1(a). The standard quantum limit refers to the CSS angular resolution $\Delta\phi_{\mathrm{SQL}} = 1/\sqrt{N}$ due to pointing fluctuations inherent to the CSS. Due to the lack of entanglement in a CSS, the noise distribution is isotropic to the mean spin direction. In an entangled spin squeezed state, uncertainty in one direction is reduced at the expense of increasing uncertainty in another direction (see Fig. 1.1(b)), as required by Heisenberg uncertainty relations. The squeezed quadrature provides enhanced angular resolution that can be used to sense a quantum phase below the standard quantum limit (SQL).

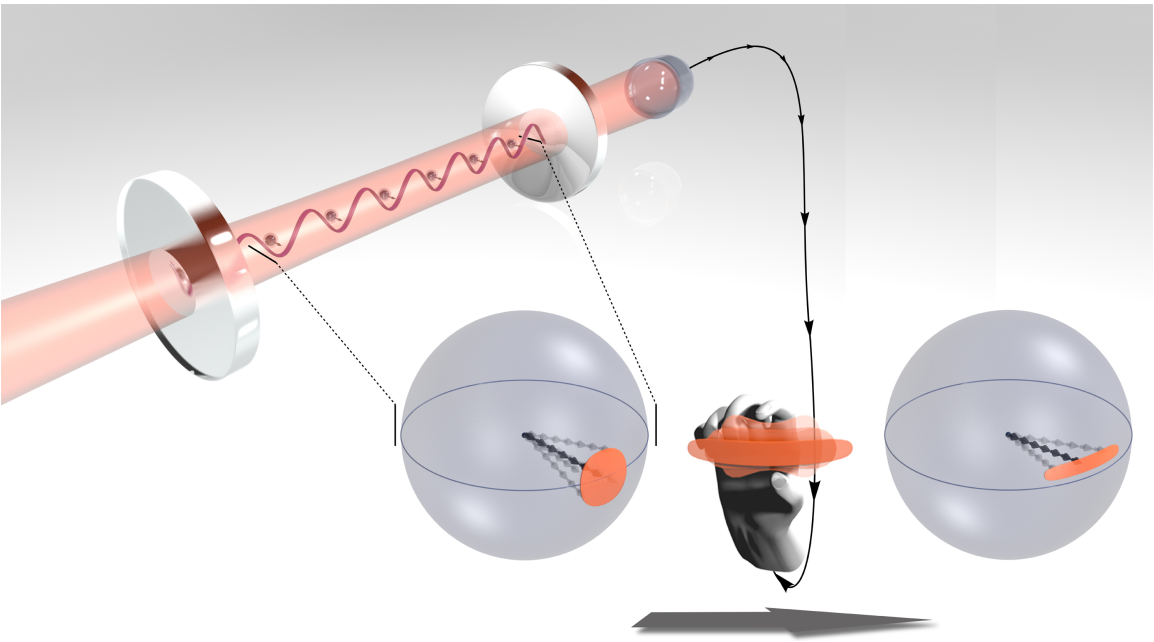

Figure 1.2: Essential concepts behind our squeezing experiment. Our setup consists of an optical cavity filled with rubidium atoms. The atoms behave like little pieces of glass with state-dependent refractive index. The phase shift imposed by the atoms on the cavity mode causes the cavity resonance frequency to shift depending on the *collective populations* $N_\uparrow$ in spin up and $N_\downarrow$ in spin down. We send a laser through the cavity to determine the frequency shifts, from which we can determine the population differences or equivalently the collective spin projection J_z. The information gained is then used to reduce the quantum projection noise below the CSS noise for one of the two components describing the spatial orientation of the collective spin. Because the measurement is collective in nature, the probing causes little shortening (single atom wavefunction collapse) of the collective spin, preserving coherence. The net polar angular uncertainty of the post-measurement state is reduced below that SQL set by the initial CSS composed of identical, un-entangled atoms. Image credit: Richard Baxley, JILA.

In the experiment described in this thesis, we generate spin squeezed states by directly measuring the quantum fluctuations in the spin projection J_z of identically prepared CSS, shown schematically in Fig. 1.2. Our CSS is composed of $\sim 10^6$ elementary spins formed by the two clock states of ^{87}Rb. This measurement is implemented by probing the atomic ensemble, prepared in a CSS, with laser light tuned such that quantum fluctuations of the CSS are imposed on the light phase and/or amplitude. Knowledge of J_z is then obtained by measuring the light. When the measurement imprecision is below that of the CSS quantum noise, we would have reduced the uncertainty along $\hat{z}$ below the initial CSS uncertainty. However, the measurement process may cause the collective spin to shorten due to free space scattering of the probe light. Free space scattering reveals individual spin states, effectively taking individual spins pointing along $\hat{x}$ and randomly putting them into spins pointing up (along $\hat{z}$) or down (along $-\hat{z}$), shortening the collective spin length along $\hat{x}$. The shortening would degrade the phase sensitivity as the angular uncertainty is set by the ratio of the quantum noise in a spin projection perpendicular to the mean spin to the mean spin length in the small angle limit. In our cavity-aided quantum nondemolition measurement [12], collective information is obtained (largely) without revealing individual spin states, thus preserving the mean spin length. Using the measurement outcome from the pre-measurement, the quantum noise can be subtracted from subsequent measurements, effectively creating a spin squeezed state with improved angular resolution or equivalently phase sensitivity over the SQL.

In this introductory chapter, I will present an overview of precision metrology and provide motivation for why spin squeezing is important. As mentioned earlier, the fundamental measurement precision achievable with un-entangled ensembles is given by the SQL, which improves with the ensemble size N as $\Delta\phi_{\mathrm{SQL}} = 1/\sqrt{N}$. However, there may be situations where scaling up N is non-trivial or not desirable. These situations provide motivation for going beyond the SQL using entangled states of atoms, a research field known as quantum-enhanced metrology. An important class of such states are spin squeezed states, the realization of which forms the core focus of this thesis. Following a brief description of my contributions to a different research topic, namely superradiant lasers, I will lay out the organization of the thesis. This thesis will focus only on spin squeezing.

1.1 Precision Metrology

The central goal of quantum metrology is to measure physical quantities very *precisely*. Precision is defined by the root mean squared (rms) fluctuation of the output of a quantum standard or sensor that would be observed over many independent experimental trials. We will first describe how information is encoded in a quantum standard/sensor, and then the precision with which the information can be extracted.

The basis on which most atomic sensors operate is estimating a quantum phase that evolves in a dark time using Ramsey spectroscopy[1] . This quantum phase ϕ is encoded as a relative phase in the superposition $\left(|\downarrow\rangle + e^{i\phi}|\uparrow\rangle\right)/\sqrt{2}$ of the two quantum states $|\uparrow\rangle$ and $|\downarrow\rangle$ employed as the sensor. The rate at which the quantum phase ϕ evolves is set by the frequency difference $\omega_{\uparrow\downarrow}$ between the two states $|\uparrow\rangle$ and $|\downarrow\rangle$. This frequency can depend on externally applied fields, or conversely, can be extremely insensitive to the environment in the case of atomic clocks. By measuring this frequency very precisely, quantum sensors of exquisite sensitivity can be realized [13]. As the phase cannot be measured directly, it is instead mapped onto populations that can be discriminated via fluorescence detection or other means. However, even if there is no detection noise, there is still fundamental quantum noise due to probabilistic collapse of the atoms into spin up or down, much like N independent coin flips with the probability of heads or tails corresponding to the probability of collapsing into spin up or down.

Using large ensembles of N atoms allows many identical experiments to be run in parallel rather than simply one after another. This is the reason that large ensembles of un-entangled atoms are extensively used as precise sensors of time [14–18], acceleration, rotation, gravity [19–22], magnetic fields [23], and for tests of fundamental physics [24–28]. The quantum nature of the sensors imposes a limit known as the standard quantum limit (SQL) on their ultimate precision. The SQL states that the rms uncertainty on the measurement of the quantum phase is $\Delta\phi_{\mathrm{SQL}} = 1/\sqrt{N}$. Microwave fountain clocks have operated at the SQL since 1999 [29]. More recently, an optical lattice clock was demonstrated that operated only 3 dB above the SQL for $\sim 10^3$ atoms [18]. By introducing entanglement, it is possible to surpass the SQL, with the fundamental limit allowed by quantum mechanics given by the Heisenberg limit $\Delta\phi_{\mathrm{HL}} = 1/N$ [5].

---

[1] Ramsey spectroscopy on internal states of atoms is also analogous to Mach-Zehnder interferometry with electrons, neutrons, atoms, molecules and photons.

Entanglement-enhanced precision may be a future key technology in atomic quantum sensors. This is because the atomic ensemble size may be limited by both technical constraints or atom-atom collisions that introduce systematic inaccuracies and loss of precision. The atom-atom interactions present in atomic systems is fundamentally distinct from the vast majority of photon-based sensors. Due to the lack of direct photon-photon interactions, photon-based sensors can achieve a lower absolute phase sensitivity by simply using more un-entangled photons. While radiation pressure shot noise from the photons can degrade the measurement precision [30], such effects are not a limitation unless the optical power is extremely high, and has not been observed until very recently [31, 32]. This is the reason why squeezed light has only recently found an application in the field of gravity wave detection such as the Laser Interferometer Gravitational Wave Observatory (LIGO) and the GEO600 detector [33–35], an optical interferometer that performs near fundamental measurement limits. In contrast, atom-atom collisions already introduce systematic errors that must be carefully studied and corrected in optical lattice clocks [36].

Learning to prepare entangled states of large ensembles with noise properties below the SQL will be key to extending both the precision [37] and/or bandwidth [38] of atomic sensors. Higher measurement precision in atomic clocks would also allow a clock to average down to its ultimate accuracy faster. From a fundamental physics perspective, creating large scale quantum entanglement is also very important for answering foundational questions. For instance, the violation of Bell's inequalities rules out local hidden variable theories of quantum mechanics [39–41]. Tests of quantum mechanics at macroscopic scales with Schrödinger Cat states [42–44] probe interactions between quantum mechanics and gravity [45, 46], and modifications of unitary dynamics [47]

The goal of this thesis is to realize entangled spin squeezed states using collective cavity quantum nondemolition measurements.

1.2 Contributions to Superradiant Lasers

Besides spin squeezing, I have also contributed to research on superradiant lasers as part of a collaborative lab effort. Because this thesis will focus on spin squeezing only, I shall briefly describe my contributions to the field of superradiant lasers in this section.

The broad research theme in our lab seeks to exploit collective atomic effects to advance precision measurements in ways that single atom physics cannot. Going below the standard quantum limit via collective cavity-aided QND measurements as demonstrated in this thesis has been one of the major thrusts in our lab. A parallel thrust in our lab is to explore a relatively unexplored regime of the Schawlow-Townes linewidth limit and sensitivity to cavity frequency pulling by studying steady-state superradiant lasers that operate deep in the bad-cavity regime in which the cavity linewidth κ is much greater than atomic gain medium linewidth Γ.

In Ref. [48], we realized the first quasi-continuous laser that operates with < 1 intra-cavity photon on average. The system relies on collectively enhanced emission known as superradiance. Our system relies on Raman transitions between ground hyperfine states of ^{87}Rb, and serves as a physical analogue to future ultra-narrow lasers based on highly forbidden optical transitions in atoms such as Sr, Yb, Ca or Mg [49]. In a superradiant laser, defined by its operation in the bad-cavity limit ($\kappa \gg \Gamma$), the phase flywheel resides in the collective atomic coherence instead of the cavity field, as is the case in a good-cavity optical laser ($\kappa \ll \Gamma$); the roles of the atoms and photons are partially swapped compared to a good-cavity laser. The standard Schawlow-Townes linewidth and the cavity-pulling equations apply only in the good-cavity limit but analogous limits apply to a bad-cavity laser with the roles of the cavity linewidth κ and atomic gain medium linewidth Γ interchanged.

While our superradiant Raman laser does not possess an ultra-narrow linewidth, it is an extremely useful test-bed to explore the physics of superradiant lasers over the parameter space spanned by the induced spontaneous Raman decay rate Γ from $\sim 2\pi \times (0.3\text{ Hz})$ to $2\pi \times (100\text{ Hz})$, thus operating in the regime relevant to some candidate optical clock transitions [50]. The lasing transition decay rate is tuned via the Raman dressing laser intensity and detuning in our Raman model system. In contrast, the decay rate of optical clock transitions is fixed by nature.

Building on the fact that the superradiance can be dynamically controlled with the Raman-dressing laser, we demonstrated and analyzed a proof-of-concept hybrid active-passive sensor of collective atomic coherence [51] in an atomic clock configuration. We have also applied the hybrid sensor concept in a magnetometer configuration demonstrating both wideband and narrowband sensing of magnetic fields [52].

In our Raman superradiance system, dispersive tuning of the dressed cavity mode with atomic populations gives rise to rich dynamics, namely cavity feedback mechanisms, that are not present in the original proposal paper [49]. We have observed and analyzed the amplitude stability of Raman superradiant lasers using our ^{87}Rb model system and revealed a cavity feedback mechanism that can damp or amplify the superradiant laser output amplitude depending on the relative detuning between the Raman-dressing laser and the dressed-cavity mode [53].

In summary, our ^{87}Rb Raman superradiant laser provides a useful model system for studying how future superradiant lasers might operate, and for understanding potential limitations to their stability.

1.3 Organization of Thesis

Having described my contributions to superradiant lasers research, I shall devote the rest of this thesis to spin squeezing.

In Chapter 2, I present an overview of spin squeezing, provide a summary of other spin squeezing-related results and methods, and develop a high-level description of how we generate spin squeezed states via collective cavity quantum non-demolition measurements. This then provides a natural transition point to delve into the theoretical details of our method in Chapters 3 and 4 [54]. To achieve spin squeezing, sub-projection noise measurement sensitivity is required. Sub-projection noise limited measurements are useful not only for squeezing, but also for low noise readout of a Ramsey interferometer experiment. In Chapter 3, we theoretically analyze projection-noise-limited cavity-aided nondemolition measurements as a function of the cavity detuning from atomic resonance. The first half of Chapter 4 then discusses the three types of probe-induced back-action and derives limits on the measurement imprecision of the collective spin projection J_z. Squeezing requires sufficient preservation of coherence when probing with sub-projection noise measurement sensitivity. The second half of Chapter 4 derives limits on the spectroscopic enhancement relative to the SQL attainable by balancing probe measurement imprecision against probe-induced back-action.

The core of this thesis is in Chapter 5, where we experimentally demonstrate the generation of conditionally spin-squeezed states in a large $N = 7 \times 10^5$ ensemble via cavity-aided QND measurements [12]. The theory developed in the previous chapters are important for understanding the experiment. In Chapter 6, we discuss scalings and advantages of probing the coupled atoms-cavity system in the resonant limit. Experimental data demonstrating some of these advantages are presented.

Performing microwave rotations that add little noise relative to the SQL for the large ensemble size used in our squeezing experiment turns out be be a non-trivial undertaking. In Chapter 7, we provide experimental details for performing precise microwave rotations that enabled the squeezing results of Chapter 5. Besides relying on suppression or cancellation of static errors, a low phase noise microwave local oscillator source that adds little noise to the squeezed quadrature is employed [55]. Chapter 8 presents a linear response theory for quantifying the impact of local oscillator phase noise, or equivalently detuning noise, on rotations of a Bloch vector [56]. Experimental verification of special cases of the theory are demonstrated.

Finally, in Chapter 9, I consider our experimental squeezing results in the context of recent squeezing results and also frame our work more broadly as it pertains to the precision measurement and quantum metrology community. As an outlook to the next generation of QND measurement squeezing experiments in our lab, I analyze the amount of optimal squeezing attainable by probing on an optical cycling transition for ^{87}Rb and show that it could potentially realize much larger amounts of spectroscopic enhancements that demonstrate Heisenberg-like scaling with ensemble size [54]. This analysis is relevant to current efforts in the lab that have already yielded quite promising improvements in squeezing. Finally, I suggest some experimental improvements to the current setup, and finish with a brief summary.

Chapter 2

Spin Squeezing: Overview and Context

This Chapter reviews concepts related to spin squeezing. To begin, I present a convenient mathematical representation of collective spins useful for understanding Ramsey spectroscopy with ensemble spins. The standard quantum limit (SQL) set by the projection noise of un-entangled atoms in a CSS is derived. A discussion on going beyond the SQL with entangled spin-squeezed states and the Wineland criterion [57, 58] for quantifying spectroscopic enhancement is given. Different methods of generating spin squeezed states and recent experimental results are discussed, together with considerations of their relative advantages and disadvantages. Finally I give a elementary outline of our experiment that generates conditionally spin squeezed states using collective cavity QND measurements. Though elementary, the basic description captures the essential physics and also provides a natural transition to Chapter 3, where I present the theory of quantum projection noise limited measurements via cavity-aided probing of an atoms-cavity system. For a recent review on the theoretical and experimental aspects of spin squeezing, I point the reader to Ref. [59].

2.1 Collective Spins, Coherent Spin States, and the SQL

This section lays the foundations for describing collective spins and coherent spin states that will be relied upon throughout the thesis. Notation developed here also carries through to the end of the thesis.

2.1.1 Collective Spins

The concept of a collective spin is an elegant visualization and formalism for discussing Ramsey spectroscopy with an ensemble of N spin-1/2 atoms. A collective spin $\hat{\mathbf{J}}$ is simply a sum over its constituent spins $\hat{\mathbf{s}}^{(i)} = \frac{1}{2}(\hat{\sigma}_x^{(i)}, \hat{\sigma}_y^{(i)}, \hat{\sigma}_z^{(i)})$

$$\hat{\mathbf{J}} = \sum_{i=1}^{N} \hat{\mathbf{s}}^{(i)} \,. \tag{2.1}$$

The collective spin $\hat{\mathbf{J}} = \hat{J}_x \hat{x} + \hat{J}_y \hat{y} + \hat{J}_z \hat{z}$ may be described by its collective spin operators $\hat{J}_k$ given by the sum over the individual spin operators (Pauli matrices) $\frac{1}{2}\hat{\sigma}_k^{(i)}$, where $k = \{x, y, z\}$

$$\hat{J}_k = \sum_{i=1}^{N} \frac{1}{2} \hat{\sigma}_k^{(i)} \,. \tag{2.2}$$

The mean spin components are then given by expectation values of the collective spin operators as $J_k = \langle \hat{J}_k \rangle$. Since the Pauli matrix $\hat{\sigma}_z^{(i)}$ is given by $|\uparrow_i\rangle\langle\uparrow_i| - |\downarrow_i\rangle\langle\downarrow_i|$, the collective spin operator $\hat{J}_z$ can also be expressed as the population difference as

$$\hat{J}_z = \frac{\hat{N}_\uparrow - \hat{N}_\downarrow}{2} \,, \tag{2.3}$$

where $\hat{N}_\uparrow = \sum_i |\uparrow_i\rangle\langle\uparrow_i|$ and $\hat{N}_\downarrow = \sum_i |\downarrow_i\rangle\langle\downarrow_i|$ are the collective atomic population operators for spin up and spin down respectively. Unlike $\hat{J}_x$ and $\hat{J}_y$, the collective population difference $\hat{J}_z$ is a directly and easily measurable quantity via fluorescence detection or other methods. Throughout this thesis, $\hat{J}_z$ will be considered to be the spin projection that can be measured in experiments. Other spin projections can be accessed by first rotating the collective spin and then measuring the spin projection $\hat{J}_z$.

The collective spin operators obey the angular momentum commutation relations $[\hat{J}_i, \hat{J}_j] = i\epsilon_{ijk}\hat{J}_k$ where ϵ_{ijk} is the Levi-Civita symbol. The commutation relations lead to a Heisenberg uncertainty relationship between ΔJ_z and ΔJ_y given by

$$\Delta J_z \Delta J_y \geq |J_x|/2 \,, \tag{2.4}$$

where $\Delta J_z = \sqrt{\langle \hat{J}_z^2 \rangle - \langle \hat{J}_z \rangle^2}$ is the standard deviation of the measurement outcomes of the spin projection J_z for many identical preparations and measurements of the same collective spin state (and similarly for the spin projection J_y). I note here that Eq. 2.4 is completely general. Specifically, it does not rely on any assumption of the orientation of the collective spin. Identical relationships can be written down by permuting the coordinate labels $\{x, y, z\}$, however, the relationship given by Eq. 2.4 is the relevant case for this thesis in which the mean spin will be oriented along $\hat{x}$. I shall show in the next section that the Heisenberg uncertainty relation is the source of uncertainty in quantum phase estimation. This source of uncertainty is fully equivalent to the random projection noise due to measurement-induced collapse.

2.1.2 Coherent Spin States and the SQL

Coherent spin states (CSS) are the most classical-like quantum states of a symmetric ensemble of N spin-1/2 particles. A CSS is made up of N identical but independent spin-1/2 particles with no quantum correlations/entanglement between the particles. Mathematically, a CSS is constructed by placing all the N particles in the same state

$$|\theta, \phi\rangle = \prod_{i=1}^{N} \cos\frac{\theta}{2}|\uparrow_i\rangle + e^{i\phi}\sin\frac{\theta}{2}|\downarrow_i\rangle \,. \tag{2.5}$$

The physical significance of θ and ϕ is that the mean spin vector $\mathbf{J} = \langle\hat{\mathbf{J}}\rangle = \langle\theta, \phi|\hat{\mathbf{J}}|\theta, \phi\rangle$ points in the direction given by the spherical coordinates (θ, ϕ) where θ is the polar angle and ϕ is the azimuthal angle (see Fig. 2.1(c)). The tip of the so-called Bloch vector resides on the surface of a sphere of radius $J = N/2$. Without considering fluctuations or noise in the spin projections, the vector will behave classically.

Quantum mechanics introduces uncertainty in the spin projections as introduced by the Heisenberg uncertainty relationships of the form Eq. 2.4. Our visualization of the CSS can be extended to include this quantum uncertainty by the addition of an isotropic noise distribution perpendicular to the mean spin at the tip of the vector as shown in Fig. 2.1(b). The size of the distribution conveys the magnitude of the rms fluctuations in the spin projections ΔJ_y and ΔJ_z.

The minimum magnitude and shape of the noise distribution for a CSS can be understood by realizing that it is a factorizable state. As a result the fluctuation of the total spin vector is

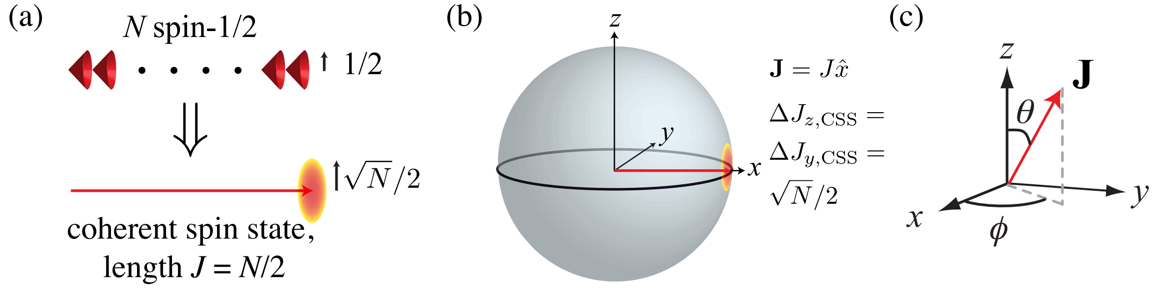

Figure 2.1: (a) Construction of a coherent spin state (CSS) from N identical but otherwise independent spins. Each spin-1/2 has length 1/2 and rms uncertainty 1/2 in directions orthogonal to the spin, visualized as an uncertainty cone. The length adds up coherently as $J = N/2$ while the uncorrelated noise averages to $\sqrt{N}/2$. (b) Bloch sphere representation of a CSS. In this illustration and for the rest of the thesis, I will assume the CSS is prepared along $\hat{x}$ unless otherwise noted. The quasi-probability distribution for the CSS noise in J_y and J_z or equivalently the mean spin polar angle ϕ and θ respectively (coordinate system defined in (c)) is shown as a noise blob (red-orange disc) at the tip of the collective spin $\hat{\mathbf{J}}$ (red arrow). The standard quantum limit $\Delta\theta_{\text{SQL}} = \Delta\phi_{\text{SQL}} = 1/\sqrt{N}$ on quantum phase estimation with a CSS, formed by identically prepared but otherwise independent atoms, is set by the quantum noise $\Delta J_{z,\,\text{CSS}} = \Delta J_{\text{y},\,\text{CSS}} = \sqrt{N}/2$, normalized to the mean spin length $|\langle\hat{\mathbf{J}}\rangle| = N/2$ in the limit of small angles. (c) Coordinate system defining the collective spin polar angle θ and azimuthal angle ϕ. The cartesian components of the collective spin $\hat{\mathbf{J}}$ in the x, y and z directions are J_x, J_y and J_y.

just given by the incoherent sum of the fluctuations of the N individual spins as illustrated in Fig. 2.1(a). To be quantitative, I will assume for concreteness that the CSS is $|\pi/2, 0\rangle$ because this is the point of maximum sensitivity in Ramsey spectroscopy, discussed in the next section. The mean collective spin that represents this CSS is $\mathbf{J} = \frac{N}{2}\hat{x}$ so that $J_x = N/2$, see Fig. 2.1(b). Each individual spin in the CSS is in the state $|x\rangle = (|\!\uparrow\rangle + |\!\downarrow\rangle)/\sqrt{2}$. Using properties of the Pauli matrices, an individual spin has an uncertainty in the spin projection $\Delta s_z = \sqrt{\langle x|\hat{\sigma}_z^2|x\rangle - \langle x|\hat{\sigma}_z|x\rangle^2} = 1/2$. Similarly $\Delta s_y = 1/2$. As mentioned earlier, the uncertainties ΔJ_z is equal to the incoherent sum of the uncertainties of each individual spin Δs_z, with the result that $\Delta J_{z,\,\text{CSS}} = \sqrt{N}/2$. Similarly, $\Delta J_{\text{y},\,\text{CSS}} = \sqrt{N}/2$. Note that since $\Delta J_{z,\,\text{CSS}} \Delta J_{\text{y},\,\text{CSS}} = |J_x|/2$ saturates the Heisenberg uncertainty relation given in Eq. 2.4, the CSS corresponds to a minimum uncertainty state.

The noise $\Delta J_{z,\,\text{CSS}}$ along J_z is equivalent to quantum projection noise arising from measurement-induced probabilistic collapse of each spin in the ensemble into $|\!\uparrow\rangle$ or $|\!\downarrow\rangle$ [58]. Recall that each spin in the CSS $|\pi/2, 0\rangle$ is in the state $|x\rangle = (|\!\uparrow\rangle + |\!\downarrow\rangle)/\sqrt{2}$. In performing a projective population measurement, each spin would collapse into $|\uparrow\rangle$ or $|\downarrow\rangle$ with probability 1/2 each, *independent* of what the other spins are doing. Therefore, for N spins, the resulting collective spin population $N_\uparrow$ in $|\uparrow\rangle$ would be $N/2$ on average. Random and independent collapse of each of the N spins into $|\uparrow\rangle$ or $|\downarrow\rangle$ results in Poissonian fluctuations or equivalently shot noise around the average. It is no surprise then that the rms collective spin population fluctuation $\Delta N_\uparrow = \sqrt{N}/2$ contains the famous $\sqrt{N}$ smoking gun for shot noise fluctuations. The same could be said for the collective spin population $N_\downarrow$. However, the fluctuations $\Delta N_\uparrow$ and $\Delta N_\downarrow$ are anti-correlated, that is $\Delta N_\uparrow = -\Delta N_\downarrow$, due to conservation of particle number $N_\uparrow + N_\downarrow = N$. Thus, the rms fluctuations $\Delta N_\uparrow$ and $\Delta N_\downarrow$ translates into an equivalent rms uncertainty in the collective spin projection J_z via $\Delta J_z = \Delta(N_\uparrow - N_\downarrow)/2 = \sqrt{N}/2$. This uncertainty ΔJ_z is exactly the same as the CSS uncertainty $\Delta J_{z,\,\mathrm{CSS}}$ derived earlier, demonstrating the equivalence of $\Delta J_{z,\,\mathrm{CSS}}$ and quantum projection noise.

Information in a quantum sensor is ultimately encoded in a polar angle θ which must be estimated from measurements of J_z or equivalently collective spin populations $N_\uparrow$ and $N_\downarrow$. Heisenberg uncertainty relations sets a fundamental limit on our ability to measure the collective spin polar angle θ or azimuthal angle ϕ. In the small angle limit, the fluctuations in the spin projection J_z sets a limit on the uncertainty $\Delta\theta_{\mathrm{SQL}}$ given by

$$\Delta\theta_{\mathrm{SQL}} = \frac{\Delta J_{z,\,\mathrm{CSS}}}{|\langle\hat{\mathbf{J}}\rangle|} = \frac{1}{\sqrt{N}}\,, \tag{2.6}$$

a limit known as the standard quantum limit (SQL) for a coherent spin state[1] . In this thesis, we will experimentally demonstrate that quantum nondemolition measurements can be used to generate entanglement and realize phase estimation uncertainty below the SQL.

2.2 Ramsey Spectroscopy with Coherent Spin States

In this section, I will review the canonical Ramsey spectroscopy that is used in a broad range of atomic sensors, and show how the SQL for quantum phase estimation can be surpassed by using

---

[1] The standard quantum limit is not really "standard" in the sense that different communities define an equivalent SQL for their very specific measurement context, just like we do here in the context of quantum phase estimation using Ramsey spectroscopy. For example, in the field of opto-mechanics, the SQL for measuring a simple harmonic oscillator's position is reached at a measurement strength where the measurement imprecision is equal to the added noise from measurement back-action [60].

entangled states in Ramsey spectroscopy.

Ramsey spectroscopy with a CSS proceeds as shown in Fig. 2.2(a). The collective spin is first prepared in the CSS $|\theta=\pi,\phi=0\rangle=\prod_{i=1}^{N}|\downarrow\rangle$. An initial $\pi/2$-pulse about the $-\hat{y}$-axis rotates the collective spin up to the x-axis, producing the state $|\theta=\frac{\pi}{2},\phi=0\rangle=\prod_{i=1}^{N}\frac{|\uparrow_i\rangle+|\downarrow_i\rangle}{\sqrt{2}}$. The rotation is induced with electromagnetic radiation at frequency ω_{LO} nearly resonant with the spin transition frequency $\omega_{\uparrow\downarrow}$. The collective spin is now allowed to evolve for a duration T_{evol} such that each constituent spin acquires a phase $\phi=(\omega_{\uparrow\downarrow}-\omega_{\mathrm{LO}})T_{\mathrm{evol}}$ in the spin up state relative to the spin down state in a frame rotating at frequency ω_{LO}. The CSS wavefunction at the end of the evolution time is given by $|\theta=\frac{\pi}{2},\phi\rangle=\prod_{i=1}^{N}\frac{|\uparrow_i\rangle+e^{i\phi}|\downarrow_i\rangle}{\sqrt{2}}$, corresponding to a precession of the collective spin through an angle ϕ.

The goal of Ramsey spectroscopy is to measure ϕ very precisely. Because one cannot measure ϕ directly, ϕ is mapped onto the the collective spin projection $J_z=(N_\uparrow-N_\downarrow)/2$ which is measurable via fluorescence detection or other methods. This mapping is performed by a final $\pi/2$-pulse about the $\hat{x}$-axis and leaves the collective spin in the final state $|\frac{\pi}{2}-\phi,0\rangle=\prod_{i=1}^{N}\cos\frac{\pi/2-\phi}{2}|\uparrow_i\rangle+i\sin\frac{\pi/2-\phi}{2}|\downarrow_i\rangle$ up to a global phase. At this stage, the phase information ϕ has been translated into the polar angle θ. The collective spin projection of the final state that is measured is $J_z=\frac{N}{2}\sin\phi$. During the measurement process, wavefunction collapse of the individual spins from a superposition state to one of the eigenstates $|\uparrow\rangle$ or $|\downarrow\rangle$ results in quantum projection noise, sometimes called atom shot noise, $\Delta J_z=\frac{\sqrt{N}}{2}\cos\phi$ in the measurement result. See Fig. 2.3(a) for the resulting signal and projection noise.

The rms uncertainty $\Delta\phi$ in determining ϕ is set by ratio of the quantum projection noise ΔJ_z to the slope of the Ramsey signal $dJ_z/d\phi$

$$\Delta\phi=\frac{\Delta J_z}{|dJ_z/d\phi|}=\frac{1}{\sqrt{N}}\,, \tag{2.7}$$

which is independent of ϕ. In the presence of technical noise, it is advantageous to operate at the point of maximum slope $\phi=0,\,\pi$. Note that this derivation shows that the quantum-limited signal-to-noise (i.e. no additional sources of noise other than quantum projection noise) in Ramsey

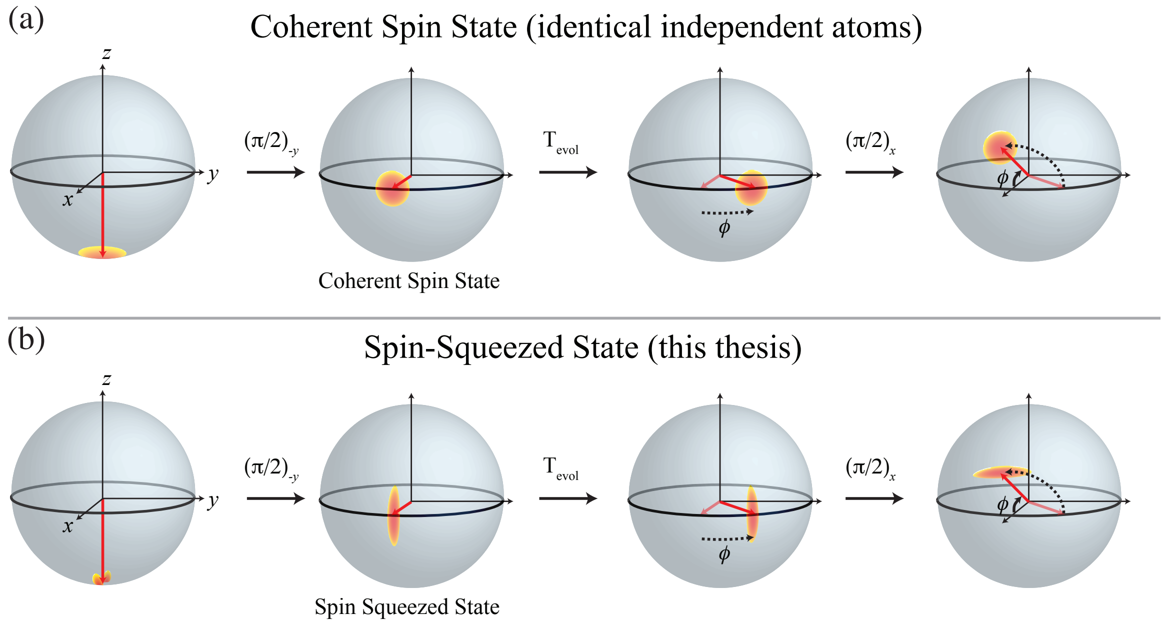

Figure 2.2: Ramsey spectroscopy with a coherent spin state (a) and a spin squeezed state (b) illustrated in a frame rotating at the LO frequency. In (a) and (b), a $\pi/2$ global rotation rotates the collective spin (red arrow) from pointing along $-\hat{z}$ to $\hat{x}$. The fuzzy disc/ellipse at the tip of the collective spin represents its intrinsic quantum noise. During the evolution time T_{evol}, the collective spin freely precesses about the z-axis and accumulates a phase $\phi = (\omega_{\uparrow\downarrow} - \omega_{\text{LO}})T_{\text{evol}}$. The phase is then mapped onto populations, equivalently J_z with a final $\pi/2$ rotation about $\hat{x}$. The observable J_z is then read out with fluorescence detection or other techniques. Measurement-induced-collapse of the wavefunction results in quantum projection noise ΔJ_z. In the illustration, ΔJ_z is given by the projection of the quantum noise distribution onto the z-axis. The goal of this thesis is to generate entangled spin squeezed states for quantum metrology.

spectroscopy with a CSS is exactly the SQL $\Delta\phi_{\text{SQL}} = 1/\sqrt{N}$ described earlier.

To go beyond the SQL set by un-entangled atoms, quantum entanglement can be used to either lower the quantum projection noise ΔJ_z or increase the slope $dJ_z/d\phi$. Spin squeezing, the subject of this thesis, employs the former strategy at the expense of increased noise in ΔJ_y which is not observed, while maximally entangled cat states employ the latter strategy [61–67].

2.3 Surpass SQL with Spin Squeezed States

In Fig. 2.2(b), I show how the spin squeezed states we generate in our experiment can be used in Ramsey spectroscopy to surpass the SQL. The Ramsey sequence is only sensitive to noise in one quadrature so that the quiet quadrature can be used, while the noisy quadrature is not

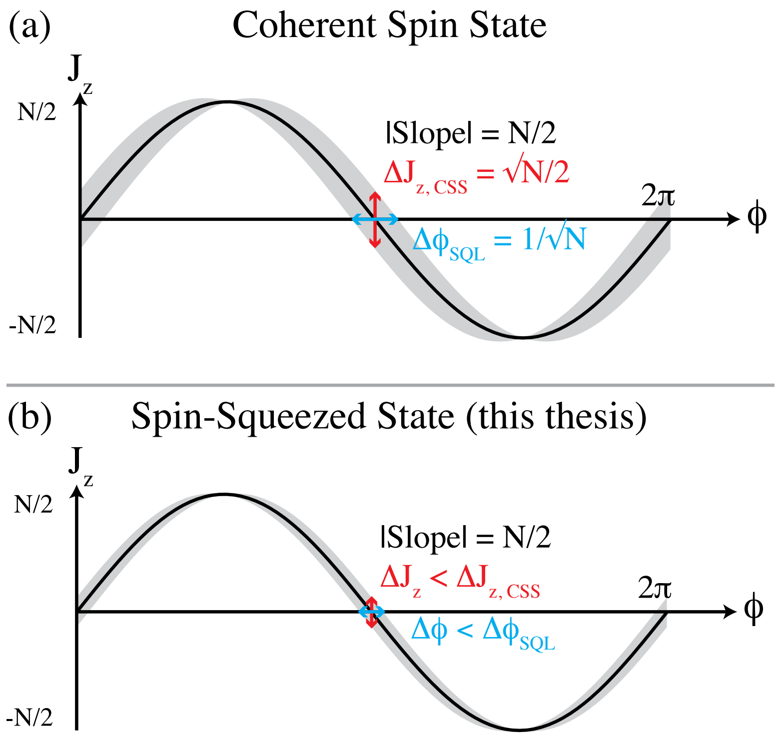

Figure 2.3: Ramsey spectroscopy signals with a CSS input (a) and a spin squeezed state input (b). The shaded area represents rms fluctuations in the measured observable J_z that would be observed if the experiment is repeated many times. (a) Using large ensembles of N un-entangled atoms averages the quantum projection noise as $\Delta J_{z,\,\mathrm{CSS}} = \sqrt{N}/2$, as exemplified by the CSS. The quantum projection noise $\Delta J_{z,\,\mathrm{CSS}}$ in conjuction with the slope of the Ramsey signal sets the SQL for the phase uncertainty $\Delta\phi_{\mathrm{SQL}} = 1/\sqrt{N}$. (b) The phase sensitivity can be enhanced beyond the SQL by using a spin squeezed state with reduced projection noise $\Delta J_z < \Delta J_{z,\,\mathrm{CSS}}$.

used. Spin squeezed states reduce the projection noise ΔJ_z that appears during the readout, while maintaining the same signal slope $dJ_z/d\phi$, therefore enhancing phase sensitivity beyond the SQL, as illustrated in Fig. 2.3(b).

Having seen how squeezing can improve the spectroscopic sensitivity of Ramsey spectroscopy, it is important to quantify the amount of spectroscopic enhancement relative to the SQL. Squeezing has been defined various ways in the literature. The review article [59] provides a comprehensive list of spin squeezing definitions.

As we are primarily interested in applying squeezing to metrology, we shall take spin squeezing to be spectroscopic enhancement $\xi_{\mathrm{m}}^{-1} \equiv (\Delta\theta_{\mathrm{SQL}}/\Delta\theta)^2$ relative to the SQL $\Delta\theta_{\mathrm{SQL}} = 1/\sqrt{N}$ set by the CSS, where $\Delta\theta$ is the polar angle uncertainty of the spin squeezed state. Since we generate squeezed states with reduced uncertainty in the polar angle in this thesis, we use θ here instead of ϕ. Spin squeezing with $\xi_{\mathrm{m}}^{-1} \geq 1$ represents a spectroscopic enhancement in sensitivity that must arise from entanglement [68]. Entanglement, while necessary, is not a sufficient condition for spectroscopic enhancement [68].

The above definition for spectroscopic enhancement, synonymous with squeezing in this thesis, is referred to as the Wineland criterion [57, 58] in the literature. The Wineland criterion accounts for both spin noise reduction and the coherence or Ramsey contrast $\mathcal{C} = |\langle \hat{\mathbf{J}} \rangle|/J$ of the resulting state, where $J = N/2$ is the mean spin length corresponding to the fully symmetric CSS of N spin-1/2 particles. Experimentally, the mean spin length $|\langle \hat{\mathbf{J}} \rangle|$ is measured via Ramsey spectroscopy or Rabi flopping. The measured J_z oscillates with an amplitude set by the mean spin length $|\langle \hat{\mathbf{J}} \rangle|$ as the angle between the mean spin and the rotation axis is varied in Ramsey spectroscopy or as the pulse area is varied in Rabi flopping. The spectroscopic enhancement can be expressed as the signal-to-noise ratio in the following form

$$\xi_{\mathrm{m}}^{-1} = \left(\frac{\Delta J_z}{\Delta J_{z,\,\mathrm{CSS}}} \right)^{-2} \mathcal{C}^2 \,. \tag{2.8}$$

Accounting for the loss of signal is important because in generating spin squeezed states, the mean spin length $|\langle \hat{\mathbf{J}} \rangle|$ may be reduced below its initial value $J = N/2$. See Fig. 2.7 for an illustration.

A related quantity frequently encountered in the spin squeezing literature is the spin noise reduction

$$\xi_{\mathrm{n}}^{-1} \equiv \left(\frac{\Delta J_z}{\Delta J_{z,\,\mathrm{CSS}}} \right)^{-2} \tag{2.9}$$

defined by Kitagawa and Ueda [69]. It is sometimes referred to as number squeezing, especially in the context of Bose-Einstein Condensates. It is possible to have number squeezing according to the definition 2.9 and yet have phase estimation sensitivity worse than the SQL.

2.4 Generation of Spin Squeezed States

Spin squeezed states in large ensembles have been generated using many diverse approaches. Generally, the approaches may be divided into two experimental categories as: atom-light interaction-based and atomic collisions-based squeezing. The underlying mechanism that creates squeezing can be broadly divided into two categories that exploit two different aspects of quantum mechanics: quantum non-demolition measurements and non-linear Hamiltonians. In the following sections, I will discuss these approaches, review demonstrated squeezing results, and discuss their relative advantages and disadvantages from the perspective of applying squeezing to metrology. To facilitate discussion, I will assume the collective atomic spin is initially prepared in a CSS along $\hat{x}$.

2.4.1 Collisional Interactions

In Bose-Einstein Condensates, atom-atom collisions lead to a nonlinear term in the Hamiltonian $H_{\mathrm{OAT}} = \chi \hat{J}_z^2$ [68] ($\hbar = 1$ here), referred to as the one-axis twisting (OAT) Hamiltonian by Kitagawa and Ueda [69]. To explain how squeezing is generated, consider the evolution of a CSS along $\hat{x}$ under this Hamiltonian. The Dicke states [70] $|J, M\rangle$ are eigenstates of the OAT Hamiltonian with eigenvalue χM^2, and evolves phase in time as $e^{-i\chi M^2 t}$. This implies the precession frequency of the state $|J, M\rangle$ scales linearly with M as $2\chi M$ in a rotating frame whose frequency is proportional to M. As the CSS is a (weighted) superposition of the Dicke states, the noise components of the CSS with larger M would precess faster than those with smaller M. Also, noise components with positive M would precess in the opposite sense compared to noise components with negative M. This process is depicted pictorially in Fig. 2.4 with the resulting noise distribution sheared such that noise in one direction is lower than the CSS projection noise[2] . The shearing process can be viewed as arising from twisting the Bloch sphere about the z-axis, hence the name one-axis twisting. A small rotation can be performed to rotate the squeezed quadrature to lie along $\hat{y}$ or along $\hat{z}$.

---

[2] Our semi-classical picture of shearing of the noise distribution breaks down when the shearing wraps around the Bloch sphere, where in fact the system would evolve into a cat state appropriate for Heisenberg-limited spec-

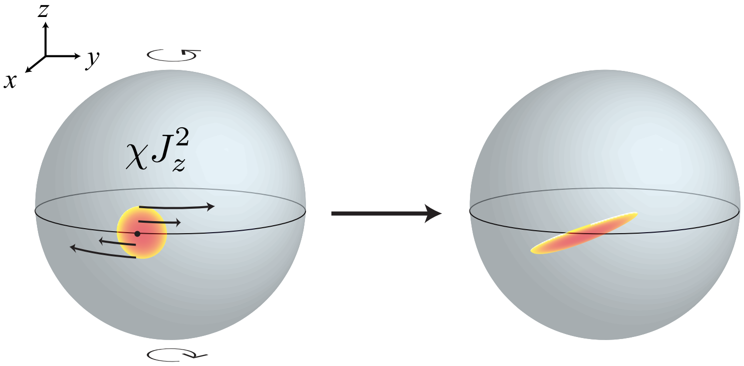

Figure 2.4: A CSS evolves into a spin squeezed state under a one-axis twisting Hamiltonian that creates a J_z-dependent precession frequency, causing the noise distribution to shear.

Recent experiments employing this collision-induced OAT has produced $\xi_{\mathrm{m}}^{-1} \sim 4$ to 8 dB of inferred squeezing after background subtraction in the groups of Oberthaler, Treutlein and Schmiedmayer [72–76] in ensemble sizes of $N \sim 400$ to 2000 atoms. It is in fact, not necessary to utilize Bose-Einstein Condensates, and anti-squeezing has been observed in the non-degenerate ^{87}Sr fermion optical lattice clock at JILA [77].

Direct collisional interactions causing parametric pair generation into two modes can generate two-mode squeezing, an effect analogous to parametric down conversion in non-linear optics. The states created are called twin-Fock states and ideally could attain Heisenberg-limited phase sensitivity $\Delta\theta_{\mathrm{HL}} = 1/N$ [78]. Because the mean spin length $|\langle\hat{\mathbf{J}}\rangle|$ is zero, an observable different from J_z is required [79]. Parametric two-mode squeezing has been demonstrated in the group of Klempt [80] with inferred squeezing $\xi_{\mathrm{m}}^{-1} = 2.5(1.0)$ dB at $N = 7\times10^3$. In related setups, parametric two-mode spin noise reduction has been observed in the groups of Schmiedmayer and Chapman [81, 82]. Continuous-variable entanglement with parametric pair generation has also been observed [83].

2.4.2 Light-mediated One-Axis Twisting Hamiltonians

Spin squeezed states have been prepared with atom-light interactions that generate effective long range interactions on demand (inferred squeezing $\xi_{\mathrm{m}}^{-1} = 9.6(1.0)$ dB at 3×10^4 atoms) in

---

troscopy [61, 71].

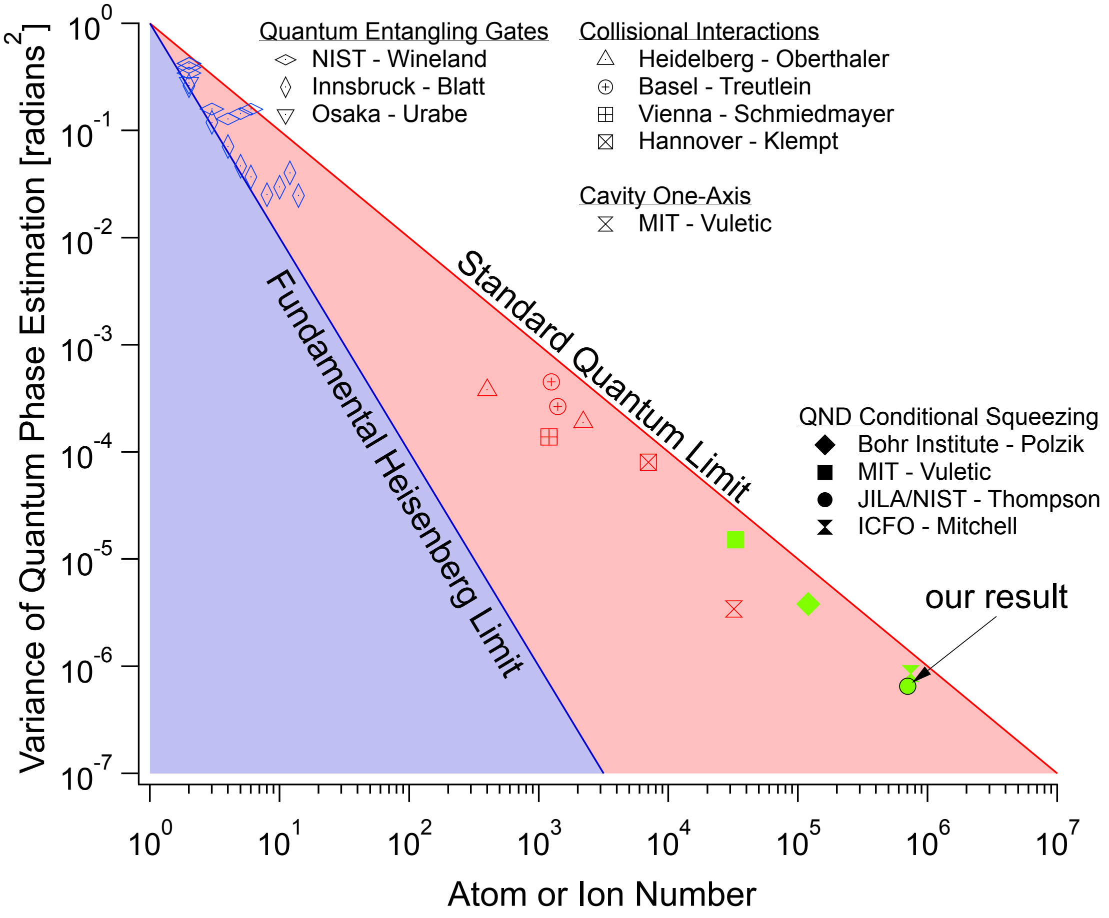

Figure 2.5: Graphical summary of results demonstrating spectroscopic enhancement arising from *inter-particle entanglement* to date (May 2013). Inferred values based on background subtraction are plotted. To emphasize the regimes that are technologically relevant for atomic sensors, the absolute phase uncertainty is plotted versus the ensemble size. Trapped ion optical clocks operate with < 10 ions [17]. Atom chip sensors (clocks, atom interferometers, magnetometers) operate with 10^2 to 10^4 atoms [84, 85]. Neutral atom optical lattice clocks operate with 10^3 to 10^5 atoms [16, 18]. Primary and secondary microwave frequency standards employ 10^5 to 10^6 atoms [14, 29]. Free space atom interferometers and vapor cell magnetometers operate with large ensembles from 10^5 up to 10^{12} atoms [19, 20, 23, 24, 86–88]. The ranges provided here are approximate, and certainly will change as technology evolves.

Nearly maximally entangled states generated in ion traps are depicted in blue, spin-squeezed states generated by atomic collisions or light-mediated interactions in red, and conditional squeezing via QND measurements in green.

The absolute phase uncertainty *inferred* after subtracting out the readout and other technical noise sources from the observed phase uncertainty is plotted where available. When not available, the observed phase uncertainty is plotted. The inferred phase uncertainty represents the potential for spectroscopic enhancement when all other noise sources are made negligible. The readout can be separately optimized from the generation of entanglement or squeezing in principle.

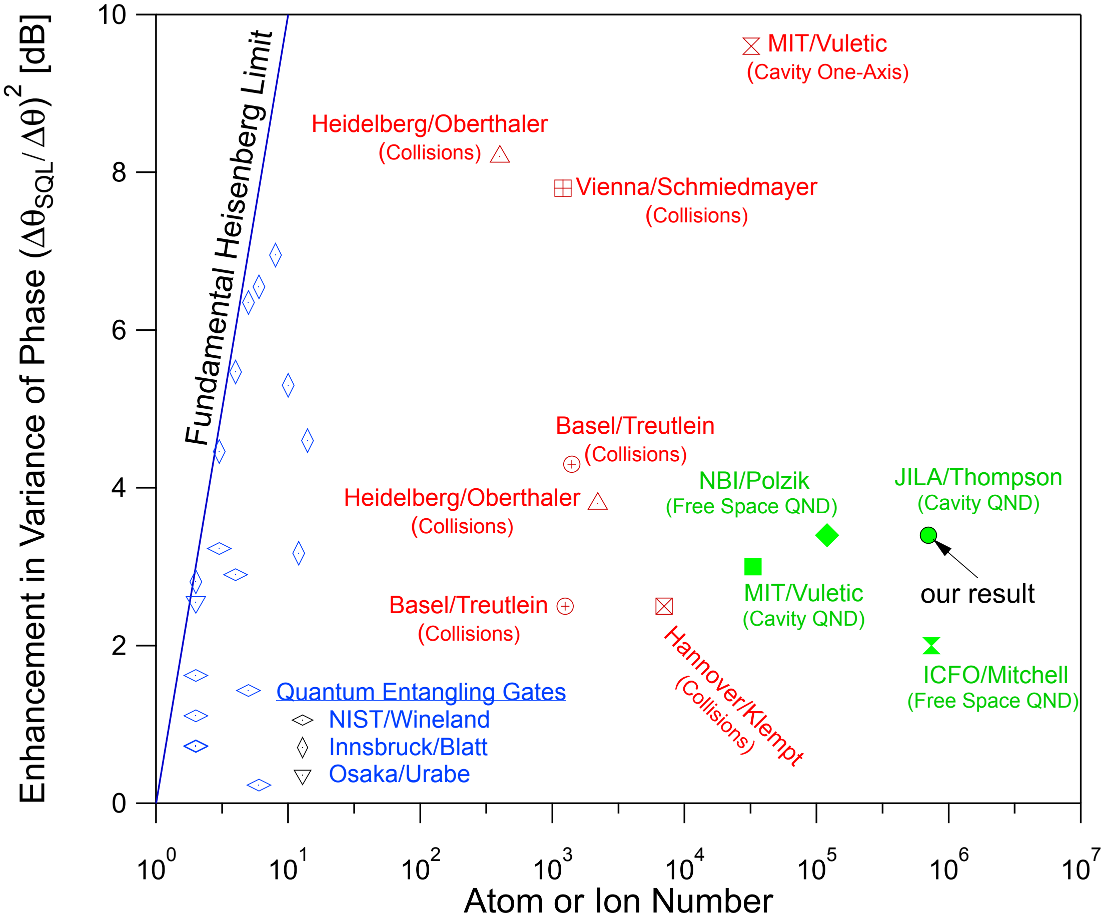

Figure 2.6: Same data as Fig. 2.5, plotted with inferred spectroscopic enhancement in dB on the vertical axis for better visibility. Nearly maximally entangled states generated in ion traps are depicted in blue, spin-squeezed states generated by atomic collisions or light-mediated interactions in red, and conditional squeezing via QND measurements in green.

a cavity-QED setup [89]. In brief, the approach demonstrated in Ref. [89] begins by imprinting quantum fluctuations ΔJ_z of the collective spin onto probe light which is then filtered by a cavity response and finally fed-back onto the collective spin. The cavity feedback is tuned such that it imposes a J_z -dependent ac-Stark shift, i.e. precession frequency, thus implementing an effective OAT Hamiltonian. Inherent dissipation in this approach due to free space scattering of probe light, and noise associated with photon number fluctuations in the probe does not result in a truly coherent evolution. Theoretical proposals on coherent feedback methods to generate OAT have been developed for cavities [90, 91] and in free space [92, 93].

Internal state squeezing has been generated in large spin-f atoms using effective OAT Hamiltonians engineered by tensor light shifts [94, 95]. The internal state squeezing generates entanglement between the nuclear spin and the electronic spin without inter-atom entanglement. In Ref. [94], $\xi_{\mathrm{m}}^{-1} \sim 4$ dB of inferred squeezing within the $F = 3$ Zeeman manifold of ^{133}Cs was demonstrated with $N \sim 10^6$ atoms. In Ref. [95], $\xi_{\mathrm{m}}^{-1} = 2.7(8)$ dB of inferred squeezing within the $F = 4$ Zeeman manifold of ^{133}Cs using a macroscopic ensemble of $N \sim 10^{12}$ atoms.

2.4.3 Quantum Non-demolition Measurements

A quantum nondemolition (QND) measurement of J_z that also preserves coherence can be used to prepare conditionally spin squeezed states with spectroscopic sensitivity below the SQL [96–98], an approach successfully demonstrated in this thesis. In this thesis, we choose to make a distinction between nondemolition (ND) measurements and QND measurements, illustrated in Fig 2.7. In the QND measurement approach, probe light interacts with J_z such that the quantum fluctuation $\Delta J_{z,\,\mathrm{CSS}}$ is imprinted on the probe. Then a measurement performed on the probe will project the initial CSS into a post-measurement state consistent with the measurement outcome. If the measurement imprecision of the probe is sufficient to resolve projection noise fluctuations $\Delta J_{z,\,\mathrm{CSS}}$, then the post-measurement state would have its spin noise reduced below the CSS spin noise. Provided the coherence $\mathcal{C} = |\langle \hat{\mathbf{J}} \rangle|/J$ is sufficiently preserved by the measurement, as discussed earlier in Sect. 2.3, a conditionally spin squeezed state would result. The squeezing is conditional in

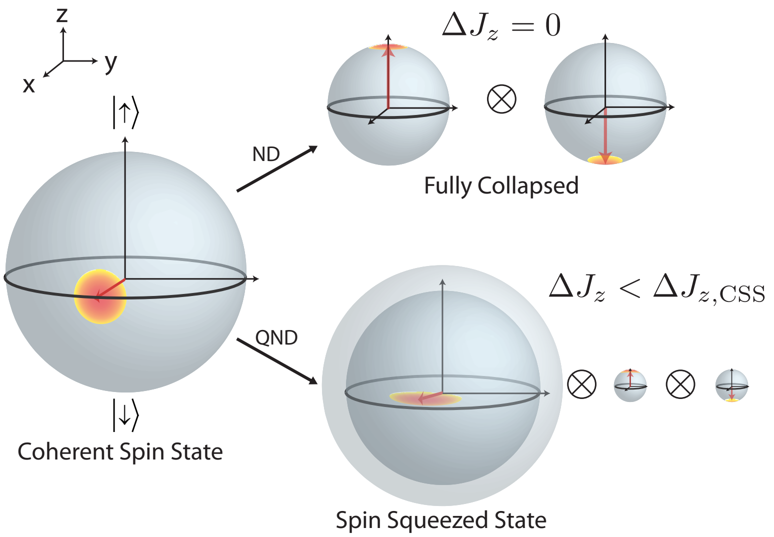

Figure 2.7: Visualization of a nondemolition (ND) (upper right) and a quantum nondemolition (QND) (lower right) measurement. A CSS for an ensemble of N spin-1/2 atoms prior to measurement is represented as a collective spin (red arrow) of length $J = N/2$. The quantum noise in the orientation of the collective spin is visualized as a quasi-probability distribution (red/yellow region) perpendicular to the mean spin, with rms opening angle at the SQL $\Delta\theta_{\mathrm{SQL}} = 1/\sqrt{N}$. A nondemolition measurement in this thesis refers to a measurement of of the spin projection $J_z = (N_\uparrow - N_\downarrow)/2$ with an rms imprecision $\Delta J_z < \Delta J_{z,\mathrm{CSS}} = \sqrt{N}/2$, and with the majority of the atoms remaining around in the trapping or probing region after the measurement. For example, in the ND measurement visualized on the right, the measurement imprecision is $\Delta J_z = 0$, but after the measurement the atoms are described by a product state of atoms in spin up and down due to single-atom information gained by the environment via free space scattering of light. We define a quantum nondemolition measurement to satisfy the additional requirement that a sufficiently large number of atoms remain in a coherent superposition of spin up and down such that the resulting state, conditioned on the measurement outcome, has a polar angle uncertainty $\Delta\theta < \Delta\theta_{\mathrm{SQL}}$ and can be used to sense a quantum phase below the SQL of an ensemble of uncorrelated atoms. The lower right QND example visualizes the conditional state as a product state of a spin-squeezed state and the atoms that have been collapsed into spin up and down.

the sense that the obtained spin squeezed state is randomly distributed within the range defined by the initial uncertainty $\Delta J_{z,\mathrm{CSS}}$ (see Fig. 2.8). Thus the produced squeezed state is random across independent experimental trials. If the measurement outcome is not used to predict the value of a subsequent measurement of J_z (within the same experimental trial), then no squeezing would be observed.

QND measurements of large atomic ensembles have recently become precision measurement tools with the demonstration of QND measurement-based spin-squeezing. In this thesis, cavity-

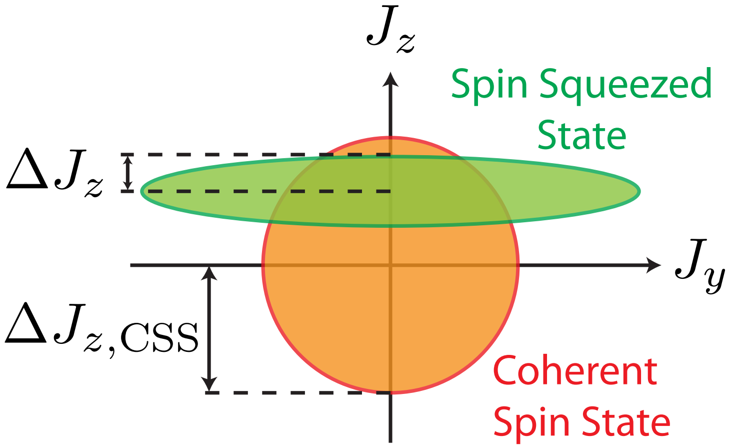

Figure 2.8: Concept of conditional squeezing via QND measurements. A QND measurement of the spin projection J_z of a CSS prepared along $\hat{x}$ would yield a random measurement outcome within the range set by the initial CSS uncertainty $\Delta J_{z,\mathrm{CSS}}$ (orange region). The QND measurement projects the state into one that is consistent with the measurement outcome and the measurement uncertainty. When the measurement uncertainty ΔJ_z is lower than the CSS uncertainty and coherence is sufficiently preserved (not shown), the post-measurement state would be a spin squeezed state with reduced uncertainty in J_z at the expense of increased uncertainty in J_y (green region), conditioned on the measurement outcome.

aided QND measurements of a large ensemble of pseudo-spins composed of the ^{87}Rb clock transition projects the ensemble into a conditionally spin squeezed state. The prepared spin squeezed state has an inferred spectroscopic improvement $\xi_{\mathrm{m}}^{-1} = 3.4(6)$ dB over the SQL. At $N = 7 \times 10^5$ atoms, this work represents the largest clock ensemble squeezed to date [12]. QND measurement squeezing has also been demonstrated for clock transitions with atoms in free space in Polzik's group (inferred squeezing $\xi_{\mathrm{m}}^{-1} = 3.4$ dB at $N = 1.2 \times 10^5$ [99]) and in a cavity in Vuletić's group (inferred squeezing $\xi_{\mathrm{m}}^{-1} = 3.0$ dB at $N = 3.3 \times 10^4$ [100]). In our work, the cavity mode couples to the atoms resonantly in the strong collective coupling regime of cavity-QED, generating two new normal modes, called the vacuum Rabi splitting, that contained equal wavefunction amplitudes in the atom and cavity components. We then probe both normal modes to project a CSS into a spin squeezed state. In a similar cavity-QED setup in Vuletić's group [100], the cavity frequency is tuned such that the cavity mode couples to the atoms in the far-detuned dispersive regime. In this case, the normal modes of the system remain mostly atom-like and cavity-like, with some dressing of the cavity by the atoms and vice versa. The cavity-like mode is then probeed to generate conditional spin squeezed states. Very recently, spin squeezing (inferred squeezing $\xi_{\mathrm{m}}^{-1} = 2.0$ dB at $N = 7.4 \times 10^5$ atoms) in a spin-1 system demonstrating inter-particle entanglement in a magnetometer configuration from Mitchell's group was reported [101]. Conditional two-mode squeezing of a room temperature vapor of $N = 10^{12}$ atoms has enabled magnetometry with $\xi_{\mathrm{m}}^{-1} = 1.5$ dB of observed spectroscopic enhancement and an increased measurement bandwidth [102]. Several experiments [103–106] have reported spin noise reduction without quantifying the loss of signal, so spectroscopic enhancements are not available for these results. Back-action was observed in Ref. [107]. Spin squeezing of optical lattice clocks using the trap lattice as a QND probe has been proposed [108]. A graphical summary of these and other squeezing results can be found in Figs. 2.6 and 2.5.

2.5 Relative advantages and disadvantages to different approaches

Spin squeezing based on atom-light interactions offers the advantage that the probe light can be completely turned off. As an additional bonus, low noise readout techniques that are required to read out the squeezed state are automatically present in the QND approach. In squeezing experiments exploiting direct atom-atom interactions, it is not clear if the collisional interactions required for generating squeezing can be turned off sufficiently. These interactions would cause systematic mean field shifts, i.e. inaccuracies, and quantum noise redistribution during Ramsey spectroscopy, and may destroy the squeezing or even make the phase resolution worse than the standard quantum limit. Conversely, it has been observed that relative number squeezing in atom interferometers can reduce fluctuations in the relative phase shift arising from fluctuating mean field shifts in the two interferometer paths [76, 109]. The collisional interaction strength χ can be tuned via magnetic Feshbach resonances or with state-dependent potentials, achieving about a factor of 100 in the on/off ratio in current experiments [73, 74]. Furthermore, inelastic collisions concomitant with the elastic collisions necessary to generate squeezing would degrade or even limit the amount of squeezing achievable, as was the case in Ref. [73].

For the particular approach of squeezing on the internal states within an atom, the maximum spectroscopic enhancement permissible is set by the Heisenberg limit corresponding to the number of internal states, and not by the ensemble size. Since the number of internal states is necessarily limited by atomic structure, this method is clearly not scalable. However, internal state squeezing may be combined with inter-atomic squeezing to produce larger amounts of squeezing [110].

Finally, in cavity-based approaches to spin squeezing, either using QND measurements or cavity feedback, the fundamental limit to the amount of squeezing is set by the collective cooperativity of cavity-QED physics, equivalent to optical depth in free space samples. The collective cooperativity is essentially the single pass optical depth of the sample multiplied by the number of bounces the light makes in the cavity, which is of the order of the cavity finesse F. Therefore compared to free space approaches, larger amounts of squeezing are attainable in a cavity at the same atomic densities. Alternatively, a cavity-based approach can achieve the same amount of squeezing as a free space experiment but at atomic densities lowered by order the cavity finesse F. The reduced atomic density would mitigate density shifts as a source of inaccuracy in the context of clock applications.

2.6 Other work on entanglement-enhanced metrology

Nearly maximally entangled states of 2 to 14 trapped ions have been generated in the groups of Wineland, Blatt and Urabe [62–67], with demonstrated observed spectroscopic sensitivities near the Heisenberg limit $\Delta\theta_{\mathrm{HL}} = 1/N$ as shown in Figs. 2.6 and 2.5. These states are typically generated via phonon-mediated global entangling gates [61] or phonon-mediated stimulated rapid adiabatic passage [67]. While trapped ion systems have demonstrated near-Heisenberg limited sensitivity, it may be nontrivial to scale up the method and the ion number to achieve large absolute spectroscopic gains. Further, it is an open question as to whether such approaches could be applied to much larger neutral atom systems that lack long-range Coulomb interactions.

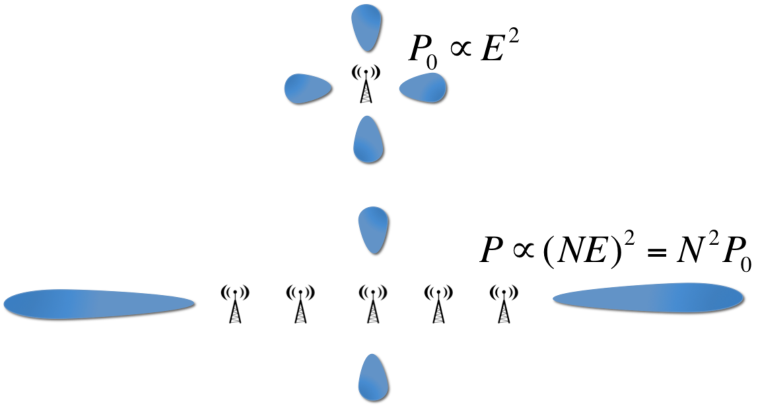

Figure 2.9: Phase array analogy to collectively enhanced coupling. A single classical dipole radiates isotropically with power P_0 proportional to the the radiated electric field E^2 (top panel). An array of phase synchronized classical dipoles radiate with a factor of N enhancement, a phenomena known as superradiance, over an array of dipoles with random phases (not shown) into the "end-fire" modes due to constructive interference in the electric field amplitudes (bottom panel). Consequently, the phase array radiates at single dipole rates (on average) in directions different from the end-fire modes due to destructive interference. The collective enhancement can be viewed as arising from the collective coupling of the dipoles to the end-fire modes. The collective coupling causes the array to decay into the end-fire modes faster than decaying into all other modes (directions). The same concept applies to array of quantum atomic dipoles. The phase of a quantum atomic dipole is set by the relative phase between $|\uparrow\rangle$ and $|\downarrow\rangle$ in a superposition state of $|\uparrow\rangle$ and $|\downarrow\rangle$. Strong collective coupling to an array of atoms to a probe mode may be achieved in free space with optically dense samples along the probing direction. In the strong collective coupling regime, collective information about the ensemble can be extracted from a detuned probe mode faster than the rate of decoherence via free-space-scattering into the all directions. The collective coupling can be enhanced by putting the sample in an optical cavity, the approach pursued in this thesis, so that the probe light interacts with the same sample multiple times.

2.7 Outline of our squeezing experiment

In this section, I provide an elementary outline that captures the essential physics of how we generate spin squeezed states using cavity-aided QND measurements. In brief, we use $\sim 10^6$ ^{87}Rb laser cooled and trapped inside an optical cavity. The pseudo-spin-1/2 system is comprised of the microwave clock states $|\uparrow\rangle \equiv |F=2, m_F=0\rangle$ and $|\downarrow\rangle \equiv |F=1, m_F=0\rangle$, see Fig. 2.10(a) for schematic. The two-level system we utilized is a pseudo-spin-1/2 because the transition frequency between $|\uparrow\rangle$ and $|\downarrow\rangle$ does not tune with a magnetic field to first order. We prepare a CSS along $\hat{x}$ by optical pumping into $|\downarrow\rangle$ followed by a $\pi/2$ rotation with resonant microwaves. At this point, each

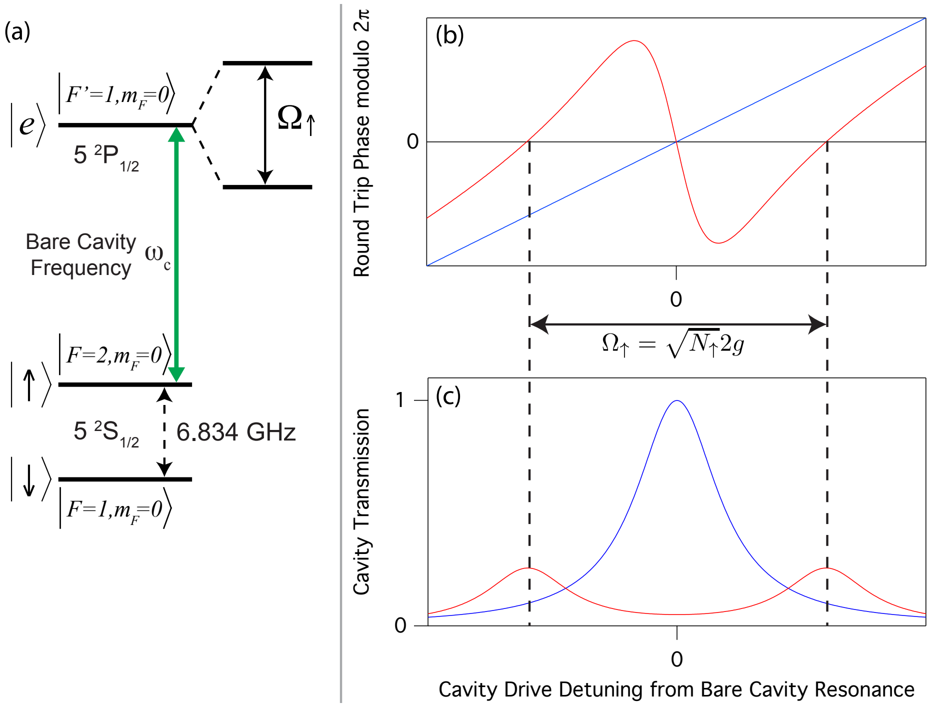

Figure 2.10: (a) Basic energy level scheme of the experiment. The pseudo-spin-1/2 system comprises of the microwave clocks states $|\uparrow\rangle \equiv |F = 2, m_F = 0\rangle$ and $|\downarrow\rangle \equiv |F = 1, m_F = 0\rangle$. The bare (empty) cavity frequency is degenerate with the atomic $|\uparrow\rangle$ to $|e\rangle \equiv |F' = 1, m_F = 0\rangle$ optical transition. The strong collective coupling of the atomic ensemble to the cavity mode creates a normal mode splitting, known as the collective vacuum Rabi splitting $\Omega_\uparrow$, which we probe to measure the collective spin population $N_\uparrow$. In our setup, only atoms in $|\uparrow\rangle$ couple to the cavity mode. (b) The origin of the collective Rabi splitting [111] is completely classical and can be understood as follows. A cavity transmission resonance occurs when the round trip phase shift of the light is an integer multiple of 2π due to constructive interference. In an empty cavity, the round trip phase shift is linear with cavity drive detuning (blue line), resulting in a single transmission resonance at the bare cavity frequency (and at multiples of the cavity free spectral range). An atomic medium in the cavity imposes a dispersive phase shift centered on the atomic resonance frequency on top of the free space propagation phase shift (red curve). In our probing scheme, the bare cavity frequency is degenerate with the atomic frequency. The two outer zero crossings result in transmission resonances while the middle zero crossing does not because of atomic absorption of resonant probe light. (c) Cavity power transmission curves corresponding to (b). The frequency splitting between the transmission resonances is called the Rabi splitting $\Omega_\uparrow$. In our experiment, $\Omega_\uparrow = \sqrt{N_\uparrow}2g$ where $2g$ is the single atom Rabi frequency.

atom is in the same superposition state $(|\uparrow\rangle + |\downarrow\rangle)/\sqrt{2}$. The atoms behave like little pieces of glass with state-dependent refractive index. The phase shift imposed by the atoms on the cavity mode causes the cavity resonance frequency to shift depending on the *collective populations* $N_\uparrow$ in spin up and $N_\downarrow$ in spin down. To simplify the discussion, I assume for now that the cavity frequency shift is proportional to the collective spin projection $J_z = (N_\uparrow - N_\downarrow)/2$. By measuring the cavity resonance frequency precisely[3] , we can measure J_z precisely, but in a way that does not reveal *which* atom is in spin up or down, therefore preserving coherence. The collective coupling of the ensemble to the cavity mode, which extracts collective information, over the rate of free space scattering into all other modes, is the mechanism for preservation of coherence. This collective enhancement in an atoms-cavity system is analogous to the enhancement in emission rate in the "end-fire" directions of a phased array antenna, illustrated in Fig. 2.9.

We first measure J_z with measurement imprecision below the projection noise limit $\Delta J_{z,\,\mathrm{CSS}}$, thus conditionally projecting the initial CSS into a state with reduced spin noise. In order to verify the spin noise reduction, we show that repeated measurements of the same CSS are correlated below the projection noise level. In order to claim spectroscopic enhancement, we measure the mean spin length $|\langle \hat{\mathbf{J}} \rangle|$ with a Ramsey sequence and show that the coherence (contrast) is sufficiently preserved after the first pre-measurement such that the net signal-to-noise of the post-measurement state is improved beyond the SQL for un-entangled atoms.

Most cavity-aided probing experiments have operated in the dispersive regime. In our experiment, we actually operate in the resonant regime of strong collective coupling cavity-QED. We access this regime by setting the bare cavity frequency to be resonant with the atomic optical transition frequency as shown in Fig. 2.10(a). The resonant exchange of cavity photons and atomic excitations leads to a normal mode splitting when the coupling rate $\Omega_\uparrow$ exceeds the dissipation rates due to cavity power decay rate κ and atomic optically excited state decay rate Γ. The origin of the normal mode splitting, also called the collective vacuum Rabi splitting, arises from dispersive phase shifts imposed by the atomic medium (see Fig. 2.10(b, c), and is therefore completely classical in nature [111]. In our probing scheme, the Rabi splitting $\Omega_\uparrow = \sqrt{N_\uparrow} 2g$ depends only on the collective spin population $N_\uparrow$ and the single atom Rabi frequency $2g$ set by the atomic optical dipole moment and the electric field of a single cavity photon. In order to measure J_z, which requires knowledge of $N_\uparrow$ and $N_\downarrow$, we first prepare a CSS along $\hat{x}$ and measure the size of the Rabi splitting to determine

---

[3] As is well known, a good way to measure any quantity precisely is to convert it into a frequency.

$N_\uparrow$. We then use a microwave π-pulse to phase coherently swap $N_\uparrow$ with $N_\downarrow$ and perform a second Rabi splitting measurement to determine $N_\downarrow$.

By operating in the resonant regime instead of the dispersive regime, we hope to reinforce the idea that the quality of a coherence-preserving QND measurement is *not* fundamentally linked to the probe's large detuning from atomic resonance. Instead, it is the magnitude of the collective cooperativity parameter $N_\uparrow C$ (equivalent to the optical depth for a free space experiment [38]) that sets the fundamental quality of the QND measurement. Here $C = (2g)^2/\kappa\Gamma$ is the single atom cooperativity, or equivalently the single atom optical depth. Operating in the resonant regime also offers advantages in terms of maximizing the absolute size of the cavity frequency fluctuations caused by projection noise, and technical relative probe-cavity frequency noise immunity.

Chapter 3

Theory: Probing atoms-cavity system with projection-noise-limited sensitivity

3.1 Introduction

Probing the collective spin state of an ensemble of atoms provides a means to reduce heating via the photon recoil associated with the measurement and provides a robust, scalable route for preparing highly entangled states with spectroscopic sensitivity below the SQL set by the CSS. The collective probing relies on obtaining a very large optical depth that can be effectively increased by placing the ensemble within an optical cavity such that the probe light passes many times through the ensemble. In this Chapter, we analyze projection-noise-limited cavity-aided nondemolition measurements as a function of cavity detuning δ_c from atomic resonance as well as cavity finesse, cavity length, cavity linewidth, mode waist, and atom number.

It is well known that significant improvements in readout sensitivity can be achieved by optically probing ensembles in free space along directions of large resonant optical depth. This approach has been extensively analyzed theoretically [38, 93, 96, 97, 112–119], and experimentally studied [99, 102, 103, 120–126].

More recently, the technique of free space probing of large optical depth samples has been extended to using optical cavities to effectively increase the optical depth of the atomic ensemble by passing the probe light through the same sample many times as shown in Fig. 3.1 [12, 98, 100, 107, 127–130]. In most of these experiments and proposals, the cavity is far-detuned from the optical transition that was probed. Operating in the resonant regime $\delta_c = 0$, as demonstrated in our squeezing experiment (Chapter 5), is an exception rather than the norm. In principle, the cavity detuning δ_c can be chosen almost arbitrarily. Therefore, a natural question to ask is: How does cavity detuning affect both the fundamental and technical atomic population measurement imprecision or the degree of spin squeezing for a given cavity geometry and cavity finesse?

To answer the question posed above, we provide detailed expressions in this chapter for the fundamental scalings for probing an atomic ensemble using an optical cavity that smoothly connects the resonant regime to the far-detuned regime in this Chapter. We apply our results to estimate the amount of free space scattering, equivalent to photon-recoil heating and potentially wave-function collapse of the ensemble when the cavity-aided measurement reaches an imprecision at the quantum projection noise level. The average number of photon recoils per atom sets the degree to which the measurement can be considered nondemolition. We show that the collective cooperativity parameter NC plays a crucial role in determining the resolution of cavity-aided nondemolition measurements. The collective cooperativity parameter NC plays a similar role to the resonant optical depth of atoms in free space, where N is the number of atoms in the probe volume and C is the single particle cooperativity parameter [131].

This Chapter is organized as follows. In Section 3.2, we begin with a review of the properties of the coupled atoms-cavity system including dissipation. This review also provides definitions and notation used throughout the thesis. In Section 3.3, we derive the quantum-limited signal-to-noise ratio for nondemolition measurements of atomic populations considered as a function of the cavity detuning δ_c from atomic resonance (see Fig. 3.1a). We identify three different operating regimes, a resonant regime and two detuned regimes separated by a critical detuning δ_c°.

3.2 Coupled atoms-cavity modes

To begin, we briefly review the open coupled atoms-cavity system with the goal of both providing a framework for understanding the experimental work and explicitly enumerating the assumptions made to reduce this system to a classical two-mode system [132–134]. The dynamics of the system under a classical drive and dissipation are then studied with the goal of obtaining the full complex response of the reflected and transmitted cavity field. Finally, a discussion of the

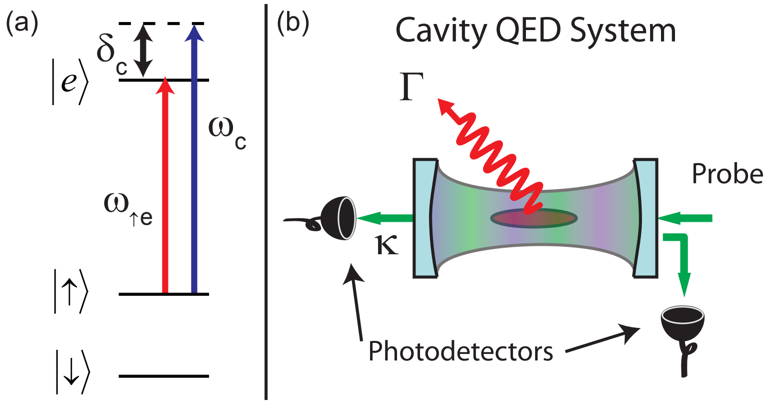

Figure 3.1: (a) Relevant energy levels. The pseudo-spin-1/2 system typically comprises two metastable states $|\uparrow\rangle, |\downarrow\rangle$, which are utilized in atomic sensors and clocks. The number of atoms $N_\uparrow$ in $|\uparrow\rangle$ modifies the cavity resonance frequency. Initially, we will assume the optically excited state $|e\rangle$ does not shift $|\downarrow\rangle$ because of dipole selection rules or because the coupling is highly non-resonant $\delta_c \ll \omega_{\mathrm{hf}}$, where ω_{hf} is the hyperfine frequency separation between $|\uparrow\rangle$ and $|\downarrow\rangle$. (b) Transmitted and/or reflected probe light is monitored to determine the cavity resonance frequencies and hence the number of atoms in $|\uparrow\rangle$. An applied NMR-like microwave rotation can swap the populations between ground states so that a subsequent measurement can also determine the $|\downarrow\rangle$ population $N_\downarrow$. The ensemble of atoms are trapped in an intracavity optical lattice (blue-green). The total cavity power decay rate is κ. Single atom spontaneous decay from $|e\rangle$ into non-cavity modes at rate Γ leads to photon recoil heating and single-atom wavefunction collapse. The goal then is to extract collective information from the probe mode more rapidly than the undesired single-atom photon scattering into free space.

probe signal-to-noise sets the stage for addressing measurement imprecision at the projection noise level in Section 3.3.

3.2.1 Linearized response

We consider an ensemble of N atoms with two ground states $|\uparrow\rangle$ and $|\downarrow\rangle$ whose populations we wish to estimate precisely. The ensemble is confined and collectively coupled to a cavity mode (see Fig. 3.1(b)). Atoms in $|\uparrow\rangle$ can interact with the cavity mode by absorbing a cavity photon and being promoted to an optically excited state $|e\rangle$. On the other hand, atoms in $|\downarrow\rangle$ are assumed to not interact with the cavity mode because of dipole selection rules, a large energy splitting between the ground states, or otherwise. A quantum phase may be encoded in the coherence between $|\uparrow\rangle$ and $|\downarrow\rangle$ for realizing an atomic sensor, but is otherwise not important in this section.

Ignoring dissipation, the Tavis-Cummings Hamiltonian that describes the coupled atoms-cavity system is

$$H = \hbar\delta_c \hat{c}^\dagger \hat{c} + \hbar g \left(\hat{\sigma}_- \hat{c}^\dagger + \hat{\sigma}_+ \hat{c} \right) . \tag{3.1}$$

The Hamiltonian is written in a frame rotating at the atomic transition $|\uparrow\rangle \rightarrow |e\rangle$ angular frequency $\omega_{\uparrow e}$. In this Chapter, we assume every atom couples to the cavity mode with the same coupling strength parameterized by the coupling angular frequency g. Appropriate renormalization of g and N in the case of inhomogeneous coupling will be given in Chapter 5. The cavity field is described by the photon annihilation operator $\hat{c}$, with cavity photon number given by $\hat{M}_c = \hat{c}^\dagger \hat{c}$. The cavity detuning is $\delta_c = \omega_c - \omega_{\uparrow e}$, where ω_c is the empty cavity frequency. The collective raising and lowering operators (no superscript (i)) $\hat{\sigma}_\pm = \sum_i \hat{\sigma}_\pm^{(i)}$ are written in terms of the single atom raising and lowering operators $\hat{\sigma}_+^{(i)} = |e_i\rangle\langle\uparrow_i|$ and $\hat{\sigma}_-^{(i)} = |\uparrow_i\rangle\langle e_i|$. The atomic populations are given by the collective projection operators $\hat{N}_\uparrow = \sum_i |\uparrow_i\rangle\langle\uparrow_i|$, $\hat{N}_\downarrow = \sum_i |\downarrow_i\rangle\langle\downarrow_i|$, and $\hat{N}_e = \sum_i |e_i\rangle\langle e_i|$. For brevity, we use the following abbreviations: $N_\uparrow \equiv \langle\hat{N}_\uparrow\rangle$, $N_\downarrow \equiv \langle\hat{N}_\downarrow\rangle$ and $N_e \equiv \langle\hat{N}_e\rangle$.

Although the atoms may in general exist in a superposition of $|\uparrow\rangle$ and $|\downarrow\rangle$, in the following analysis we will consider the atoms to be in a definite eigenstate $N_\uparrow$ of the $\hat{N}_\uparrow$ operator. We will then reintroduce the fluctuations in the operator $\hat{N}_\uparrow$ for atoms in a superposition of $|\uparrow\rangle$ and $|\downarrow\rangle$ in terms of the rms projection noise about the mean value $\Delta N_\uparrow = \sqrt{\left\langle (\hat{N}_\uparrow - \langle\hat{N}_\uparrow\rangle)^2 \right\rangle}$.

We assume that the system is driven weakly so that the mean number of atoms in the optically excited state $|e\rangle$ is a small fraction of the total number of atoms in $|\uparrow\rangle$, such that $N_e/N_\uparrow \ll 1$. In the weak excitation limit, one can make the Holstein-Primakoff approximation [135] that can be visualized as replacing the three dimensional vector describing the two-level system composed of states $|e\rangle$ and $|\uparrow\rangle$ by its vector projection onto the two dimensional $x-y$ plane (see Fig. 3.2(a)). When no probe light is applied, the system relaxes into its ground state orientation $-\hat{z}$. When the system is weakly excited by probe light, and a small fraction of the atoms are promoted to the optically excited state $|e\rangle$, the lowest order effect on the vector is a small angular deflection of the vector away from $-\hat{z}$.

In the Holstein-Primakoff approximation, one specifically replaces the atomic raising and

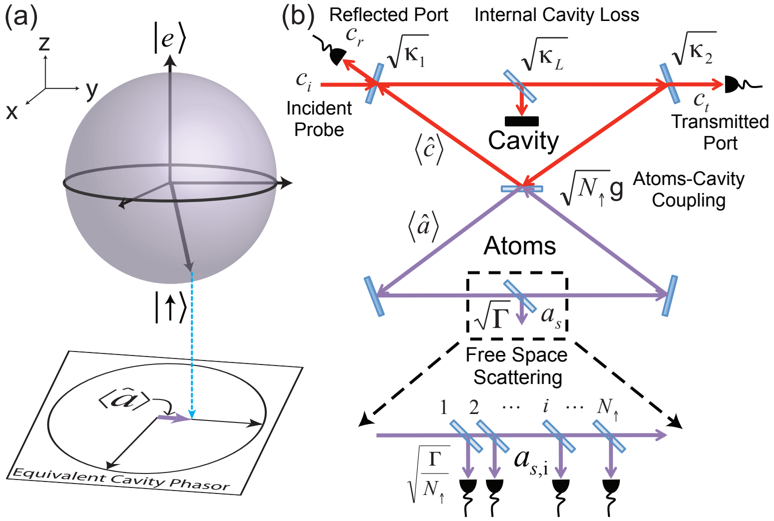

Figure 3.2: (a) Graphical representation of the linearization achieved via the Holstein-Primakoff approximation. The atomic sub-system $|\uparrow\rangle$ and $|e\rangle$ is described by a vector of length $(N_\uparrow + N_\mathrm{e})/2$. In the regime in which the probe light only weakly excites the atoms such that $N_\mathrm{e} \ll N_\uparrow$, the two-level system can be described by its projection onto a 2D plane equivalent to that describing a light field. (b) With this approximation, the collective atomic mode may be treated as an equivalent cavity mode (lower purple mode) whose coupling to the actual cavity (upper red mode) is governed by a partially reflecting mirror (center) described by a field coupling rate constant ($\sqrt{N_\uparrow}g$) that depends on the number of atoms in state $|\uparrow\rangle$. The physical mirrors have transmission coefficients described by the field coupling rates $\sqrt{\kappa_1}$ and $\sqrt{\kappa_2}$, and internal cavity losses are described by $\sqrt{\kappa_L}$, such that the total power decay rate is $\kappa = \kappa_1 + \kappa_2 + \kappa_L$. Decay of the atoms by emission of a photon into free space is described by the field transmission coefficient $\sqrt{\Gamma}$ that is the sum of the field scattering into free space modes by the atoms in $|\uparrow\rangle$. Because the scattered modes are distinguishable (expanded view of free space scattering port), it is possible to tell which atoms are in $|\uparrow\rangle$ from the free-space-scattered photons, destroying any coherent superposition between $|\uparrow\rangle$ and another state $|\downarrow\rangle$ (not shown) that may have been prepared for sensing a quantum phase.

lowering operators with effective creation and annihilation operators as $\hat{a}^\dagger \approx \hat{\sigma}_+/\sqrt{N_\uparrow}$ and $\hat{a} \approx \hat{\sigma}_-/\sqrt{N_\uparrow}$ that satisfy the usual commutation relation $[\hat{a}, \hat{a}^\dagger] = 1$. The number of atoms in $|e\rangle$ is described by the number operator $\hat{N}_e = \hat{a}^\dagger\hat{a}$. After substitution in Eq. 3.1, the resulting Hamiltonian describes the coherent coupling of two cavities through a beam-splitter whose transmission coefficient increases with the number of atoms in $|\uparrow\rangle$

$$H = \hbar\delta_c\hat{c}^\dagger\hat{c} + \hbar\sqrt{N_\uparrow}g\left(\hat{a}\hat{c}^\dagger + \hat{a}^\dagger\hat{c}\right) . \tag{3.2}$$

A visualization of the coupled cavities model is shown in Fig. 3.2(b). The coupled Heisenberg equations of motion for the cavity and atomic operators are

$$\begin{aligned}\frac{d\langle\hat{c}\rangle}{dt} &= -\imath\delta_c\langle\hat{c}\rangle - \imath\sqrt{N_\uparrow}g\langle\hat{a}\rangle\ , \\ \frac{d\langle\hat{a}\rangle}{dt} &= -\imath\sqrt{N_\uparrow}g\langle\hat{c}\rangle\ . \end{aligned} \tag{3.3}$$

The eigenfrequencies of the above coupled equations are

$$\omega_\pm = \frac{\delta_c \pm \sqrt{\delta_c^2 + \Omega_\uparrow^2}}{2}\,, \tag{3.4}$$

where

$$\Omega_\uparrow \equiv \sqrt{N_\uparrow}2g \tag{3.5}$$

is the collective vacuum Rabi splitting $\Omega_\uparrow$ that sets the difference in the normal mode frequencies $\omega_+ - \omega_-$ at zero detuning $\delta_c = 0$. The normal mode frequencies in the laboratory frame are $\omega_{\uparrow e} + \omega_\pm$. A useful relation for simplifying expressions involving the mode frequencies is $\omega_+\omega_- = -\Omega_\uparrow^2/4$.

Any arbitrary superposition of atomic and cavity amplitudes can be written in terms of complex normal mode amplitudes $B_\pm$ and unit vectors $\mathbf{b}_\pm$ as $(\langle\hat{c}\rangle, \langle\hat{a}\rangle) = e^{-\imath\omega_+ t}B_+\mathbf{b}_+ + e^{-\imath\omega_- t}B_-\mathbf{b}_-$. At resonance $\delta_c = 0$, the normal mode vectors are $\mathbf{b}_\pm = (1, \pm 1)/\sqrt{2}$, and the normal modes beat against one another at relative frequency $\Omega_\uparrow$. For example, if at $t = 0$ there are no atoms in the excited state, then $B_\pm = 1/\sqrt{2}$. The light in the cavity will Rabi flop (or be converted) into purely excited-state atoms after a time $\pi/\Omega_\uparrow$, and then Rabi flop back into light in the cavity after $2\pi/\Omega_\uparrow$.

More generally, the unit vectors can be expressed in terms of a mode-mixing angle $\theta_{\text{mix}} = \arctan(\Omega_\uparrow/2\omega_+)$ as $\mathbf{b}_+ = (\cos\theta_{\text{mix}}, \sin\theta_{\text{mix}})$, and $\mathbf{b}_- = (-\sin\theta_{\text{mix}}, \cos\theta_{\text{mix}})$. When $\delta_c \gg \Omega_\uparrow$, the $\mathbf{b}_+$ normal mode is predominantly cavity-like, while the $\mathbf{b}_-$ normal mode is predominantly atom-like. The converse is true when $\delta_c \ll -\Omega_\uparrow$. This normal mode structure is demonstrated in Fig. 3.3 with an experimental measurement, described in Chapter 5, of the transmitted probe power through the cavity as a function of the probe laser detuning δ_{pe} from the atomic transition frequency $\omega_{\uparrow e}$ and the cavity detuning δ_c.

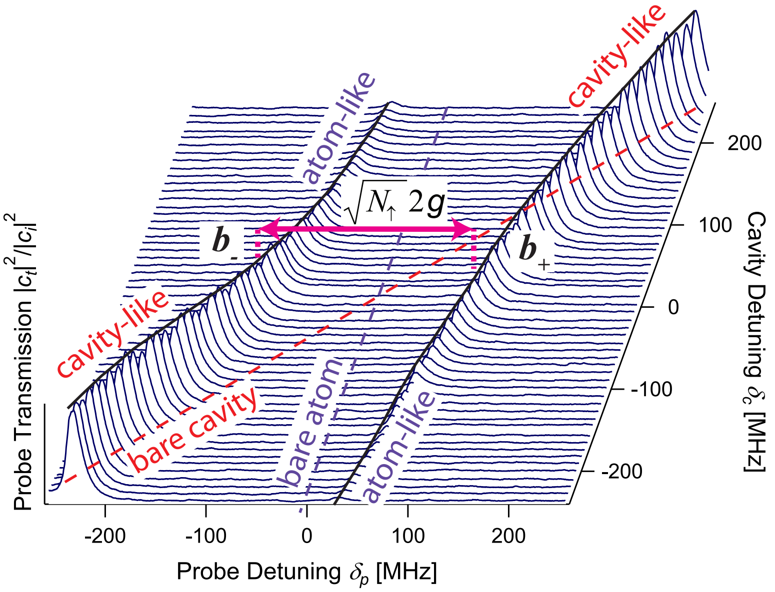

Figure 3.3: The normal modes of the coupled atoms-cavity system $\mathbf{b}_\pm$ exhibit an avoided crossing in the transmission spectrum at $\delta_c = 0$, where the size of the collective vacuum Rabi splitting is $\Omega_\uparrow = \sqrt{N_\uparrow}2g$.

3.2.2 Driven and damped dynamics

The Heisenberg equations of motion of Eq. (3.3) can be extended to include cavity damping and driving, as well as atomic damping via free space scattering of light (i.e., not into the cavity mode) as follows:

$$\begin{aligned} \frac{d\langle\hat{c}\rangle}{dt} &= -\left(\imath\delta_c + \frac{\kappa}{2}\right)\langle\hat{c}\rangle - \imath\sqrt{N_\uparrow}g\,\langle\hat{a}\rangle + \sqrt{\kappa_1}c_i\,, \\ \frac{d\langle\hat{a}\rangle}{dt} &= -\frac{\Gamma}{2}\langle\hat{a}\rangle - \imath\sqrt{N_\uparrow}g\,\langle\hat{c}\rangle\ . \end{aligned} \tag{3.6}$$

The complex amplitude c_i, with units of $\sqrt{\text{photons/sec}}$, describes the incident cavity driving field at frequency ω_p in the lab frame. As the above equation is written in a rotating frame at the atomic frequency $\omega_{\uparrow e}$, the cavity field c_i in Eq. 3.6 is $c_i = |c_i|e^{-i\delta_{pe}t}$ where $\delta_{pe} = \omega_p - \omega_{\uparrow e}$ is the drive detuning from the optically excited state $|e\rangle$. These equations include the additional non-unitary damping and drive terms shown schematically in Fig. 3.2(b). The additional terms are derived using input-output theory [136] and will now be discussed. But first, we note that at large $\Omega_\uparrow$, the finite damping terms introduce small corrections to $\omega_\pm$ of order $(\Gamma-\kappa)^2/\Omega_\uparrow$ [111] that may in general be safely neglected in this thesis as we always operate in the well-resolved vacuum Rabi splitting regime.

3.2.2.1 Cavity damping and input-output fields

As shown in Fig. 3.2(b), the damping of the cavity field at rate $\kappa/2 = (\kappa_1 + \kappa_2 + \kappa_L)/2$ is set by the mirror power transmission coefficients $T_{1,2}$ such that $\kappa_{1,2} = T_{1,2} \times f_{\mathrm{FSR}}$. The cavity free spectral range is $f_{\mathrm{FSR}} = c/2l$, with $2l$ being the round-trip cavity length, and c the speed of light. The total round-trip scattering and absorption fractional power losses at the mirrors L can be modelled by an additional beam splitter with field decay rate $\kappa_L = L \times f_{\mathrm{FSR}}$.

The cavity field is driven by an external incident probe field described by the complex amplitude c_i. The reflected and transmitted complex field amplitudes, c_r and c_t respectively, will be detected to infer the number of atoms in $|\uparrow\rangle$. The external field normalizations are chosen such that $|c_{i,r,t}|^2$ is the flux of incident, reflected, and transmitted probe photons in units of photons/second. The average number of incident, reflected, and transmitted photons $M_{i,r,t}$ in a measurement time interval from t' to $t' + T_m$ is then

$$M_{i,r,t} = \int_{t'}^{t'+T_m} \left|c_{i,r,t}(t'')\right|^2 \mathrm{d}t''. \tag{3.7}$$

In our experiments, it is convenient to express the number of probe photons coupled into the atoms-cavity system in terms of the directly measured "missing" photons in the reflected mode compared to the incident beam $M_m \equiv M_i - M_r$.

The steady-state reflected and transmitted fields can be found by first solving the coupled-driven Eq. (3.6) for $\langle \hat{c} \rangle$ in steady-state (which oscillates at the cavity drive frequency δ_{pe} in the rotating frame) and then using the results in the approximate relationships

$$\begin{aligned} c_r &= \sqrt{\kappa_1}\,\langle \hat{c} \rangle - c_i\,, \\ c_t &= \sqrt{\kappa_2}\,\langle \hat{c} \rangle\,, \end{aligned} \tag{3.8}$$

that hold in the limit of a high finesse cavity $T_{1,2}, L \ll 1$.

3.2.2.2 Atomic damping via free space decay

The atomic damping via scattering of light into free space (i.e. not into the cavity mode) is described by an effective amplitude damping rate $\Gamma/2$. To good approximation, the probability decay rate Γ is simply the single-particle excited state $|e\rangle$ decay rate in free space [1] . The rate of scattering into free space is described by the field amplitude $a_s = \sqrt{\Gamma}\,\langle\hat{a}\rangle$, normalized such that the rate of photons scattered into free space is simply $\dot{M}_s = |a_s|^2$.

The above picture of atomic damping can be further refined as shown in Fig. 3.2(b). While the decay of excitation from the cavity mirrors is single-mode in nature, the atoms scatter light into many free space modes. This multimode scattering can be envisioned by replacing the single decay process via a single mirror with $N_\uparrow$ independent weak beam splitters, i.e. one for each atom in $|\uparrow\rangle$. If the ensemble is optically thin along all directions except the cavity mode, then one can approximate that each atom decays into its own bath of states with an amplitude $a_{s,i} = \sqrt{\Gamma}\left(\langle\hat{a}\rangle/\sqrt{N_\uparrow}\right)$. The normalization is necessary to impose the fact that if a single photon is emitted into free space, the probability that it was the ith atom that scattered the photon is reduced as the number of atoms $N_\uparrow$ increases. The total scattering rate is the incoherent sum of the decay rates, reproducing the previous decay rate $\dot{M}_s = \Gamma\,|\langle\hat{a}\rangle|^2$. However, this refinement importantly emphasizes that the multimode free space scattering leads to in-principle information gain as to which particular atoms are in $|\uparrow\rangle$, causing single particle collapse of the atomic wavefunction from a coherent superposition into an energy eigenstate, for example $\left(|\uparrow\rangle + |\downarrow\rangle\right)/\sqrt{2} \rightarrow |\uparrow\rangle$, thus destroying coherence. In contrast, the decay of light through the cavity mirrors leads to only collective information as to how many atoms in total are in spin up and therefore preserves coherence. Thus information gained through the cavity will be useful for preparing conditionally spin squeezed states, while the free space scattering is a competing decoherence mechanism that serves to reduce the attainable degree of spin squeezing.

---

[1] The approximation that the single-particle decay rate Γ into all modes other than the cavity mode is not modified by the presence of the cavity holds true in the limit that the cavity subtends a small fraction of the total solid angle as seen by the atom [137].

3.2.2.3 Dressed mode linewidth

The atomic and cavity damping cause the normal modes to decay, resulting in a mode broadening or narrowing. The approximate Lorentzian full width at half maximum (FWHM) resonance linewidth given by a weighted average linewidth as

$$\kappa'_{\pm} = \frac{\kappa + \left(\frac{\Omega_{\uparrow}}{2\omega_{\pm}}\right)^{2}\Gamma}{1 + \left(\frac{\Omega_{\uparrow}}{2\omega_{\pm}}\right)^{2}} . \tag{3.9}$$

For measuring $N_{\uparrow}$ via a cavity drive, probing the normal mode that is farthest from atomic resonance, also known as the dressed cavity mode, is most useful because this mode decays predominantly via photons leaking out of the cavity which can be collected with high efficiency. In contrast, probing the normal mode closest to atomic resonance with a cavity drive results in most of the information being carried away by the free-space-scattered photons rather than leaking out through the cavity mode. For the sake of brevity, we refer to the further detuned mode's linewidth and frequency as simply κ' and ω such that $\kappa' = \kappa'_{\pm}$ and $\omega = \omega_{\pm}$ when $|\omega_{\pm}| \geq |\omega_{\mp}|$.

3.2.3 Full complex field response to probing

The reflected and transmitted fields relative to the incident field $c_{r,t}/c_i = I_{r,t} + \imath Q_{r,t}$ can be described in the complex plane by the real amplitudes $I_{r,t}$ and $Q_{r,t}$. We consider a single incident cavity drive, or equivalently cavity probe, close to resonance such that the probe frequency ω_p is detuned by $\delta_p = (\omega_p - \omega_{\uparrow e} - \omega)$ from the mode resonance frequency. We assume the probe is near resonance $|\delta_p| \ll \omega_+ - \omega_-$ and that the normal modes are well resolved $\omega_+ - \omega_- \gg \kappa'_{\pm}$ so that interference effects between normal modes can be ignored. The normalized transmitted electric field through the cavity is then, to a good approximation, given by

$$I_t = \frac{\mathcal{A}}{1 + (2\delta_p/\kappa')^2} , \tag{3.10}$$

$$Q_t = \frac{\mathcal{A}\,(2\delta_p/\kappa')}{1 + (2\delta_p/\kappa')^2} , \tag{3.11}$$

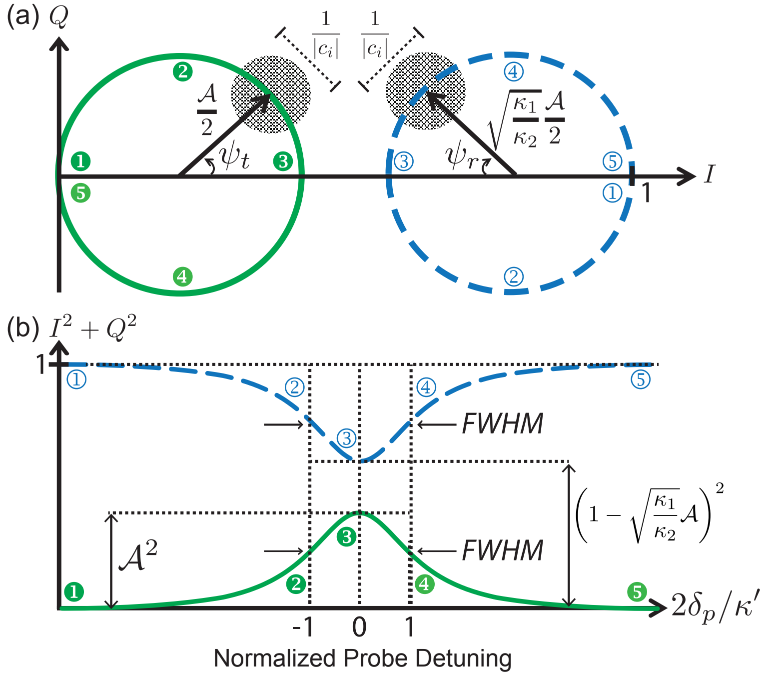

Figure 3.4: Transmitted and reflected probe electric fields from driving the atoms-cavity system through the cavity mode. (a) The electric field phasors trace out circles in the I, Q-quadrature plane as the probe detuning δ_p from the dressed cavity resonance varies from below to above resonance. The normalization is chosen such that the reflected electric field goes to 1 when far away from resonance. The quantum noise of the probe normalized to the incident electric field is represented as a fuzzy blob with rms diameter $1/|c_i|$. In this illustration, a symmetric cavity $\kappa_1 = \kappa_2$ is assumed, so that the circles have the same diameter $\mathcal{A}$. (b) Corresponding power transmission and reflection signals.

where the unitless amplitude $\mathcal{A}$ is given by

$$\mathcal{A} = \frac{2\sqrt{\kappa_1\kappa_2}}{\kappa + \Gamma\left(\frac{\Omega_\uparrow}{2\omega}\right)^2}\,. \tag{3.12}$$

From Eq. (3.8), the reflected field c_r is just the sum of the transmitted field (rescaled for relative transmission coefficients) and the promptly reflected field such that $I_r = 1 - \sqrt{\kappa_1/\kappa_2}I_t$, and $Q_r = \sqrt{\kappa_1/\kappa_2}Q_t$.

As shown in Fig. 3.4(a), the phasor c_t traces out a circle of diameter $\mathcal{A}$ in the complex plane as δ_p varies from $\ll -\kappa'$ to $\gg \kappa'$. The translation $I_t' = I_t - \mathcal{A}/2$ centers the circle traced out by the phasor $I_t' + \imath Q_t$ at the origin. One then sees that the angle with respect to the real axis is given by $\psi_t = \arctan(Q_t/I_t') = \arctan(2\delta_p/\kappa')$. Similarly, the translation $I_r' = I_r - (1 - \sqrt{\kappa_1/\kappa_2}\mathcal{A}/2)$

centers the circle traced out by the phasor $I'_r + \imath Q_r$ at the origin with the angle with respect to the real axis $\psi_r = \arctan(-Q_r/I'_r) = \psi_t$. The angles ψ_r and ψ_t are the same, but the quantum-limited estimation of these phases may be different if $\kappa_1 \neq \kappa_2$.

3.2.4 Probe vacuum noise and measurement imprecision

The size of the quantum vacuum noise that contributes uncertainty to measuring the position of the phasor is not changed by a linear transformation of coordinates in the complex plane. For our purposes, the noise can be described as a Gaussian probability distribution with equal and uncorrelated real and imaginary rms fluctuations of magnitude $\sigma_{\text{vac}} = 1/2$. The rms quantum vacuum uncertainty $\Delta\psi_t$ on the angle ψ_t is then independent of the average value ψ_t and is set only by the average number of detected photons in transmission $M_d = q_d M_t$ as

$$\Delta\psi_t = \frac{1}{2\sqrt{M_d}}\,. \tag{3.13}$$

The detection quantum efficiency q_d includes any light loss and any excess technical or thermal noise of the detector relative to vacuum noise. The uncertainty $\Delta\psi_t$ maps onto an uncertainty on the estimation of δ_p through $\Delta\delta_p = |d\delta_p/d\psi_t|\,\Delta\psi_t = \kappa'\Delta\psi_t/2\eta_d$. The detection sensitivity η_d is given by

$$\eta_d = \frac{1}{1 + (2\delta_p/\kappa')^2}\,. \tag{3.14}$$

Probing near resonance $\delta_p = 0$, one finds $\eta_d = 1$. For side-of-fringe probing $\delta_p = \kappa'/2$, one finds $\eta_d = 1/2$. If the probe frequency is linearly and adiabatically scanned from $\delta_p \ll -\kappa'$ to $\delta_p \gg \kappa'$ such that the total number of detected photons is fixed to the same M_d as in the two previous scenarios, one finds $\eta_d = 1/2$. The optimal readout assumes that as δ_p is changed, an adaptive homodyne readout [138] is employed to maximize the measurement sensitivity to small changes in ψ_t. For the spin squeezing experiment presented in Chapter 5, heterodyne detection is employed so that adaptive detection is not required. However, the effective quantum efficiency q_d was reduced by 1/2 as a result of the heterodyne detection.

It is straightforward to extend the analysis to a probe signal detected in reflection. However, one must parameterize in terms of the measurable average number of missing photons in the reflection port M_m and the average number of incident photons M_i such that in Eq. (3.13), one substitutes $M_d \to (\kappa_2/\kappa_1) M_i q_d (1 \mp \sqrt{1 - M_m/M_i})^2$ when $\mathcal{A}\sqrt{\kappa_1/\kappa_2} \lesseqgtr 1$.

3.3 Quantum-limited signal-to-noise and free space scattering

The measurement of the atomic population $N_\uparrow$ in $|\uparrow\rangle$ is achieved by precisely measuring the dressed mode frequency ω_+ or ω_- or some combination of the two (as was done in our spin squeezing experiment described in Chapter 5). In essence, the approach used here converts the problem of measuring an atomic population into a frequency measurement. For atoms in a coherent superposition of $|\uparrow\rangle$ and $|\downarrow\rangle$, quantum projection noise in the atomic population $N_\uparrow$ causes the dressed mode frequency to fluctuate.

In this section, we derive the fluctuations on the dressed mode frequency due to quantum projection noise as a function of cavity detuning δ_c. We then use the results of Section 3.2 to obtain the average number of detected probe photons M_d^{proj} and free-space-scattered photons per atom m_s^{proj}, when the measurement imprecision on the probe field is sufficient to resolve the projection noise fluctuations of the mode frequency $\Delta\omega^{\mathrm{proj}}$. The quantity m_s^{proj} is the *key figure of merit* that characterizes the degree to which a measurement is nondemolition. Three limits of cavity probing are identified, and a summary table of various key quantities in different regimes is presented.

3.3.1 Projection-noise-driven fluctuations of mode frequencies

As stated earlier, the atom number $N_\uparrow$ can be determined by precisely measuring one or both dressed mode frequencies ω_+, ω_- with a cavity probe. The collective enhancement of the Rabi splitting by $\sqrt{N_\uparrow}$ produces a key enhancement of the measurement sensitivity needed to resolve projection noise. To concretely analyze the measurement imprecision of the probing, we consider a measurement procedure most relevant to Ramsey spectroscopy as shown in Fig. 2.2(a): we assume that for each experimental trial, all of the $N \gg 1$ total atoms are initially prepared in spin down via optical pumping or otherwise. Each atom is then rotated into an equal superposition of spin up and down, preparing the ensemble in a CSS along $\hat{x}$. As discussed in Chapter 1, in a CSS prepared along $\hat{x}$, the population in spin up and down fluctuate about the average $N_\uparrow = N_\downarrow = N/2$ with equal magnitude but perfectly *anti-correlated* projection noise fluctuations $\Delta N_\uparrow = -\Delta N_\downarrow = \sqrt{N}/2$ so that $\Delta J_{z,\,\mathrm{CSS}} = \Delta(N_\uparrow - N_\downarrow)/2 = \sqrt{N}/2$.

The rms fluctuation $\Delta\omega^{\mathrm{proj}}$ of the individual mode frequencies $\omega_\pm$ caused by the projection-noise-driven fluctuations in $N_\uparrow$ is found by linear expansion as $\Delta\omega^{\mathrm{proj}} = |d\omega_\pm/dN_\uparrow|\Delta N_\uparrow$ evaluated at $N_\uparrow = N/2$. Making use of Eq. (3.4), one finds

$$\Delta\omega^{\mathrm{proj}} = \frac{g}{2\sqrt{2}}\frac{\Omega_\uparrow}{\sqrt{\Omega_\uparrow^2 + \delta_c^2}}\,. \tag{3.15}$$

Note that $\Delta\omega^{\mathrm{proj}}$ depends on $N_\uparrow$ via the Rabi splitting $\Omega_\uparrow$. The fluctuations of the two mode frequencies are equal in magnitude but opposite in sign such that the rms differential fluctuation is $\Delta(\omega_+ - \omega_-)^{\mathrm{proj}} = 2\Delta\omega^{\mathrm{proj}}$.

The projection noise variance $(\Delta\omega^{\mathrm{proj}})^2$ decreases as a Lorentzian versus the bare cavity detuning δ_c with half width at half maximum (HWHM) $\Omega_\uparrow$. Figure 3.5(b) shows this scaling with detuning (black, left curve). The technical requirements on the experiment for resolving $\Delta\omega^{\mathrm{proj}}$ are increased with detuning. Other experimental imprecision and inaccuracies scale relative to the mode linewidth κ' that one must split to the level of $\Delta\omega^{\mathrm{proj}}$, therefore the ratio $\Delta\omega^{\mathrm{proj}}/\kappa'$ is shown in Fig. 3.5(b, left) for three different bare cavity linewidths $\kappa/\Gamma = 0.01, 1, 100$ (blue, red, green). Note that in the good cavity limit $\kappa/\Gamma \ll 1$ (blue), the experimental requirement on splitting the mode line can be somewhat reduced at larger detuning owing to the rapid fall off of κ' as $1/\delta_c^2$ in the approximate region $\delta_c/\Omega_\uparrow \in \{1, 10\}$.

3.3.2 Fundamental measurement imprecision and free space scattering at arbitrary detuning δ_c

The resonance frequency ω of the dressed-cavity mode is measured relative to the known frequency of a coherent (and unsqueezed) laser probe. The rms uncertainty on the probe detuning

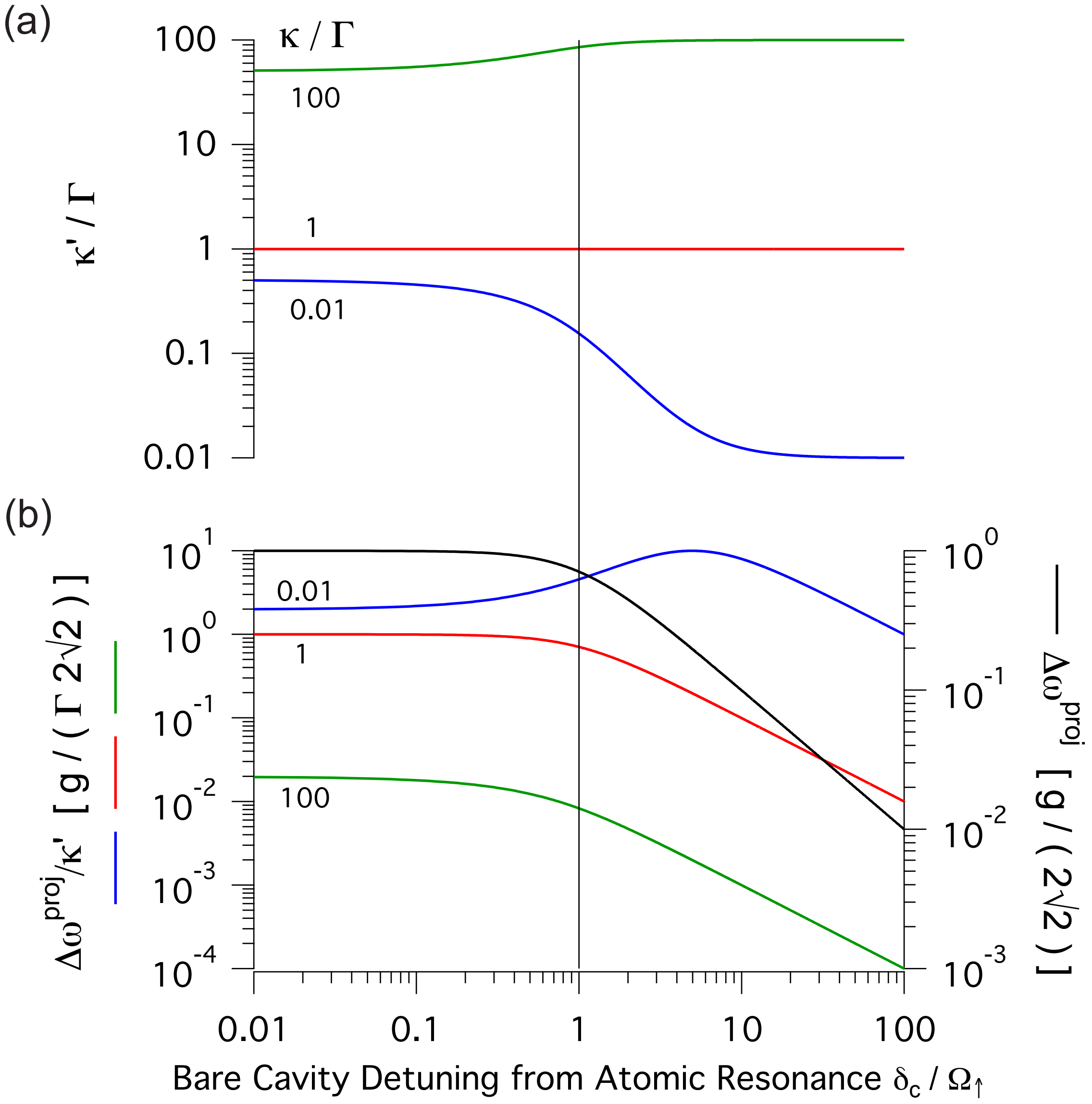

Figure 3.5: Theoretical scaling of key quantities with cavity detuning δ_c expressed in units of the the collective vacuum Rabi splitting $\Omega_\uparrow$. (a) The dressed cavity linewidth κ' in units of the atomic excited state linewidth Γ. In (a) and (b), the scaling for different cavity finesses is shown for $\kappa/\Gamma =$ 0.01, 1, and 100 (blue, red, and green, respectively). (b, right, black curve) The rms fluctuation of the dressed cavity mode frequency due to projection noise fluctuations $\Delta\omega_+^{\text{proj}}$ decreases as $1/\delta_c$ above $\delta_c/\Omega_\uparrow = 1$. The normalization is chosen such that one should multiply by $g/2\sqrt{2}$. (b, left, red, blue, green curves). The ratio of the projection noise fluctuation of the cavity mode to the dressed cavity linewidth $\Delta\omega^{\text{proj}}/\kappa'$ is shown normalized such that the plotted values should be multiplied by $g/(2\sqrt{2}\Gamma)$. A large ratio is desirable because technical noise may limit the ability to split the probed resonance by more than a fractional amount.

$\Delta\delta_p$ is equal to the projection noise fluctuation level $\Delta\omega^{\mathrm{proj}}$ at an average detected photon number of

$$M_d^{\mathrm{proj}} = \frac{1}{2\eta_d}\left(\frac{\kappa'}{g}\right)^2\left(1+\frac{\delta_c^2}{\Omega_\uparrow^2}\right). \tag{3.16}$$

The passage of light through the cavity also leads to the scattering of $M_s = |a_s|^2 T_m$ probe photons into free space modes by the atoms in spin up. The ratio of free space scattered to detected photons $R_s = M_s/M_d$ is given by a weighted ratio of the atomic to cavity damping rates using Eq. 3.9 as

$$R_s = \frac{1}{q_d\eta_s}\frac{\Gamma}{\kappa}\left(\frac{\Omega_\uparrow}{2\omega}\right)^2. \tag{3.17}$$

The factor η_s plays an equivalent role to a quantum efficiency and separately accounts for photons exiting the cavity via an undetected port. In the symmetric cavity example we consider here, only the transmission port (port 2) is measured, and $\eta_s = \kappa_2/\kappa$. See Fig. 3.2(b) for an illustration.

The *key* number of scattered photons into free space normalized to the total number of atoms N, denoted m_s^{proj}, may then be found from Eqs. (3.17) and (3.16) as

$$m_s^{\mathrm{proj}} = \frac{R_s M_d^{\mathrm{proj}}}{N} \tag{3.18}$$

$$= \frac{1}{4qN_\uparrow C}\left(\frac{\kappa'}{\kappa}\right)^2\left(1+\frac{\delta_c^2}{\Omega_\uparrow^2}\right)\frac{\Omega_\uparrow^2}{\omega^2}, \tag{3.19}$$

where C is the single particle cooperativity parameter

$$C = \frac{(2g)^2}{\kappa\Gamma}, \tag{3.20}$$

and q is the total effective quantum efficiency

$$q = q_d\eta_d\eta_s. \tag{3.21}$$

Neglecting any other noise mechanisms, arbitrarily low probe measurement imprecision $\Delta J_{z,\,\mathrm{imp}}$ relative to the projection noise level $\Delta J_{z,\,\mathrm{CSS}}$ may be attained at large m_s relative to m_s^{proj}

$$\left(\frac{\Delta J_{z,\,\mathrm{imp}}}{\Delta J_{z,\,\mathrm{CSS}}}\right)^2 = \frac{m_s^{\mathrm{proj}}}{m_s}. \tag{3.22}$$

The above result refers to the probe measurement imprecision only. However, the total measurement uncertainty is governed by both the probe measurement imprecision treated in this Chapter, and the noise added by probe-induced spin flip diffusion of J_z, forthcoming in Chapter 4.

A key result is that the average free space scattered photons per atom m_s at a given measurement imprecision $\Delta J_{z,\,\mathrm{imp}}$ saturates to a finite value

$$m_s \to \frac{1}{4qN_\uparrow C\left(\frac{\Delta J_{z,\,\mathrm{imp}}}{\Delta J_{z,\,\mathrm{CSS}}}\right)^2} \text{ as } |\delta_c| \to \infty. \tag{3.23}$$

How far must one detune to approach this bound? Below we will show that this bound is nearly reached for detunings greater than the critical detuning $\delta_c > \delta_c^\circ$. The reason for the saturation of free space scattering is because in Eq. (3.19), the ratio of free space to detected photons asymptotically decreases as $1/\delta_c^2$, but the required number of detected photons increases asymptotically as δ_c^2. Thus the net asymptotic dependence of m_s on detuning δ_c cancels. The nondemolition character of the measurement is ultimately set, not by the detuning δ_c, but by the product of the collective cooperativity parameter and the quantum efficiency $qN_\uparrow C$. This quantity physically sets the maximum rate at which collective information can be extracted from the ensemble compared to the rate at which single-particle information is gained by the environment via multimode scattering of light into free space. This result is intimately connected to the picture of superradiance in Fig. 2.9. The single particle forward scattering rate of photons that provide collective information is collectively enhanced by a factor of NC.

In the good cavity limit $\kappa \ll \Gamma$, the frequency dependence δ_c of Eq. (3.19) can be understood in three regimes: the far-detuned dispersive regime $|\delta_c| > \delta_c^\circ$, the near-detuned dispersive regime $|\delta_c| < \delta_c^\circ$, and the resonant regime $\delta_c = 0$. The critical cavity detuning δ_c° is written in two equivalent and useful forms as

$$\delta_c^\circ = \sqrt{\frac{\Gamma}{\kappa}}\frac{\Omega_\uparrow}{2}\frac{1}{\sqrt{q}} = \frac{\Gamma}{2}\sqrt{\frac{N_\uparrow C}{q}}\,. \tag{3.24}$$

The critical detuning is the cavity detuning at which the dressed cavity linewidth is $\kappa' = 2\kappa$, possible only in the good cavity limit $\kappa \ll \Gamma$. Expressions for the number of photons scattered

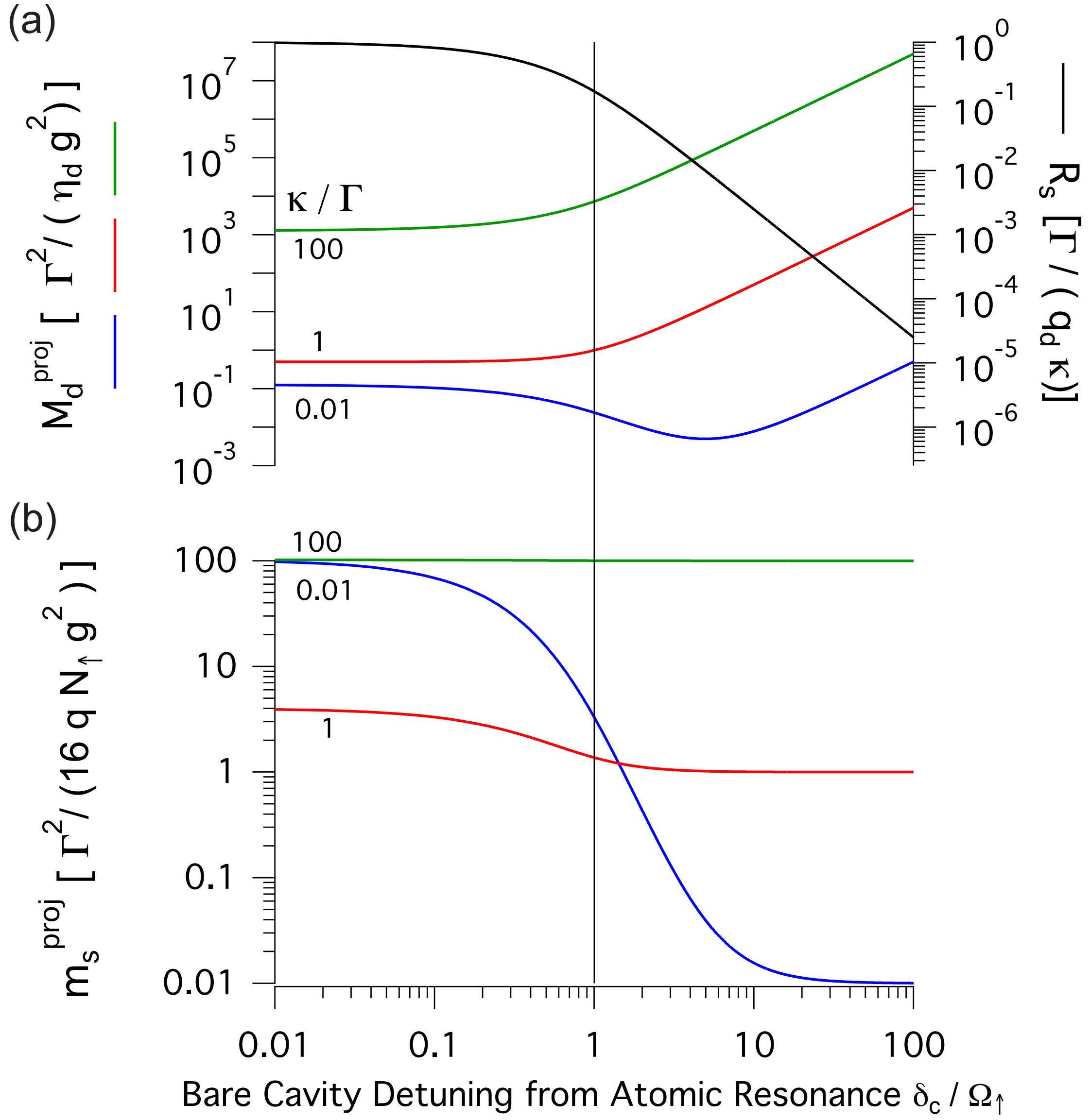

Figure 3.6: Theoretical scaling of key quantities with cavity detuning δ_c expressed in units of the the collective vacuum Rabi splitting $\Omega_\uparrow$. In (a) and (b), the scaling for different cavity finesses is shown giving $\kappa/\Gamma = 0.01$, 1, and 100 (blue, red, and green, respectively). (a, left, blue, red, green) The average number of detected photons needed to resolve the projection noise fluctuations M_d^{proj} normalized such that the plotted values should be multiplied by $\Gamma^2/(\eta_d g^2)$. (a, right, black) The ratio of the number of free-space-scattered photons for every detected photon R_s, normalized such that the plotted values should be multiplied by $\Gamma/(q_d\kappa)$. (b) The crucial average number of scattered photons into free space per atom m_s^{proj} when the atomic population measurement imprecision is equal to the projection noise fluctuations. The normalization is such that the plotted values should be multiplied by $\Gamma^2/(16qN_\uparrow g^2)$. In the bad-cavity limit of $\kappa \gg \Gamma$ (green curves), there is little fundamental advantage to operating away from resonance $\delta_c = 0$. The technical requirements are simply increased as a result of detuning. As the finesse of the cavity F is increased, the amount of free space scattering falls roughly as $1/F$ until the good cavity regime is reached when $\kappa \ll \Gamma$ (blue curves). Here, one must detune by roughly the critical detuning δ_c° in order to realize the full advantage of having increased the cavity finesse. Importantly, note that m_s^{proj} does not significantly decrease above δ_c° owing to cancellation in this regime of the scaling of $R_s \sim 1/\delta_c^2$ with the scaling of $M_d^{\mathrm{proj}} \sim \delta_c^2$.

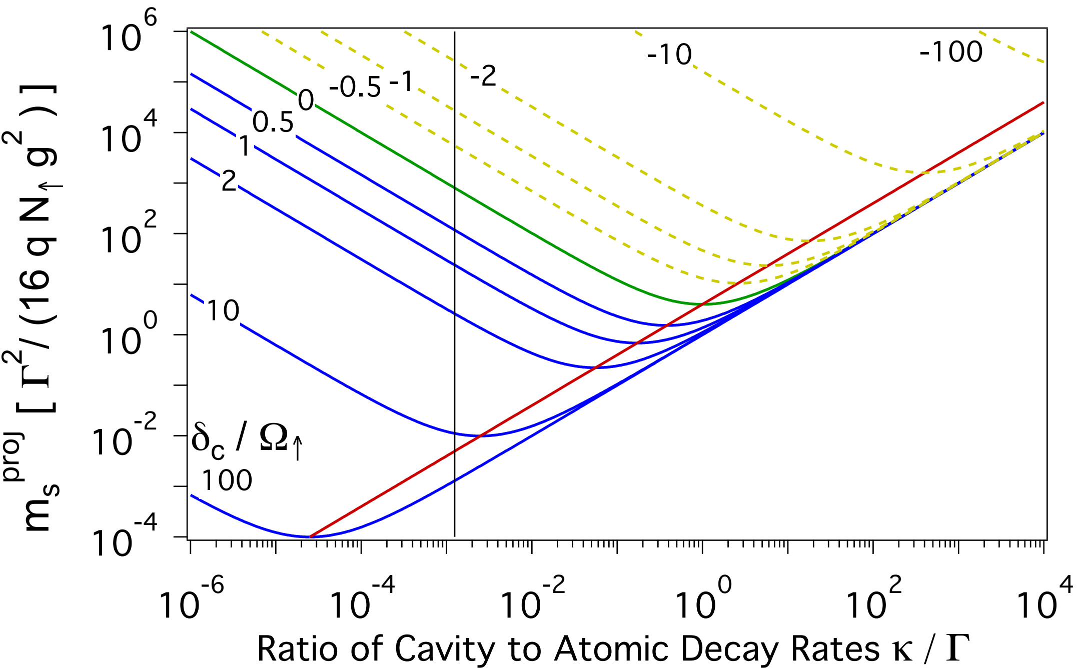

Figure 3.7: The crucial average number of scattered photons into free space per atom such that the detected probe light allows resolution of projection noise fluctuations m_s^{proj} versus the ratio of the cavity power to atomic population decay rates κ/Γ. The normalization is chosen such that the plotted values should be multiplied by $\Gamma^2/(16qN_\uparrow g^2)$. Here, we assume that κ is varied by changing the cavity finesse while holding the cavity length fixed (such that g is constant). Each trace represents a fixed ratio of the bare cavity detuning to the collective vacuum Rabi splitting $\delta_c/\Omega_\uparrow$, with values labeled on the traces and blue denoting $\delta_c/\Omega_\uparrow > 0$, green $\delta_c/\Omega_\uparrow = 0$ and dashed yellow $\delta_c/\Omega_\uparrow < 0$. Here we consider probing the dressed mode at frequency ω_+. At a fixed detuning (and therefore fixed projection-noise-driven frequency fluctuation size) a minimum is reached below which a better cavity is detrimental due to the dressed cavity linewidth κ' becoming clamped while the ratio of free space scattering to detected photon number R_s continues to rise. In the units above, the locus of the minimum is just $4\kappa/\Gamma$ (red line). Including the normalization, the locus of the minimum reduces to $m_s^{\mathrm{proj}} = 1/(qN_\uparrow C)$. When including the dependence of g^2, $\kappa \sim 1/l$ on cavity length l, the minimum value of m_s^{proj} is not changed by just shortening the cavity at fixed finesse. Only shortening the cavity length while simultaneously increasing the cavity finesse (such that κ is constant) leads to a net fundamental reduction of m_s^{proj}. Finally, the vertical black line indicates the cavity linewidth for a finesse $F = 10^6$ cavity, near the highest currently achievable, for ^{87}Rb and $l = 2$ cm (approximately the same as our cavity length).

into free space per atom m_s^{proj}, the absolute size of the projection noise fluctuations of the mode frequency $\Delta\omega^{\text{proj}}$, and the dressed cavity linewidth κ' are summarized in these different regimes in Table 3.1. Again, the quantity m_s^{proj} is critical for understanding the fundamental limits on both probe-induced heating of the sample and potential improvements on measurement sensitivity beyond the SQL. Note that collective information gained from the cavity results from a forward scattering process that leaves the momentum state of the atom un-modified and therefore does not cause recoil heating. The probing-induced free space scattering always cause recoil heating on average, even if the atoms are tightly confined in the Lamb-Dicke regime in all three dimensions.

Table 3.1: Regimes of cavity probing. The regime name and assumptions used to define the regime are provided in the first and last columns. The quantity m_s^{proj} is the average number of photons scattered into free space normalized to the total atom number N, required to resolve an rms fluctuation $\sqrt{N}/2$ in the spin up population $N_\uparrow$ equal to the projection noise level. The quantity $\Delta\omega^{\text{proj}}$ is the rms angular frequency fluctuation of a single coupled atoms-cavity mode $\omega_\pm$ due to projection noise. The quantity κ' is the dressed cavity power decay linewidth, here taken for the mode detuned farthest from atomic resonance. The single-particle cooperativity C, the number of atoms in spin up $N_\uparrow = N/2$, the single-particle cavity coupling g, the empty cavity power and atomic population decay rates κ and Γ respectively, and the collective vacuum Rabi splitting $\Omega_\uparrow$ are related by the following: $\Omega_\uparrow = \sqrt{N_\uparrow}2g$, $N_\uparrow C = N_\uparrow(2g)^2/\kappa\Gamma$. The detuning of the empty cavity resonance frequency from the atomic transition frequency is δ_c, and the critical detuning at which $\kappa' = 2\kappa$ is $(\delta_c^\circ)^2 = \Omega_\uparrow^2\Gamma/4\kappa$, assuming the good cavity limit $\kappa \ll \Gamma$. The maximally detuned regime assumes that the quantity $N_\uparrow C$ is chosen to minimize m_s^{proj} in the presence of the constraint that the cavity detuning cannot be made larger than some maximum value δ_{max} set by technical constraints on resolving the projection noise fluctuations or fundamental constraints set by the internal energy level structure of the atoms being probed (for instance the ground state hyperfine splitting in ^{87}Rb).

Regime Name	m_s^{proj} $\left[\times \frac{1}{4q}\right]$	$\Delta\omega^{\text{proj}}$	κ' $[\times\kappa]$	Assumptions
Resonant	$\frac{1}{N_\uparrow C}\left(1+\frac{\Gamma}{\kappa}\right)^2$	$\frac{g}{2\sqrt{2}}$	$\frac{1}{2}\left(1+\frac{\Gamma}{\kappa}\right)$	$\delta_c = 0$
Detuned	$\frac{1}{N_\uparrow C}\left(\frac{\kappa'}{\kappa}\right)^2$	$\sqrt{\frac{N_\uparrow}{2}}\frac{g^2}{\lvert\delta_c\rvert}$	$1+\frac{N_\uparrow g^2}{\delta_c^2}\left(\frac{\Gamma}{\kappa}-1\right)$	$\delta_c \gg \Omega_\uparrow$
Near Detuned, Good Cavity	$N_\uparrow C\frac{\Gamma^4}{(2\delta_c)^4}$	$\sqrt{\frac{N_\uparrow}{2}}\frac{g^2}{\lvert\delta_c\rvert}$	$\frac{N_\uparrow g^2}{\delta_c^2}\frac{\Gamma}{\kappa}$	$\delta_c^\circ \gg \delta_c \gg \Omega_\uparrow; \Gamma \gg \kappa$
Critically Detuned, Good Cavity	$\frac{4}{N_\uparrow C}$	$\frac{g}{\sqrt{2}}\sqrt{\frac{\kappa}{\Gamma}}$	2	$\delta_c = \delta_c^\circ \gg \Omega_\uparrow; \Gamma \gg \kappa$
Far Detuned	$\frac{1}{N_\uparrow C}$	$\sqrt{\frac{N_\uparrow}{2}}\frac{g^2}{\lvert\delta_c\rvert}$	$1+\frac{N_\uparrow g^2}{\delta_c^2}\frac{\Gamma}{\kappa}$	$\delta_c \gg \delta_c^\circ, \Omega_\uparrow; \Gamma \gg \kappa$
Maximally Detuned, Good Cavity, Optimized	$\left(\frac{\Gamma}{2\delta_{\text{max}}}\right)^2$	$\frac{g}{\sqrt{2}}\sqrt{\frac{\kappa}{\Gamma}}$	2	$\delta_c = \delta_{\text{max}} \gg \Omega_\uparrow; \Gamma \gg \kappa;$ $N_\uparrow C = \left(\frac{2\delta_{\text{max}}}{\Gamma}\right)^2$

3.3.3 Minimizing m_s^{proj} at fixed maximum detuning

In some experimental situations, a maximum useful probe detuning $|\delta_c| \leq \delta_{\max}$ is set by the energy structure of the atom. For instance, the 6.8 GHz ground state hyperfine splitting in ^{87}Rb imposes $\delta_{\max} \approx 6.8/2$ GHz. One could of course detune farther but the two states being probed become less distinguishable with respect to the probe light. An optimum value of $N_\uparrow C$ can be found that minimizes m_s^{proj} when $|\delta_c| = \delta_{\max}$. The scaling for this case is shown in the last line of Table 3.1. Physically, the optimum value of $N_\uparrow C$ is reached (at a fixed detuning) when the dressed cavity linewidth is related to the bare cavity and atomic linewidths by $\kappa'/\kappa = 2\Gamma/(\Gamma+\kappa)$. In the resonant limit, $\delta_c = 0$, one finds an optimum $\kappa'/\kappa = 1$, while in the detuned limit one finds $\kappa'/\kappa \approx 2$, i.e., the detuned cavity resonance is broadened by a factor of 2 at the optimum. In this same limit, the ratio of rms fluctuation size to dressed cavity HWHM is given by $2\Delta\omega^{\mathrm{proj}}/\kappa' = \sqrt{C/8}$. Larger single atom cooperativity parameter C reduces the technical requirements on resolving the projection noise fluctuations of the cavity mode.

3.4 Summary

In this Chapter, we have focussed on the problem of gaining information on the collective spin projection J_z by probing the coupled atoms-cavity system with an externally applied cavity drive. We have touched on one aspect of the disturbance imposed by probing the atoms — namely free-space-scattering, which can cause recoil heating and shortening of the collective spin due to single particle wavefunction collapse. We emphasize that the theory presented here is very general and may be adapted to the many collective cavity-QED setups around the world. The theory can be adapted with minor modifications taking into account the multi-level structure of real atoms to predict experimentally relevant quantities. In Chapter 9, we predict the optimum amount of spectroscopic enhancements in our ^{87}Rb system both as an example of how the theory can be adapted for real atoms and also as an outlook on prospects for further squeezing experiments.

In Chapter. 4, we will consider the effect of free-space-scattering shortening of the collective spin in more detail, as well as two other probe-induced back-actions on the collective spin — fundamental back-action in J_y (anti-squeezing) and probe-induced Raman spin-flip causing J_z diffusion. We will then derive limits on measurement imprecision limits on J_z and spectroscopic enhancement in the polar angle sensitivity $\xi_{\mathrm{m}}^{-1} \equiv (\Delta\theta_{\mathrm{SQL}}/\Delta\theta)^2$ in the presence of probe-induced back-action.

Chapter 4

Theory: Probe-induced back-action

The present Chapter discusses the three types of probe-induced back-action, as shown in Fig. 4.1, and the limits that the back-action sets on measurement imprecision in J_z as well as on spectroscopic enhancement or squeezing. In Appendix A, we briefly discuss how coherence preserving nondemolition measurements at or near the projection noise level can be used to reduce recoil heating in a full Ramsey spectroscopy cycle to allow neutral atom traps to operate in a duty cycle regime more like ion traps.

As the collective spin is a 3-dimensional vector, there are three types of back-action associated with each direction. For concreteness, we assume the collective spin is initially prepared in a CSS along $\hat{x}$, i.e. $\mathbf{J} = \frac{N}{2}\hat{x}$ throughout this Chapter. It is important to note that results in this Chapter are valid only for CSS prepared in this orientation. The first back-action, ΔJ_y, arises from fundamental Heisenberg uncertainty relations and does not impact squeezing to lowest order. The second back-action, shortening of the mean spin $|\langle\hat{\mathbf{J}}\rangle|$ length, due to probe-induced free space scattering impacts squeezing by reducing the signal size or contrast $\mathcal{C}$. Finally, the third back-action, diffusion of J_z due to probe-induced Raman spin-flips impacts squeezing through increasing noise in one's ability to estimate J_z. The linear scaling of this back-action's noise variance with the probe photon number is analogous to radiation pressure shot noise in optomechanical systems [31, 32]. The following sections will discuss these back-actions in greater detail.

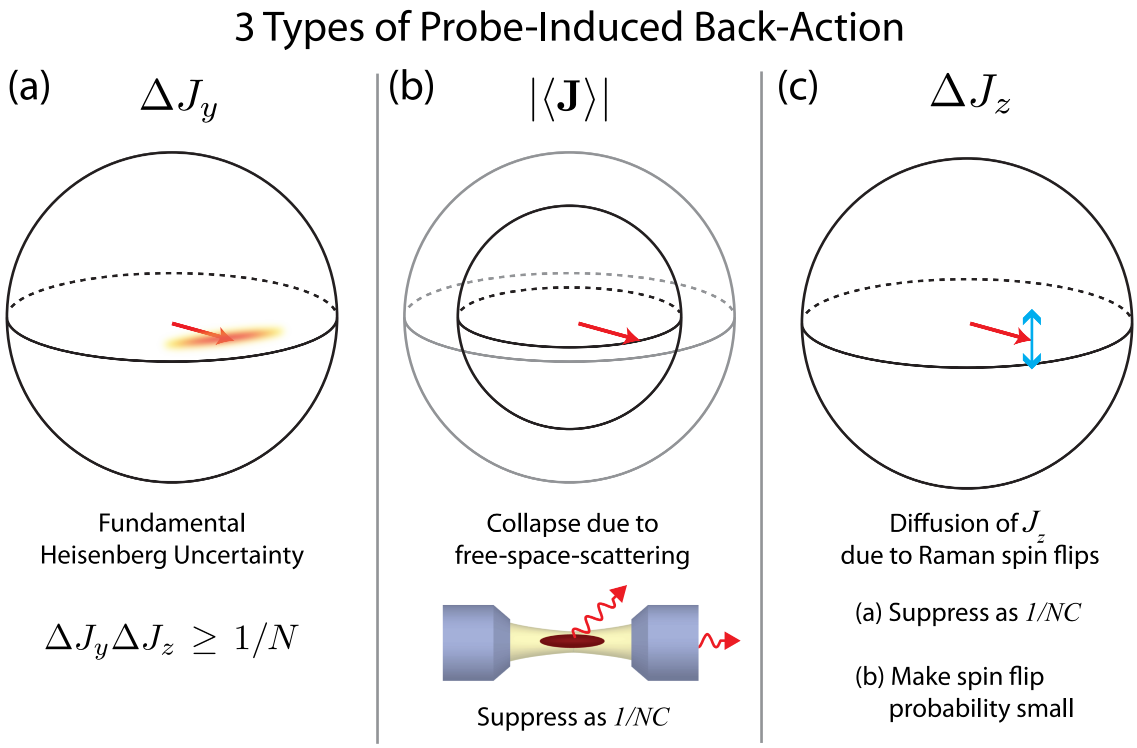

Figure 4.1: The 3 types of probe-induced back-action associated with measuring J_z. (a) Fundamental Heisenberg uncertainty in the conjugate variable J_y that cannot be engineered away. (b) Shortening of the collective spin due to single atom wavefunction collapse from free space scattering of probe photons can be suppressed by enhancing the forward scattering rate which scales as the collective cooperativity $N_\uparrow C$ over the free space scattering rate which stays constant at the single particle particle rate. (c) Free space scattering events that flip the spin state of the atom causes J_z to change by ±1 per spin flip. Fluctuations in the number of spin flip events cause J_z to undergo diffusion, equivalent to a random walk. Raman spin flips can be suppressed by making free space scattering low with large $N_\uparrow C$ or by choosing a probing scheme that has a low spin flip probability when undergoing a free space scattering event.

4.1 Back-action on J_y

For a CSS prepared along along $\hat{x}$, the Heisenberg uncertainty relation Eq. 2.4 implies $\Delta J_z \Delta J_y \geq N/4$. In a given J_z measurement scheme, the best possible measurement imprecision $\Delta J_{z,\,\mathrm{perfect}}$, assuming perfect quantum efficiency in the probe detection process, would result in a fundamental, i.e. minimum, back-action $\Delta J_y = N/(4\Delta J_{z,\,\mathrm{perfect}})$, schematically shown in Fig. 4.1(a). The back-action ΔJ_y is also called anti-squeezing. In practice, losses and technical noise limit the effective detection quantum efficiency, resulting in an observed uncertainty

$\Delta J_z > \Delta J_{z,\,\mathrm{perfect}}$. Since the actual measurement uncertainty $\Delta J_z \geq \Delta J_{z,\,\mathrm{perfect}}$ is worse, the Heisenberg uncertainty relation $\Delta J_y \Delta J_z \geq 1/N$ is satisfied.

The anti-squeezing ΔJ_y does not degrade the polar angle sensitivity $\Delta\theta \approx \Delta J_z/|\langle\hat{\mathbf{J}}\rangle|$ of the post-measurement state to lowest order. Anti-squeezing ΔJ_y can be thought of as spreading the collective spin out in its azimuthal phase. Provided the anti-squeezing is small compared to the length of the initial collective spin, i.e. $\Delta J_y/J \ll 1$ where $J = N/2$, the fractional shortening of the mean collective spin after the measurement and the impact on the polar angle sensitivity is second order in $\Delta J_y/J$, and is therefore usually not a problem. In most experimental situations, the direct shortening of the collective spin due to probe-induced free space scattering discussed in Section 4.2 or the diffusion noise cause by probe-induced Raman spin flips discussed in Section 4.3 practically limits the polar angle sensitivity of the post-measurement state.

4.2 Back-action on $|\langle\hat{\mathbf{J}}\rangle|$

The second type of probe-induced back-action shown in Fig. 4.1(b) is the shortening of the collective spin $\hat{\mathbf{J}}$ as a result of probe-induced free space scattering. Free space scattering provides in-principle information as to which atoms in the ensemble have emitted the photons, leading to single atom wavefunction collapse, destroying their superposition states, or equivalently a loss of coherence. The shortened length leads in decrease phase sensitivity because the angular resolution $\Delta\theta \approx \Delta J_z/|\langle\hat{\mathbf{J}}\rangle|$ is inversely proportional to the mean spin length $|\langle\hat{\mathbf{J}}\rangle|$.

In Section 3.3, we have analyzed the amount of free space scattering due to sending probe photons into the atoms-cavity system and have shown that the key figure of merit m_s^{proj} scales inversely as the collective cooperativity $N_\uparrow C$ at sufficiently large detuning δ_c of the cavity resonance from the atomic transition frequency. To remind the reader, m_s^{proj} is the number of free space scattered photons per atom when the probe measurement imprecision is equal to projection noise fluctuations of the mode frequency $\Delta\omega^{\mathrm{proj}}$. Therefore decoherence can be reduced by engineering systems with large collective cooperativity $N_\uparrow C \gg 1$.

The contrast decays exponentially with the number of scattered photons per atom m_s as

$$\mathcal{C} = \mathcal{C}_i e^{-m_s}\,, \tag{4.1}$$

provided the free space scattering rate for each spin is unchanged by the scattering process. Here $\mathcal{C}_i$ is the initial contrast before probing. The initial contrast $\mathcal{C}_i$ may be reduced below 1 due to background decoherence processes such as dephasing due to differential trapping potentials for the $|\uparrow\rangle$ and $|\downarrow\rangle$ states or free space scattering caused by the trap light.

Note that both Rayleigh and Raman scattering lead to a reduction in the mean spin length. Whereas Raman scattering always leads to single atom wavefunction collapse, in certain cases, free space Rayleigh scattering does not cause single atom wavefunction collapse [139]. However, this immunity to collapse requires indistinguishability in the scattering process with respect to the spin up and spin down state, which also reduces the information that can be extracted from the probe mode.

4.3 Back-action on J_z

Raman spin flips caused by free space scattering results in noise added back into the measurement quadrature J_z, causing J_z to diffuse, as shown in Fig. 4.1(c). Measuring with more probe photons averages down photon shot noise but introduces more Raman spin flips as a result of measuring harder. We will find that this back-action presents limits on the measurement resolution of J_z. We will employ a simple 3-level model to calculate this limit and use that result in Section 4.5 to calculate spectroscopic enhancements relative to the SQL. This simple model will be extended to include the effect of Raman transitions to other states than $|\downarrow\rangle$ in Chapter 9.

4.3.1 Simple three-level model

In this section, we consider how the free space scattering changes atomic population in the spin up and spin down two-level manifold through Raman or spin flip events. For arriving at the results presented in this section, only the atomic populations matter, and coherences are irrelevant.

A detailed accounting of all possible Raman scattering processes is required to make accurate predictions for a multi-level atom. To capture the essential physics, we consider the simplest model here. In this toy model, the only states in the problem are the two-level system $|\uparrow\rangle$, $|\downarrow\rangle$ and the optically excited state $|e\rangle$, as described in Fig. 3.1(b). We assume that a free space scattering event causes an atom to spin flip from $|\uparrow\rangle$ to $|\downarrow\rangle$ via the intermediate state $|e\rangle$ with probability p. It is easy to see that the average change in the spin up population per photon scattered into free space is $dN_\uparrow/dM_s = -p$, and correspondingly $dJ_z/dM_s = -p$.

4.3.2 Diffusion of J_z

Free space scattering causes J_z to change on average by a certain amount, while the random nature of the spin flip process leads to a random walk or diffusion of the collective spin projection J_z. Provided multiple scattering can be neglected, i.e. $pm_s \ll 1$, the diffusion process can be described by the relation

$$\left(\frac{\Delta J_{z,\,\mathrm{ba}}}{\Delta J_{z,\,\mathrm{CSS}}}\right)^2 = 4\,p\,m_s\,, \tag{4.2}$$

where $\Delta J_{z,\,\mathrm{ba}}$ denotes the back-action noise from J_z diffusion, with the the diffusion constant $4p$ set by the spin flip probability p. To remind the reader, m_s is average free space scattered photons per atom induced by the probe.

4.4 Measurement limits on J_z

Given the diffusion in J_z, and the photon shot noise in the probe, we must ask: How well can one measure J_z or equivalently the atomic population $N_\uparrow$? The total measurement uncertainty $(\Delta J_z)^2$ in the estimate of J_z can be estimated by adding the noise variances from probe measurement imprecision $(\Delta J_{z,\,\mathrm{imp}})^2$ (Eq. 3.22) and Raman spin-flip-induced diffusion $(\Delta J_{z,\,\mathrm{ba}})^2$ (Eq. (4.2)):

$$\begin{aligned}\left(\frac{\Delta J_z}{\Delta J_{z,\,\mathrm{CSS}}}\right)^2 &= \left(\frac{\Delta J_{z,\,\mathrm{imp}}}{\Delta J_{z,\,\mathrm{CSS}}}\right)^2 + \left(\frac{\Delta J_{z,\,\mathrm{ba}}}{\Delta J_{z,\,\mathrm{CSS}}}\right)^2 && (4.3)\\ &= \frac{m_s^{\mathrm{proj}}}{m_s} + 4\,p\,m_s\,. && (4.4)\end{aligned}$$

Averaging down photon shot noise determines the J_z more and more precisely. Eventually, however, probe-induced diffusion of J_z causes the value of J_z measured at earlier times to become less correlated with the value of J_z measured at later times, adding noise to the estimate of J_z, as shown in Fig. 4.2. We note lowering spin-flip probability p allows one to average down photon shot noise further to reach a lower measurement imprecision before spin-flip diffusion noise takes over, a situation analogous to back-action-evasion in optomechanical contexts.

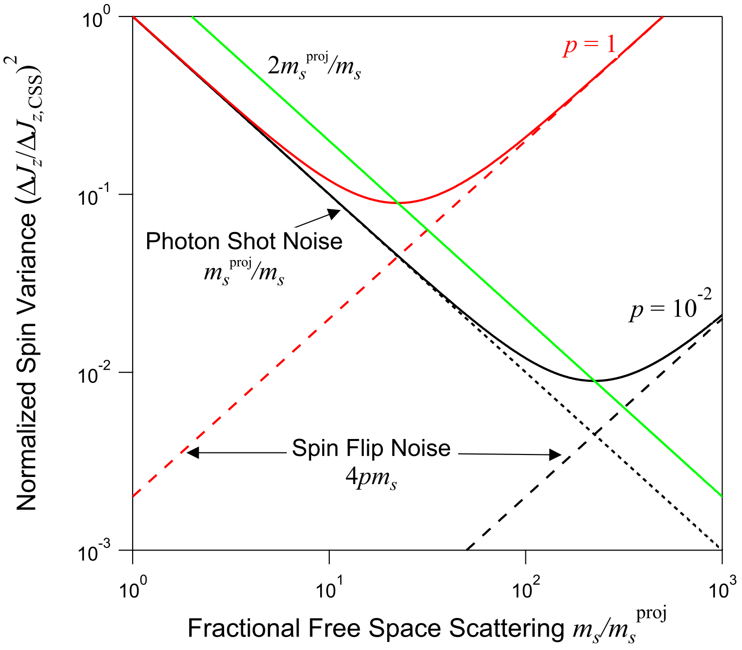

Figure 4.2: Normalized spin noise variance versus fractional free space scattering m_s/m_s^{proj} for $NC = 10^3$. The measurement variance decreases as $1/m_s$ from averaging down photon shot noise (dotted black line) until noise due to Raman spin flips (dashed red and black lines) takes over at large m_s. The minimum noise variance is $4\sqrt{pm_s^{\mathrm{proj}}} \to \sqrt{8p/NC}$ assuming perfect quantum efficiency and probing in the far-detuned limit. This minimum is reached when two noise contributions are equal at $m_s^{\mathrm{opt}} = \sqrt{m_s^{\mathrm{proj}}/4p} \to 1/\sqrt{8pNC}$ assuming perfect quantum efficiency and probing in the far-detuned limit. A larger collective cooperativity NC or lower spin flip probability p (analogous to back-action evasion in optomechanics) allows photon shot noise to be averaged down more before spin flip noise takes over, as illustrated by the two curves for $p/NC = 10^{-5}$ (black) and 10^{-3} (red). The locus of the minimum variance is $2m_s/m_s^{\mathrm{proj}}$ (green).

The optimal uncertainty $\Delta J_z^{\mathrm{opt}}$ occurs at an optimal scattering m_s^{opt} where the noise contributions from measurement imprecision and diffusion due to Raman spin flips are equal:

$$m_s^{\rm opt} = \frac{1}{\sqrt{8pqNCh(\delta_c)}}\,, \tag{4.5}$$

$$\left(\frac{\Delta J_z^{\rm opt}}{\Delta J_{z,\,\rm CSS}}\right)^2 = \sqrt{\frac{8p}{qNCh(\delta_c)}}\,, \tag{4.6}$$

where the detuning dependence has been lumped into

$$h(\delta_c) = \left(\frac{\kappa}{\kappa'(\delta_c)}\frac{\omega(\delta_c)}{\sqrt{\delta_c^2+\Omega_\uparrow^2}}\right)^2\,, \tag{4.7}$$

where $\kappa'(\delta_c)$ is the dressed cavity mode linewidth introduced in Eq. (3.9), $\omega(\delta_c)$ is the dressed cavity mode frequency introduced in Eq. (3.4), and $\Omega_\uparrow = \sqrt{N_\uparrow}2g$ is the collective vacuum Rabi splitting. The parameter $h(\delta_c^\circ) = 1/4$ at the critical detuning, and $h(\delta_c) \to 1$ as $|\delta_c| \to \infty$. In the far-detuned limit, Raman spin flip noise limits the achievable imprecision to $\left(\frac{\Delta J_z^{\rm opt}}{\Delta J_{z,\,\rm CSS}}\right)^2 = \sqrt{8p/qNC}$.

4.4.1 Single spin measurement resolution

Single spin resolution $\Delta J_z^{\rm opt} \le 1/2$ is required for conditionally preparing states with spectroscopic sensitivity at the Heisenberg limit as well as reading out cat states [140], or Dicke states [78]. Single spin resolution in ensembles of ~ 100 ^{87}Rb atoms has recently been demonstrated using cavity-aided nondemolition measurements [130]. We find that in the far-detuned limit and with no prior knowledge, single spin resolution is reached for $p \le \frac{qC}{8N}$, quantifying how ideal a cycling probe transition needs to be in order to resolve single spins. For $qC \sim 1$ and $N \sim 10^6$, one would need $p \le 10^{-7}$, which is highly unrealistic for real multi-level alkali-atoms due to off-resonant scattering from other hyperfine states, as will be discussed in Chap. 9 for the case of ^{87}Rb. Alternatively, with high single atom cooperativity, $qC \ge 8Np$, single spin resolution could be attained without a cycling transition. For example, with $qC \sim 100$ and a worst-case open transition with $p = 1/2$, single spin resolution would be reached for $N \le 25$ atoms.

4.5 Spectroscopic enhancement

In this section, we derive the fundamental limits to the spectroscopic sensitivity — a *key result* of this chapter in which the effects of both J_z back-action and signal reduction back-action in $|\langle\hat{\mathbf{J}}\rangle|$ are combined. Spectroscopic sensitivity refers to the ability to resolve the angle through which a collective spin is rotated. To a first approximation, the polar angle resolution $\Delta\theta \approx \Delta J_z/|\langle\hat{\mathbf{J}}\rangle|$ is set by the spin noise reduction $(\Delta J_z/\Delta J_{z,\,\mathrm{CSS}})^2$, discussed in Section 4.4, and the mean spin length $|\langle\hat{\mathbf{J}}\rangle|$, proportional to the contrast $\mathcal{C}$, that remains after probing, discussed in Section. 4.2.

Angular resolution is improved if the spin noise is reduced by a greater amount than the probe-induced loss of coherence/contrast $\mathcal{C}$. Putting Eq. 4.4 and Eq. 4.1 into Eq. 2.8, the spectroscopic enhancement for a perfect initial contrast $\mathcal{C}_i = 1$ is given by

$$\begin{aligned}\xi_{\mathrm{m}}^{-1} &= \left(\frac{\Delta J_z}{\Delta J_{z,\,\mathrm{CSS}}}\right)^{-2}\mathcal{C}_f & (4.8)\\ &= \left(\frac{\Delta J_z}{\Delta J_{z,\,\mathrm{CSS}}}\right)^{-2} e^{-2m_s}\,. & (4.9)\end{aligned}$$

To relate to our experiment where the initial contrast $\mathcal{C}_i < 1$, the above equation needs to be modified. An partially decohered reference state with $\mathcal{C}_i < 1$ may be represented as a CSS with a shorter mean spin length $|\langle\hat{\mathbf{J}}\rangle| = \mathcal{C}_i N/2$. The shorter mean spin length leads to a higher SQL in the polar angle resolution $\Delta\theta_{\mathrm{SQL}} = \sqrt{\mathcal{C}_i}\Delta J_{z,\,\mathrm{CSS}}/|\langle\hat{\mathbf{J}}\rangle| = 1/\sqrt{\mathcal{C}_i N}$ where $\Delta J_{z,\,\mathrm{CSS}} = \sqrt{N}/2$ as before. As a result, one should normalize the spectroscopic enhancement to the larger SQL set by the shorter initial collective spin

$$\begin{aligned}\xi_{\mathrm{m}}^{-1} &= \left(\frac{\Delta J_z}{\sqrt{\mathcal{C}_i}\Delta J_{z,\,\mathrm{CSS}}}\right)^{-2}\left(\frac{\mathcal{C}}{\mathcal{C}_i}\right)^{2} \\ &= \left(\frac{\Delta J_z}{\Delta J_{z,\,\mathrm{CSS}}}\right)^{-2}\frac{\mathcal{C}^2}{\mathcal{C}_i}\,. & (4.10)\end{aligned}$$

For the remainder of this Chapter, we shall take $\mathcal{C}_i = 1$.

The optimal spectroscopic enhancement exhibits different scaling with respect to the effective collective cooperativity qNC in different regimes. If Raman spin-flips dominate over Rayleigh scattering events, the optimal spectroscopic enhancement $\xi_{\mathrm{m,\,opt}}^{-1} \sim \sqrt{qNC/p}$ is limited by spin-flip diffusion noise as considered in sub-section 4.5.1. If Rayleigh scattering dominates, then the optimal spectroscopic enhancement $\xi_{\mathrm{m,\,opt}}^{-1} \sim qNC$ is limited by the reduction of contrast $\mathcal{C}$, discussed in Section 4.5.2. The change in the scaling of $\xi_{\mathrm{m,\,opt}}^{-1}$ from $\sqrt{NC}$ in the Raman spin-flip limit to NC in the cycling transition limit allows far greater amounts of squeezing on a cycling transition. The loss of quantum efficiency q degrades squeezing as $\xi_{\mathrm{m,\,opt}}^{-1} \sim q$ on a cycling transition, compared to the more forgiving scaling $\xi_{\mathrm{m,\,opt}}^{-1} \sim \sqrt{q}$ in the Raman spin-flip limited regime. However, the Raman spin-flip limited regime is not really favorable in that the amount of squeezing will typically be worse in the Raman spin-flip regime even at small quantum efficiency q since we typically operate with $NC \gg 1$.

4.5.1 Spin-Flip Diffusion-Noise-Limited Squeezing/Raman Limit

Here we consider the case where the reduction in the contrast $\mathcal{C}$ may be ignored. This is justified if the optimal scattering m_s^{opt} that optimizes the measurement imprecision of J_z is small, $m_s^{\mathrm{opt}} \ll 1$, equivalently $pqNC\,(\kappa/\Gamma)^2 \gg 1$ for probing in the far-detuned limit. In this regime, the mean spin length $|\langle\hat{\mathbf{J}}\rangle|$ remains approximately $N/2$, so that the spectroscopic enhancement is primarily set by the reduction in the spin noise, discussed previously in Section 4.3

$$\xi_{\mathrm{m,\,opt}}^{-1} \approx \left(\frac{\Delta J_z^{\mathrm{opt}}}{\Delta J_{z,\,\mathrm{CSS}}}\right)^{-2}, \tag{4.11}$$

where $\left(\frac{\Delta J_z^{\mathrm{opt}}}{\Delta J_{z,\,\mathrm{CSS}}}\right)^2$ has been introduced in Eq. 4.6. In in the far-detuned limit, Raman spin flip noise limits the achievable squeezing to $\xi_{\mathrm{m,\,opt}}^{-1} = \sqrt{qNC/8p}$. This result is valid provided $\xi_{\mathrm{m,\,opt}}^{-1} \lesssim 0.193/p$ so that the loss of contrast may be neglected (see Fig. 4.3).

4.5.2 Decoherence-Limited Squeezing/Cycling Limit

Here we consider the case where the reduction of contrast $\mathcal{C}$ plays an important role in determining the angular resolution. If the probing is performed on a nominally closed transition where Raman scattering spin-flips due to probe polarization imperfections and off-resonant scattering are very improbable, spin-flip diffusion noise is negligible and the only limit to spectroscopic enhance-

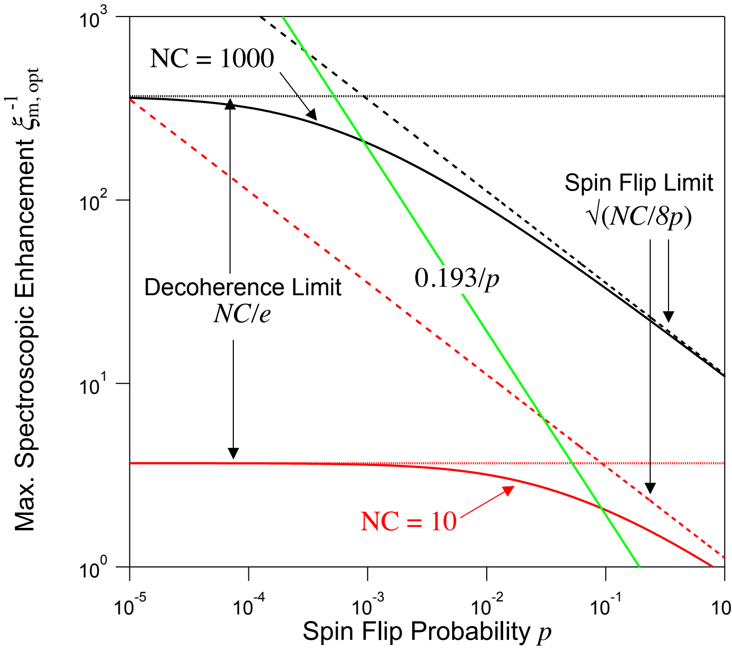

Figure 4.3: Optimal squeezing $\xi^{-1}_{\rm m,\, opt}$ versus spin flip probability p for $NC = 1000$ (black curve) and $NC = 10$ (red curve) for probing in the far-detuned limit, assuming perfect quantum efficiency $q = 1$. Both curves take into account spin flip noise and decoherence. The decoherence-limited squeezing $\xi^{-1}_{\rm m,\, opt} = NC/e$ (dotted lines) is approached for $p \ll e^2/8NC$, and the spin-flip-limited squeezing $\xi^{-1}_{\rm m,\, opt} = \sqrt{NC/8p}$ (dashed lines) is approached for $p \gg e^2/8NC$. The locus of optimal squeezing at the crossover point $p = e^2/8NC$ is $0.193/p$ (green line).

ment is the loss of contrast due to free space (Rayleigh) scattering. The probing is performed in the decoherence-limited or cycling transition regime when the optimal scattering $m_s^{\rm opt}$ that optimizes the measurement imprecision of J_z is not small. Formally, this regime is valid when the Raman spin-flip limited spectroscopic enhancement calculated from Eq. (4.11) is $\xi^{-1}_{\rm m,\, opt} \geq 0.193/p$.

In the decoherence-limited regime, the spectroscopic enhancement is given by $\xi^{-1}_{\rm m} = \frac{m_s}{m_s^{\rm proj}} e^{-2m_s}$. An optimum is reached at $m_s^{\rm opt} = 1/2$, reducing the contrast $\mathcal{C}$ by a factor $1/\sqrt{e} \approx 0.6$. The optimum squeezing is then $\xi^{-1}_{\rm m,\, opt} = 1/(2e\, m_s^{\rm proj})$. In the far-detuned limit, the optimal squeezing $\xi^{-1}_{\rm m,\, opt} \rightarrow qNC/e$. We caution that the simple model presented here is not valid near the Heisenberg limit because while measurement imprecision below a single spin may be achieved, the effective spin noise variance must be clamped to $1/4$ in order to enforce the Heisenberg limit on spectroscopic sensitivity.

4.6 Conclusions

In conclusion, we have presented detailed expressions for how cavity-aided nondemolition measurements of atomic populations and spectroscopic enhancement scale with key experimental parameters: cavity linewidth, collective cooperativity, and Raman transition probabilities in Chapters 3, 4. This analysis will be important in future experiments for reducing photon-recoil heating and for producing highly entangled states with enhanced spectroscopic sensitivities relative to the SQL. With the theoretical foundation laid down, we will describe the experimental generation of conditional spin-squeezed states in Chapter 5 – the key results in this thesis — and provide motivations for probing in the resonant regime $\delta_c = 0$ in Chapter 6.

Chapter 5

Experiment: Spin squeezing via cavity-aided QND measurements

In this centerpiece chapter, we demonstrate the preparation of conditionally spin squeezed states of a collective atomic pseudo-spin via cavity-aided QND measurements of the vacuum Rabi splitting, published in [12]. We infer a 3.4(6) dB improvement in quantum phase estimation relative to the SQL for a CSS composed of un-entangled atoms. The measured collective spin is composed of the two-level clock states of nearly 10^6 ^{87}Rb atoms confined inside a medium finesse $F = 710$ optical cavity. This technique may improve atomic sensor precision and/or bandwidth, and may lead to more precise tests of fundamental physics.

5.1 Energy levels and probing scheme

In this chapter, I will use the abbreviated state notation $|F, m_F\rangle$ to denote ground hyperfine states in the $5^2S_{1/2}$ manifold of ^{87}Rb and $|F', m_F\rangle$ to denote optically excited hyperfine states in the $5^2P_{1/2}$ manifold of ^{87}Rb. The two-level system whose populations we wish to measure are the clock states $|\uparrow\rangle = |2, 0\rangle$ and $|\downarrow\rangle = |1, 0\rangle$ of ^{87}Rb with microwave transition frequency $\omega_{\mathrm{hf}}/2\pi = 6.834$ GHz (see Fig. 5.1).

An ensemble of $N_{\mathrm{tot}} \approx 10^6$ ^{87}Rb atoms are loaded into the TEM$_{00}$ mode of an optical cavity whose frequency is made resonant with the $|\uparrow\rangle$ to $|e\rangle$ optical transition with wavelength $\lambda = 795$ nm. Here, the electronic excited state is $|e\rangle = |1', 0\rangle$. For π-polarized probe light, the states $|\uparrow\rangle$ and $|e\rangle$ form a nearly ideal two-level cavity-QED system because the dipole matrix element between $|\uparrow\rangle$ and the only other nearby state $|2', 0\rangle$ is zero. Therefore we would not expect ac-Stark shifts

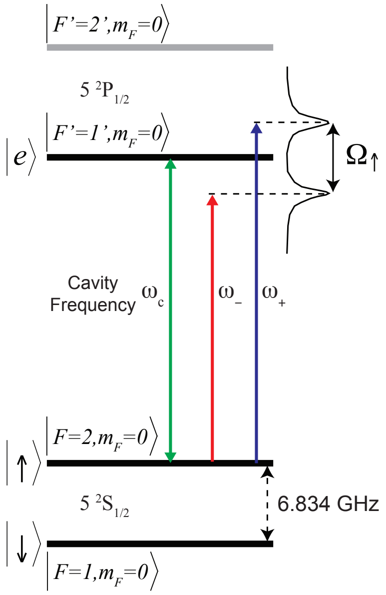

Figure 5.1: The clock states $|\uparrow\rangle$ and $|\downarrow\rangle$ form a pseudo spin-$\frac{1}{2}$ system. The population $N_\uparrow$ is measured by probing near the $|\uparrow\rangle$ to $|e\rangle$ transition, which couples to a degenerate cavity mode, creating a collective vacuum Rabi splitting $\Omega_\uparrow$. A feature of this probing scheme is that the optically excited state $|F' = 2', m_F = 0\rangle$ ($|F' = 1', m_F = 0\rangle$) does not couple to $|\uparrow\rangle$ ($|\downarrow\rangle$) due to selection rules, thus eliminating potential sources of ac-Stark shifts that would otherwise have been caused by off-resonant cross-couplings if these couplings were dipole-allowed.

(or equivalently level repulsion) from off-resonant coupling of $|\uparrow\rangle$ to $|2', 0\rangle$. Similarly, the dipole matrix element between $|\downarrow\rangle$ and $|e\rangle$ is zero, so we expect no off-resonant shifts of the collective Rabi splitting from the $N_\downarrow$ atoms in $|\downarrow\rangle$.

Resonant coupling of the π-polarized cavity mode to the atoms generates a normal mode splitting called the vacuum Rabi splitting $\Omega_\uparrow = \sqrt{N_\uparrow}2g$. The goal is to produce spin squeezed states with spectroscopic sensitivity below the SQL by measuring the *collective spin projection* J_z or equivalently *collective populations* $N_\uparrow$ and $N_\downarrow$ precisely via the Rabi splitting without causing (much) decoherence.

5.2 Atom-cavity coupling

The atom-cavity coupling is a key parameter in our experiments. Here, we will provide details for computing this coupling strength and discuss its significance for our collective cavity-

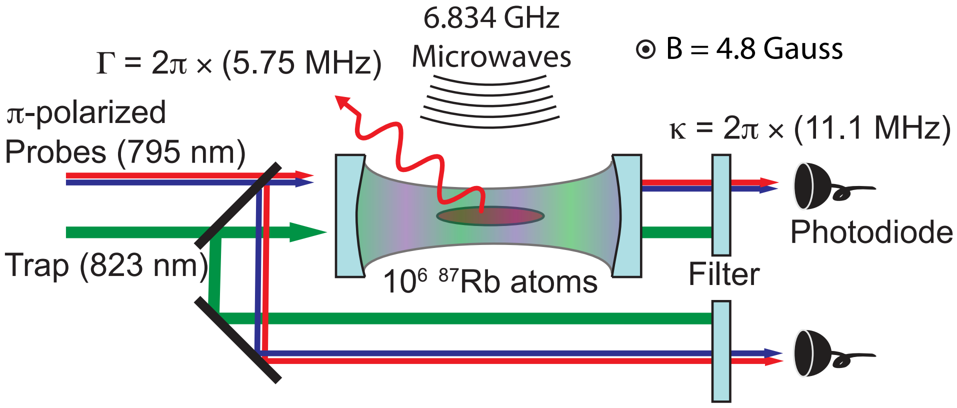

Figure 5.2: Salient aspects of the experimental setup. An ensemble of 10^6 atoms are tightly confined within the TEM_{00} mode of the cavity using a 1D intra-cavity optical lattice at 823 nm. The cavity decay and atomic free-space-scattering rates are κ and Γ respectively. A heterodyne interferometer (expanded out in Fig. 5.4) is used to probe the atoms-cavity resonances in both transmission and reflection. The collective nature of the Rabi splitting prevents loss of coherence as atoms remain in a superposition after the measurement. Microwaves, launched into free space via a dipole antenna, provide coherent manipulations of the collective spin required for state preparation, constructing a measurement of J_z, and to spin-echo away probe-induced dephasing.

QED experiment. We begin by computing the peak single atom vacuum Rabi frequency [137] for an atom at the antinode of the cavity mode and at the cavity waist

$$
\begin{aligned}
2g_0 &= \sqrt{\frac{2cd_{\uparrow e}^2}{\hbar\lambda\epsilon_\circ V_m}} && (5.1)\\
&= 2\pi \times (607.1(5)\,\mathrm{kHz})\,. && (5.2)
\end{aligned}
$$

The atomic dipole moment is $d_{\uparrow e} = 1.465$ C·m (Clebsch-Gordon coefficient included) [141], c is the speed of light, λ is the the wavelength of the $|\uparrow\rangle$ to $|e\rangle$ transition. $\epsilon_\circ$ is the electric permittivity of vacuum, and $\hbar$ is Planck's constant. Including the effect of divergence of the mode from waist, the mode volume is $V_m = \frac{1}{4}\pi w_0^2 l$ for the TEM_{00} mode of a standing wave cavity with mode waist w_0 and length l[1] . We will later define an effective single atom vacuum Rabi frequency $2g$ and effective atom number N to account for the effects of inhomogeneous coupling of the cavity mode to the atoms in Section 5.4. For the discussion in the next paragraph, all that is required to know is that

---

[1] For macroscopic cavities $l \gg \lambda$, the effect of the photon field penetration into the mirror multi-layer dielectric coatings (single layer thickness typically $\lambda/4$) may be neglected. The cavity length is simply given by the spacing between the mirrors. For very short cavities, $l \sim \lambda$, the penetration depth can constitute a major correction to the mode volume V_m.

$2g = 2\pi \times (506 \text{ kHz})$.

The effective single atom cooperativity is given by $C = (2g)^2/\kappa\Gamma$ where the cavity power decay rate or FWHM linewidth is $\kappa/2\pi = 11.1(2)$ MHz, and the excited state $|e\rangle$ population decay rate is $\Gamma/2\pi = 5.75$ MHz. C is the optical depth presented by a single atom to the cavity mode. Equivalently, C is the fraction of solid angle subtended by the cavity mode, multiplied by the number of round trips $2F/\pi$. A single atom in $|e\rangle$ will decay into the cavity mode with rate $C\Gamma$ and at rate Γ into free space modes. As $C = 4.02(6) \times 10^{-3} \ll 1$, a single atom hardly feels the presence of the cavity mode at all.

By using many atoms, the coupling of the atoms to the cavity mode is collectively enhanced so that the ratio of cavity emission to free space emission is NC. With $NC \gg 1$, the rate at which collective atomic information is extracted from the cavity mode is enhanced relative to the rate at which single particle information is revealed via free space scattering. In other words, free space scattering can be engineered away by using large collective cooperativity NC. Information obtained through the cavity mode preserves coherence or quantum superpositions as cavity emission does not provide in-principle information about which atom forward scattered into the cavity mode. Free space scattering into optically thin modes, however, leads to single atom wavefunction collapse because the environment has in-principle information to figure out which atom has scattered the photon. In our experiment, coupling to the cavity mode is enhanced by using up to $N = 7 \times 10^5$ so that the collective cooperativity parameter during the QND measurements $N_\uparrow C \approx 1400$ is large.

5.3 Key experimental details for Science Cavity and atomic ensemble

5.3.1 Science Cavity

We determined the Science Cavity parameters at 795 nm by accurately measuring the cavity FSR and transverse mode spacings by measuring the frequency beat between two lasers that are simultaneously resonant with the relevant cavity modes. The parameters for the Science Cavity are summarized in Table. 5.1.

Parameter @ 795 nm	
Cavity length l	1.9149(2) cm
Mirror radius of curvature R_c	5.000(8) cm
Rayleigh length z_R	1.968(2) cm
Free spectral range f_{FSR}	7828(1) MHz
Frequency slitting between TEM_{01} and TEM_{00} mode	2257(2) MHz
Frequency splitting between TEM_{02} and TEM_{00} mode	4515(3) MHz
Linewidth $\kappa/2\pi$	11.1(2) MHz
Linewidth due to mirror transmission only (ATF's datasheet) $\kappa_0/2\pi$	5.29 MHz
Linewidth due to absorption and scattering losses $\kappa_L/2\pi$	5.8(2) MHz
Finesse F	710(10)
Mode waist w_0	70.56(4) μm
Mode volume V_m	$7.488(8) \times 10^{-5}$ cm^3
Antinode cooperativity $C_0 = (2g_0)^2/\kappa\Gamma$	$5.8(1) \times 10^{-3}$
Effective cooperativity $C = (2g)^2/\kappa\Gamma$ (includes thermal averaging)	$4.02(6) \times 10^{-3}$
Antinode single atom Rabi frequency $2g_0/2\pi$	607.1(5) kHz
Effective single atom Rabi frequency $2g/2\pi$ (includes thermal averaging)	506(8) kHz

Table 5.1: Science Cavity Parameters

5.3.2 Atomic ensemble properties

Key details for the atomic ensemble and the intracavity optical lattice are summarized in Tables 5.2 and 5.3, respectively. Here, we describe how these parameters were measured and inferred. We measured a radial temperature of 25(12) μK for the atomic ensemble using a release and probe (time of flight) method, where we measure the expansion of the atomic cloud versus time of flight through the reduction of coupling of the atoms to the cavity mode. To take a snapshot of the dynamics in the lattice at full power, the lattice was switched off on a time scale much faster than the radial trap frequency. Together with the calculated average lattice depth of $U_0/h = 7.4(5)$ MHz or 360(30) μK, we infer the rms radial extent of the ensemble in the x and y directions to be $x_{\mathrm{rms}} = y_{\mathrm{rms}} = 10(2)$ μm. Assuming the axial temperature is in thermal equilibrium with the radial temperature, the rms amplitude of atomic motion in the axial direction is $z_{\mathrm{rms,\,pancake}} = 24(6)$ nm.

The axial extent of the atomic ensemble was measured by spatially selective population tomography. To do so, we selectively remove atoms in all but a small sliver of region illuminated by a light sheet coming from the side of the cavity. The atomic population $N_\uparrow$ is then measured as a function of the light sheet position via the vacuum Rabi splitting measurement, described in Section. 5.6.1. The measured axial distribution of the atomic population is well described by a Gaussian with rms width $z_{\text{rms, ensemble}} = 0.84(9)$ mm. With this measurement, the center of the atomic ensemble is also confirmed to < 1 mm from the center of the cavity. These length scales are much smaller than the Rayleigh length of the cavity mode $z_R = 1.968(2)$ cm, the characteristic length scale over which the cavity mode waist increases from $w(0) = w_0$ to $w(z_R) = \sqrt{2}w_0$. The small axial extent and good centering of the atoms will result in only a small reduction in the coupling of the ensemble to the cavity mode, as we shall see in the next section.

Atomic Ensemble Property	Value
Excited state linewidth $\Gamma/2\pi$	5.7500(56) MHz [141]
Dipole Matrix Element $d_{\uparrow e}$	1.728(1) ea_0 or $1.465(1) \times 10^{-29}\,\text{C}\cdot\text{m}$ [141]
rms axial extent $z_{\text{rms, ensemble}}$	0.84(9) mm or $\sim$ 2000 pancakes
rms radial extent x_{rms}	10(2) μm
rms axial oscillation amplitude in each pancake $z_{\text{rms, pancake}}$	24(6) nm
Axial Lamb-Dicke parameter $k_{795}z_{\text{rms, pancake}}$	0.2
Offset from center of cavity	< 1 mm
Radial Temperature $k_B T_{\text{radial}}/h$	25(15) μK
Peak atom number per pancake (at center of cavity)	$\sim$ 200

Table 5.2: Atomic Ensemble Properties

Lattice Parameter	Value
Wavelength λ_{latt}	822.9(6) nm
Circulating power $P_{\text{latt,circ}}$	0.90(7) W
Trap depth or Average ground state ac Stark shift U_0/h	7.4(5) MHz or 360(30) μK
Differential ground state ac Stark shift	3.1(2) kHz or -413 ppm of avg ac Stark shift
Axial frequency f_{axial}	320(10) kHz
Radial frequency f_{radial}	0.82(3) kHz
Cavity mode waist @ 823 nm $w_{0,\text{latt}}$	71.78(4) μm
Cavity mirror transmission @ 823 nm from ATF datasheet	3615 ppm
Probe-Lattice beat length	13 μm or 32 lattice sites

Table 5.3: Intracavity Optical Lattice Parameters

5.4 Inhomogeneous coupling: effective coupling $2g$ and effective atom number N

The atomic ensemble of N_{tot} atoms experiences inhomogeneous coupling to the standing-wave probe mode at 795 nm because of the incommensurate 823 nm intra-cavity lattice, with some atoms essentially uncoupled to the probe mode. Thus the standard quantum limit (SQL) for the sub-ensemble of probed atoms is larger than that of the total ensemble N_{tot}. To account for this inhomogeneous coupling, we define effective atom numbers $N_\uparrow$, $N_\downarrow$ and $N = N_\uparrow + N_\downarrow$, and an effective coupling g. The definitions of the effective atom number N and effective coupling g are set by the two requirements that the combination correctly yield both the (1) average and the (2) rms fluctuations of the cavity frequency shifts. These two requirements can be expressed by the following two relationships respectively:

$$\left\langle \sum_{i=1}^{N_{\mathrm{tot}}} \hat{P}_{\uparrow,i}(2g(\vec{r}_i))^2 \right\rangle = N_\uparrow (2g)^2 \tag{5.3}$$

$$\left\langle \left(\sum_{i=1}^{N_{\mathrm{tot}}} \hat{P}_{\uparrow,i}(2g(\vec{r}_i))^2 \right)^2 \right\rangle - \left\langle \sum_{i=1}^{N_{\mathrm{tot}}} \hat{P}_{\uparrow,i}(2g(\vec{r}_i))^2 \right\rangle^2 = N_\uparrow (2g)^4/2 \tag{5.4}$$

Here, $g(\vec{r}_i)$ is the probe coupling constant for the ith spin at position $\vec{r}_i$, and $\hat{P}_{\uparrow,i} = |\uparrow_i\rangle\langle\uparrow_i|$ is the spin up projection operator for the ith spin. The expectation values are evaluated for a CSS along $\hat{x}$, and also include averaging over the thermal distribution of atomic positions $\vec{r}_i$. For the TEM_{00} mode of the standing wave cavity, $2g\left(\vec{r}\right) = 2g_0 \frac{w_0}{w(z)} e^{-\frac{x^2+y^2}{w(z)^2}} \sin(kz)$ where $w(z) = w_0\sqrt{1+(z/z_R)^2}$. Refer to Table. 5.1 for a summary of the Science Cavity properties.

Accounting for both the axial and radial averaging of the probe-atom coupling due to the finite thermal spread and axial extent of the ensemble, the two conditions Eqs. 5.3, 5.4 yield an effective coupling g related to the peak coupling g_0 by

$$2g = 0.963(15) \times \frac{\sqrt{3}}{2} \times 2g_0 \tag{5.5}$$

$$= 2\pi \times (506(8)\,\mathrm{kHz}) \tag{5.6}$$

where the factor $\frac{\sqrt{3}}{2}$ accounts for the inhomogeneous coupling and the factor 0.963(15) represents a reduction in coupling due to thermal spread in the radial directions and the increasing mode waist size along the axial direction. Similarly, the effective atom number N that goes hand in hand with the effective single atom vacuum Rabi frequency is

$$\begin{aligned} N &= 0.996(4) \times \frac{2}{3} \times N_{\text{tot}} \qquad (5.7) \\ &= 0.664(3) \times N_{\text{tot}} \qquad (5.8) \end{aligned}$$

where the factor $\frac{2}{3}$ accounts for the inhomogeneous coupling and the factor 0.996(4) arises from thermal averaging. The uncertainties in $2g$ and N are dominated by the atom temperature uncertainty. To restate, these definitions are chosen such that the observed vacuum Rabi splitting is given by $\Omega_\uparrow = \sqrt{N_\uparrow}2g$, and the fluctuations due to projection noise fluctuations in $N_\uparrow$ for a CSS along $\hat{x}$ is given by $\sqrt{N}/2$, consistent with the results of Chapter 3.

5.5 Sample preparation

In this brief section, I describe how the sample is initialized prior to the QND measurements. The temperature measurements described earlier were also performed after this initialization step. ^{87}Rb atoms are loaded trapped in a magneto-optical trap (MOT) at the middle of the cavity for about 1 second. The atoms are then loaded and cooled into the one-dimensional intra-cavity lattice trap at 823 nm and at zero magnetic field. Atom number is controlled by the lattice loading time. A quantization magnetic field of 4.8 Gauss along the lab physical coordinate system $\hat{x}$ (see Fig. 5.2) is turned on and the atoms are optically pumped into $|\downarrow\rangle$ with a π-polarized free space laser beam on $F = 1$ to $F' = 1'$ at 780 nm. Repumper beams at $F = 2$ to $F' = 2'$ at 780 nm recycles atoms that end up in $F = 2$ back down to $F = 1$. As $|\downarrow\rangle$ is dark with respect to both the optical pumping beam and 3D repumping beams, the atoms eventually accumulate in $|\downarrow\rangle$. To clear out any atoms in $F = 2$, the repumper beams are left on for 100 μs longer after the optical pumping beam is turned off. At this stage the ensemble ready to be manipulated with microwave rotations and probed with light through the optical cavity. After the squeezing operation or other experiments are concluded with the sample, a fresh sample is prepared by repeating the initialization steps.

5.6 Measuring J_z

In our probing scheme, we do not measure J_z in single Rabi splitting measurement because the Rabi splitting $\Omega_\uparrow$ only depends on the atomic population $N_\uparrow$. However, by performing a π-pulse to phase coherently swap the population between $|\downarrow\rangle$ and $|\uparrow\rangle$, and performing a Rabi splitting measurement again with the results labeled $\Omega_\downarrow$ and $N_\downarrow$, we can construct $J_z = (N_\uparrow - N_\downarrow)/2$ from the measurements. The experimental sequence is illustrated in Fig. 5.3.

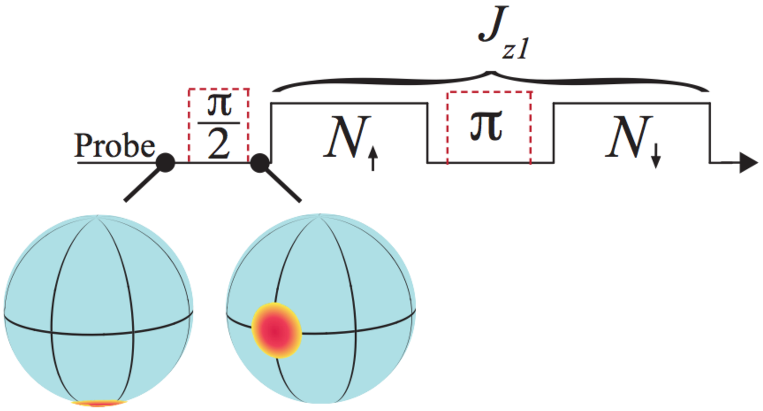

Figure 5.3: Experimental Sequence for a single measurement of J_z. The measurement sequence consists of microwave rotations (dashed line) and QND population measurements (solid line). Each QND population measurement is implemented by simultaneously probing both modes of the collective vacuum Rabi splitting $\Omega_{\uparrow,\downarrow}$, discussed in Section 5.6.1. The atomic populations are then obtained from the measured Rabi splittings $\Omega_{\uparrow,\downarrow}$ via $N_{\uparrow,\downarrow} = \left(\frac{\Omega_{\uparrow,\downarrow}}{2g}\right)^2$. Finally J_z is constructed from $N_{\uparrow,\downarrow}$ via the relation $J_z = (N_\uparrow - N_\downarrow)/2$.

5.6.1 Single Rabi splitting measurement

In this section, we describe how a single measurement of the vacuum Rabi splitting $\Omega_\uparrow$ or $\Omega_\downarrow$ is performed. We employed heterodyne detection of the probe sidebands, directly IQ demodulated so that the full amplitude and phase response during a frequency sweep could be used to extract the mode resonance frequencies, as described in Section 3.2.3.

The probe beam was phase modulated at 150 MHz using a free space electro-optic-modulator (EOM) (Thorlabs EO-PM-NR-C1, $V_\pi = 180$ V) and a high power rf amplifier (Minicircuits LZY-

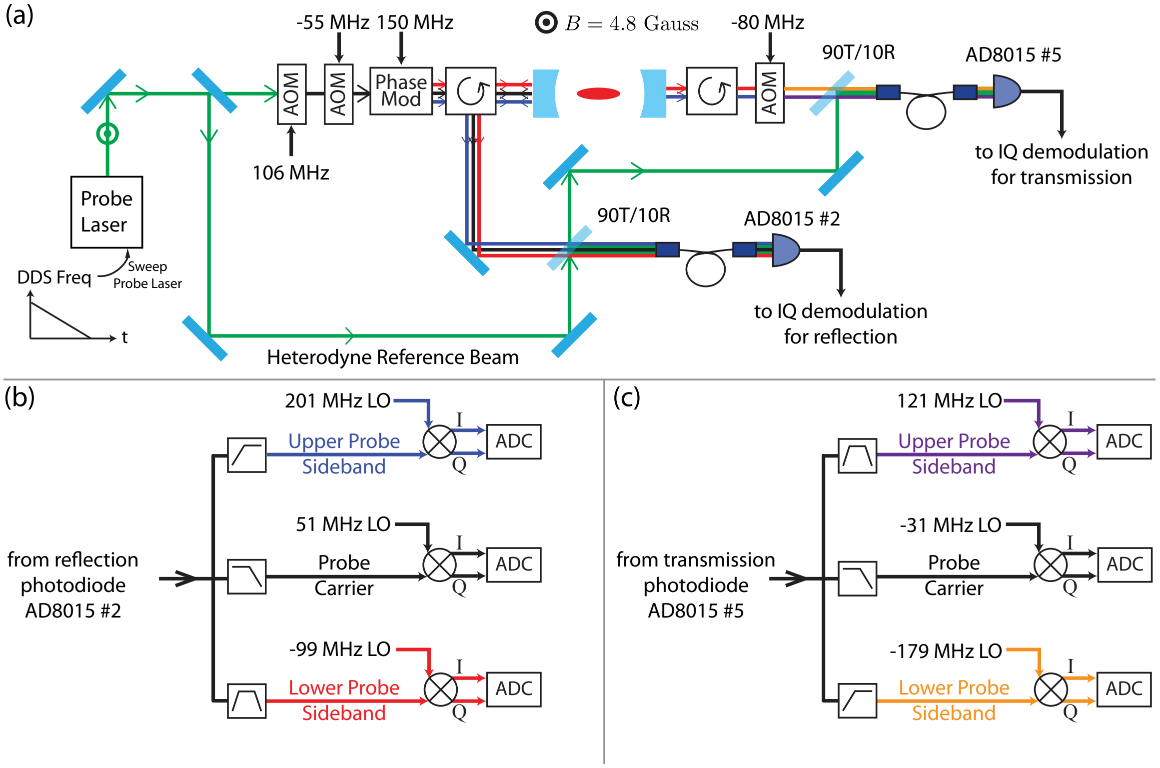

Figure 5.4: Experimental schematic of the heterodyne IQ detection system used to probe the vacuum Rabi splitting. (a) Resonant coupling of the atoms to the cavity mode generates a collective vacuum Rabi splitting $\Omega_\uparrow = \sqrt{N_\uparrow}2g$. The trapping optical lattice is not shown here. Both components of the vacuum Rabi splitting are simultaneously probed using the first order phase modulation sidebands spaced ±150 MHz from the carrier. During a single $\Omega_\uparrow$ or $N_\uparrow$ measurement, the probe laser frequency is linearly swept from high to low optical frequency. Phase coherent modulation and demodulation of the probe signals is accomplished by generating all frequencies with phase-coherent DDSs. An AOM frequency shifts the transmission signals to avoid frequency degeneracy with the contaminating reflected probe signals on the recycled heterodyne reference beam. (b, c) The IQ demodulation frequencies were adjusted appropriately to mix the reflection and transmission signals down to DC. The demodulation frequencies are given by the probe component optical frequency minus the heterodyne reference beam frequency. In transmission, the carrier signal is not present when probing atoms because the transmission resonances have shifted to the dressed atoms-cavity mode frequencies. It is used as a diagnostic for probing the bare cavity.

1+). The phase modulation generates a high frequency and a low frequency probe sideband, depicted as blue and red colored beams respectively in Fig. 5.4(a), with a modulation index $\beta \sim 1.5$. For probe sideband power calibration, we measure the fraction of probe power in each first order probe sideband to be 0.30(2) of the total probe power. The overall probe power is set by the 55 MHz AOM rf power level, and we typically probe with 1-10 nW total probe power incident at

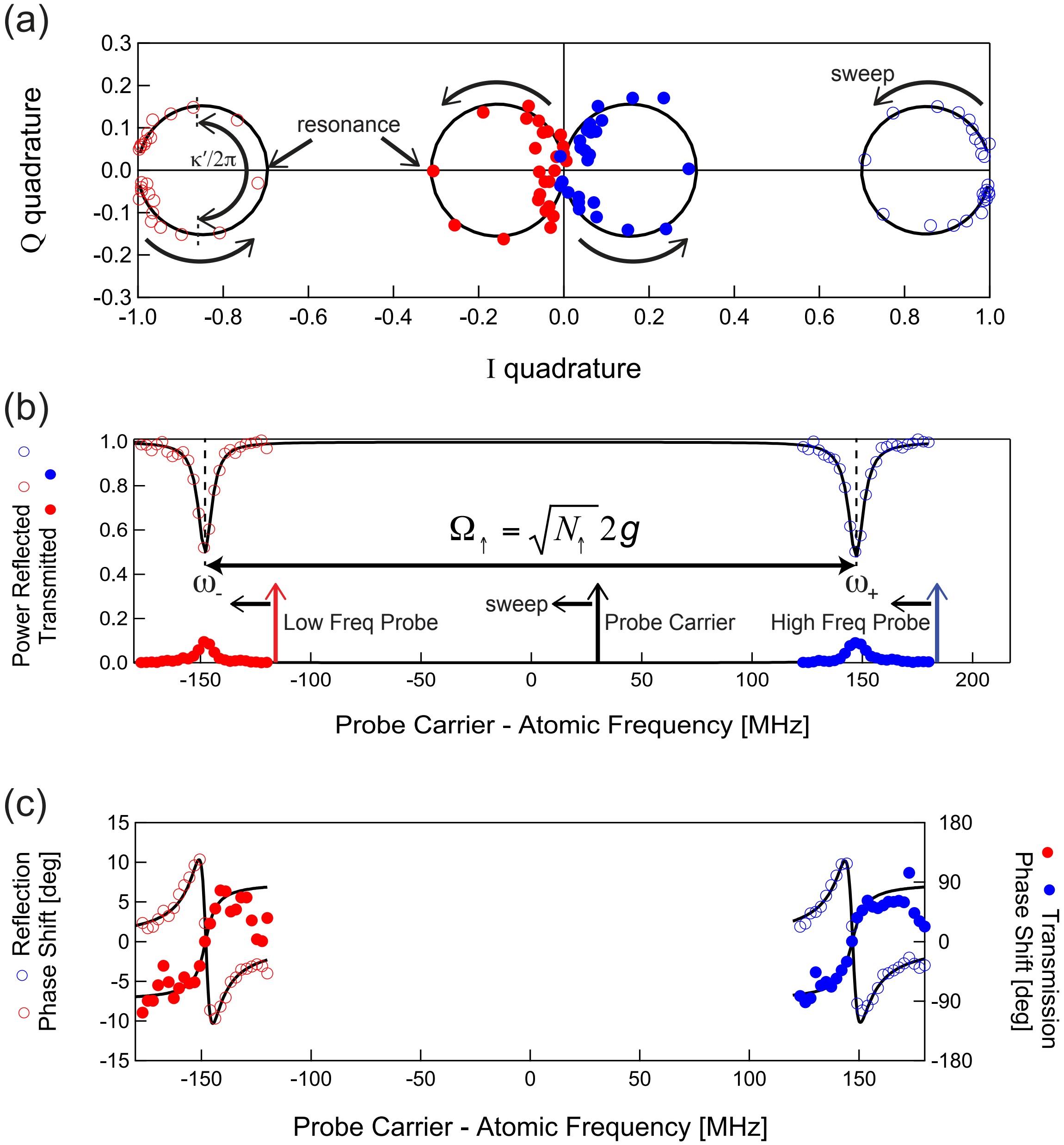

Figure 5.5: Simultaneous probing of the vacuum Rabi splitting in transmission and reflection. The blue and red data points are the individual Rabi splitting signals $\omega_\pm$ simultaneously measured by sweeping the phase-modulated probe laser frequency. The resonance frequencies are extracted from fits (black curves) to the data plotted parametrically versus the probe frequency in the IQ plane (a). A rotation has been applied to align the circles along the I-quadrature for presentation purposes. The corresponding power $I^2 + Q^2$ (points – data, curve – from IQ fit results) (b), and phase shift $\arctan(Q/I)$ (points – data, curve – from IQ fit results) for both transmission and reflection (c). The size of the fitted vacuum Rabi splitting $\Omega_\uparrow = \omega_+ - \omega_-$ determines the population in $|\uparrow\rangle$ from $N_\uparrow = (\Omega_\uparrow/2g)^2$. A single scan requires 60 μs. Note: for presentation purposes, only every 5th data point is plotted.

the cavity.

Probing both the high and lower frequency dressed modes simultaneously is advantageous for probe-induced ac-Stark shift cancellation, to be discussed in Chapter 6. Simultaneous probing is achieved by adjusting the atom number to produce a Rabi splitting $\Omega_{\uparrow}/2\pi = 300$ MHz splitting that matches the probe sidebands frequency separation. The probe laser optical frequency is swept at -1184 MHz/ms by linearly ramping a DDS frequency source used to phase lock the probe laser to a fixed frequency reference laser.

In a single 60 μs measurement of $\Omega_{\uparrow}$, or equivalently $N_{\uparrow}$, the probe laser is swept over a span of 71 MHz, spending ~ 7 μs on the dressed modes resonances that have FWHM of $\sim 8.5(3)$ MHz (see Fig. 5.9). A single measurement of J_z requires two population measurement windows, each taking 60 μs, and a 14.5 μs microwave π-pulse to phase coherently swap the populations $N_{\downarrow}$ and $N_{\uparrow}$ in between the two measurement windows. The π-pulse plays a crucial role in spin echoing away inhomogenous probe-induced and lattice-induced ac-Stark shifts that would otherwise lead to severe loss of coherence if left un-cancelled. Chapter 6 will discuss spin-echo in more detail.

To make full use of the available information, both ports of our symmetric cavity are detected. Nearly photon shot-noise-limited detection of the weak probe ($\sim$nW) is achieved via heterodyne detection. The reflected probe light is overlapped with a strong heterodyne reference beam on a 90/10 beamsplitter and then coupled into a single mode fiber for good mode matching before sending to a low noise photodiode. The transmission setup is very similar. The detection path efficiency is approximated 0.3 in transmission and 0.5 in reflection. The photodiode (Hammamatsu S5973) internal quantum efficiency is 84%. The relative contribution of the photodiode electronic noise to the total photocurrent noise at a detected heterodyne power of 1.2 mW reduces net quantum efficiency by about 1 dB. Transfer function and noise characteristics of the detection photodiode are made available in Appendix C.

The probe-sidebands and heterodyne beam produce a distinct rf beatnotes that can be frequency separated using rf filters. The beatnote frequencies for the various probe frequency components are given in Fig. 5.4(b, c). Full amplitude and phase information of the probe electric field, or equivalently the full in-phase (I) and quadrature (Q) amplitudes are obtained by phase coherently demodulating the heterodyne signals down to DC.

Phase stabilization of the heterodyne interferometer may be important for getting a good phase estimate from the IQ fits. However, the measurements are only sensitive to phase drifts on time scales comparable to a single population measurement. By sweeping across the resonances quickly, phase stabilization of the interferometer was not crucial for obtaining high quality fits of the IQ data.

Figure 5.5(a) shows typical IQ signals recorded in both reflection and transmission. The high (low) frequency probe component sweeps across the resonance ω_+ (ω_-), with the resulting signals shown in blue (red) in Fig. 5.5(b, c, d). The signals are sampled into our data acquisition program and fitted in real time. See Figure. 5.6 for a screenshot of the data acquisition program. The resonance frequencies were extracted using least squares fitting in the IQ-quadrature plane, yielding estimates $\Omega_\uparrow^{\text{refl}}$ ($\Omega_\uparrow^{\text{trans}}$) of the Rabi splitting from the IQ reflection (transmission) fit, respectively. Empirically, we find that the weighted average $(0.61\Omega_\uparrow^{\text{refl}} + 0.39\Omega_\uparrow^{\text{trans}}) \equiv \Omega_\uparrow$ exhibited the least noise in two repeated measurements of the same Rabi splitting. This ratio reflects the relative quantum efficiencies in reflection and transmission.

Figure 5.6: Screenshot of data acquisition program showing experimental control sequence table (left monitor, middle), raw data (left monitor, top), real-time fitting of the IQ signals in the complex plane (right monitor, left top) and accumulation of measurement statistics from different experimental trials (right monitor, right panel).

5.6.2 Measurement uncertainty ΔJ_z

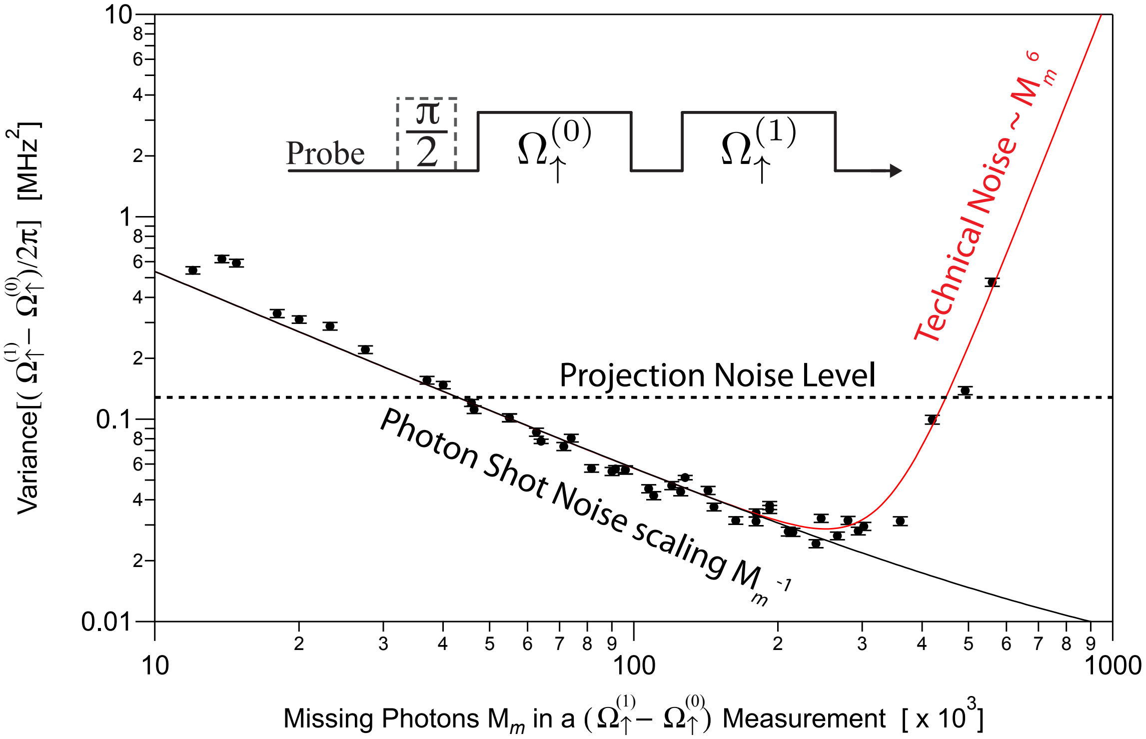

Figure 5.7: Measurement uncertainty estimated from the noise in the difference of two repeated measurements of the same vacuum Rabi splitting $\Omega_\uparrow$. Inset shows sequence for this measurement. This measurement is used for calibration because it is insensitive to projection noise. The data (black dots) versus missing photons M_m (definition of M_m is given in Section 3.2.4) displays photon shot noise scaling as M_m^{-1} (black line, fitted to data below 1.8×10^5 missing photons) until technical induced by frequency chirping of the resonances takes over sharply. An empirical fit to the full range of data indicates that the technical noise variance (red line) scales as M_m^6. The projection noise variance is $\Delta(\Omega_\uparrow - \Omega_\downarrow)^2_{\text{CSS}}/(2\pi)^2 = 0.128\ \text{MHz}^2$ (dotted line) and is independent of the atom number N. Sub-projection noise sensitivity is achieved from $M_m \sim 5 \times 10^4$ to 4×10^5 photons. This data was taken at $N = 7 \times 10^5$ atoms.

The probe photon shot noise along with technical noise contribute an uncertainty ΔJ_z to the estimate of the projection J_z. To calibrate this noise, we start with all atoms in $|{\downarrow}\rangle$ (i.e. $\theta = \pi$), perform a $\pi/2$ rotation to prepare a CSS along $\hat{x}$. The vacuum Rabi splitting is then measured twice with the results labeled $\Omega_\uparrow^{(0)}$ and $\Omega_\uparrow^{(1)}$. Each measurement may fluctuate from one trial to the next due to total atom number fluctuations, microwave power fluctuations, and quantum projection noise; however, these sources of noise are common to both measurements within a single trial and cancel, at least to lowest order. Statistical error bars of the standard deviation $\Delta(\Omega_\uparrow^{(1)} - \Omega_\uparrow^{(0)})$ are estimated via $\Delta(\Omega_\uparrow^{(1)} - \Omega_\uparrow^{(0)})/\sqrt{2(n_{\text{trials}} - 1)}$, where n_{trials} is the number of experimental trials, typically around 1000 for this data, at each missing probe photon number M_m. The measurement uncertainty data $\Delta(\Omega_\uparrow^{(1)} - \Omega_\uparrow^{(0)})$ versus missing probe photon number M_m displayed in Fig. 5.7 was taken at our squeezed ensemble size of $N = 7 \times 10^5$ atoms. The measurement uncertainty variance shows photon shot noise scaling M_m^{-1} until a technical noise variance that scales as $\sim M_m^6$ takes off at around about $M_m \sim 3 \times 10^5$ photons.

The measurement uncertainty is taken to be $\Delta J_z = \Delta\left(\left(\frac{\Omega_\uparrow^{(1)}}{2g}\right)^2 - \left(\frac{\Omega_\uparrow^{(0)}}{2g}\right)^2\right)/2$. For our reported squeezing result (to be discussed later), we used an average number of missing probe photons $M_m = 0.96(5) \times 10^5$ probe photons for a single measurement of $\Omega_\uparrow$, we achieve a probe measurement imprecision 6.5(5) dB below the projection noise level for $N = 7.0(3) \times 10^5$ atoms obtained from the relative noise between two repeated $\Omega_\uparrow$ measurements on the same atomic ensemble. This is close to the optimal measurement precision achievable in our system.

5.6.3 Probe-induced Raman scattering

This section is aimed at trying to understand the increase in measurement uncertainty as M_m is increased in Fig. 5.7. We will also make use of results in this section when discussing loss of coherence due to free space scattering later in Section 5.9.

Frequency chirping of the dressed modes resonances necessitate sweeping the probe frequency rather than just parking the probe frequencies on resonance. The chirping occurs because of free space scattering of the probe photons. The free space scattering causes $N_\uparrow$ to effectively decrease, thus reducing the size of the Rabi splitting $\Omega_\uparrow = \sqrt{N_\uparrow}2g$, and hence chirping of the dressed mode resonance frequency with time.

The chirping leads to added noise as photon number is increased above $M_m \sim 3 \times 10^5$ photons as clearly shown in Fig. 5.7, and the differential line broadening shown in Fig. 5.9. We hypothesize that the resonance frequencies fluctuate strongly at high photon number due to a positive feedback between Raman scattering and the vacuum Rabi splitting. The chirping causes more photons to be coupled into the cavity, which causes more chirping, which then causes even more photons to be coupled in and so on. This positive feedback could amplify initially small probe power fluctuations into large fluctuations in the Rabi splitting.

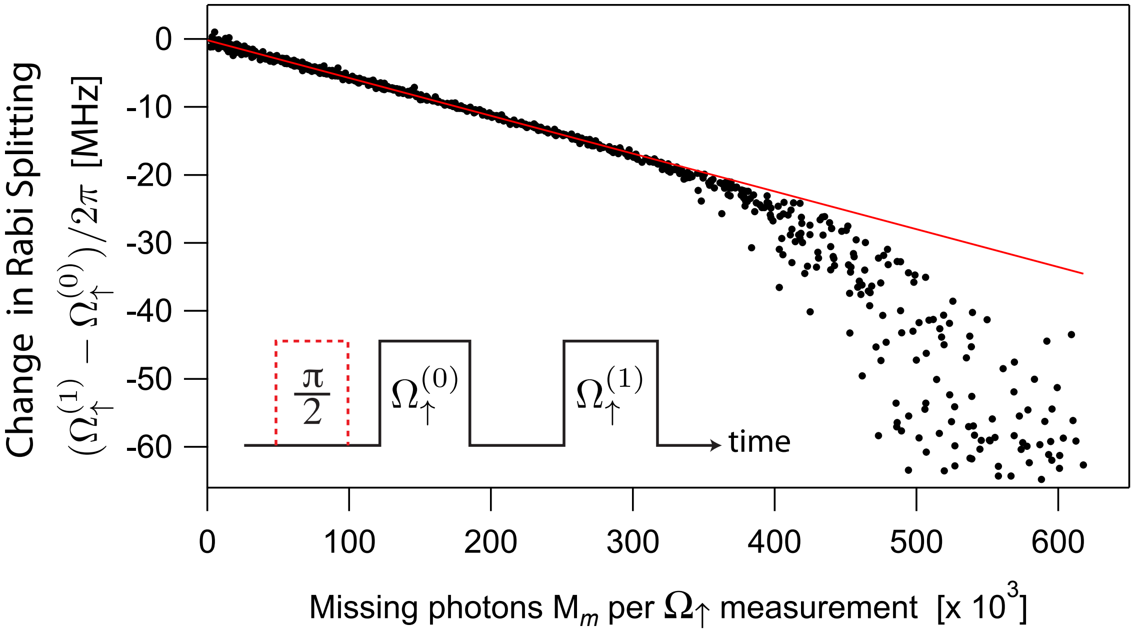

Figure 5.8: We observed a linear decrease in the difference $\Omega_\uparrow^{(1)} - \Omega_\uparrow^{(0)}$ with missing photon number M_m below 3×10^5 photons. Above 3×10^5 photons, severe chirping of the resonances discussed in Fig. 5.9 results in large fluctuations in the fitted resonance frequencies. The red line is a linear fit to to low $M_m < 2.5 \times 10^5$ missing photons to guide the eye.

To quantify the fundamental loss of coherence in Section 5.9 due to probe-induced free space scattering (technical loss of contrast may result from dephasing, probe-induced or otherwise), we need to understand the relationship between the directly measured number of missing probe photons M_m in the reflected port and the number of free space scattered photons M_s which is difficult to measure directly. By Eq. (3.12), we find that M_s is related to M_m by the following linear relation

$$\frac{M_s}{M_m} = \frac{\Gamma}{\Gamma + \kappa - \kappa_1}, \tag{5.9}$$

which evaluates to $M_s/M_m = 0.405(6)$ for our system. This relation is valid provided multiple scattering can be neglected.

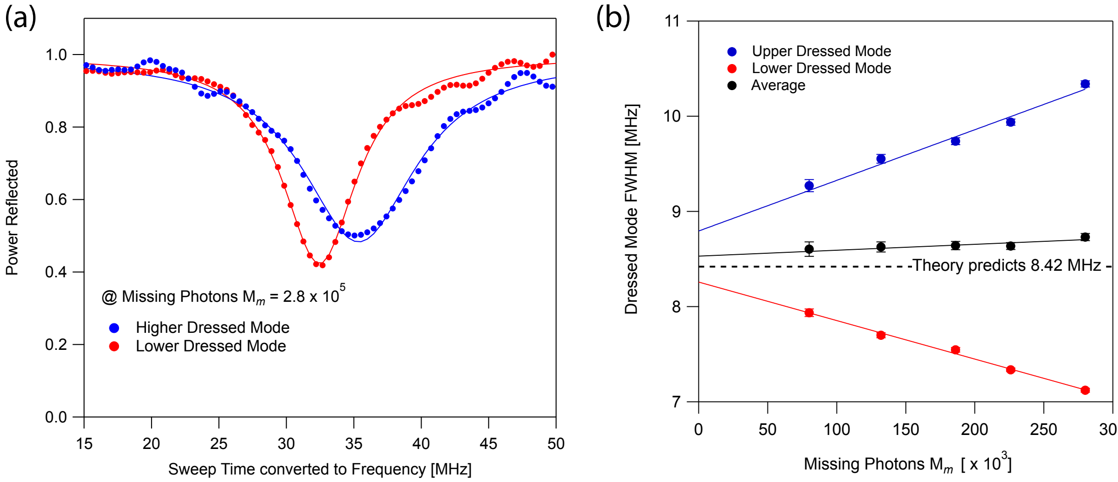

Figure 5.9: (a) Distortion of signals caused by Raman scattered induced chirping of the resonances. The distortion arises from a combination of a linear frequency sweep of the probe laser and a symmetric shrinking of the Rabi splitting about the center of the splitting during the probing. During probing, the Rabi splitting shrinks symmetrically about bare cavity frequency due to Raman free space scattering of the probe photons. As the probe laser is swept from higher to lower optical frequency, the higher frequency probe sideband would be "chasing after" the higher frequency dress mode of the shrinking Rabi splitting. Conversely, the lower frequency probe sideband would be "running into" the lower frequency dressed mode. This relative chirp causes the linewidth of the higher (lower) dressed mode to appear higher (lower) than it actually is. For the data shown here, the upper dressed mode has a fitted apparent linewidth of 10.3 MHz, and the lower dressed mode has a fitted apparent linewidth of 7.1 MHz. (b) Theory predicts the dressed mode linewidths, given by the average linewidths of the cavity and atom linewidths to be $\kappa'_{\pm} = 2\pi \times (8.4(1)\ \mathrm{MHz})$ with the uncertainty dominated by the cavity linewidth κ. Chirping of the resonances lead to an apparent linear increase (decrease) in the linewidths (blue and red data points) of the higher (lower) frequency dressed mode with the number of missing probe photons M_m as shown by the fits (blue and red lines). We average the apparent dressed mode linewidths to provide an estimate of the actual dressed mode linewidth (black data points). The slope of the linear fit to the average apparent linewidth data (black line) shows a factor of about 9 suppression compared to the fitted slopes for the upper and lower dressed mode apparent linewidths. The average of the black data points over the measurement range gives $(\kappa'_+ + \kappa'_-)/2 = 2\pi \times (8.5(3)\ \mathrm{MHz})$ and agrees with the theory prediction of 8.4(1) MHz to 1%.

To verify this prediction, we measure the decrease in the Rabi splitting $\Omega_\uparrow$ versus the missing photons M_m, obtaining the readily measurable $d\Omega_\uparrow/dM_m$. The Rabi splitting decreases because atoms that have undergone a Raman free space scattering event can end up in $|2, \pm1]\rangle$ and $|1, \pm1\rangle$, with lower coupling strengths to the cavity mode. In fact atoms scattered into $|1, \pm1\rangle$ have negligible coupling to the cavity mode because of the 6.8 GHz detuning from the ground state hyperfine splitting.

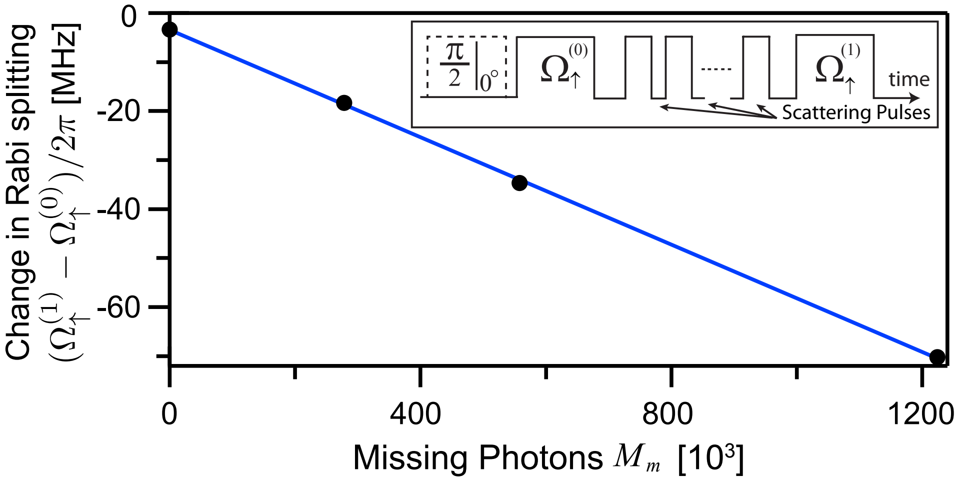

Figure 5.10: Change in Rabi splitting $(\Omega_\uparrow^{(1)} - \Omega_\uparrow^{(0)})/2\pi$ due to free space scattering versus missing photons M_m follows a linear scaling. The slope is predicted to be $-\frac{7}{16}\frac{g}{\sqrt{N_\uparrow}}\frac{M_s}{M_m}$. Using the independently and accurately known values of $2g = 2\pi \times (506(8)\text{ kHz})$ and $N_\uparrow = 3.50(15) \times 10^5$, we inferred $M_s/M_m = 0.408(4)$ from the measured data. This result is in excellent agreement (0.7% level) with an independent theory prediction of 0.405(6). The fit (blue line) is indistinguishable from the theoretical prediction. The inset shows the experimental sequence used to measure $\Omega_\uparrow^{(1)} - \Omega_\uparrow^{(0)}$. A CSS is prepared using the $\pi/2$ pulse (dashed line), and then the first measurement $\Omega_\uparrow^{(0)}$ is made. Next, the system is probed with M_m missing photons by applying a variable number of probe pulses which induces free space scattering while avoiding nonlinearities at high M_m. Finally, a second measurement $\Omega_\uparrow^{(1)}$ is made to determine the change $\Omega_\uparrow^{(1)} - \Omega_\uparrow^{(0)}$.

To connect the experimentally measurable quantity $d\Omega_\uparrow/dM_m$ to M_s/M_m, we need to calculate $d\Omega_\uparrow/dM_s$. Reproducing the results of Section 4.3.1 for the 3-level toy model here, the change in the atomic population $N_\uparrow$ per free space scattered photon is

$$\frac{dN_\uparrow}{dM_s} = -p\,, \tag{5.10}$$

where p is the spin flip probability from $|\uparrow\rangle$ to $|\downarrow\rangle$. Accounting for the multi-level structure of ^{87}Rb, we find the the "spin flip" probability per photon scattered into free space for an *actual physical atom* is $p_{\text{actual}} = 7/24$. I put spin flip in quotation marks because in our system, spin flips from $|\uparrow\rangle$ to $|\downarrow\rangle$ via the intermediate state $|e\rangle$ are actually not optical-dipole-allowed. However, Raman scattering takes the atoms from $|\uparrow\rangle$ to $|2, \pm1]\rangle$ and $|1, \pm1\rangle$ which changes the Rabi splitting. Therefore it is in this sense that the Raman scattering behaves like spin flips. In fact, it is more appropriate to treat these events as loss. Because of the inhomogeneous coupling present in our system, the "spin flip" of an *actual physical atom* is equivalent to "spin flips" of $0.996 \times 3/2 \approx 3/2$ *effective atoms*, therefore the effective "spin flip" probability per photon scattered into free space is $p = 3/2 \times p_{\text{actual}} = 7/16$. The change in Rabi splitting per free space scattered photon is then

$$\begin{aligned} \frac{d\Omega_\uparrow}{dM_s} &= -p\frac{g}{\sqrt{N_\uparrow}} \\ &= -\frac{7}{16}\frac{g}{\sqrt{N_\uparrow}}\,, \end{aligned} \tag{5.11}$$

and the experimentally measurable change in Rabi splitting per missing photon is

$$\frac{d\Omega_\uparrow}{dM_m} = -\frac{7}{16}\frac{g}{\sqrt{N_\uparrow}}\frac{M_s}{M_m}\,. \tag{5.12}$$

Experimentally, we observed a linear decrease in the Rabi splitting versus the missing photons M_m as shown in Fig. 5.10. From the slope $d\Omega_\uparrow/dM_m$, we inferred $M_s/M_m = 0.408(4)$, in excellent agreement (0.7% level) with the theory prediction of $M_s/M_m = 0.405(6)$.

5.7 Observation of quantum projection noise in J_z

To ensure that we are observing quantum projection noise as opposed to technical noise, we check that the observed noise variance in J_z scales linearly with N, and that it also agrees with our *a-priori* prediction for the absolute noise level. The ratio of the variances of measured to predicted projection-noise-driven fluctuations in $\Omega_\uparrow - \Omega_\downarrow$ is 1.02(6). This level of agreement is possible due to the very well-defined geometry of the cavity-mode, the trapping intra-cavity lattice and the cold temperature of the atomic ensemble.

In the resonant coupling limit $\delta_c = 0$ used in our experiments, the predicted projection noise $\Delta J_{z,\,\text{CSS}}$ would produce rms fluctuations in the vacuum Rabi splittings of

$$\begin{aligned} \Delta\left(\Omega_\uparrow - \Omega_\downarrow\right)_{\text{CSS}} &= \sqrt{2}g && (5.13) \\ &= 2\pi \times (358(6)\ \text{kHz}) && (5.14) \end{aligned}$$

independent of the atom number N. All other QND probing schemes demonstrated to date have been performed in the detuned limit $\delta_c \gg \Omega_\uparrow$ [100], where the rms fluctuations of the dressed cavity mode frequency due to projection noise scales as $\sqrt{N}$.

We measure the variance of $\Omega_\uparrow - \Omega_\downarrow$, and subtract from it the measured detection noise variance measured from the variance of $\Omega_\uparrow^{(1)} - \Omega_\uparrow^{(0)}$ measured in a separate series of trials (see Fig. 5.7). The noise background subtracted variance $\Delta\left(\Omega_\downarrow^{(1)} - \Omega_\uparrow^{(0)}\right)^2$ is defined as follows

$$\Delta\left(\Omega_\uparrow - \Omega_\downarrow\right)^2_{\text{bcksub}} = \Delta\left(\Omega_\uparrow - \Omega_\downarrow\right)^2 - \Delta\left(\Omega_\uparrow^{(1)} - \Omega_\uparrow^{(0)}\right)^2 \tag{5.15}$$

Note that the background subtraction is small at high atom number, but becomes appreciable at low atom number because the probe photon number must also be reduced to avoid contributions of Raman-scattering noise to the measurements at small N. Statistical error bars of the standard deviation ΔX are estimated via $\Delta X/\sqrt{2(n_{\text{trials}} - 1)}$, where $X = \Omega_\uparrow - \Omega_\downarrow$ or $\Omega_\uparrow^{(1)} - \Omega_\uparrow^{(0)}$ here, and n_{trials} is the number of experimental trials, typically between 400 to 600, at each atom number.

The background-free noise data $\Delta\left(\Omega_\uparrow - \Omega_\downarrow\right)_{\text{bcksub}}$, shown in Fig. 5.11(a) agrees with the *a priori* prediction (line) for the projection noise level $\Delta\left(\Omega_\uparrow - \Omega_\downarrow\right)_{\text{CSS}} = \sqrt{2}g/2\pi = 358(6)$ kHz to 2(6)%. By converting the measured fluctuations in the Rabi splitting to equivalent atom number variance, we confirmed the predicted projection noise variance $(\Delta J_{z,\,\text{CSS}})^2$ to 2(6)% (see Fig. 5.11(c) (fits not shown)). Projection noise results in a linear dependence of the variance with atom number, whose magnitude is determined using low order polynomial fits. The fitted linear contribution is 1.02(6) times $(\Delta J_{z,\,\text{CSS}})^2$. In this thesis, we conservatively normalize spin noise variances to the predicted projection noise variance instead of the slightly higher (2% higher) measured projection noise variance.

Technical noise from the atoms or (homogeneous) microwave rotation noise would exhibit a noise variance in ΔJ_z^2 scaling as N^2, illustrated by the orange dashed lines in Fig. 5.11. The ratio of the fitted technical noise variance to the projection noise variance is 21(7)% at our squeezed ensemble size of $N = 7 \times 10^5$ atoms. In Chapter 7, we will provide details regarding microwave rotations added noise.

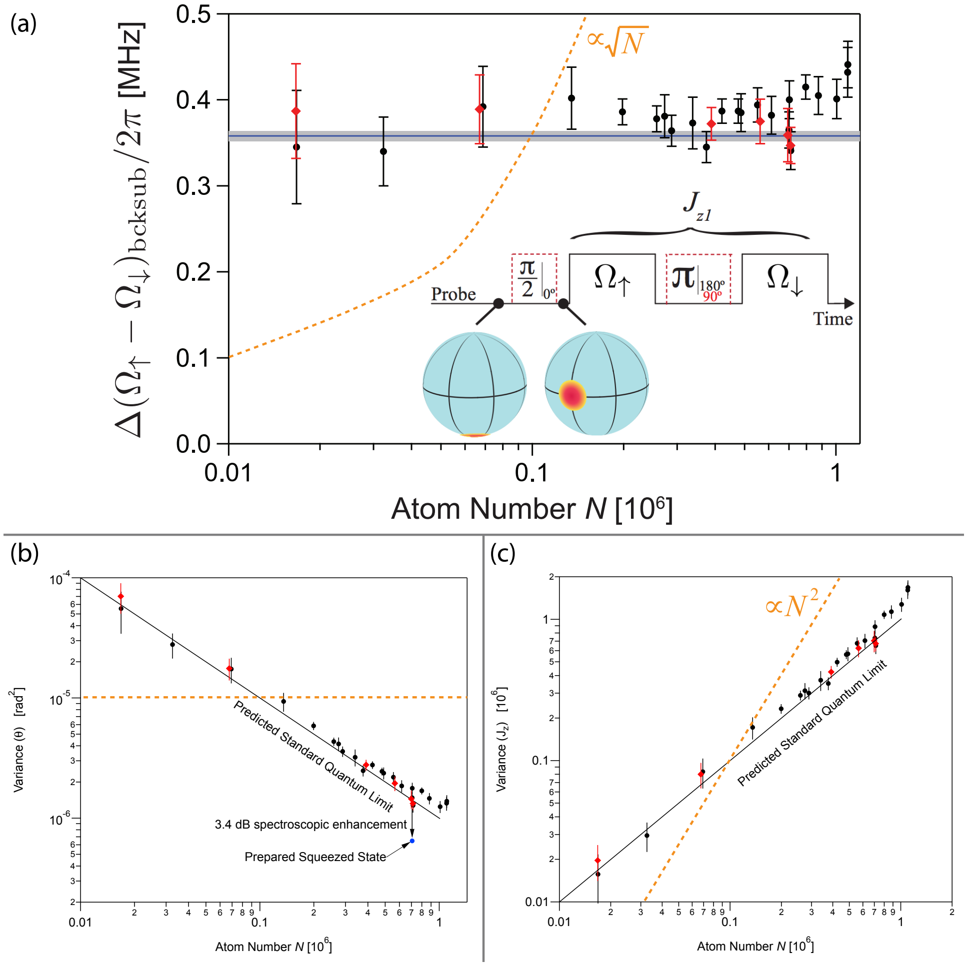

Figure 5.11: (a) In the resonant limit $\delta_c = 0$, the rms projection noise fluctuation of the population $N_\uparrow$ is independent of total atom number N. Shown here are the measured rms fluctuations of the dressed cavity modes $\Delta(\Omega_\uparrow - \Omega_\downarrow)_{\mathrm{bcksub}}/2\pi$ after subtracting out the noise background in quadrature. The data agrees with the *a priori* prediction (solid line) for the projection noise level $\sqrt{2}g/2\pi = 358(6)$ kHz to 2(6)%. The shaded gray area represents the error range of our theory prediction. At larger atom numbers $N > 7 \times 10^5$, additional technical noise was observed. In contrast, probing in the off-resonant regime results in a cavity mode frequency noise variance that scales linearly with N, and is always smaller than in the resonant limit [see Eq. (3.15)]. To constrain potential added noise from the π-pulse rotation that swaps the two atomic populations $N_\uparrow$ and $N_\downarrow$ between the two splitting measurements, we apply the rotation about an axis perpendicular to the CSS (black points), and about an axis parallel to the CSS (red diamonds). See Chapter 7 for constraints on microwave rotations added noise.

(b) Same data in (a) converted into fluctuations of the collective spin polar angle showing the observed variance of θ versus atom number N confirms the predicted SQL. In this Chapter, we demonstrate the preparation of conditionally spin squeezed states with an *inferred* spectroscopic sensitivity 3.4 dB below the SQL at a large ensemble size of $N = 7 \times 10^5$ atoms (blue point). At this ensemble size, the SQL is $\Delta\theta_{\mathrm{SQL}} = 1.2$ mrad and the generated squeezed state has an angular resolution of 0.8 mrad.

(c) Same data in (a) converted into variance in J_z, showing the linear scaling of quantum projection noise with atom number.

In all three plots, the scaling of technical noise with atom number N is schematically illustrated with an orange dashed curve/line.

5.8 Conditional spin variance

We now demonstrate that repeated measurements of J_z are correlated below the projection noise level $\Delta J_{z,\,\mathrm{CSS}}$. A first measurement J_{z1} estimates J_z to a precision set primarily by the measurement uncertainty ΔJ_z, preparing a sub-projection noise state when $\Delta J_z < \Delta J_{z,\,\mathrm{CSS}}$. As shown in Fig. 5.12, quantum projection noise plus added classical and detection noise causes fluctuations in the measured J_{z1} from one trial to the next, but the fluctuations are highly correlated with a second measurement J_{z2} (Fig. 5.12(b)). The degree of correlation between the two measurements J_{z1} and J_{z2} is characterized by the correlation coefficient ρ:

$$\rho \equiv \frac{\mathrm{cov}(J_{z1}, J_{z2})}{\mathrm{var}(J_{z1})}\,, \tag{5.16}$$

where the covariance is $\mathrm{cov}(J_{z1}J_{z2}) \equiv \langle J_{z1}J_{z2}\rangle - \langle J_{z1}\rangle\langle J_{z2}\rangle$, and the variance is $\mathrm{var}(J_{z1}) \equiv \langle J_{z1}\rangle^2 - \langle J_{z1}\rangle^2$. The variance $\mathrm{var}(J_{z1})$ is given by the sum of the measurement uncertainty variance $(\Delta J_z)^2$ from probe measurement imprecision and back-action and state preparation noise variance denoted $(\Delta J_{z,\,\mathrm{prep}})^2$

$$\mathrm{var}(J_{z1}) = (\Delta J_z)^2 + (\Delta J_{z,\,\mathrm{prep}})^2\,. \tag{5.17}$$

The state preparation noise variance $(\Delta J_{z,\,\mathrm{prep}})^2$ is the sum of the quantum projection noise variance $(\Delta J_{z,\,\mathrm{CSS}})^2$ as well as any classical rotation noise variance from the first $\pi/2$-pulse in the CSS preparation step.

The first measurement J_{z1} can be used to predict a second measurement J_{z2} with an optimal estimator ρJ_{z1}, allowing the state preparation noise to be partially canceled in the difference $J_{z2} - \rho J_{z1}$ (Fig. 5.12(c)). The estimator ρJ_{z1} is optimal in the sense that it minimizes the variance $(\Delta(J_{z2} - \rho J_{z1}))^2$. While the state preparation noise is common-mode to both measurements J_{z1} and J_{z2}, the measurement uncertainty ΔJ_z is independent for both measurements. If the measurement uncertainty ΔJ_z is zero, then the two measurements J_{z1} and J_{z2} would be perfectly correlated, i.e. $\rho \to 1$. In reality, finite probe measurement uncertainty and uncorrelated microwave rotation noise degrades the correlation ρ between the two measurements J_{z1} and J_{z2}.

At $N = 7.0(3) \times 10^5$ atoms and a missing probe photon number of $M_m = 1.9(1) \times 10^5$ per measurement of J_z, the *observed* conditional spin noise reduction relative to the projection noise limit was

$$\left(\frac{\Delta(J_{z2} - \rho J_{z1})}{\Delta J_{z,\,\mathrm{CSS}}}\right)^2 = -2.6(3)\,\mathrm{dB}\,, \tag{5.18}$$

where $\rho = 0.72(6)$ is estimated using Eq. 5.16. Subtracting the measurement uncertainty ΔJ_z of the second measurement in quadrature gives a conservative estimate of the uncertainty in the *inferred* conditional spin noise reduction $J_{z,\mathrm{inferred}}$ relative to the projection noise limit

$$\left(\frac{\Delta J_{z,\mathrm{inferred}}}{\Delta J_{z,\,\mathrm{CSS}}}\right)^2 \equiv \left(\frac{\Delta(J_{z2} - \rho J_{z1})}{\Delta J_{z,\,\mathrm{CSS}}}\right)^2 - \left(\frac{\Delta J_z}{\Delta J_{z,\,\mathrm{CSS}}}\right)^2 = -4.9(6)\,\mathrm{dB}\,. \tag{5.19}$$

The measurement uncertainty was $\left(\Delta J_z/\Delta J_{z,\,\mathrm{CSS}}\right)^2 = -6.5(5)$ dB as determined from fluctuations in the difference of two time adjacent $\Omega_\uparrow$, or equivalently $N_\uparrow$, measurements in Section. 5.6.2.

A different approach to estimating the measurement uncertainty is to assume each QND measurement has the same measurement uncertainty, whereas the quantum projection noise (as well as classical state preparation noise) is common mode to both measurements. Under this assumption, the difference $J_{z2} - J_{z1}$ then exhibits twice the amount of measurement uncertainty variance than a single J_z measurement. Using the measured value of $\left(\Delta(J_{z2} - J_{z1})/\Delta J_{z,\,\mathrm{CSS}}\right)^2 = -2.1(3)$ dB and dividing by 2 (i.e. subtracting 3 dB) yields a slightly better conditional spin noise reduction of $\left(\Delta J_{z,\mathrm{inferred}}/\Delta J_{z,\,\mathrm{CSS}}\right)^2 = -5.1(6)$ dB. Note that this estimate also agrees with the earlier estimate of $-4.9(6)$ dB within error bars. In this thesis, I will use the slightly more conservative inferred conditional spin noise reduction $\left(\Delta J_{z,\mathrm{inferred}}/\Delta J_{z,\,\mathrm{CSS}}\right)^2 = -4.9(6)$ dB to quantify squeezing.

5.9 Loss of coherence

Reduction of spin noise alone does not allow improved quantum phase estimation unless the length of the collective spin $|\langle \hat{\mathbf{J}} \rangle|$ is sufficiently unchanged. To claim spectroscopic enhancement or squeezing, we need to measure the coherence remaining after the QND measurement J_{z1} and show that the conditional reduction in spin noise more than makes up for the loss of signal due to probe-induced decoherence.

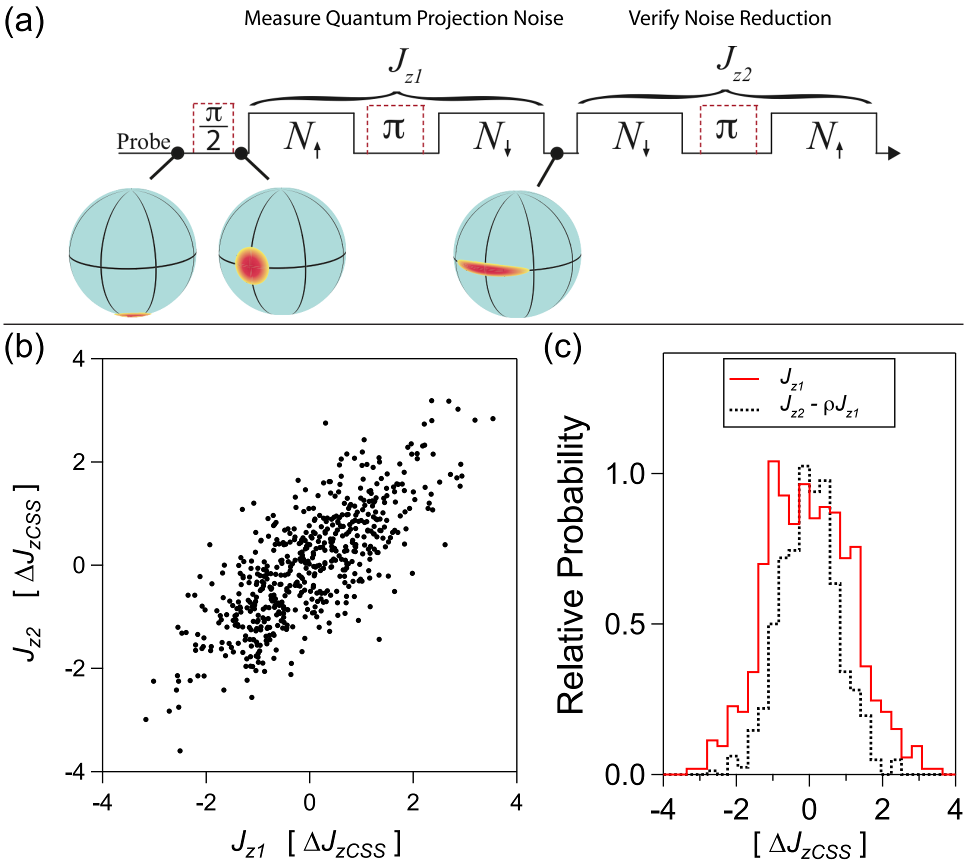

Figure 5.12: a) Measurement sequence for observing Correlation between successive QND measurements. (b) The first and second QND measurements of J_z exhibit correlated fluctuations that arise largely due to projection noise. Number of trials $n_{\text{trials}} \approx 570$. (c) The degree of correlation ρ between J_{z1} and J_{z2} can be used to conditionally reduce the spin noise of the resulting state after the first J_{z1} measurement to -4.9(6) dB below the CSS noise after subtracting out the measurement uncertainty.

In this section, we quantify the amount of coherence remaining versus the number of missing probe photons M_m used in a single QND measurement of J_z. The normalized length of the collective spin is measured by varying the polar angle θ from 0 to 2π and determining the contrast $\mathcal{C} = |\langle \hat{\mathbf{J}} \rangle|/J$ from the resulting variation of the population $N_\uparrow$ (see Fig. 5.13).

Having instilled confidence in our theory prediction for the ratio of free space scattered photons to missing probe photons via experimental verification in Section 5.6.3, we now use that theory to predict the *fundamental* probe-induced loss of coherence/contrast. If each free space scattered photon leads to the collapse of a single spin, we predict from Eqs. (4.1) and (5.9) that the

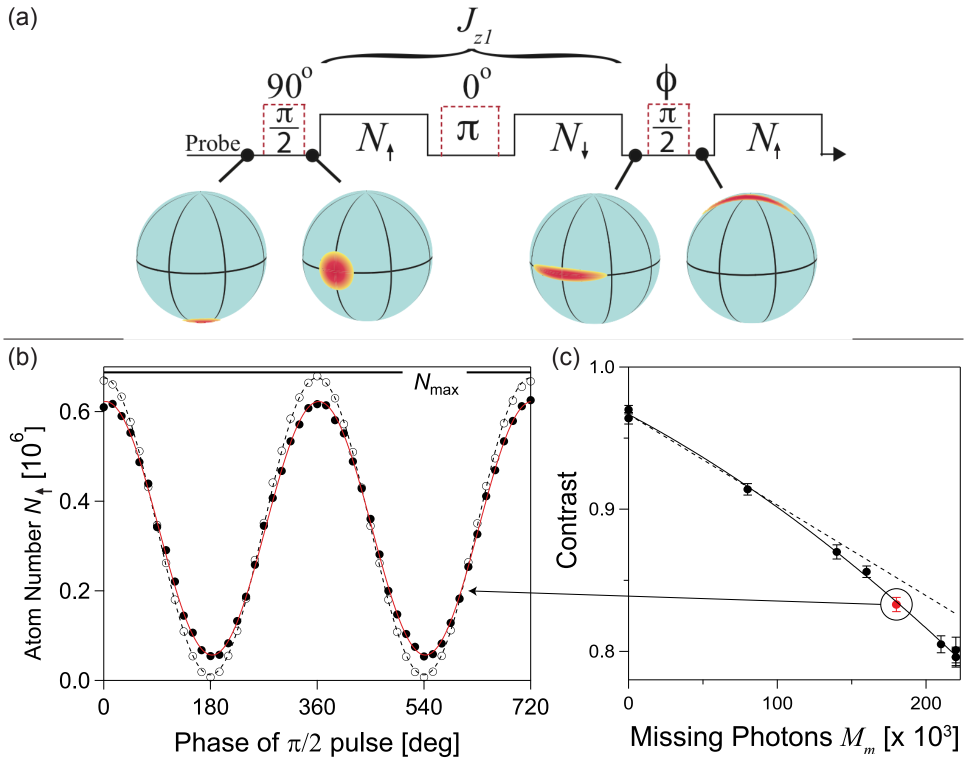

Figure 5.13: (a) The degree of coherence remaining after the measurement J_{z1} is determined using the sequence: $(\frac{\pi}{2})$–(measure $N_\uparrow$)–(π)–(measure $N_\downarrow$)–$(\frac{\pi}{2})$–(measure $N_\uparrow$). For the coherence measurements, a large dynamic range in J_z (compared to measuring projection noise fluctuations $\Delta J_{z,\text{CSS}}$ of a CSS) is required. To obtain a large dynamic range, we scan the probe laser (without sidebands) across the the full Rabi splitting $\Omega_\uparrow$, and detect the probe carrier in reflection. (b) The sequence is repeated and the final measured value of $N_\uparrow$ is plotted versus the phase of the final $\frac{\pi}{2}$-pulse. With no measurements (empty circles), the background contrast is $\mathcal{C}_i = 0.97(1)$. Probing with 1.8×10^5 missing photons (filled circles), causes a small reduction in contrast despite a measurement sensitivity below the projection noise level. (c) Measured contrast versus missing probe photon number (solid circles), second order polynomial fit (solid line), and the predicted contrast loss due to free space scattering alone (dashed line).

fractional reduction in contrast is $k_{1,\text{pred}} = 6.4(3) \times 10^{-7}$ per missing probe photon at $N = 7 \times 10^5$ atoms. This prediction is valid provided multiple scattering may be neglected, i.e. the actual loss of contrast is small.

Fig. 5.13 shows that the measured contrast $\mathcal{C}$ versus missing probe photon number M_m is well described by $\mathcal{C} = \mathcal{C}_i - k_1 M_m - k_2 M_m^2$. The fitted value, $k_{1,\text{fit}} = 5.5(7) \times 10^{-7}$ per missing probe photon, agrees with the prediction to 15%, and confirms the fundamental role of free space scattering as the dominant source of decoherence.

The quadratic variation of $\mathcal{C}$, $k_2 = 1.0(3)\times 10^{-12}$ per (missing probe photon)^2, arises from uncanceled inhomogeneous probe-induced light shifts that result in dephasing of the ensemble. These light shifts are largely spin-echoed away with the π-pulse used to measure J_{z1}. The uncanceled dephasing arises from radial motion in the trap, which will be discussed in Chapter 6. At fixed measurement uncertainty relative to the projection noise level, the magnitude of the dephasing increases linearly with probe detuning, making it easier to reach a scattering-dominated regime in this work compared to work in a far-detuned dispersive regime [100].

Before the QND measurements of J_z, the measured contrast is $\mathcal{C}_i = 0.97(1)$. Using $M_m = 1.9(1)\times 10^5$ missing probe photons in total for the first measurement J_{z1} at $N = 7.0(3)\times 10^5$ atoms reduces the contrast to $\mathcal{C}_f = 0.82(2)$. At this probe photon number, free space scattering of probe photons is the dominant source of decoherence loss. Loss of coherence from un-canceled ac-Stark shifts accounts for only 25% of the total loss of coherence.

5.10 Net spectroscopic enhancement

The ability to estimate the mean spin polar angle θ is largely set by the noise in J_z and the signal size $|\langle\hat{\mathbf{J}}\rangle|$. For a mean spin lying close to the $x-y$ plane, $\Delta\theta \approx J_z/|\langle\hat{\mathbf{J}}\rangle|$. Using the Wineland criterion [58], the directly *observed* spectroscopic enhancement is given by

$$\begin{aligned}\xi_{\mathrm{m}}^{-1} &= \left(\frac{\Delta J_{z,\,\mathrm{CSS}}}{\Delta\left(J_{z2}-\rho J_{z1}\right)}\right)^2 \frac{\mathcal{C}_f^2}{\mathcal{C}_i} \\ &= 1.1(4)\ \mathrm{dB}\end{aligned}$$

below the SQL. We *infer* the ability to prepare states with enhanced spectroscopic sensitivities of

$$\begin{aligned}\xi_{\mathrm{m}}^{-1} &= \left(\frac{\Delta J_{z,\,\mathrm{CSS}}}{\Delta J_{z,\mathrm{inferred}}}\right)^2 \frac{\mathcal{C}_f^2}{\mathcal{C}_i} \\ &= 3.4(6)\ \mathrm{dB}\end{aligned}$$

relative to the SQL for quantum phase estimation for $N = 7\times 10^5$ atoms, the *largest* ensemble size on which squeezing on a clock transition has been demonstrated to date. The demonstration of spin squeezing also implies inter-atomic entanglement in this large ensemble [68].

The small correction from $\mathcal{C}_i$ normalizes the spectroscopic enhancement relative to the SQL set by the partially decohered collective spin with shortened mean spin length as discussed in Section 4.5, Eq. 4.10). Because our initial coherence $\mathcal{C}_i = 0.97(1)$ is high, this results in a very small correction (increase of 0.1 dB in squeezing) for our reported results[2] .

5.11 Back-action

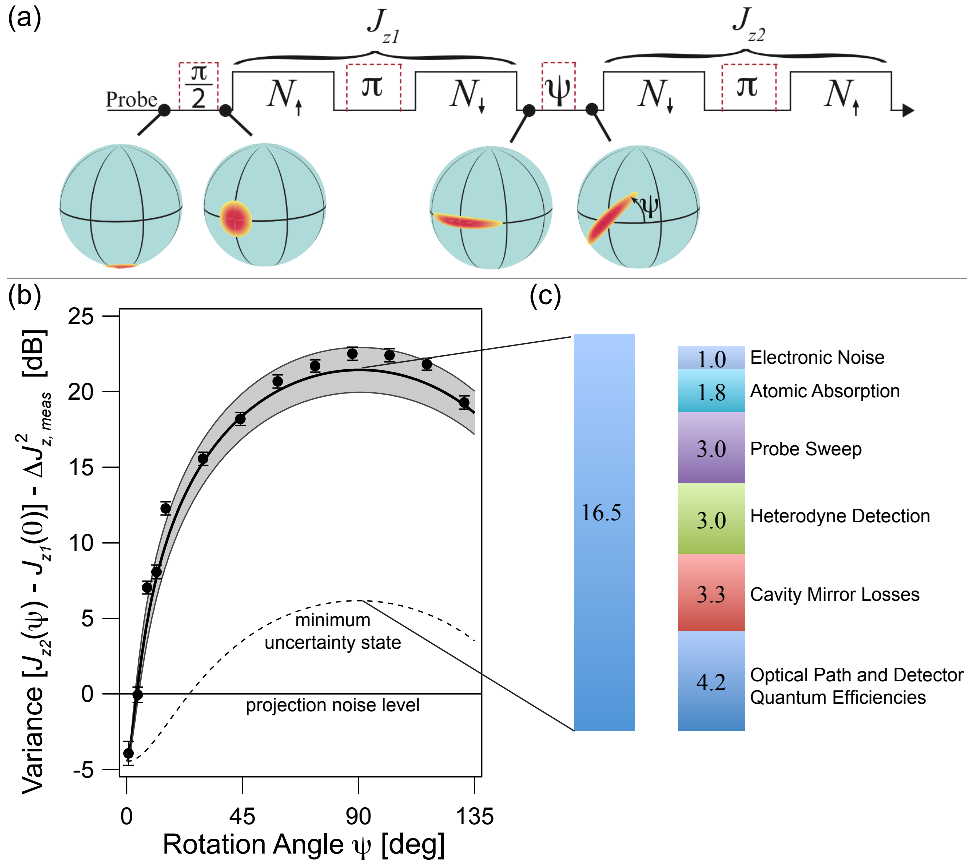

Figure 5.14: (a) Sequence for measuring back-action. Noise in the back-action quadrature is observed by inserting a rotation through angle ψ between the QND measurements J_{z1} and J_{z2}. (b) Back-action noise normalized to the projection noise level versus rotation angle ψ. The dashed curve is the calculated response for a minimum uncertainty squeezed state, while the solid curve with the gray 68% confidence interval is the predicted back-action from the intra-cavity probe vacuum noise. (c) The ratio of the predicted anti-squeezed quadrature at $\psi = \pi/2$ and that of a minimum uncertainty squeezed state is about 16.5 dB (left column) due to finite quantum and technical efficiencies. The right column gives the detailed breakdown from various estimated contributions. These contributions account for an estimated 16.3 dB of the excess back-action.

---

[2] For comparison, in Ref. [100], the initial contrast was $\mathcal{C}_i = 0.7$, resulting in 1.5 dB correction.

The un-measured quadrature J_y, or azimuthal angle ϕ_B in the limit of slight shortening of the collective spin, is driven by fluctuating ac-Stark shifts arising from the intra-cavity probe vacuum noise. Noise in the back-action quadrature is observed by inserting a rotation through an angle ψ between the QND measurements J_{z1} and J_{z2}, see Fig. 5.14(a). The measured and predicted quantum back-action noise levels are 22.3(1) dB and 21.4(1.5) dB relative to projection noise respectively. The ratio of the predicted anti-squeezed quadrature at $\psi = \pi/2$ to that of a minimum uncertainty squeezed state is 16.5 dB due to finite quantum and technical efficiencies in the probe detection process. We estimate that the compounding effects of finite quantum and technical efficiencies accounts for 16.3 dB out of the predicted 16.5 dB excess back-action. Detailed breakdown of these effects are shown in Fig. 5.14(c).

5.12 Conclusions

The key result of my thesis — the experimental demonstration of spectroscopic enhancement and entanglement as a result of collective QND measurements — has been presented in this Chapter. Specifically we have demonstrated the preparation of spin squeezed states with *inferred* spectroscopic enhancement

$$\begin{aligned} \xi_{\mathrm{m}}^{-1} &= \left(\frac{\Delta J_{z,\,\mathrm{CSS}}}{\Delta J_{z,\mathrm{inferred}}}\right)^2 \frac{\mathcal{C}_f^2}{\mathcal{C}_i} \\ &= 3.4(6)\ \mathrm{dB} \end{aligned}$$

relative to the SQL in a *large* ensemble of $N = 7 \times 10^5$ atoms, demonstrating the power of a top-down approach to generating entangled states for quantum metrology. This result is enabled by strong collective coupling $N_\uparrow C \approx 1400 \gg 1$. This proof-of-principle experiment may open the way for QND techniques to enhance the fundamental sensitivity of precision measurements with large ensembles of neutral atoms.

Chapter 6

Advantages of operating in resonant-coupling regime

The goal of this Chapter is to provide motivations and analyze unique aspects of probing in the resonant-coupling limit, $\delta_c = 0$. In Section 6.1, we review theoretical results of Section 3.3 in the limit of $\delta_c = 0$. Section 6.2 and 6.3 details technical advantages and sources of common-mode noise rejection obtained by working in the resonant limit and simultaneously probing both dressed cavity modes. Section 6.4 discusses the effects of radial motion of the atoms in the trap on the probing. Section 6.5 considers the effects of spatial mode mismatch of the probe modes in a standing-wave cavity on the correlation between the dressed mode frequencies.

6.1 Fundamental scalings related to projection noise

In the resonantly coupled regime $\delta_c = 0$, the *absolute* size of the projection noise fluctuations is *maximized* (see Fig. 3.5), i.e.,

$$\Delta\omega_{\pm}^{\text{proj}} = \frac{g}{2\sqrt{2}}\,, \tag{6.1}$$

making it easier to observe projection noise fluctuations in the presence of technical noise in the detection system. Note that the rms fluctuation is independent of N, as experimentally demonstrated in Fig. 5.11(a). The same is true for the FWHM linewidth which is simply equal to the average linewidth [111] due to the equal photonic and atomic contributions to the normal modes:

$$\kappa'_{\pm} = (\kappa + \Gamma)/2\,. \tag{6.2}$$

To be able to resolve projection noise, one must detect, on average, a number of probe photons in transmission given by

$$M_{d\pm}^{\text{proj}} = \frac{1}{2\eta_d}\left(\frac{\kappa'_\pm}{g}\right)^2 . \tag{6.3}$$

The ratio of free-space-scattered photons to detected probe photons in transmission is

$$R_{s\pm} = \frac{1}{q_d \eta_s}\frac{\Gamma}{\kappa} . \tag{6.4}$$

Finally, the number of scattered photons into free space for measurement uncertainty at the projection noise level normalized to the total number of atoms N is

$$m_{s\pm}^{\text{proj}} = \frac{1}{2qNC}\left(1+\frac{\Gamma}{\kappa}\right)^2 . \tag{6.5}$$

If the cavity length and mode volume are fixed by experimental constraints, then one is, in principle, free to minimize Eq. (6.5) by varying the finesse of the cavity mirrors, until a minimum value of $m_s^{\text{proj}} = 2/qNC$ is reached when $\kappa = \Gamma$. The minimization with respect to cavity finesse accounts for the fact that the cooperativity C scales as $1/\kappa$.

6.2 Noise rejection in the resonant limit

Section 6.1 has outlined fundamental quantum limits on detection in the $\delta_c = 0$ regime. In this section, we describe how the $\delta_c = 0$ regime is useful for rejecting several sources of technical noise. Simultaneous probing of both transmission resonances $\omega_\pm$ is advantageous for canceling technical, but important, laser frequency noise and cavity frequency noise. Importantly, the previous analysis for the value of m_s^{proj} is not modified if $M_d^{\text{proj}}/2$ photons are used to measure each mode frequency ω_+ and ω_-.

From Eq. (3.4), we find that the measured differential quantity $\omega_+ - \omega_- \approx \Omega_\uparrow\left(1+\frac{\delta_c^2}{2\Omega_\uparrow^2}\right)$ is only quadratically sensitive to the cavity detuning δ_c. Note that the absolute sensitivity to δ_c is decreasing as $1/\sqrt{N_\uparrow}$, a favorable scaling for working with large atom number. As an example, a typical $\Omega_\uparrow/2\pi = 300$ MHz and a detuning of $\delta_c/2\pi = 1$ MHz causes a change in the measured splitting 100 times smaller than projection noise fluctuation in the collective Rabi splitting $\Delta\Omega_{\uparrow}^{\mathrm{proj}} = 2\Delta\omega_{\pm}^{\mathrm{proj}} = g/\sqrt{2}$.

Simultaneous or near-simultaneous measurements of both resonances can strongly suppress the impact of laser frequency noise. To make these measurements, one can use low phase noise RF modulation of a single laser with much higher phase noise to generate probe components near ω_+ and ω_- as was discussed in Section 5.6. The laser carrier frequency noise is common-mode to the two probes and cancels in the difference $\omega_+ - \omega_-$. The measured power spectral density (PSD) of the probe-cavity relative frequency noise $S_\nu(f)$, shown in Fig. 6.1, was measured for our system using side-of-fringe transmission. If both the upper and lower transmission resonances are measured for time T_m with time separation τ_m between the measurements, the noise variance in the measured splitting due to laser noise is

$$\left(\frac{\Delta\Omega_{\uparrow}^{\mathrm{laser}}}{2\pi}\right)^2 = \int_0^\infty S_\nu(f)T(f)\mathrm{d}f\,, \tag{6.6}$$

where the transfer function $T(f)$ is

$$T(f) = \frac{4\sin^2(\pi f\tau_m)\sin^2(\pi f T_m)}{(\pi f T_m)^2}\,. \tag{6.7}$$

If the laser possesses a Lorentzian lineshape with FWHM $\Delta\nu$ in Hz as measured in heterodyne versus a perfect reference laser, the PSD is constant with value $S_\nu(f) = \Delta\nu/\pi$. Integrating Eq. (6.6), we find $(\Delta\Omega_{\uparrow}^{\mathrm{laser}}/2\pi)^2 = S_\nu\tau_m/T_m^2$ for good time overlap $\tau_m < T_m$, and S_ν/T_m for no time overlap $\tau_m > T_m$. Completely unoverlapped measurements would yield an absolute measurement uncertainty of $\Delta\Omega_{\uparrow}^{\mathrm{laser}}/2\pi = \sqrt{\Delta\nu B_m/\pi}$, the geometric mean of the measurement bandwidth $B_m = 1/T_m$ and the laser FWHM linewidth $\Delta\nu$. For a typical extended-cavity-diode-laser $\Delta\nu = 100$ kHz, and $\Delta\Omega_{\uparrow}^{\mathrm{laser}}/2\pi \approx 180\ \mathrm{kHz}\sqrt{\mu\mathrm{s}/T_m}$. For partial time overlap $\Delta\Omega_{\uparrow}^{\mathrm{laser}}/2\pi \approx 180\ \mathrm{kHz}\sqrt{\mu\mathrm{s}}\sqrt{\tau_m/T_m^2}$.

In practice, lasers exhibit low frequency $1/f$ noise, but so long as $1/\tau_m$ is much larger than the noise corner frequency, the above description is adequate. The laser noise can be reduced by spreading the M_d detected probe photons over a longer measurement period, but at the possible expense of additional decoherence of the atomic quantum state (arising from non-probe related mechanisms) and the potential additional contributions from $1/f$ laser and cavity frequency noise.

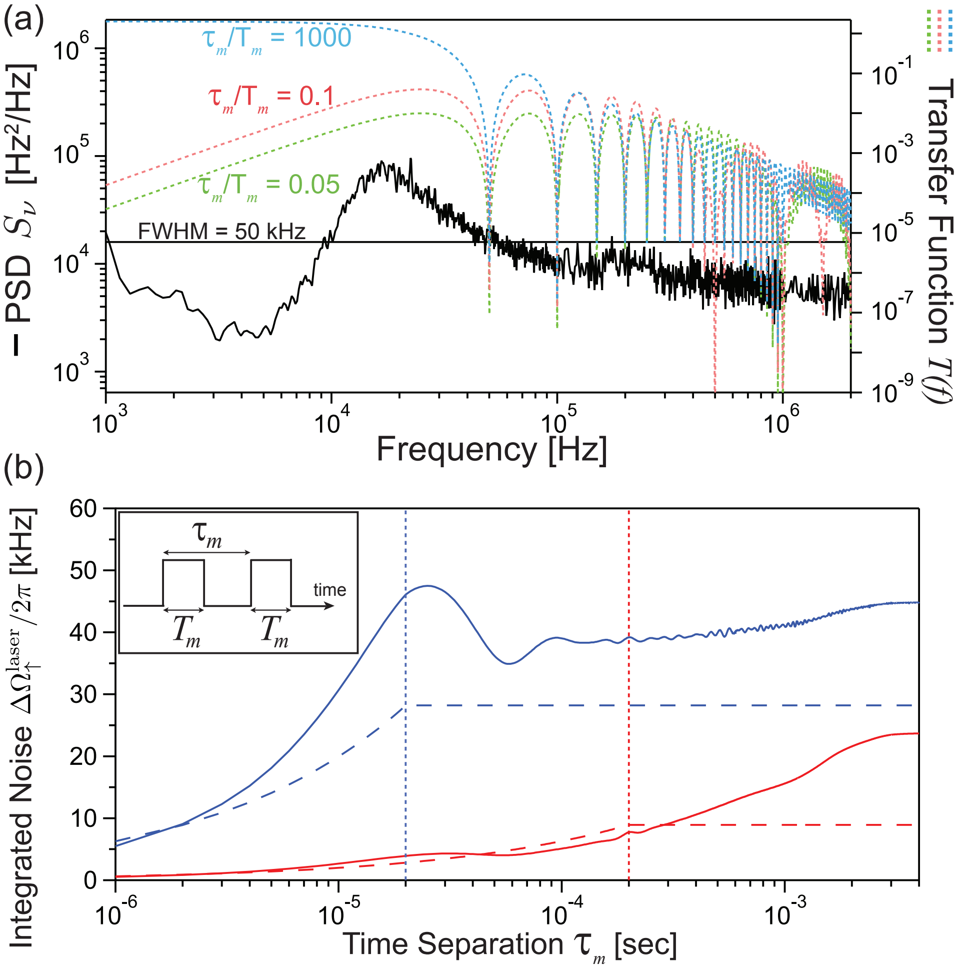

Figure 6.1: (a) Measured probe laser frequency noise spectrum $S_\nu(f)$ (solid black curve) and for reference the calculated white frequency noise level for a Lorentzian 50 kHz FWHM linewidth laser (horizontal black line). Also shown are theoretical transfer functions relating laser frequency noise to Rabi splitting noise for $T_m = 20\mu\text{s}$ and $\tau_m/T_m = 0.05, 0.1, 1000$ (dotted green, blue, and red curves, respectively) The inset of (b) defines the measurement timeing. For the case $\tau_m/T_m = 1000$, the $\sin^2(\pi f T_m)/(\pi f T_m)^2$ envelope of the transfer function is shown here. obtained by averaging over the underlying fast oscillations. (b) RMS noise in the Rabi splitting noise $\Delta\Omega_\uparrow^{\text{laser}}/2\pi$ due to the measured laser frequency noise versus τ_m for $T_m = 20\ \mu\text{s}$ (solid blue curve) and for $T_m = 200\ \mu\text{s}$ (solid red curve). For a white laser frequency noise spectrum of the level shown in (a), the integrated Rabi splitting noise spectrum versus τ_m is shown in dashed blue and red curves. Vertical dashed lines indicate the two different T_m used for the transfer function integration. Most of the integrated noise at larger τ_m can be attributed to the laser frequency noise bump near 17 kHz.

6.3 ac-Stark shift cancellation

The intra-cavity probe light induces an ac-Stark or light-shift of the $|\uparrow\rangle$ state. At resonance, simultaneous probing of both modes $\omega_\pm$ leads to a cancellation of the shift as the induced shifts have opposite signs. The cancellation arises from symmetrically spaced probe components above and below the atomic transition frequency $\omega_{\uparrow e}$. In the case of inhomogeneous coupling of the atoms to the cavity mode, the ac Stark shifts are inhomogeneous and lead to a loss of signal and a reduction in the effectiveness of composite pulse sequences used for manipulating the ground state spin manifold. The integrated phase shift caused by passing probe light through the cavity was measured using a microwave spin echo sequence and observing the phase shift of the spin echo fringe versus the number of photons coupled into the atoms-cavity system. In Fig. 6.2, we show the probe-induced phase shift if only the ω_+ mode or the ω_- mode is probed. We then show the high degree of cancellation of the phase shift, and therefore the average induced ac-Stark shift, when both the ω_+ and ω_- modes are probed simultaneously.

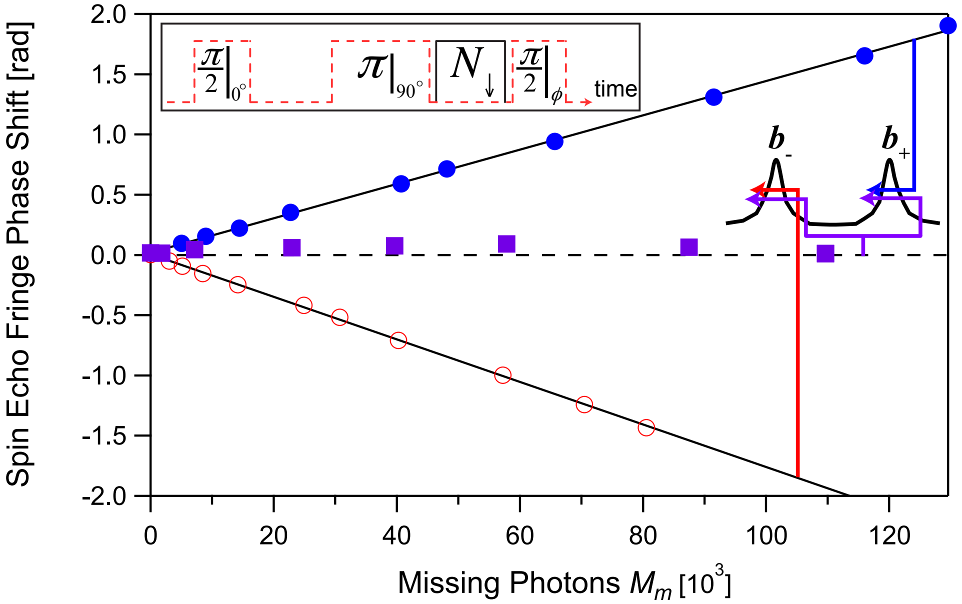

Figure 6.2: The relative quantum phase between states $|\uparrow\rangle$ and $|\downarrow\rangle$ is light shifted by passing probe photons through the atoms-cavity system near only the upper normal mode frequency ω_+ (blue solid circles) or only near the lower normal mode frequency ω_- (red open circles). The shifts have opposite sign and cancel if probe photons are simultaneously passed through the atoms-cavity system at both frequencies (purple squares). Black lines are fits to the data.The measurements are performed using a variable number of photons coupled into the atoms-cavity system M_m during a microwave spin-echo sequence (inset) employed to remove background dephasing from the trapping optical lattice.

While simultaneous probing was successful in canceling average ac-Stark shifts, Fig. 6.3 shows

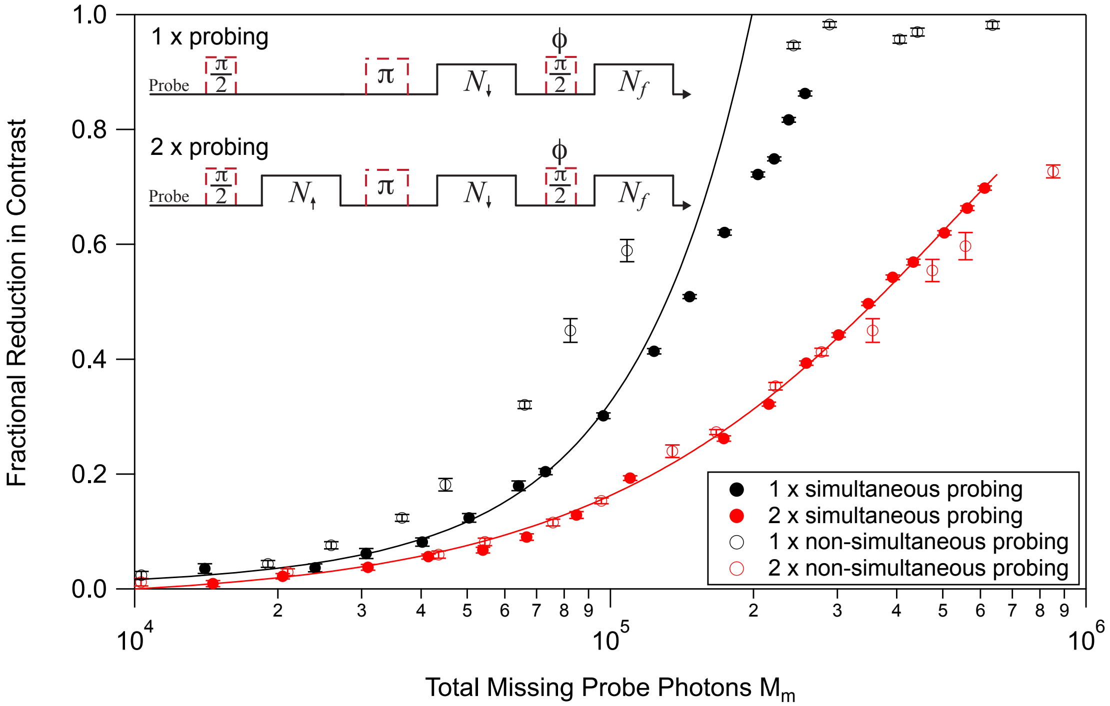

Figure 6.3: Simultaneous probing effect on contrast. The fractional reduction in contrast $(\mathcal{C} - \mathcal{C}_{\text{probing}})/\mathcal{C}$, where $\mathcal{C}_{\text{probing}}$ $(\mathcal{C})$ is the contrast with (without) probing. The total missing probe photons M_m is the sum of the number of missing photons used in both timing windows adjacent to the π-pulse. For the simultaneous probing data, the probes sweep through the 8.4 MHz FHWM of the resonances at the same time. For non-simultaneous probing, the probes are offset in time within a single population measurement window of $N_\uparrow$ or $N_\downarrow$. The red (black) curves are quadratic fits to the 2(1) time window simultaneous probing data (red solid points (black solid points)) respectively. This plot shows that probing in both time windows, rather than simultaneous probing, is crucial for reducing the dephasing. Inhomogeneous ac-Stark shifts from imbalance in upper and lower in the probe sideband photons coupled into the cavity could explain the observations.

that simultaneous probing was not as effective in canceling out inhomogenous ac-Stark shifts. When probing only in the second time window in a echo sequence, the fraction loss of contrast is invariably worse than when probing in both time windows adjacent to the π-pulse. The fractional loss of contrast is defined as $(\mathcal{C} - \mathcal{C}_{\text{probing}})/\mathcal{C}$ where $\mathcal{C}_{\text{probing}}$ is the contrast remaining after probing with M_m total missing probe photons in the whole echo sequence. The data shows that there is some benefit from simultaneous probing when probing in one of the two time window only. However, when both time windows are probed, there is little, if any, benefit to probing simultaneously. Instead, it is crucial to probe in both time windows. This observation could be a result of inhomogeneous ac-Stark shifts imposed by probing both modes; simultaneous or not, is not important. Imbalance in the number of upper and lower probe sideband photons coupled into the cavity would result in un-cancelled inhomogeneous ac-Stark shifts. Probing in both time windows, in conjunction with the π-pulse, would reverse the inhomogeneous ac-Stark shifts, leading to re-phasing. However, the π-pulse alone cannot by itself reverse the inhomogeneous ac-Stark shifts when the probing is applied in one time window only.

6.4 Radial oscillations

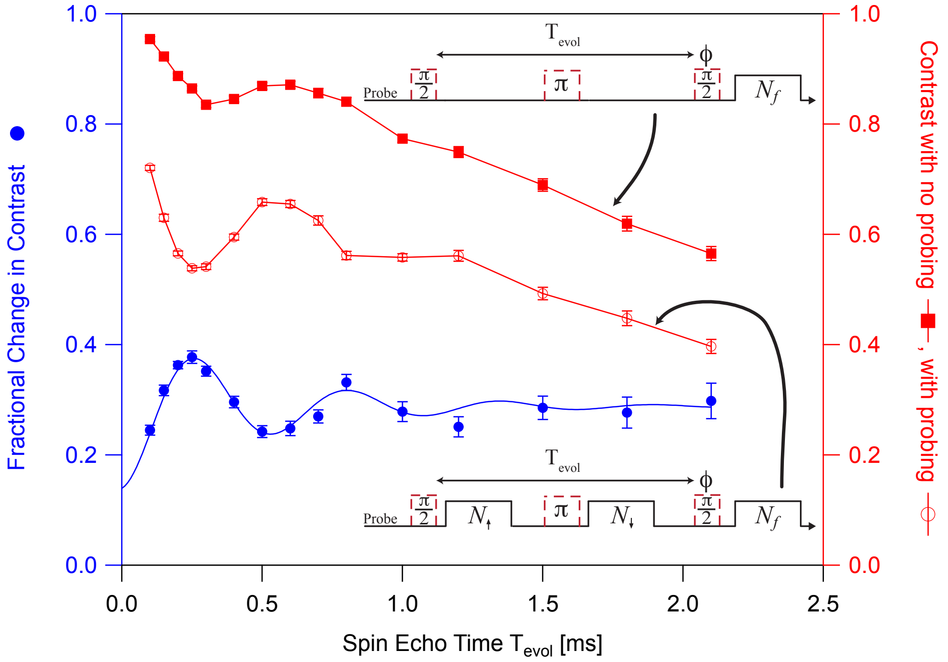

Figure 6.4: Radial motion of atoms in the trap manifests as oscillations in the spin echo fringe contrast. The raw contrast $\mathcal{C}$ (red filled squares, right axis) and the contrast with probing $\mathcal{C}_{\text{probing}}$ (red hollow circles, right axis) show small hints of oscillations that are amplified in the fractional change in contrast $(\mathcal{C}_{\text{probing}} - \mathcal{C})/\mathcal{C}$ (blue filled circles, left axis). The frequency of the oscillations is expected to be at twice the trap radial frequency. A exponentially damped sinusoidal fit (blue curve) to the fractional change in contrast yields a fitted radial trap frequency of $f_{\text{radial,fit}} = 0.92(2)$ kHz, in excellent agreement with the radial frequency $f_{\text{radial,pred}} = 0.91(3)$ kHz predicted from the measured lattice power. In this data set, $N = 7 \times 10^5$ and $M_m = 2.6 \times 10^5$ in total for both the $N_\uparrow$, $N_\downarrow$ measurements.

Signatures of radial oscillations of the atomic sample in the trapping lattice can be observed on the spin echo fringe contrast curves, but they are relatively weak, see red color data points in Fig. 6.4. By comparing the contrast with and without probing, the radial motion is made more apparent via the fractional reduction in contrast $(\mathcal{C} - \mathcal{C}_{\text{probing}})/\mathcal{C}$ (blue data points in Fig. 6.4), which subtracts out the dominant background dephasing from the trapping lattice. The fractional reduction in contrast is well described by a damped sinusoid that oscillates at twice the trap radial frequency of about 1 kHz. While this oscillation in contrast might be interesting, it is not useful for our experiment. The key point to take away is that while we could choose a specific spin echo evolution T_{evol} time to coincide with a local peak in the contrast curve (which would correspond to a T_{evol} of ~ 0.6 ms for our system), the loss of contrast would still significant compared to performing the probing as fast as possible $T_{\text{evol}} \to 0$. Thus our strategy is go probe as quickly as possible, completing a complete J_z measurement in $\sim 150\,\mu$s.

6.5 Spatial mode matching of atoms-cavity modes

In a standing-wave cavity, the $\omega_\pm$ modes arise due to coupling of the cavity mode to atoms located away from the nodes of the standing-wave of each mode. By probing at two different frequencies, it is possible that the two standing-wave probe modes effectively couple to two slightly different sub-ensembles of atoms. Projection noise fluctuations in the two sub-ensembles are not perfectly correlated such that the fluctuations of ω_+ and ω_- are also no longer perfectly correlated. The contribution of projection noise to the difference of the mode frequencies $\omega_+ - \omega_-$ would then be reduced. In the extreme limit of the nodes of the ω_+ mode being aligned with the antinodes of the ω_- mode, the two sub-ensembles are completely independent. The projection noise driven rms fluctuations in the difference $\Delta(\omega_+ - \omega_-)$ would then be $\sqrt{2}$ lower than for the case of perfect overlap. Here we calculate this effect and provide numerical results indicating that this effect is small in our experiment.

In vacuum, the wave vectors for resonant probe light $k_\pm = \omega_\pm/c$ have a differential wave vector given by $k_+ - k_- = \Omega_\uparrow/c$. However, if the atoms uniformly fill the cavity mode along the axial or $\hat{z}$ direction, then the index of refraction of the atoms at the resonant frequencies $\omega_\pm$ must be such that two wavevectors $k'_{\pm} = n_{\pm}k_{\pm}$ are identical inside the atomic medium. This is guaranteed by the round trip phase being a multiple integer of 2π at resonance.

If, however, the atoms do not uniformly fill the cavity, then the wavevectors of the probe modes in vacuum and inside the atomic ensemble can be different, leading to coupling to slightly different atomic sub-ensembles. Using the original condition, one finds the indices of refraction of the atomic ensemble at position z along the cavity axis evaluated for probe frequencies at the nominal resonance frequencies $\omega_{\pm}$ are

$$n_{\pm}(z) = 1 \mp \frac{\Omega_{\uparrow}}{4 f_{\mathrm{FSR}}} \frac{1}{k_{\pm}} \rho_{\uparrow}(z)\,. \tag{6.8}$$

where $f_{\mathrm{FSR}} = c/2l$ is the cavity free spectral range, and $\rho_{\uparrow}(z)$ is the coarse-grained linear probability distribution function that an atom in $|\uparrow\rangle$ is located at z and normalized such that integrating over all of space yields 1. The coarse graining is performed over many lattice sites, and quantum fluctuations are ignored in this expression as they are a higher order effect.

As a first application, we assume the atoms uniformly fill a region of space of length d centered in the middle of the cavity of length l. In the atomic medium, the spatial phase deviation $\phi_{\pm}(z)$ of the standing-wave electric fields $\cos(\omega_c z/c + \phi_{\pm})$ from the empty cavity spatial phase is given by

$$\phi_{\pm}(z) = \pm \frac{z\,\Omega_{\uparrow}}{4 f_{\mathrm{FSR}}} \left(\frac{1}{l} - \frac{1}{d} \right) \quad \text{for } |z| \leq \frac{d}{2}. \tag{6.9}$$

In the limit of uniform filling $d = l$, the two probe modes are spatially matched, otherwise they acquire a differential spatial phase $\phi_{+}(z) - \phi_{-}(z)$ that grows linearly as z.

In our experiment, the atoms were roughly Gaussian distributed along the cavity axis with standard deviation $z_{\mathrm{rms,\,ensemble}} \approx 1$ mm much less than the cavity length $l \approx 2$ cm (see Table 5.2 for exact numbers). In this case, the spatial phase deviation of the standing-wave probe modes from the empty cavity spatial phase in the atomic medium is given by

$$\phi_{\pm}(z) = \pm \frac{\Omega_{\uparrow}}{4 f_{\mathrm{FSR}}} \left(\frac{z}{l} - \frac{1}{2} \mathrm{Erf}\left(\frac{z}{\sqrt{2}\, z_{\mathrm{rms,\,ensemble}}} \right) \right)\,, \tag{6.10}$$

where $\mathrm{Erf}(\cdot)$ is the error function.

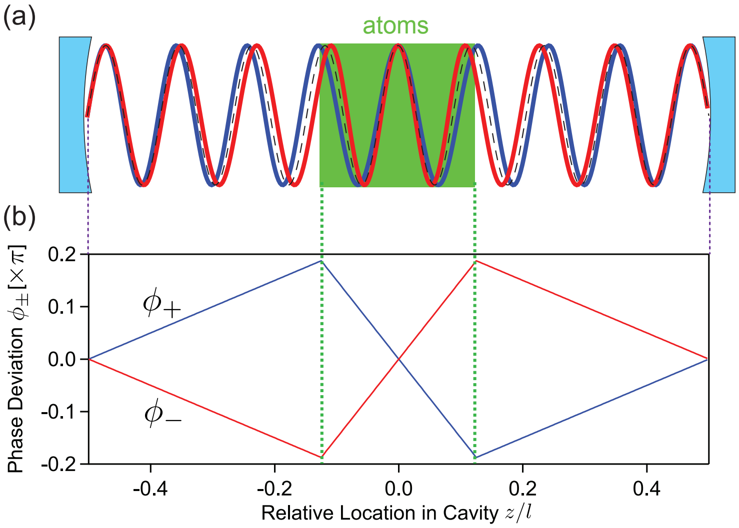

Figure 6.5: Illustration of the concept of spatial mode-matching of the atoms-cavity modes. (a) In vacuum, the electric field of the higher frequency mode ω_+ (blue) has a shorter wavelength than the lower frequency mode ω_- (red), leading to a phase advance of the ω_+ mode relative to the ω_- mode as it advances from the left mirror to the left edge of the atomic medium (green). In the atomic medium, the refractive index $n_\pm$ at frequency $\omega_\pm$ is such that the ω_+ mode has a longer wavelength than the ω_- mode so that the two modes phase up in the middle of the cavity. For reference, the electric field for the bare cavity mode ω_c (dashed black) is shown. The phase mismatch in this illustration is deliberately made large by choosing $\Omega_\uparrow/2\pi = f_{\text{FSR}}$. The length of the uniformly distributed atomic medium is set to $d = l/4$, again for illustration. (b) The spatial phase deviation $\phi_\pm$ of the $\omega_\pm$ modes from the empty cavity spatial phase. The red(blue) curves corresponding to ϕ_+ and ϕ_- respectively are used to generate the standing-wave modes in (a).

At a typical $\Omega_\uparrow = 2\pi \times (300\text{ MHz})$, the differential probe spatial phase $\phi_+(z) - \phi_-(z)$ is expected to be only 31(3) mrad at $z = z_{\text{rms, ensemble}}$. Numerical simulations of the phase mismatch and projection noise show that this phase mismatch leads to $< 1\%$ reduction in the variance of the difference $\omega_+ - \omega_-$ relative to the variance in the same quantity for perfect spatial overlap of the two modes with one another.

6.6 Summary

The previous chapter and this chapter have focussed on probing aspects of our collective cavity-QED system. The next two chapters will finally focus on the microwave rotation aspects of squeezing experiment. In our experiments, a significant portion of our time was spent learning how to perform precise rotations (Chapter 7) and developing a linear response theory for quantifying the impact of phase noise on the rotations (Chapter 8). Precise rotations (at the 1 mrad level in the polar angle θ) are necessary so that microwave π-pulse required for a J_z measurement does not an amount of noise into the measurement larger than the SQL or squeezing we were aiming to observe.

Chapter 7

Experiment: Realization of precise rotations

To first observe quantum projection noise and then demonstrate conditional squeezing in Chapter 5, the microwave rotations must add little noise into J_z relative to the projection noise level. For our large ensemble of $N = 7 \times 10^5$ atoms, the projection noise level sets the SQL of $\Delta\theta_{\mathrm{SQL}} = 1.2$ mrad. In order to measure below the SQL, the microwave rotations need to add less than ~ 1 mrad of noise to the polar angle θ of the collective spin vector.

Precise rotations are key for the the squeezing experiment in Chapter 5, that is we can consistently rotate the collective spin vector to the same polar angle within a single experimental trial. Added noise in the azimuthal angle ϕ due to microwave rotations much less of a concern because ϕ is the anti-squeezing quadrature; adding noise into ϕ does not affect the squeezed quadrature. Also, the mean spin length $|\langle\hat{\mathbf{J}}\rangle| \propto \cos\Delta\phi$ is only sensitive to second order in $\Delta\phi$.

In Section 7.1, we demonstrate a tuning procedure to achieve good alignment of the rotation axis to the collective spin. In Section 7.2, we present constraints on added-noise from microwave rotations with the help of auxiliary rotations. Finally, in Section 7.3, we describe a microwave source with sufficiently low noise to allow spin-squeezing on the ^{87}Rb clock transition. This source has been published in Ref. [55].

7.1 Aligning rotation axis to collective spin vector

In order to prevent low frequency amplitude and detuning noise from coupling into the measurement quadrature J_z, we need to know the rotation axis relative to the collective spin vector very well so that we can perform an aligned π-pulse or perpendicular π-pulse back through the south-pole as shown in Fig. 7.1. In our experiment, we find it necessary to tune the phase of the microwave rotation pulse carefully to achieve quiet rotations due to phase shifts that occur during the time between the CSS preparation to the π-pulse rotation necessary for a J_z measurement.

A source of phase shift is attributed to ac-Stark shifts from off-resonant microwaves. Due to metallic structures around the atoms, finite extent of the atomic cloud and imperfections in the microwave dipole antenna, the polarization of the microwave field at the atoms is not purely π-polarized. Circularly polarized microwaves couple the $|F, 0\rangle$ clock states ($F = 1, 2$) off-resonantly to the $|F, \pm 1\rangle$ states , giving rise to microwave ac-Stark shifts. At the applied quantization field of 4.8 Gauss, the Zeeman splitting is 3.4 MHz. The Rabi frequency for the clock transition is about 40 kHz. Assuming the amplitude of $\sigma_{\pm}$-polarized microwaves are the same as the π-polarized microwaves, the ac-Stark shift from a pair of coupled levels is on the order of 120 Hz[1] . When we apply the microwave rotations, the microwave frequency is set to the dressed microwave transition frequency to avoid detuning errors coupling into the measurements. However, when the microwaves are turned off, the collective spin precesses at a frequency not dressed by the microwaves, leading to relative phase accumulation between the collective spin and the microwave source. This accumulated phase offset may be measured and tuned away in the procedure described in Fig. 7.2.

It is also important to make sure microwaves are completely turned off during the QND measurements. To do so, we have found it necessary to use two microwave TTL switches (Minicircuits ZASWA-2-50DR+). With only one TTL switch at the input of the high power microwave amplifier, we measured a Rabi frequency of 48 Hz when the switch is in the “off” state, compared to a Rabi frequency of 34.5 kHz in the “on” state, corresponding to an isolation of 57 dB, consistent with network analyzer measurements of the switch isolation. This would cause a residual rotation of the collective spin vector of 300 mrad/ms in the worst case scenario where the rotation axis is

---

[1] While ac-Stark shifts from the σ_+ and σ_- transitions would cancel due to their opposite signs of detuning from the clock transition, we do not have control over the microwave polarization and hence the Rabi frequencies and the relative magnitudes of these ac-Stark shifts. In the worse case scenario, there is power in only one of the two $\sigma_{\pm}$-transitions, which would result in the full microwave ac-Stark shift.

(a) Parallel-π Rotation Axis

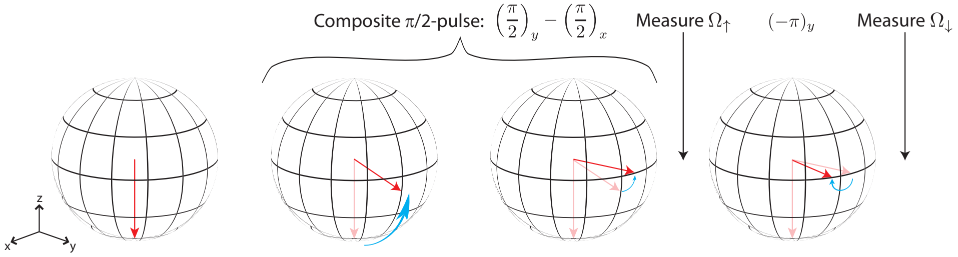

(b) Perpendicular-π Rotation Axis

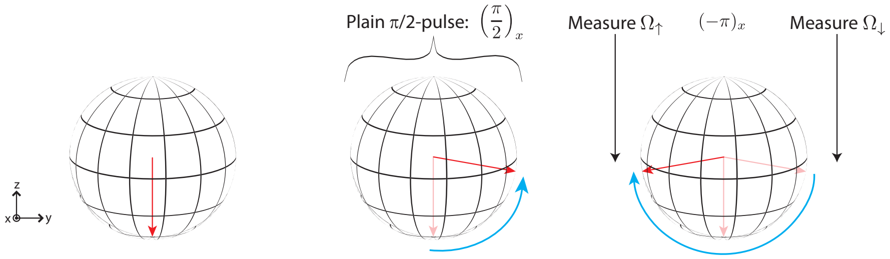

Figure 7.1: The two rotation sequences used to observe projection noise mapped out on the Bloch sphere. The collective spin vector (rotation) is shown in red (blue). To observe projection noise in the difference $\Omega_\uparrow - \Omega_\downarrow$, classical rotation noise added by the microwave π-pulse required in the probing sequence needs to be smaller than the quantum noise we are trying to observe. Static rotation errors would add an offset but not increase the noise. However, nothing is truly static. Slowly varying rotation errors would show up as a varying offset, increasing the measured variance. To mitigate slowly varying drifts in the Rabi frequency, we employed sequences that ensure the z-projection of the mean spin J_z is (a) zero to first order in the fractional Rabi frequency error or (b) common-mode between the $\Omega_\uparrow$ and $\Omega_\downarrow$ measurements. Note that the quantum noise ΔJ_z remains anti-correlated between the two measurements, as it should be. While slow amplitude errors are cancelled by these rotations, fast amplitude errors would introduce uncorrelated classical noise in J_z. We empirically found that fast amplitude noise is not a limiting factor. To reduce the impact of phase noise or equivalently detuning added during π-pulse, we used a low phase noise microwave source, described in Section 7.3, to perform the rotations.

perpendicular to the collective spin vector. For the 150 μs time scale of the squeezing operation, the collective spin vector would be tipped by 45 mrad, much larger than the SQL of ~1 mrad we aimed to observe. While a consistent rotation would not add noise in our measurements, only a 2% fluctuation in the amount of microwave isolation would add noise equivalent to the SQL. Therefore we took precautions to install a second microwave TTL switch. We constrain the final microwave leakage by measuring how much the collective spin vector rotates versus hold time when both switches are in the "off" state to result in a Rabi frequency of 0.07(4) Hz, or a rotation rate of 0.5(2) mrad/ms and an angle of 0.07(3) mrad in 150 μs in the worst case. Note this constrain

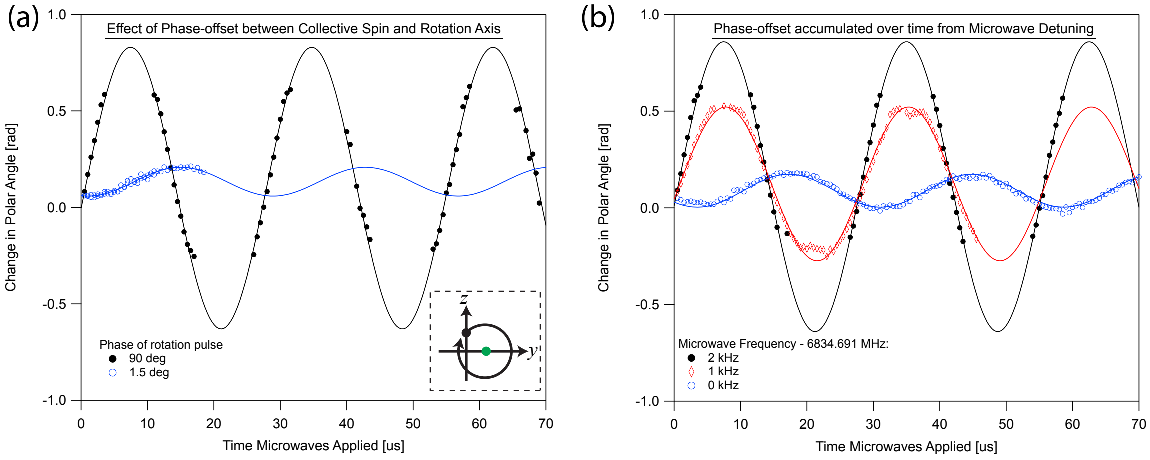

Figure 7.2: (a) Tuning phase offset between CSS and rotation axis. The CSS is prepared along nominally $\hat{x}$, with potentially a small offset along the z-axis due to microwave amplitude error (inset, black dot showing the tip of the CSS). A rotation through a variable angle is then applied using resonant microwaves for a variable amount of time. The phase offset between the rotation axis (inset, green dot showing tip of rotation axis) and the CSS sets the radius of the circle the tip of the CSS traces on the Bloch sphere (inset, black arrow). The spin projection J_z therefore varies sinusoidally with the angle rotated through. By fitting the J_z oscillations (black, blue symbols) to a sinusoid (black, blue curves), the phase offset between the rotation axis and the CSS can be determined. Deflections more than ~ 0.5 rad are not observed due to limited dynamic range of the measurement. (b) Phase offset can also accumulate from microwave detuning during free evolution time. Same experiment as (a) except that instead of changing the phase of the microwave pulse performing the rotation, the phase of the pulse is kept fixed here. Here a phase offset is accumulated from a microwave frequency detuning during a 80 μs free evolution window before the variable rotation was applied. The detuning was implemented by a (phase continuous) frequency offset of the DDS frequency source that sets the microwave LO frequency. This shows the importance of accounting for the effect of frequency detuning during free evolution time causing phase offsets between the rotation axis and the CSS.

provided by the atoms is consistent with the expected attenuation of 114 dB with two TTL switches.

7.2 Constraining noise from microwave rotations

A classical spin vector can exhibit fluctuations in the measured polar angle θ that arise due to classical noise introduced during a rotation. In principle, one might mistake such classical fluctuations for the quantum fluctuations due to projection noise. To constrain the possible added-noise in θ due to rotations, we perform a set of auxiliary rotation and measurement sequences (summarized in Table 7.1), each with sensitivity to different types of errors in the rotation process.

Rotation-induced noise in θ is distinguished from projection noise by selecting rotations that nominally return all collective spin vectors to their original orientation before each measurement of a vacuum Rabi splitting. The chosen rotations constrain the added noise from microwave amplitude and phase noise, and transition frequency noise (arising from the trapping potential for instance.) These noise sources are equivalent to fluctuations in the angle of rotation, and the axis of rotation. For the two rotation sequences used to actually observe projection noise in Section 5.7 (see Table 7.2), we estimate that the rotations contribute at most $-14(3)$ dB of added noise in θ relative to the predicted projection noise level for $N = 7 \times 10^5$ atoms.

If the rotations are imperfect in length, then noise from the anti-squeezed quadrature can leak into the measurement quadrature. Estimates of the imperfections in the rotation lengths constrain this noise leakage to < -8 dB and < -35 dB for the two rotation sequences of Table 7.2.

In order to achieve these low noise rotations, we have built and characterized a custom low phase noise microwave source, and will be described in Section. 7.3. Long term amplitude stability was enhanced by installing microwave absorbing material near the atoms.

7.3 Low phase noise microwave source

In this Section, we provide an augmented version of Ref. [55], where we describe and characterize a simple, low cost, low phase noise microwave source that operates near 6.800 GHz for agile, coherent manipulation of ensembles of ^{87}Rb. Low phase noise is achieved by directly multiplying a low phase noise 100 MHz crystal to 6.8 GHz using a non-linear transmission line and filtering the output with custom band-pass filters. The fixed frequency signal is single sideband modulated with a direct digital synthesis frequency source to provide the desired phase, amplitude, and frequency control. Before modulation, the source has a single sideband phase noise near -140 dBc/Hz in the range of 10 kHz to 1 MHz offset from the carrier frequency and -130 dBc/Hz after modulation. The resulting source is estimated to contribute added spin-noise variance 16 dB below the quantum projection noise level during QND measurements of the clock transition in an ensemble 7×10^5 ^{87}Rb atoms.

Table 7.1: Auxiliary rotation and measurement sequences were used to constrain the magnitude of the added noise $\Delta\theta$ in the polar angle of the collective spin vector caused by imperfections in the rotations. The added noise is expressed in dB relative to the predicted projection noise level at $N = 7 \times 10^5$ atoms. The atoms are initially prepared in state $|\downarrow\rangle$ ($\theta = \pi$). The rotations are parameterized as $R\left[\psi, \phi\right]$, where ψ specifies the angle of rotation about an axis, while ϕ specify the azimuthal of the rotation axis in the $x - y$ plane. The rotation axis is always in the $x - y$ plane nominally. Each measurement $N_{1,2}$ corresponds to a measurement of the number of atom in $|\uparrow\rangle$ obtained by measuring the vacuum Rabi splitting. The fluctuations in the difference of the measurements $N_2 - N_1$ provides a measure of the fluctuations $\Delta\theta$. The rotation noise sources constrained by each sequence are given in the second column, expressed to leading order in the small fluctuating parameters ϵ_i. The amplitude fluctuations ϵ_i are re-expressed in terms of either differential ϵ_- or common-mode ϵ_+ amplitude fluctuations. The impact of microwave phase noise and atomic transition noise (for instance, due to power fluctuations in the trapping optical lattice) can be constrained on both fast and slow time scales.

Auxiliary Sequence	$\Delta\theta$	Measured $\left\langle \Delta\theta^2 \right\rangle$ [dB]
$R\left[\pi/2, 0\right]$ measure N_1 $R\left[2\pi, \pi/2\right]$ measure N_2	fast transition frequency noise, microwave phase noise	$-16(6)$
$R\left[\pi/2, 0\right]$ measure N_1 $R\left[\pi, \pi/2\right]$ $R\left[\pi, -\pi/2\right]$ measure N_2	slow and fast transition frequency noise, microwave phase noise	-14(3)
$R\left[(\pi/2)(1+\epsilon_1), 0\right]$ measure N_1 $R\left[\pi\left(1+\epsilon_2\right), 0\right]$ $R\left[\pi\left(1+\epsilon_3\right), -\pi\right]$ measure N_2	$\pi\epsilon_-$ $\epsilon_- = \epsilon_3 - \epsilon_2$	$-16(3)$
$R\left[(\pi/2)(1+\epsilon_1), 0\right]$ measure N_1 $R\left[\pi\left(1+\epsilon_2\right), 0\right]$ $R\left[\pi\left(1+\epsilon_3\right), 0\right]$ measure N_2	$2\pi\epsilon_+$ $\epsilon_2, \epsilon_3 \approx \epsilon_+$	$+4(1)$

Table 7.2: The added noise from rotations for the two pulse sequences used to observe projection noise. Two independent rotation sequences were used to observe projection noise–each with different sensitivities to the noise sources measured with the auxiliary rotations and measurements of Table 7.1. The predicted added noise from each source is expressed in dB relative to the calculated projection noise for $N = 7 \times 10^5$ atoms. The phases of the microwave pulses were adjusted such that $\phi_{1,2,3} < 35$ mrad or 2°.

Measurement Sequence	Amplitude Noise		Phase Noise	Transition Noise
	$\Delta\theta$	[dB]	[dB]	[dB]
$R\left[(\pi/2)\left(1+\epsilon_2\right), 0\right]$ $R\left[(\pi/2)\left(1+\epsilon_1\right), \pi/2+\phi_2\right]$ measure N_1 $R\left[\pi\left(1+\epsilon_3\right), \pi/2+\phi_3\right]$ measure N_2	$\pi^2\epsilon_+^2 + \pi\epsilon_+(\phi_3 - \phi_2)$ $\epsilon_1, \epsilon_2, \epsilon_3 \approx \epsilon_+$	< -30	-17(3)	-20(3)
$R\left[(\pi/2)\left(1+\epsilon_1\right), 0\right]$ measure N_1 $R\left[\pi\left(1+\epsilon_2\right), \pi+\phi_2\right]$ measure N_2	$\frac{\pi}{2}\phi_2^2\epsilon_+ + \pi\epsilon_-$ $\epsilon_- = \epsilon_2 - \epsilon_1$ $\epsilon_1 \approx \epsilon_+$	$-14(3)$	< -28	< -34

7.3.1 Context

Low phase noise microwave sources are crucial for a broad range of applications, including radar, communications, navigation, and timing-keeping [142]. For quantum sensors [143, 144], quantum gates [145, 146], and tests of fundamental physics [147, 148], microwaves are often applied to perform rotations on pseudo-spins formed from two atomic hyperfine energy levels separated by spin-flip resonant frequencies in the microwave regime.

In many atomic physics applications, the microwave source can be narrowband in its tuning range, since it is being used to address extremely stable atomic transitions. However, the source must have nimble phase control in order to implement composite pulse sequences [149–151] that are used to cancel slowly varying amplitude and detuning errors. When resonant microwaves are applied at the spin-flip frequency, one can view the pseudo-spin as being rotated about a fixed axis in the $x - y$ plane, with the rotation axis's azimuthal angle set by the phase of the microwaves. Composite pulses reduce the impact of amplitude and/or detuning errors for a single rotation about an axis by implementing several rotations about several axes with different azimuthal angles. Thus, it is necessary to be able to quickly change the microwave phase between several values. Conversely, if the microwave phase randomly fluctuates during the rotation, the orientation of the pseudo-spin at the end of the rotation may fluctuate from one realization to the next, swamping quantum sources of orientation noise, such as quantum projection noise, that are of fundamental interest [57, 58].

Here we present the details of a custom, low phase noise microwave source near 6.8 GHz, with tuning bandwidth of approximately 40 MHz, where rapid changes of phase, frequency, and amplitude are possible. The 40 MHz tuning range is sufficient to span hyperfine transitions in the widely used ^{87}Rb atom, and only minor modifications are needed for operation with other commonly used alkali-atoms such as ^{133}Cs, ^{85}Rb, etc. In the range of 10 to 100 kHz offset frequencies from the carrier, the single sideband phase noise of the source is nearly 20 dB lower than a commonly used YIG oscillator phase locked to the same crystal reference.

The offset frequency range 10 to 100 kHz is particularly relevant for our spin-squeezing experiments. In particular, during a crucial π-rotation one finds that only phase noise spectral components near the Rabi-frequency $f_R \approx 40$ kHz contribute significant noise into J_z (see Chapter 8), whose value must be resolved below the projection noise level.

Compared to other microwave frequency sources with the necessary stability and agility, the source we present is also a cost-efficient option. The total component cost is below $\$3,300$, when the Rb atomic reference is excluded. The source achieves lower phase noise than many broadband commercial microwave synthesizers, such as the Agilent E8257D, which is also roughly an order of magnitude more expensive. Other narrow-band microwave oscillators, such as cryogenic sapphire microwave oscillators [152], achieve much lower phase noise, but again at much higher cost and limited availability. Related low phase noise microwave sources based on a dielectric resonator oscillator (DRO) phase locked with a few 100 kHz bandwidth to a non-linear transmission line (NLTL) frequency comb have been reported at the ^{133}Cs 9.2 GHz [153, 154] and the ^{87}Rb 6.8 GHz [155] hyperfine transition frequencies.

7.3.2 Low noise, fixed frequency source

The microwaves are generated by first multiplying up a low phase noise crystal source to generate low noise microwaves at 6.800 GHz and then performing single sideband modulation of the carrier using a direct digital synthesis board as the modulation source (Fig. 7.3).

A low noise 100 MHz crystal oscillator (Wenzel ULN 501-16843) is phase locked to a 10 MHz Rb clock signal (Stanford Research Systems FS725) for long term frequency stability, see Figs. 7.4 and 7.5. The phase comparison between the 100 MHz crystal and the 10 MHz Rb clock is performed by first mixing with a 110 MHz derived from the 10 MHz Rb clock with a x11 multiplier (Wenzel LNOM-10-11-13-10-AA-AA), and then mixing the resulting 10 MHz signal with 10 MHz Rb clock signal. The error signal from the output of the last 10 MHz mixing stage is sent to a loop filter that feedback on the 100 MHz crystal with servo unity gain frequency of 100 Hz, with schematic shown in Fig. 7.5.

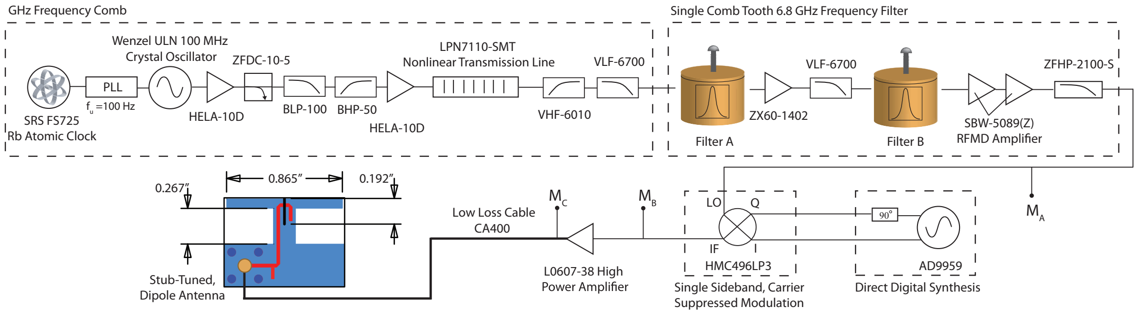

Figure 7.3: Schematic of low phase noise microwave synthesis chain. The source starts with a 100 MHz crystal oscillator phase locked to a 10 MHz atomic lock to provide very low frequency stability. The 100 MHz signal, after coupling off a monitor output, is amplified and multiplied up through a NLTL. The 68th harmonic is selected by a custom bandpass filter built from a series of commercial filters and homemade microwave resonators. The resulting NLTL source is a single harmonic that provides the LO input for a single sideband modulator. The I and Q inputs of the modulator are driven by a direct digital synthesis (DDS) board that allows phase coherent control over the frequency, amplitude, and phase of the microwave signal sent to the high power microwave amplifier. The microwaves are coupled to the atoms using a printed circuit board dipole antenna. The signal line on the antenna is in red, and the ground plane, on the opposite side of the board, is in blue. The labels $\mathrm{M_A}, \mathrm{M_B}$ and $\mathrm{M_C}$ indicates points where phase noise was measured.

The 100 MHz signal is amplified to +27 dBm (Minicircuits HELA-10D) to drive a NLTL (Picosecond Pulse Labs LPN7110-SMT) generating a comb of harmonics out to 20 GHz. For noiseless multiplication, the timing jitter is preserved, but the phase noise is increased relative to the source by $20\log_{10}(n)$ dB, where n is the harmonic order. We utilize the n=68 harmonic at 6.8 GHz yielding a fundamental phase noise increase of 36.7 dB over the crystal source. Note that the frequency comb produced by the NLTL source allows for the flexibility to choose a frequency relevant for other alkali atoms by choosing a different harmonic to filter.

The harmonic at 6.8 GHz is isolated via a combination of standard filters (Minicircuits VHF-6010, VLF-6700, ZFHP-2100-S) for broadband filtering and two high quality factor (Q) microwave resonators [156] for narrow-band filtering. At 6.8 GHz, the measured insertion losses of the VHF-6010, VLF-6700, and ZFHP-2100-S filters are 0.7, 0.8, and 0.3 dB respectively. The insertion losses are low enough that the thermal noise floor of -174 dBm/Hz at 300 K does not affect the phase noise of the synthesis chain. The ZFHP-2100-S, nominally a high pass filter with 3 dB point at 2.1 GHz, was used to attenuate high frequency harmonics above 14 GHz. The VHF-6010 high pass

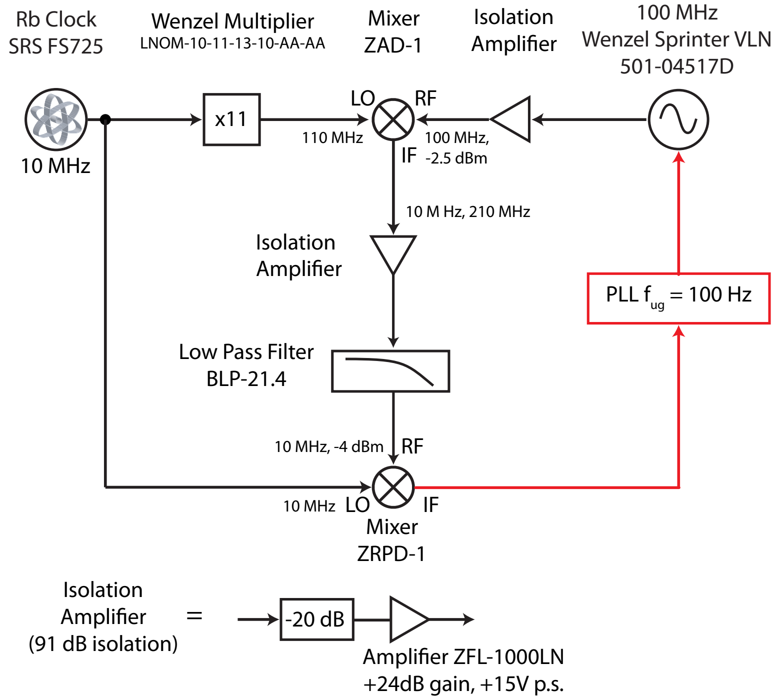

Figure 7.4: Wenzel crystal lock schematic.

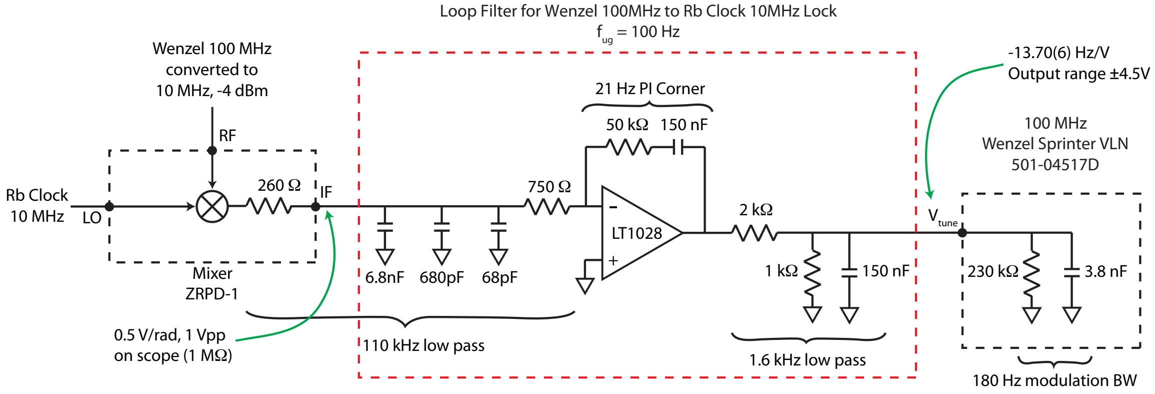

Figure 7.5: Wenzel crystal loop filter with unity gain BW ∼100 Hz.

3 dB point is at 6.01 GHz, and the VLF-6700 low pass 3 dB point is at 7.6 GHz. At an insertion loss of IL = 2.8(2) dB, the loaded quality factor is $Q_L \approx 580$, and the loaded half width at half maximum is ≈ 6 MHz, much smaller than the 100 MHz spacing between the comb harmonics. The microwave resonators have an unloaded $Q_0 = Q_L/\left(1 - 10^{-\mathrm{IL}/20}\right) \approx 2100$. Two microwave resonators are used to give strong suppression of the harmonics close to the harmonic at 6.8 GHz.

The resonators, illustrated in Fig. 7.6, are constructed from stock copper pipe (inner diameter of 1”, outer diameter of 1.5”), with a lid 0.25” thick made from copper barstock and a base from stock 0.125” copper sheet. The three pieces are held together by screws that allow for a tight fit and good conductivity, but still provide the ability for the resonator to be disassembled. We found no major improvements to the unloaded resonator Q by soldering the pieces together.

The coupling of microwaves into and out of the resonator is provided by two panel mount SMA connector feedthroughs held to the copper sheet with a lock washer and nut. Trimming the internal signal pin lengths increased the Q at the expense of increasing the insertion loss. For example, pins that had been trimmed to be 3 mm above the base plate had an insertion loss of 5.2 dB, but trimming down to 2 mm above the base plate resulted in an insertion loss of 18.9 dB. The filters used for the final NLTL source were trimmed to be 4 mm above the base plate.

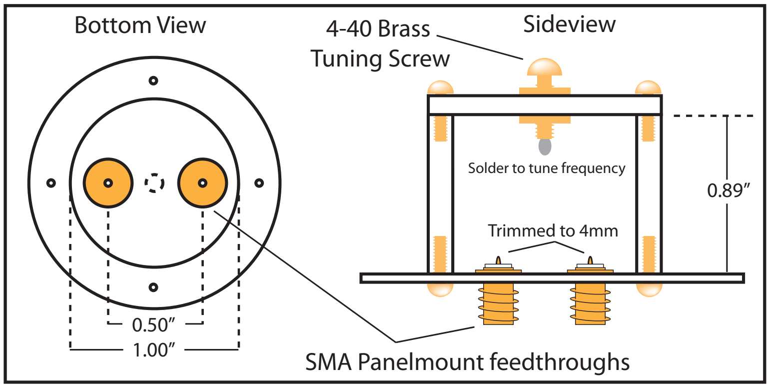

Figure 7.6: Diagram of the high-Q resonant microwave filters. The resonant cavity is constructed from a copper pipe, with copper plate used to form the lid and base. The cavity resonance frequency is tuned with a 4-40 brass screw, secured tightly for good conductivity by a nut on either side of the center of the lid, and more finely tuned through a small amount of lead solder attached to the tip of the screw (see text). The signal is injected and extracted through panel mount SMA feedthroughs, trimmed to provide 2.8 dB of insertion loss while maintaining a loaded Q of about 580.

Coarse tuning of the resonant frequency was performed by changing the depth of a brass screw inserted in the center of the lid. We found that good conductivity between the screw and the lid was one of the most important parameters for obtaining the maximum Q. The Q was also reduced when using a stainless steel tuning screw in place of the brass screw. After coarse tuning the resonance frequency to within 20 MHz of the desired 6.800 GHz, two brass nuts were placed on either side of the screw to firmly secure it in place. The final fine-tuning of the center frequency was performed by attaching a small amount of $\mathrm{Sn_{0.6}Pb_{0.4}}$ solder to the tip of the tuning screw, then successively sanding small portions of the solder away until the resonator reached the desired frequency. Tuning resolution below 2 MHz was possible with this approach.

The center frequency of the two resonators were set to 6.800(2) GHz. An amplifier (Mini-circuits ZX60-1402) was placed between the resonators to prevent the formation of a coupled-resonance. After filtering, the largest unwanted comb tooth is at 6.7 GHz, -49.5 dB below the desired 6.8 GHz comb tooth. The resonance frequencies can drift due to temperature changes with a coefficient of ~ 150 kHz/K. Mechanical vibrations can modulate the resonance frequency, giving rise to a phase modulation of the transmitted microwaves to lowest order. To mitigate both temperature drifts and vibration-induced phase modulation, we passively isolate the resonators in a foam box.

The single sideband phase noise power spectrum of the 6.8 GHz NLTL source was measured by transporting the source to the National Institute of Standards and Technology (NIST) at Boulder, CO, and using a self-homodyne phase noise detector (OEwaves OE8000). Fig. 7.8a shows the measured noise of our NLTL source at measurement point $\mathrm{M_A}$ in Fig. 7.3 (after filtering, but before modulation), a YIG oscillator (Micro Lambda Wireless MLPE-1290) phase locked to the same ULN crystal reference, and the measurement noise floor of the OE8000 calibrated using a Poseidon sapphire oscillator at 10 GHz. Our ability to measure phase noise is limited by the measurement noise floor below ~ 500 Hz offset frequencies, thus the displayed data is an upper bound for the phase noise below ~ 500 Hz.

The NLTL source is quieter than the YIG source by ~ 15 to 20 dB in the offset frequency range from 10 kHz to 400 kHz. The multiplied-up phase noise of the 100 MHz ULN crystal taken from the manufacturer's datasheet agrees relatively well with the observed data, indicating that there is little added technical noise at this level in the multiplication, amplification, and filtering relative to the observed noise level. The 100 MHz ULN phase noise slope changes from $1/f^2$ above 1 kHz to $1/f^3$ below 1 kHz due to $1/f$ phase noise from the crystal oscillator feedback amplifier being converted into oscillator phase noise via the Leeson effect [157]. The roll-off of the phase noise near 5 MHz is believed to arise from the high-Q microwave filters.

7.3.3 Agile control of Phase, Frequency and Amplitude

To generate amplitude, frequency and phase tunable microwaves at the hyperfine clock transition frequency 6.834693 GHz, a single sideband (SSB) modulator (Hittite HMC496LP3), with a manufacturer specified output noise floor of -150 dBm/Hz at 7 GHz, modulates the 6.8 GHz NLTL source. The SSB modulator is tuned to give -31 dB and -19 dB suppression relative to the $+1$ sideband for the 0, -1 and -2, $+2$ sidebands respectively.

The I and Q modulation ports are driven near 34 MHz using 90° relative phase signals from 2 of the 4 channels of a direct digital synthesis (DDS) frequency source (Analog Devices AD9959 evaluation board) operating near 34 MHz. The DDS source is phase stabilized to a 500 MHz reference provided by multiplying the 100 MHz ULN crystal oscillator using a diode pair (Avago HSMP-3822) and harmonic filtering provided by two bandpass filters (Minicircuits BPF-B503+), see Fig. 7.7. The DDS SSB phase noise floor specified by the manufacturer is -151 dBc/Hz at 10 kHz offset from the carrier when operated at 40 MHz with a 500 MHz reference signal, but this specified noise floor rises if the DDS is operated with a lower frequency reference, relying on a programmable internal PLL to multiply up the reference signal to 500 MHz.

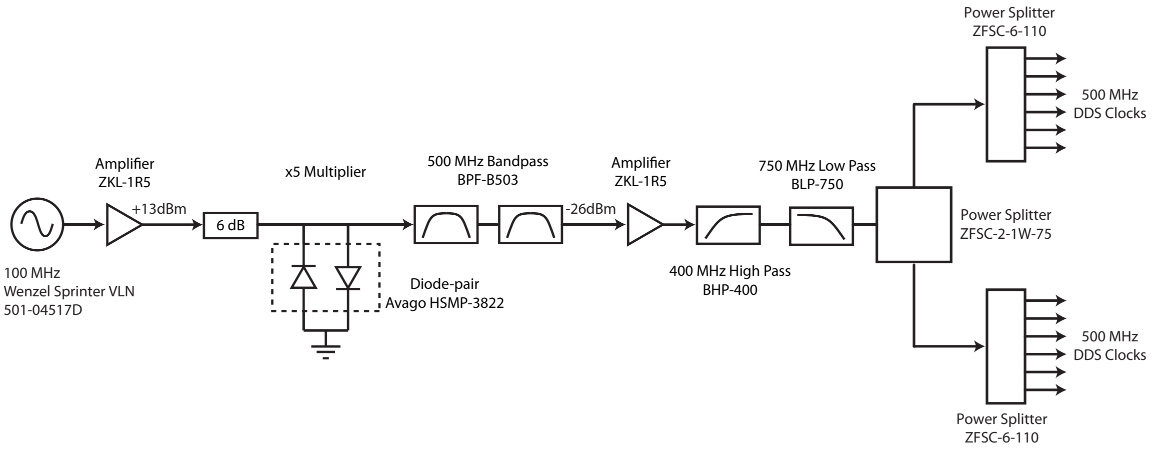

Figure 7.7: DDS 500 MHz clock generation via x5 multiplication of a ULN 100 MHz signal.

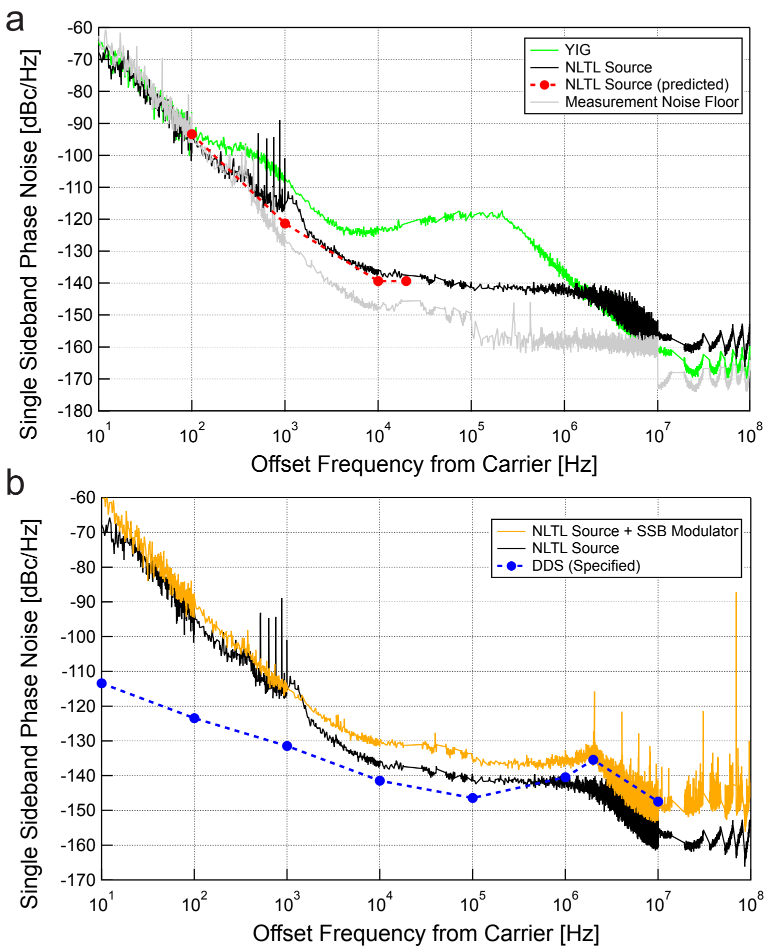

Figure 7.8: Single sideband phase noise of several microwave sources all locked to or derived from the Wenzel ULN oscillator. The measurement noise floor is in grey. **a** Comparison of noise at 6.800 GHz for a YIG oscillator (green) and our microwave NLTL source (black) measured at point M_A in Fig. 7.3. The noise in the NLTL source agrees with the prediction (red circles with dashed line to guide the eye) based on ideal scaling of the noise in the ULN oscillator specified by the manufacturer. **b** The modulated signal at 6.834 GHz (orange), measured at point M_B in Fig. 7.3, exhibits higher phase noise than the 6.8 GHz signal from the NLTL source (black). The manufacturer specified noise of the DDS (blue circles with dashed line) when operated with an internal PLL of $\times 5$ is plotted to show that the added noise primarily comes from the SSB modulator, excluding frequencies above 2 MHz where the gain peak from the internal PLL dominates. Spurious multiples of 60 Hz have been removed for presentation purposes.

We control the DDS source through a custom LabVIEW interface[2] that can update the phase, frequency and amplitude in 24, 32, and 28 μs respectively. The tuning resolutions are 0.022°, 0.12 Hz, and 0.1% of full scale amplitude respectively. Phase continuous frequency ramps and amplitude ramps are also possible which enable additional techniques, such as atomic popu-

---

[2] We thank Hsiang-Sheng Ku for programming the DDS LabVIEW control.

lation manipulation using Landau-Zener avoided crossings. The LabVIEW interface utilizes 4-bit serial communication at 2 MHz, while the DDS is capable of communication at 125 MHz. The communication rate is presently limited by the speed of the National Instruments DIO card (National Instruments PCIe-6259) used to implement the serial communication. If less flexibility or less integration with the data acquisition system is required, the DDS can also be programed through a manufacturer-provided USB interface and software, while still maintaining the ability to modulate a single parameter between as many as 16 programmable values.

The SSB modulator output is amplified to as much as 8.9 Watts using a high power microwave amplifier (Microwave Power (now Microsemi-RFIS) L0607-38). Measurements with the OE8000 at measurement point $\mathrm{M_C}$ in Fig. 7.3 show that the microwave amplifier adds a negligible amount of phase noise relative to the measured phase noise of the NLTL source derived from the ULN crystal shown in Fig. 7.8a. The microwave radiation is coupled to the atoms through a low loss 1.5 m cable (CA400) and stub-tuned dipole antenna [158] fabricated directly on a high frequency laminate circuit board (Rogers RO3035). The critical dimensions for the frequency tuning of the antenna are labeled in Fig. 7.3. The antenna is relatively broadband, with a FWHM of 400 MHz. After careful alignment of the dipole antenna, we achieved a Rabi frequency of $f_R \approx 40$ kHz with the antenna approximately 1.5" or 4 cm from the atoms [3]. When the microwaves are launched into free space using a dipole antenna, it is possible that the phase noise of the microwave field at the position of the atoms is degraded due to reflections off of nearby surfaces. One expects that such effects should have negligible impact on Q_0 since little mechanical motion is expected near the microwave Rabi frequency of $f_R \sim 40$ kHz.

The SSB modulator adds 5 to 8 dB of phase noise relative to the NLTL source, as seen in Fig. 7.8b where the measurement is taken at point $\mathrm{M_B}$ in Fig. 7.3. For frequencies below 2 MHz, we attribute the added noise to the SSB modulator. This data was taken with the the DDS referenced

---

[3] As a side note, microwave absorbing material (Laird RFLS Single Layer sheets, 0.25 inch thick, measured attenuation of 10 dB) around the glass cell vacuum chamber was necessary to reduce observed changes in the Rabi frequency of greater than 10% peak to peak caused by people walking past the optics table. With the shielding, the fluctuations are reduced to ∼1.3% peak-to-peak with people walking around and ∼0.7% with people staying still.

to the 100 MHz Wenzel ULN crystal directly, and multiplication to 500 MHz being accomplished using the internal DDS PLL multiplier set to ×5. In this configuration, the phase noise of the DDS specified by the manufacturer, and confirmed by our own measurements, only has a small contribution at offset frequencies less than 2 MHz where an expected noise peak from the DDS PLL becomes visible. This noise peak was present for the measurements in Fig. 7.8b, but is not present for the final source that has a DDS reference clock of 500 MHz obtained via external ×5 multiplication as described above.

7.3.4 Impact on QND measurements

To achieve conditional spin squeezing using QND measurements of the atomic spin projection J_z as described in Chapter 5, it was necessary to apply a π-rotation using a microwave source. Using the YIG PLL microwave source locked directly to the 10 MHz Rb atomic clock for the π-rotation, we observed added noise in the spin projection J_z that was 18 dB above the quantum projection noise level for the 7×10^5 atoms. From manufacturer specifications, the multiplied phase noise of the 10 MHz crystal is -95 dBc/Hz, for the relevant offset frequencies near f_R.

Utilizing the NLTL source locked to a slightly noisier 100 MHz crystal oscillator (Wenzel Sprinter 501-04517D) with the SSB modulation (phase noise measurements taken but not shown), the predicted added noise noise in J_z due to phase noise during the π-rotation is predicted to be 16 dB below the projection noise level. The prediction is made by simple scaling from the first measurement with the much noisier YIG oscillator. By reducing the added noise from microwave rotations, we lowered the technical noise floor of the measurement and were able to observe a 5 dB reduction in spin noise, limited by our probe quantum backaction. By changing the 100 MHz Sprinter oscillator to the ULN model and improving the added phase noise of the SSB modulator, future experiments could operate with added microwave phase noise to J_z that is 27 dB below the projection noise limit for this large ensemble size. Lower microwave phase noise can be exploited to perform composite microwave pulses that would add more noise into J_z than the plain π-rotation discussed here.

In conclusion, we have demonstrated a microwave frequency source with low phase noise that maintains the flexibility to adjust phase, frequency, and amplitude needed in high precision experiments with large atomic ensembles. The source is very cost-effective, providing a phase stability that surpasses many commercial frequency sources for a fraction of the cost. Although the source is narrowband, the center frequency can be chosen for a particular need or atom that requires a stable microwave frequency, providing an attractive option for many applications.

Chapter 8

Theory: Impact Phase Noise on Bloch Vector Rotations

In Chapter 7, we presented precise rotations in the presence of microwave amplitude, detuning and phase errors that are static within a single experimental trial but could slowly drift from trial to trial. We could have used composite π-pulses instead of plain π-pulses to suppress static errors but we did not. Indeed, composite pulses have been developed to cancel static rotation errors to any degree one desired [159].

In all treatments of composite pulses, these errors are assumed to be static for the duration of the pulse sequence. For our system, this is not a good assumption, *even* for a single rotation. Fluctuating phase or equivalent detuning errors, i.e. phase/detuning noise, near the Rabi frequency Ω_R during the rotations can add noise to J_z. The phase-noise-induced fluctuations of the collective spin polar angle prevented us from observing the SQL until we improved the phase noise of our microwave source, which was presented in Chapter 7. Even with the low phase noise source, added noise from phase noise can accumulate from many single rotations, potentially offsetting the benefits of static error cancellation from composite pulses.

In this Chapter, we quantify on the effect of phase noise on a single spin-1/2 or qubit, conveniently represented by a Bloch vector. Since the phase noise acts identically on each individual spin making up a CSS, the effect on the polar angle of a single spin in the ensemble is the same as the effect on the CSS polar angle. We present a general framework for calculating the impact of phase noise during a rotation on a Bloch vector. The analysis applies to any Bloch vector orientation, and any rotation axis azimuthal angle. The theory is experimentally verified for several special cases.

We then extend the analysis include pulse sequences assuming a white phase noise spectrum. Finally, we calculate the sensitivity of commonly used composite π-pulse sequences: CORPSE, SCROFULOUS, and BB1, used to suppress static amplitude and detuning errors respectively, and also to spin echo sequences. We expect the formalism presented in this chapter to guide the development and evaluation of future quantum manipulation protocols. For example, an optical spectrum analyzer whose noise floor is limited by atomic quantum projection noise has been realized recently [160]. The material presented in this Chapter has been published in [56].

8.1 Introduction

Atomic quantum sensors and tests of fundamental physics commonly rely on the ability to rotate a Bloch vector representing a spin-$\frac{1}{2}$ system or qubit. Besides quantum state manipulation, rotations can also be used to undo inhomogeneous errors or to reduce other sources of noise, as is done with spin echo pulses or dynamical decoupling [124, 161–166]. Precise rotations, required for manipulating collective spin-squeezed states, might also enable dynamical spin-squeezing to the two-axis squeezing limit [167] using already realized one-axis twisting in cold atoms systems [73, 74, 82, 89]. Given that actual rotations are imperfect, it is an open question whether such rotation protocols can be realized without adding large amounts of additional noise, thus destroying the squeezing.

Most rotation protocols assume that the phase of the field that rotates the qubit is perfectly stable, and that imperfections arise only due to slowly varying amplitude errors or detuning errors. Composite rotations sequences [149–151, 159, 168] and generalizations to shaped pulses [169, 170], including optimal control theory [171–173], can be used to reduce these errors to essentially arbitrary order.

In reality, the phase of the qubit-field coupling is never perfectly stable, largely due to phase noise in the local oscillator (LO) used to generate the field. The LO is typically a radio or microwave oscillator in nuclear spin, superconducting Josephson junction, quantum dot, neutral atom/ion Zeeman and hyperfine qubit systems [3]. In the case of highly-forbidden optical transitions [174], the

LO is an ultra-stable laser. Further, qubit transition frequency fluctuations can be straightforwardly mapped onto an equivalent phase noise of the LO. Such a fluctuation might arise due to noise in the DC bias current of a superconducting Josephson junction qubit [175], or differential light shifts for atomic qubits in an optical trap [174]. It is critical for future work beyond proof-of-principle experiments to develop general tools for analyzing the impact of phase noise on a rotation, both in terms of overall fidelity for quantum gates, and quadrature specific noise for manipulating states with anisotropic sensitivity to noise, such as spin-squeezed states, and Dicke states [70].

The effect of phase noise on atomic response has been studied in various contexts, for example on atomic excitation probability [176–179] under continuous drive. In the atomic sensor community, the impact of phase noise is evaluated for a single quadrature for specific Ramsey sequences [142, 180, 181]. In contrast, we present a general framework that may be applied to an arbitrary LO phase noise spectrum for continuous resonant drive without making assumptions about the orientation of the Bloch vector. The framework can be extended to arbitrary resonant pulse sequences assuming white LO phase noise. Furthermore, we fully specify all second order noise moments of the Bloch vector including covariances and variances, important for predicting the fidelity of single qubit gates and manipulations of spin-squeezed or Dicke states. The methodology and tools presented in this Chapter can help guide the development and evaluation of future quantum control and measurement protocols.

This Chapter is organized as follows. In Sec. 8.2, we describe the qubit-field interaction as a rotation of a Bloch vector. We show that the net effect of a coherently phase modulated rotation can be reduced to a small rigid rotation of the Bloch sphere. A description of the experimental system used to demonstrate the theory is provided in Sec. 8.3. Experimental examples of the response of the Bloch vector driven by phase modulated rotations are then presented. In Sec. 8.4, we extend the analysis in Sec. 8.2 assuming linear response to relate the single sideband (SSB) LO phase noise to Bloch vector noise projections through a covariance transfer matrix for a single rotation. Experimental realizations for a few special cases are also presented. The Bloch vector noise projection variances and covariances are captured in the covariance noise matrix. In Sec. 8.5, we generalize the single-rotation covariance noise matrix to that for multiple rotations/pulse sequences and apply the tools to commonly used composite π-pulse sequences: CORPSE, SCROFULOUS, and BB1 [149–151, 159, 168], and also to spin echo pulse sequences. A simple formula for the average infidelity of any pulse sequence, appropriate in the context of quantum computing, is also presented. Finally, we give a summary and provide an outlook of future work in Sec. 8.6.

8.2 Deflection of Bloch Vector due to coherently phase modulated rotation

8.2.1 System Hamiltonian

The system considered in this Chapter consists of a spin-1/2, or equivalently a qubit, with transition frequency f_a coupled to a resonant classical electromagnetic field with strength characterized by the Rabi frequency f_R proportional to the field amplitude. The system's Hamiltonian in the lab frame is

$$H_{\text{lab}} = hf_a\hat{\sigma}_z + hf_R\cos\left(2\pi f_a t + \phi(t)\right)\hat{\sigma}_x\,, \tag{8.1}$$

where h is the Planck constant, $\phi(t)$ is the LO phase as a function of time t, and $\hat{\sigma}_x\,, \hat{\sigma}_y$, $\hat{\sigma}_z$ are the Pauli matrices. The first term corresponds to the Hamiltonian of the qubit in the absence of the field, and the second term corresponds to the qubit-field interaction that drives Rabi flopping between the qubit states $|{\uparrow}\rangle$ and $|{\downarrow}\rangle$. By going into a rotating frame at the qubit transition frequency, and making the rotating wave approximation, the dynamics is described by the Hamiltonian

$$H_{\text{rot}} = \frac{hf_R}{2}\left(\cos(\phi(t))\hat{\sigma}_x + \sin(\phi(t))\,\hat{\sigma}_y\right). \tag{8.2}$$

8.2.2 LO Phase Noise

The LO phase $\phi(t)$ is random as a function of time, and its statistical properties can be captured by the autocorrelation function $\langle\phi(t)\phi(t+\tau)\rangle_t$ in the time domain, or equivalently the power spectral density of phase fluctuations $S_\phi(f_m)$ in the frequency domain, where f_m is the frequency offset from the LO carrier frequency f_{LO}. The power spectral density of phase fluctuations $S_\phi(f_m)$ is related to the autocorrelation function through the Wiener-Khinchin theorem (see Appendix D).

The SSB phase noise $\mathcal{L}(f_m) = S_\phi(f_m)/2$ of a LO is usually specified in manufacturer datasheets instead of $S_\phi(f_m)$. To facilitate application of our results in an experimental context, the SSB phase noise $\mathcal{L}(f_m)$ is used throughout this Chapter.

The phase noise spectrum of a LO is typically parametrized as a sum of $1/f$ type phase noise as follows

$$\mathcal{L}(f_m) = \sum_{k=-\infty}^{\infty} \frac{\mathcal{L}_k}{f_m^k}\,, \tag{8.3}$$

where the coefficient $\mathcal{L}_k$ characterizes the strength of the noise spectrum with dependence $1/f_m^k$. An important example is white phase noise where there is no frequency dependence. In this case, the only non-zero coefficient is for $k = 0$ corresponding to $\mathcal{L}(f_m) = \mathcal{L}_\circ$, and the autocorrelation function is given by $\langle \phi(t)\phi(t+\tau)\rangle_t = \mathcal{L}_\circ \delta(\tau)$ where $\delta(\tau)$ is the delta function. Other frequently encountered phase noise spectra include flicker noise $\mathcal{L}(f_m) = 1/f_m$ and phase diffusion noise $\mathcal{L}(f_m) = 1/f_m^2$.

8.2.3 Bloch Sphere Picture

Since length of the Bloch vector remains the same to second order in the noise, in this Chapter we normalize the length of the Bloch vector to 1 by re-defining the components of the Bloch vector $J_k \equiv \langle \hat{\sigma}_k \rangle$ where $k = \{x, y, z\}$. The tip of the Bloch vector thus resides on a Bloch sphere with radius equal to 1 (see Fig. 8.1a). The LO phase $\phi(t)$ sets the instantaneous rotation axis around which the Bloch vector rigidly rotates. For fixed LO phase $\phi(t) = \phi_R$, an initial Bloch vector $\mathbf{J}_i$ is mapped to an ideal final Bloch vector $\mathbf{J}_f^\circ$ as

$$\mathbf{J}_f^\circ = R(\phi_R, \psi)\mathbf{J}_i\,, \tag{8.4}$$

where $R(\phi_R, \psi)$ performs a counterclockwise rotation through an angle $\psi \geq 0$ about an axis in the $x - y$ plane with azimuthal angle ϕ_R measured relative to $\hat{\mathbf{x}}$. The rotation angle $\psi = 2\pi f_R t$ is set by the Rabi frequency f_R and the amount of time t the field is applied.

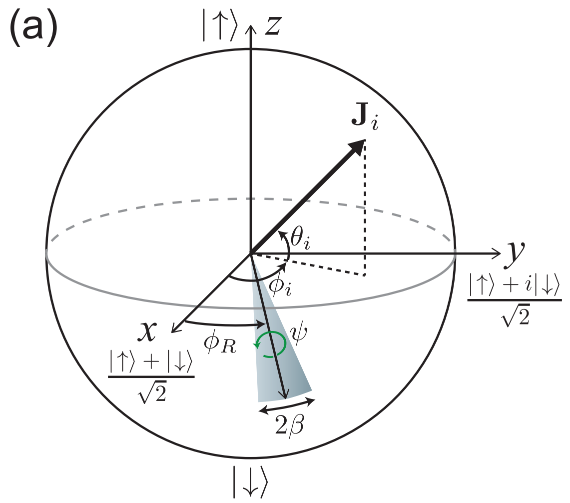

Figure 8.1: (a) Geometrical representation of the Bloch vector and a coherently phase modulated rotation on the Bloch sphere. Initial Bloch vector $\mathbf{J}_i$ is specified by polar angle θ_i and azimuthal angle ϕ_i. In the absence of phase modulation, the rotation axis is at a constant angle ϕ_R from the x-axis. With phase modulation, the rotation axis oscillates in the $x-y$ plane with amplitude β around its average position. (b) Effect of a coherently phase modulated rotation. An unmodulated rotation $R(\phi_R,\psi)$ rotates $\mathbf{J}_i$ to $\mathbf{J}_f^\circ$. With phase modulation of the rotation axis, the final Bloch vector $\mathbf{J}_f$ is deflected slightly by the vector $\mathbf{j}_f$ that can be regarded as arising from a small rotation r.

8.2.4 Small Rotation describing Phase Modulated Rotation

Our goal is to generate a general covariance transfer matrix that maps LO phase noise onto noise projections of the final Bloch vector. To do so, we consider here the response of the Bloch vector to a coherent phase modulation of the LO phase in the frequency domain, and generalize to a phase noise process in Sec. 8.4. A sinusoidal modulation of the LO phase $\phi(t)=\phi_R+\beta\sin(2\pi f_m t+\alpha_m)$ represents an oscillation of the instantaneous rotation axis in the $x-y$ plane with amplitude β about its average azimuthal angle ϕ_R as illustrated in Fig. 8.1a. The modulation frequency and phase is f_m and α_m respectively.

A phase modulated rotation causes a deflection of the final vector $\mathbf{J}_f$ from its ideal final orientation without modulation by

$$\mathbf{j}_f(\phi_R,\psi,\beta,f_m,\alpha_m)=\mathbf{J}_f-\mathbf{J}_f^\circ\,. \tag{8.5}$$

To first order in the phase modulation amplitude $\beta\ll 1$, the deflection is perpendicular to $\mathbf{J}_f^\circ$. The total effect of the modulation can be described by an additional small rotation $r(\phi_R, \psi, \beta, f_m, \alpha_m)$ applied after the ideal rotation such that

$$\mathbf{J}_f = r\mathbf{J}_f^{\circ} \,, \tag{8.6}$$

where labels on r have been suppressed. The relationships between the vectors $\mathbf{J}_i$, $\mathbf{J}_f^{\circ}$, $\mathbf{J}_f$, $\mathbf{j}_f$, and the rotations $R(\phi_R, \psi)$, r are depicted in Fig. 8.1b.

Because the dynamics with modulation can be described in terms of infinitesimal rigid rotations, the whole Bloch sphere is rigidly rotated by this additional phase modulation contribution, and r does not depend on $\mathbf{J}_i$. This is confirmed by solving for r analytically. Simple rotations about $\hat{\mathbf{z}}$ through angle ϕ_R relate the small rotation r evaluated at $\phi_R = 0$ to the small rotation evaluated at arbitrary ϕ_R through

$$r(\phi_R) = R_z(\phi_R) r(0) R_z(-\phi_R) \,. \tag{8.7}$$

Therefore, it is sufficient to determine r for the special case $\phi_R = 0$ and $\mathbf{J}_i = \hat{\mathbf{x}}$. Hereafter, quantities with a tilde ($\sim$) overhead apply to this special case only. We find

$$r(0) = R_y(-\widetilde{j}_z) R_z(\widetilde{j}_y) = \begin{pmatrix} 1 & -\widetilde{j}_y & -\widetilde{j}_z \\ \widetilde{j}_y & 1 & 0 \\ \widetilde{j}_z & 0 & 1 \end{pmatrix} , \tag{8.8}$$

where $\widetilde{\mathbf{j}}_f = (0, \widetilde{j}_y, \widetilde{j}_z)$, and only first order in the small quantities $\widetilde{j}_y$ and $\widetilde{j}_z$ are retained.

8.2.5 Solution for Deflection Vector

We now solve for the $\widetilde{j}_y$ and $\widetilde{j}_z$ that determine the small rotation matrix r defined by Eq. (8.7) and (8.8). Writing the Heisenberg equations of motion for the Bloch vector components yields to first order in the small modulation amplitude

$$\frac{d\widetilde{j}_\perp}{d\psi} + \imath \widetilde{j}_\perp = -\beta \sin\left(\nu\psi + \alpha_m\right) \,, \tag{8.9}$$

where $\widetilde{j}_\perp \equiv \widetilde{j}_z + \imath \widetilde{j}_y$, and $\nu = f_m/f_R$. The rotating wave approximation $f_m \ll f_a$ has been made. Note that this is the equation of motion for the coupled position and momentum of an undamped simple harmonic oscillator with natural resonance frequency f_R driven with an externally applied force at frequency f_m. The harmonic oscillator's displacement and velocity map onto $\widetilde{j}_y$ and $-\widetilde{j}_z$ respectively. Solving for $\widetilde{j}_y$ and $\widetilde{j}_z$ using the initial condition $\widetilde{j}_\perp(\psi = 0) = 0$, we obtain

$$\widetilde{j}_y = \frac{\beta}{1-\nu^2} \times \left[-\nu \cos \alpha_m \sin \psi - \sin \alpha_m \cos \psi + \sin \left(\nu \psi + \alpha_m \right) \right] , \tag{8.10}$$

$$\widetilde{j}_z = \frac{\beta}{1-\nu^2} \times \left[\nu \cos \alpha_m \cos \psi - \sin \alpha_m \sin \psi - \nu \cos \left(\nu \psi + \alpha_m \right) \right] . \tag{8.11}$$

The above solutions can be understood as a superposition of the "transient" and steady state response of a driven harmonic oscillator. The terms proportional to $\sin \psi$ and $\cos \psi$ in Eq. (8.10) and (8.11) correspond to the response of the harmonic oscillator at its natural frequency f_R. This response is called the transient response in damped harmonic oscillator systems. Because there is no damping in this oscillator, the "transient" response does not decay away. The terms proportional to $\sin \left(\nu \psi + \alpha_m \right)$ and $\cos \left(\nu \psi + \alpha_m \right)$ correspond to the steady state response of the oscillator at the drive frequency f_m. At $\nu = 1$, corresponding to the case of driving on resonance, the solutions take on the following limits

$$\lim_{\nu \to 1} \widetilde{j}_y = -\frac{1}{2} \left(\psi \cos \left(\psi + \alpha_m \right) - \cos \alpha_m \sin \psi \right) , \tag{8.12}$$

$$\lim_{\nu \to 1} \widetilde{j}_z = -\frac{1}{2} \left(\psi \sin \left(\psi + \alpha_m \right) + \sin \alpha_m \sin \psi \right) . \tag{8.13}$$

The amplitude of the response grows roughly linearly with ψ for large $\psi \gg 1$ as the drive is phase coherently adding momentum to the oscillator.

8.3 Experimental Verification

To connect the theory described in Sec. 8.2 to an actual physical system, we experimentally demonstrate the linear response of the Bloch vector to a coherently phase modulated rotation for a few special cases in this section.

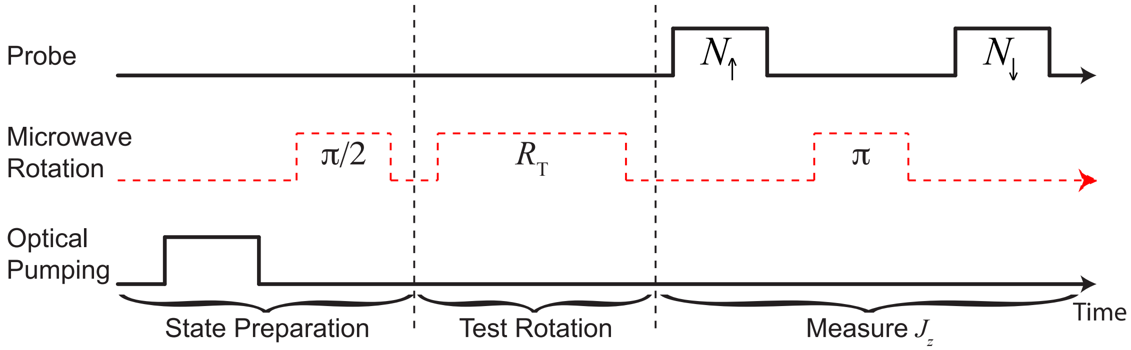

Figure 8.2: Experimental Sequence for measuring the effect of a phase modulated rotation on the Bloch vector polar angle. After preparing the initial Bloch vector $\mathbf{J}_i$ on the equator through optical pumping and a microwave $\pi/2$-pulse, a test rotation R_T is applied, and the result $J_z = (N_\uparrow - N_\downarrow)/(N_\uparrow + N_\downarrow)$ is measured probing technique described in Chapter 5. Unlike in Chapter 5 where $J_z = (N_\uparrow - N_\downarrow)/2$, J_z here has been normalized to the total ensemble size as the length of the Bloch vector has been normalized to 1 in this Chapter.

8.3.1 Physical Implementation

The experimental system used for these studies has been presented in Chapter 5, and the experiment schematic can be found in Fig. 5.4. Fig. 8.2 shows the experimental sequence for demonstrating the impact of rotation phase noise on the Bloch vector polar angle. Instead of performing the experiment on a single atom many times, we perform the experiment on many identical but otherwise independent atoms $N \sim 10^6$, achieving high single shot signal-to-noise in our quantum-limited readout. Because our measurements are collective in nature, we normalize the raw measurement results to the ensemble size to obtain single atom Bloch vector information. All atoms are initially optically pumped into $|\downarrow\rangle$. Following that, a microwave $\pi/2$-pulse rotates the Bloch vector up to the equator, initializing the system for the experiments. To a very good approximation, the effects of microwave amplitude and phase inhomogeneity across the atomic ensemble may be neglected in our experiments. The intrinsic phase noise of the microwave LO source (Agilent E8257D) is sufficiently low that we could use a small modulation amplitude β in order to remain in the linear response regime and yet not be affected by phase noise of the LO source. See Chapter 7 for experimental examples of LO phase noise masking quantum projection noise.

An experiment typically consists of a test rotation R_{T} using phase modulated resonant microwaves coupling the two-level system with Rabi frequency $f_R = 40.4$ kHz. After the rotation is completed, the Bloch vector projection $J_z = (N_\uparrow - N_\downarrow)/(N_\uparrow + N_\downarrow)$ is obtained using the cavity-aided nondemoliton measurements of the state populations $N_{\uparrow,\downarrow}$ presented in Chapter 5. The deflection j_z is obtained from the measured J_z and the J_z° for the same rotation without phase modulation using $j_z = J_z - J_z^\circ$. For future reference, $\widetilde{j}_z$ corresponds to the special case of rotation axis about $\hat{\mathbf{x}}$, i.e. $\phi_R = 0$, and initial Bloch vector $\mathbf{J}_i = \hat{\mathbf{x}}$.

8.3.2 Response to Coherently Phase Modulated Rotation

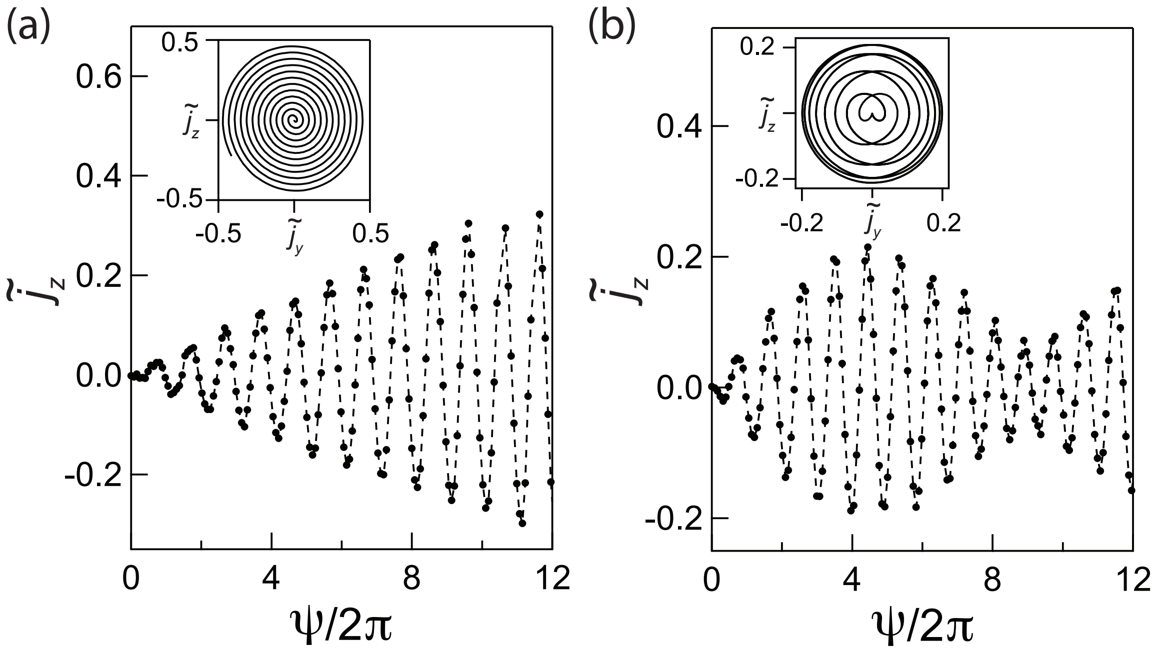

Figure 8.3: Examples of the experimentally measured evolution of the Bloch vector along the measurement axis $\hat{\mathbf{z}}$ versus rotation angle ψ, or equivalently time, for (a) resonant modulation $f_m = f_R = 40.4$ kHz, with $\beta = 0.0125$ rad, and (b) non-resonant modulation $f_m = 1.125 f_R$, with $\beta = 0.025$ rad. The modulation phase α_m is 0 for both (a) and (b). Dashed lines joins the data points (solid circles) to help guide the eye. The system responds with frequency components at f_m and f_R, leading to the observed amplitude modulation of the response in (b). Insets show the ideal theoretical spiral trajectories of the Bloch vector about $\hat{\mathbf{x}}$.

The harmonic oscillator-like response to a phase modulated rotation is experimentally demonstrated in Fig. 8.3. The Bloch vector is prepared along $\hat{\mathbf{x}}$, then rotated nominally about $\hat{\mathbf{x}}$ using microwaves whose phase is modulated at a fixed frequency f_m. After a variable rotation angle ψ, the projection $\widetilde{j}_z$ is measured. For phase modulation near resonance $f_m \approx f_R$, the envelope of the modulation grows roughly linearly with ψ, whereas away from resonance $f_m \neq f_R$, frequency components at f_R and f_m beat against one another to create amplitude modulation. The insets of Fig. 8.3 show the ideal theoretical spiral trajectories about $\hat{\mathbf{x}}$ for both cases.

8.4 Noise in Bloch Vector due to Phase Noise in a Single Rotation

8.4.1 Covariance Transfer Matrix

Having obtained and experimentally demonstrated the response of the Bloch vector to a coherently phase modulated rotation in Sec. 8.2, the goal of this section is to define a covariance transfer matrix that will allow the computation of the variance of the final Bloch vector projection along any arbitrary axis $\hat{\mathbf{n}}$ due to a randomly phase modulated rotation caused by phase noise in the LO.

We begin with modeling phase noise at a single discrete frequency f_0 by allowing the modulation phase α_m and modulation amplitude β to take on random values between realizations of the rotation. Statistical results are obtained via ensemble averaging over all possible realizations of the phase modulated rotation. The modulation phase and amplitude are fixed in a single realization but random from one realization to the next. By drawing the modulation phase α_m from a uniform distribution between 0 and 2π, and the modulation amplitude β from a Gaussian distribution with zero mean and variance $\langle\beta^2\rangle$, we model the SSB phase noise $\mathcal{L}(f_m) = \langle\beta^2\rangle\delta(f_m - f_0)/4$ (see Appendix E for details).

We define the covariance transfer matrix as the outer product $T(\phi_R, \mathbf{J}_f^\circ, \psi, f_m) \equiv 4\langle\mathbf{j}_f\mathbf{j}_f^\intercal\rangle/\langle\beta^2\rangle$, where $\langle\cdot\rangle$ denotes a statistical average over α_m and β. The normalization of T (labels suppressed) is chosen so that integrating $\hat{\mathbf{n}}^\intercal \cdot T \cdot \hat{\mathbf{n}}$ over the SSB phase noise $\mathcal{L}(f_m)$ of the LO yields the noise variance $\langle(\mathbf{j}_f \cdot \hat{\mathbf{n}})^2\rangle$ of the final Bloch vector projected along a measurement axis $\hat{\mathbf{n}}$. Using the solutions for $\widetilde{j}_y, \widetilde{j}_z$ in Eq. (8.10) and (8.11), we find the covariance transfer matrix $\widetilde{T}(\psi, f_m)$ for the special case $\phi_R = 0$ and $\mathbf{J}_i = \hat{\mathbf{x}}$

$$\widetilde{T}(\psi, f_m) = \begin{pmatrix} 0 & 0 & 0 \\ 0 & \widetilde{T}_{yy} & \widetilde{T}_{yz} \\ 0 & \widetilde{T}_{zy} & \widetilde{T}_{zz} \end{pmatrix}, \tag{8.14}$$

$$\widetilde{T}_{yy}(\psi, f_m) = \frac{2}{(1-\nu^2)^2} \times \left[(\cos\psi - \cos(\nu\psi))^2 + (\nu \sin\psi - \sin(\nu\psi))^2 \right], \tag{8.15}$$

$$\widetilde{T}_{zz}(\psi, f_m) = \frac{2}{(1-\nu^2)^2} \times \left[\nu^2 (\cos\psi - \cos(\nu\psi))^2 + (\sin\psi - \nu \sin(\nu\psi))^2 \right], \tag{8.16}$$

$$\widetilde{T}_{yz}(\psi, f_m) = \widetilde{T}_{zy}(\psi, f_m) = \frac{2}{1-\nu^2} (\cos\psi - \cos(\nu\psi)) \sin\psi \, . \tag{8.17}$$

The covariance transfer matrix T for arbitrary rotation axis azimuthal angle ϕ_R and ideal final Bloch vector position $\mathbf{J}_f^\circ = (J_x^\circ, J_y^\circ, J_z^\circ)$ is derived using the small rotation r specified in Eq. (8.7) and (8.8). The full analytic expression for T is cumbersome but can be conveniently obtained through the transformation

$$T = D(\phi_R, \mathbf{J}_f^\circ) \widetilde{T}(\psi, f_m) D(\phi_R, \mathbf{J}_f^\circ)^\intercal \, , \tag{8.18}$$

where

$$D(\phi_R, \mathbf{J}_f^0) = \begin{pmatrix} 0 & -J_y^\circ & -J_z^\circ \cos\phi_R \\ 0 & J_x^\circ & -J_z^\circ \sin\phi_R \\ 0 & 0 & J_x^\circ \cos\phi_R + J_y^\circ \sin\phi_R \end{pmatrix}. \tag{8.19}$$

As an example of this general result, we experimentally measure the projection $\widetilde{j}_z$ after rotating $\mathbf{J}_i = \hat{\mathbf{x}}$ about $\hat{\mathbf{x}}$ through different angles $\psi = \pi$, 2π and 4π while phase modulating the microwave source. Integer multiples of π were chosen to minimize sensitivity to intrinsic phase noise of the microwave source near DC. The transfer function $\widetilde{T}_{zz}$ is obtained from averaging over four discrete values of the modulation phase $\alpha_m = \{0, \frac{\pi}{2}\,\pi, \frac{3\pi}{2}\}$, while keeping the amplitude β constant, as $\widetilde{T}_{zz}(\psi, f_m) = \frac{1}{\beta^2} \sum_{n=0}^{3} \widetilde{j}_z^2(0, \psi, \beta, f_m, \frac{n\pi}{2})$. The measured and theoretical transfer function $\widetilde{T}_{zz}$ are shown in Fig. 8.4.

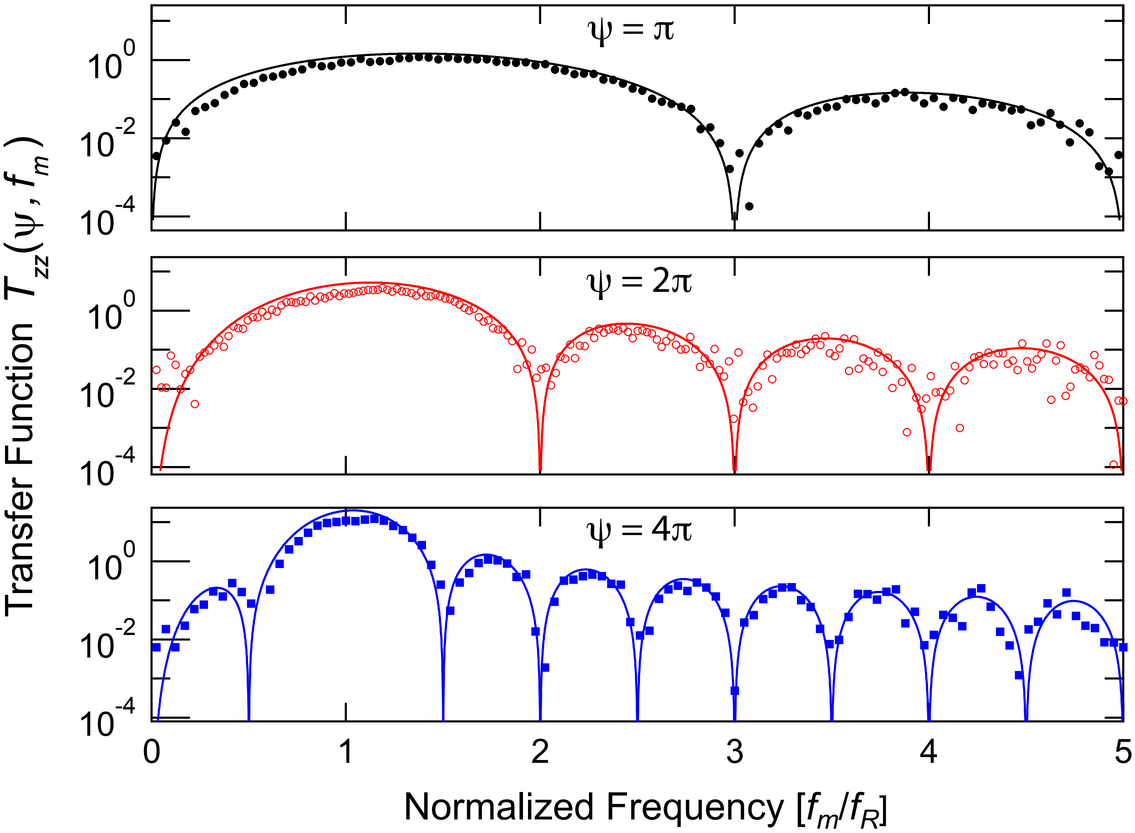

Figure 8.4: Examples of experimentally measured transfer function $\widetilde{T}_{zz}(\psi, f_m)$ for $\psi = \pi$ (black filled circles), 2π (red hollow circles) and 4π (blue filled squares) overlaid on parameter-free theoretical curves. The amplitude of the phase modulation was $\beta = 0.125, 0.05, 0.0625$ rad for the $\psi = \pi, 2\pi, 4\pi$ transfer functions respectively. The modulation amplitude $\beta \ll 1$ is chosen to keep the response small to remain in the linear regime, and yet large enough to resolve the nulls at integer multiples of f_R. The transfer function does not depend on β as long as $\beta \ll 1$ because both the response $\widetilde{j}_z$ and the modulation amplitude are proportional to β.

8.4.2 Covariance Noise Matrix

In the linear response/small signal limit, the noise in the Bloch vector in some bandwidth is simply the integral of the noise variances due to phase noise at frequency f_m over the relevant frequency bandwidth. Integrating the covariance transfer matrix $\widetilde{T}$ over the SSB phase noise $\mathcal{L}(f_m)$ of the LO yields the covariance noise matrix, defined for the largest possible bandwidth,

$$\widetilde{V}(\psi) = \int_0^\infty \widetilde{T}(\psi, f_m)\mathcal{L}(f_m)\, df_m\,. \tag{8.20}$$

The covariance noise matrix transforms to arbitrary ϕ_R and $\mathbf{J}_f^\circ$ in the same manner as the covariance transfer matrix in Eq. (8.18) via

$$V = D(\phi_R, \mathbf{J}_f^\circ)\widetilde{V}(\psi)D(\phi_R, \mathbf{J}_f^\circ)^\intercal \,. \tag{8.21}$$

Using the covariance noise matrix, the variance in the projection along $\hat{\mathbf{n}}$ may be obtained as

$$\langle(\mathbf{j}_f \cdot \hat{\mathbf{n}})^2\rangle = \hat{\mathbf{n}}^\intercal \cdot V \cdot \hat{\mathbf{n}} \,. \tag{8.22}$$

As a useful example of quantifying the noise mapping from the LO onto the Bloch vector, consider a white noise spectrum $\mathcal{L}(f_m) = \mathcal{L}_\circ$. Integrating the white phase noise spectrum over the covariance transfer matrix $\widetilde{T}(\psi, f_m)$ yields

$$\widetilde{V}(\psi) = \mathcal{L}_\circ \widetilde{\mathrm{NEB}} \,, \tag{8.23}$$

where the noise equivalent bandwidth matrix is

$$\widetilde{\mathrm{NEB}} = \pi f_R \,\mathrm{sgn}(\psi) \begin{pmatrix} 0 & 0 & 0 \\ 0 & \psi - \frac{1}{2}\sin 2\psi & -\sin^2\psi \\ 0 & -\sin^2\psi & \psi + \frac{1}{2}\sin 2\psi \end{pmatrix} . \tag{8.24}$$

A corollary to Eq. (8.24) is that as $|\psi|$ increases, the covariance transfer matrix $\widetilde{T}$ becomes more and more sharply peaked around the Rabi frequency f_R. Therefore for large $|\psi| \gg 1$, most of the Bloch vector noise contribution comes from phase noise near the Rabi frequency. As $|\psi| \to \infty$, the covariance transfer matrix $\widetilde{T}$ approaches a delta function at f_R

$$\widetilde{T}(\psi, f_m) \sim \pi f_R |\psi| \mathcal{L}_\circ \, \delta(f_m - f_R) \begin{pmatrix} 0 & 0 & 0 \\ 0 & 1 & 0 \\ 0 & 0 & 1 \end{pmatrix} . \tag{8.25}$$

The noise mapping for any rotation axis in the $x-y$ plane can be obtained by transforming to arbitrary ϕ_R, but keeping $\mathbf{J}_f^\circ = \hat{\mathbf{x}}$. We find the non-zero elements are $V_{zz} = \widetilde{V}_{zz}\cos^2\phi_R$, $V_{yy} = \widetilde{V}_{yy}$, and $V_{yz} = \widetilde{V}_{yz}\cos\phi_R$. Note that the variance V_{zz} can be driven to zero by applying the rotation perpendicular to the Bloch vector as shown in Fig. 8.5(b). Alternately, keeping $\phi_R = 0$, but letting

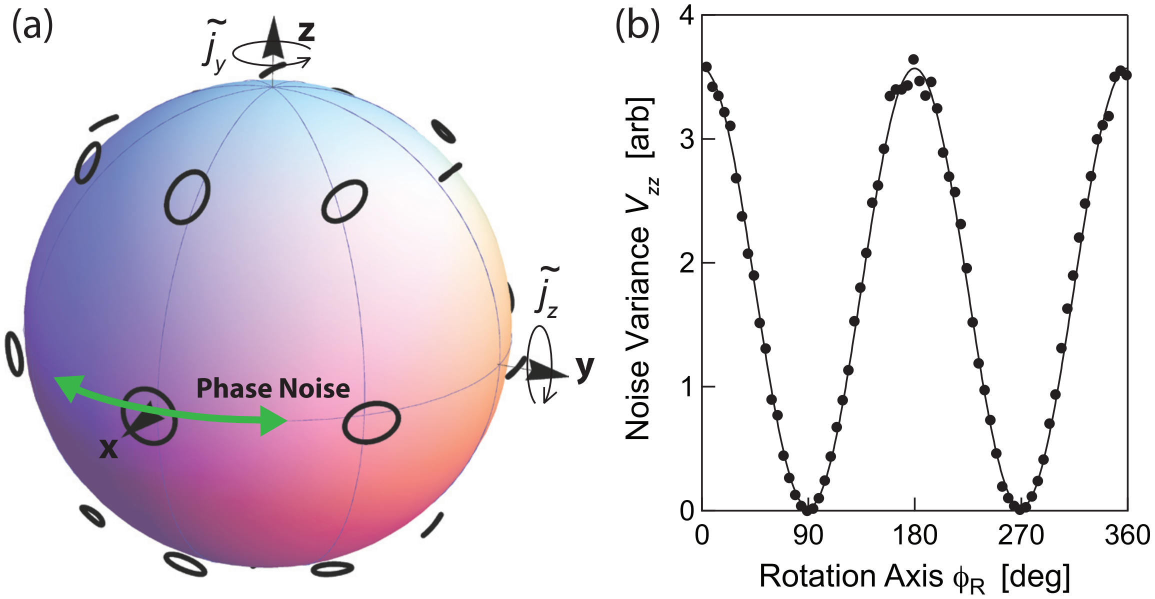

Figure 8.5: **Noise Mapping.** (a) Phase modulation of the LO causes modulation of the rotation axis (green arrow) about its mean orientation, here along $\hat{\mathbf{x}}$ or $\phi_R = 0$. The final Bloch sphere of points is deflected by an amount described by a small rigid rotation $r(0) = R_y(-\widetilde{j}_z)R_z(\widetilde{j}_y)$. The deflection of a Bloch vector depends on the ideal final vector $\mathbf{J}_f^\circ$. If a set of possible deflections for an ideal final Bloch vector $\mathbf{J}_f^\circ$ along $\hat{\mathbf{x}}$ is described by a circle $\widetilde{j}_y^2 + \widetilde{j}_z^2 = \text{const}$ (shown outside sphere for clarity), the same set of deflections for other $\mathbf{J}_f^\circ$ are described by ellipses and lines centered at $\mathbf{J}_f^\circ$. (b) The noise mapping shown in (a) for $\phi_R = 0$ and for $\mathbf{J}_f^\circ$ on the equator can be equivalently demonstrated by keeping the final vector oriented along $\mathbf{J}_f^\circ = \hat{\mathbf{x}}$ and varying the rotation axis ϕ_R. The observed noise variance V_{zz} (solid circles) of the vector projection along $\hat{\mathbf{z}}$ varies as the predicted $\cos^2\phi_R$ (solid line). The experiment was performed by applying phase modulation at a discrete frequency $f_m = 1.125 f_R$ to a rotation about $\hat{\mathbf{x}}\cos\phi_R + \hat{\mathbf{y}}\sin\phi_R$ that nominally rotates the Bloch vector $\mathbf{J}_i = \hat{\mathbf{x}}\cos 2\phi_R + \hat{\mathbf{y}}\sin 2\phi_R$ through an angle $\psi = \pi$ to $\mathbf{J}_f^\circ = \hat{\mathbf{x}}$. Averaging j_z^2 over the four modulation phases $\alpha_m = \{0, \frac{\pi}{2}, \pi, \frac{3\pi}{2}\}$ simulates phase noise at a single discrete frequency f_m.

$\mathbf{J}_f^\circ = \hat{\mathbf{x}}\cos\theta + \hat{\mathbf{z}}\sin\theta$, i.e. the ideal final vectors lie in the $x - z$ plane, one finds $V_{zz,yy} = \widetilde{V}_{zz,yy}\cos^2\theta$ and $V_{xx} = \widetilde{V}_{zz}\sin^2\theta$. This noise mapping is graphically shown in Fig. 8.5(a).

8.5 Noise in Bloch Vector due to White Phase Noise From Multiple Rotations

8.5.1 Noise Propagation

The single-rotation covariance noise matrix V allows us to analyze two crucial building blocks for coherent manipulation of quantum systems – composite pulses, used to suppress static amplitude and detuning errors, and time-separated pulse sequences designed to reduce qubit decoherence, such as spin echo and dynamical decoupling type sequences. Constituent rotations in composite pulses are applied in a back-to-back manner, leaving as little time as possible between the rotations. In contrast, time separation beween rotations in a time-separated pulse sequence may be comparable or much longer than the time it takes execute a rotation.

Assuming a white phase noise spectrum $\mathcal{L}(f_m) = \mathcal{L}_\circ$, noise from different rotations become statistically independent regardless of time separation between rotations. We also assume that dephasing of the Bloch vector during the time interval between rotations is small, a condition that is satisfied by time-separated pulse sequences designed to reduce decoherence. This ensures the opening angle between the Bloch vector and the rotation axis is well defined. Under these assumptions, the formalism for treating noise from a composite pulse, and noise from a time-separated pulse sequence are the same.

We now present the noise propagation that gives the multiple-rotation covariance noise matrix W. The symbol W for the multiple-rotation covariance noise matrix is chosen to differentiate it from the single-rotation covariance noise matrix V. A pulse sequence consists of N rotations with the kth rotation given by

$$R_k = R(\phi_k, \psi_k)\,. \tag{8.26}$$

In the absence of noise, the ideal Bloch vector after the kth rotation is

$$\mathbf{J}_k^\circ = R_k \cdots R_1 \mathbf{J}_i\,. \tag{8.27}$$

The added noise from just the kth rotation is

$$V_k = D(\phi_k, \mathbf{J}_k^\circ)\widetilde{V}(\psi_k)D(\phi_k, \mathbf{J}_k^\circ)^\intercal\,. \tag{8.28}$$

By accounting for how the noise from the previous rotation W_{k-1} is transformed by subsequent rotations, the total noise after the kth rotation may be computed iteratively using

$$W_k = R_k W_{k-1} R_k^\intercal + V_k\,, \tag{8.29}$$

with the initial condition $W_1 = V_1$. Finally, the noise variance along any arbitrary projection axis $\hat{\mathbf{n}}$ after the kth rotation is given by

$$\langle(\mathbf{j}_k \cdot \hat{\mathbf{n}})^2\rangle = \hat{\mathbf{n}}^\intercal \cdot W_k \cdot \hat{\mathbf{n}}\,, \tag{8.30}$$

where $\mathbf{j}_k$ is the noise deflection after the kth rotation.

8.5.2 Average Infidelity

While matrix elements of the covariance noise matrix W depend on pulse sequence specifics and the initial Bloch vector, we present here a simple formula that evaluates the average quality of a pulse sequence using only general properties of the pulse sequence. Within the quantum control and computing community, the state infidelity [182]

$$1 - F = \mathrm{Tr}(W)/4 \tag{8.31}$$

is an important measure of the rotation quality. While the state infidelity depends on pulse sequence details, the state infidelity averaged over the Bloch sphere of possible initial states

$$\langle 1 - F\rangle = \Psi\pi f_R \mathcal{L}_\circ/3 \tag{8.32}$$

depends only on the total rotation angle $\Psi = \sum_{k=1}^{N}\psi_k$ and not the rotation axes ϕ_k. Thus, a pulse sequence with smaller Ψ is preferred over one with larger Ψ if one is mainly concerned with the average fidelity. In spin echo and dynamical decoupling schemes, suppression of environment-induced decoherence typically improves with the number of pulses. However, this comes at the expense of increasing the average phase-noise-induced decoherence. It is, therefore, necessary to strike a balance between reducing environment-induced decoherence and reducing phase-noise-induced decoherence.

8.5.3 Composite π-pulse Comparisons

Composite pulses, designed to suppress static amplitude and detuning errors, have been thoroughly analyzed in the literature with regards to the degree of error cancellation [149–151, 159, 168]. The influence of phase noise on the Bloch vector through composite pulses, however, has received little attention in literature.

Applying the noise propagation formalism presented in Sec. 8.5.1 to the commonly used composite π-pulse sequences: CORPSE, SCROFULOUS, and BB1 [149–151], which effectively implement a π-pulse about $\hat{\mathbf{x}}$, we summarize in Fig. 8.6 the final variance W_{zz} and the state infidelity $1-F$ versus the initial Bloch vector $\mathbf{J}_i$ specified by its polar angle θ_i and azimuthal angle ϕ_i. Expressions for the composite pulse rotation sequences, covariance noise matrices, and state infidelities are provided in Appendix F. For completeness, we also summarize the static error cancellation order and static infidelity for these pulses evaluated for an rotation axis parallel and perpendicular to the Bloch vector in Appendix F.

The single quadrature variance W_{zz} is of interest in metrology applications, particularly for manipulating spin-squeezed states, as added noise in the squeezed quadrature can potentially destroy the squeezing. The state infidelity $1-F$, which includes variances from the two transverse spin components perpendicular to the ideal final Bloch vector, is particularly pertinent in quantum control for quantifying the overall quality of the rotations.

It is generally not possible to minimize phase noise sensitivity and optimize static error cancellation simultaneously. To understand the tradeoffs between phase noise sensitivity and static error cancellation, we compare and contrast the two for initial Bloch vectors in the $x-y$ plane, i.e. $\theta_i = 0$, leaving ϕ_i as the only degree of freedom. We use W_{zz} and $1-F$ as the basis for evaluating sensitivity to phase noise.

A static fractional amplitude error ϵ results in an error $\epsilon\psi$ in the rotation angle, and a static detuning error $\delta = (f_{LO} - f_a)/f_R$, where f_{LO} is the LO frequency, causes the rotation axis to be tilted up from the $x-y$ plane by an angle $\arctan(\delta)$. The degree to which the static errors ϵ, δ are suppressed can be characterized by the static error squared $W_{zz,\mathrm{st}} = j^2_{z,\mathrm{st}}(\epsilon, \delta, \phi_i)$, and the infidelity due to static error $1-F_{\mathrm{st}} = \mathrm{Tr}(W_{\mathrm{st}}(\epsilon, \delta, \phi_i))/4$. These definitions, in direct analogy to corresponding quantities for phase noise, allows meaningful comparison of the phase noise sensitivity and static error cancellation on the same footing in the next section.

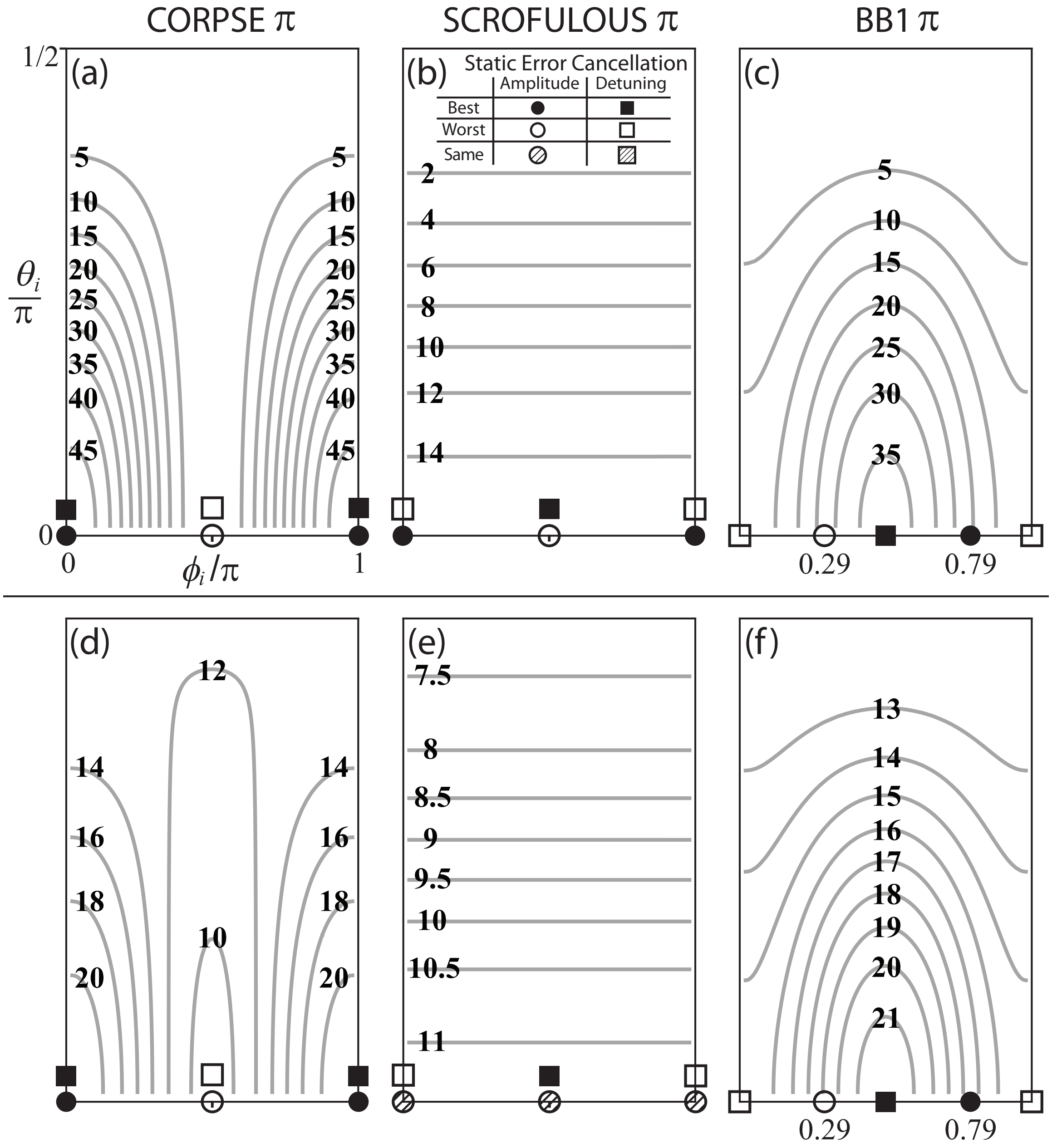

Figure 8.6: **Composite π-pulses.** Variance W_{zz} and infidelity $1-F$ of CORPSE π-pulse (a, d), SCROFULOUS π-pulse (b, e) and BB1 π-pulse (c, f) versus initial Bloch vector orientation (θ_i, ϕ_i). θ_i is measured from the $x-y$ plane and ϕ_i is measured from $\hat{\mathbf{x}}$. Contours levels are normalized to $f_R\mathcal{L}_\circ$. For scale, $\widetilde{W}_{zz}(\theta_i=0, \phi_i=0)$ for a simple π-pulse about $\hat{\mathbf{x}}$ is $\pi^2 f_R\mathcal{L}_\circ$. Points of best (solid circle), worst (hollow circle), and same (hatched circle) order of static amplitude error cancellation, and points of best (solid square), worst (hollow square), and same (hatched square) order of static detuning error cancellation (offset vertically for clarity) are shown for Bloch vectors with $\theta_i = 0$. All plots have the same axes as (a). A quadrant of the Bloch sphere is shown here. The rest of the contour plot can be generated using reflection symmetry about the $x-y$ and $x-z$ plane. The rest of the static error cancellation points can be generated via $\phi_i \to \phi_i + \pi$.

8.5.3.1 CORPSE π-pulse

The CORPSE π-pulse, used to suppress static detuning error, has the best static error cancellation at $\phi_i = 0, \pi$ where both $W_{zz,\mathrm{st}}, 1 - F_{\mathrm{st}} = O(\delta^6)$. However, it is also most sensitive to phase noise at $\phi_i = 0, \pi$ (see Fig. 8.6(a, d)). At $\phi_i = \pi/2$, the impact of phase noise is minimized at the expense of static error cancellation as both $W_{zz,\mathrm{st}}, 1 - F_{\mathrm{st}} = O(\delta^4) + O(\epsilon^2)$.

8.5.3.2 SCROFULOUS π-pulse

In contrast to the CORPSE π-pulse, sensitivity to phase noise does not vary with ϕ_i for the SCROFULOUS π-pulse designed to suppress static amplitude error. As shown in Fig. 8.6(b, e), one can simply choose ϕ_i to optimize the cancellation of static errors depending on the quantity $W_{zz,\mathrm{st}}$ or infidelity $1 - F_{\mathrm{st}}$ to be optimized, and on the dominant source of static errors (amplitude or detuning) without altering the impact from phase noise.

8.5.3.3 BB1 π-pulse

Finally, the BB1 π-pulse, which compensates for amplitude error with little to no cost to the sensitivity to detuning error, has similar impact from phase noise where the order of amplitude error cancellation is best (worst) at $\phi_i \approx 0.79\pi\,(0.29\pi)$ as shown in Fig. 8.6(c, f). Therefore one may choose to operate at $\phi_i \approx 0.79\pi$ where $W_{zz,\mathrm{st}} = O(\delta^2) + O(\epsilon^{10})$ and $1 - F_{\mathrm{st}} = O(\delta^2) + O(\epsilon^8)$. In fact, the impact from phase noise is slightly lower at $\phi_i \approx 0.79\pi$ compared to at $\phi_i \approx 0.29\pi$. On the other hand, there is a tradeoff between suppressing detuning errors and sensitivity to phase noise. Detuning error cancellation is best at $\phi_i = \pi/2$ as both $W_{zz,\mathrm{st}}, 1 - F_{\mathrm{st}}$ do not scale with δ to any order if $\epsilon = 0$. However, the impact of phase noise is also worst at $\phi_i = \pi/2$.

In general, careful evaluation of the relative scalings and contributions of phase noise, static amplitude and detuning errors is required to optimize the overall fidelity or specific noise quadratures.

8.5.4 Spin Echo Pulse Sequences

Spin echo and dynamical decoupling sequences constitute another class of manipulation protocols in quantum control and computing, important for suppressing qubit decoherence, or, for instance, to undo probe-induced dephasing as was done in our squeezing experiment. We analyze here spin echo sequences of the form $[\tau - R(\phi_1, \pi) - 2\tau - R(\phi_2, \pi) - 2\tau \cdots - R(\phi_N, \pi) - \tau]$ using the formalism developed in Sec. 8.5.1 to find the covariance noise matrix W for the sequence.

We consider the following two choices of rotation axes: (a) rotation axis always along $\hat{\mathbf{x}}$, or, (b) alternating between $\hat{\mathbf{x}}$ and $-\hat{\mathbf{x}}$ with the first π-pulse applied along $\hat{\mathbf{x}}$. Note that the widely used Carr-Purcell [161], Carr-Purcell-Meiboom-Gill [162], and Uhrig Dynamical Decoupling [164] sequences are special cases of (a) corresponding to specific orientations of the Bloch vector with respect to the rotation axis $\hat{\mathbf{x}}$.

Writing the initial Bloch vector as $\mathbf{J}_i = (J_x^i, J_y^i, J_z^i)$, the covariance noise matrix for both choice (a) and (b) reads

$$W_N = N\pi^2 f_R \mathcal{L}_\circ \begin{pmatrix} 1 - J_x^{i\,2} & s_N J_x^i J_y^i & s_N J_x^i J_z^i \\ s_N J_x^i J_y^i & J_x^{i\,2} & 0 \\ s_N J_x^i J_z^i & 0 & J_x^{i\,2} \end{pmatrix}, \tag{8.33}$$

where $s_N = (-1)^{(N+1)}$. While the noise properties for the two choices are the same, their sensitivity to static errors are different. Choice (b) offers cancellation of static amplitude error as the Bloch vector nominally retraces its path while choice (a) accumulates static amplitude error as the Bloch vector keeps rotating about the same axis in the same sense. On the other hand, choice (a) does not accumulate static detuning error while choice (b) does. In future work, we will explore the possibility of engineering noise properties of spin echo pulse sequences.

8.6 Summary

In summary, we have developed a general framework for analyzing the mapping of LO phase noise onto noise projections of a Bloch vector and extend the mapping to pulse sequences for the case of white LO phase noise. Detuning or transition frequency noise can be handled via the mapping $\beta \to \Delta_{\mathrm{FM}}/f_m$ where Δ_{FM} is the frequency modulation amplitude. Results for special but important and illustrative cases are presented, which experimentalists can readily utilize for estimation or design. Future directions may include extending the analysis to non-resonant excitation, more complex spin echo or dynamical decoupling pulse sequences, and account for the effects of $1/f$ and higher order phase noise, where time separation between pulses may no longer be ignored, and noise correlations between pulses play an important role.

Chapter 9

Broader Context, Future Prospects, and Conclusions

In this concluding chapter, we will place the observed squeezing in this work within the context of other experiments and approaches for entanglement-enhanced measurement precision. This chapter will also explore several future directions to improve the amount of observable squeezing, including probing on optical cycling transitions and technical upgrades to the experiment. The approach of using cycling transitions is currently being pursued in the laboratory with very promising initial results.

9.1 Framing our results in broader context

We have utilized the tools of cavity-QED to prepare an entangled ensemble with a 3.4(6) dB improvement in spectroscopic sensitivity over the standard quantum limit (SQL) in the largest clock-like ensemble $N = 7 \times 10^5$ to date. Our method does not require single particle addressability and requires a single fast ~ 150 μs squeezing operation. The gain in sensitivity is spectroscopically equivalent to the enhancement obtained had we created $> 10^5$ pairs of maximally entangled qubits, demonstrating the power of a top-down approach for entangling large ensembles. The probing of atomic populations via the vacuum Rabi splitting is also of broad interest for non-destructively reading out a wide variety of both atomic and solid state qubits.

From the perspective of technologies that might impact future physics, the *large ensemble size* is a crucial component. Entangled states of cold, neutral atoms are unlikely to impact the future of quantum sensors and tests of fundamental physics unless the techniques for generating the states are demonstrated to work for the 10^4 to 10^7 neutral atom ensembles typically used in frequency standards [14, 16, 18], free space atom interferometers [19, 27, 87, 183], trapped atom interferometers [72, 76, 80, 83] and magnetometers [23, 88, 102].

The approach described in this thesis allows sub-quantum-noise limited readout of a sensor with $\frac{dM_s}{dM_m} \times \frac{M_m}{N} \approx 0.1$ photon recoils/atom (at $M_m = 1.9 \times 10^5$ photons and $N = 7 \times 10^5$ atoms), producing little heating of the atomic ensemble. Applied to a state-of-the-art optical lattice clock, the non-destructive probing can result in higher clock duty cycle which improves measurement statistics, and helps to suppress the dominant aliasing of the local oscillator noise [15, 184].

The work presented in this thesis is unique in that we probe the atomic ensemble in the resonant regime of strong collective coupling cavity-QED. By doing so, we hope to counter a commonly held view that the quality of a coherence-preserving QND measurement is fundamentally linked to the probe's large detuning from atomic resonance. Instead, it is the magnitude of the collective cooperativity parameter $N_\uparrow C$ (equivalent to the optical depth for a free space experiment [38]) that sets the fundamental quality of the QND measurement as shown in Chapter. 3. In the context of free space measurements, detuning from resonance creates little enhancement in sensitivity to projection noise fluctuations once the detuned optical depth falls below one. The *absolute* size of projection noise rms fluctuations in the dispersive regime decreases as $1/\delta_{p,fs}$, where $\delta_{p,fs} = \omega_p - \omega_{\uparrow e}$ is the free space probe detuning from the $|\uparrow\rangle$ to $|e\rangle$ transition frequency. In the presence of a fixed technical noise background, resolving projection noise fluctuations become more difficult as the probe detuning $\delta_{p,fs}$ is increased. Using an optical cavity to enhance the cooperativity parameter has the potential to allow similar results to free space experiments, but at atomic densities lowered by a factor of order the cavity finesse.

The spectroscopic gain demonstrated in this thesis is far from the fundamental Heisenberg limit which scales as $1/N$, indicating that there is a lot of room for improvement. The Heisenberg limit has been approached by creating nearly maximally entangled states of 2 to 14 ions [62–64, 66, 67]. However, the spectroscopic gain relative to the SQL demonstrated in this thesis is comparable to these experiments, highlighting the fact that neutral ensembles have higher potential for spectroscopic gains than ion trap experiments because of the large ensemble size. Ensembles of $N \approx 10^3$ atoms have been spin squeezed by exploiting atom-atom collisions within a Bose-Einstein Condensate [72–76, 80–83], however these systems face the significant challenge of managing systematic errors introduced by the required strong atomic interactions.

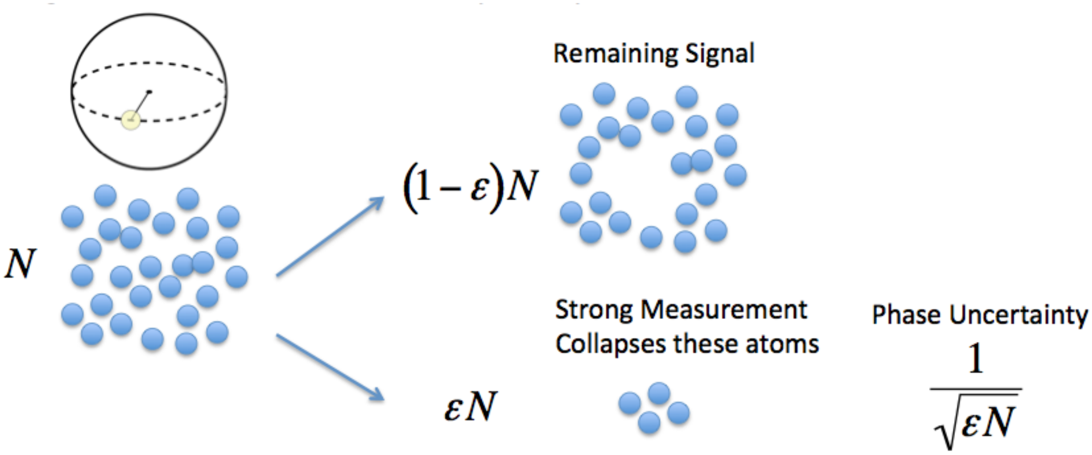

Figure 9.1: Schematic of weak sampled measurements. A small fraction ϵ of a large ensemble N of atoms could be extracted and a strong measurement of the extracted sub-ensemble's Bloch vector polar angle θ is performed. Using this classical sampling strategy, the estimate of the Bloch vector polar angle θ of the initial full ensemble is limited to the SQL for the sub-ensemble to $\Delta\theta_{\mathrm{SQL,sample}} = 1/\sqrt{\epsilon N}$. While the loss of signal in the remaining ensemble can be made small, the uncertainty attainable from measuring sub-ensemble increases concomitantly. In our experiment, $\epsilon = 0.15(2)$. The sampling strategy would provide an estimate $-10\log(\epsilon) = 8.2(7)$ dB noisier than the SQL for the initial full ensemble $\Delta\theta_{\mathrm{SQL}}$ and 13.2(9) dB noisier compared to the spin-noise-reduction demonstrated in Chapter. 5 using a coherence-preserving QND measurement.

The coherence-preserving nature of the QND measurements presented in this thesis should also be contrasted with weak, sampled measurements in order to compare this work to fluorescence detection of an optically thin ensemble. Equivalently, the angle θ of the full ensemble could be estimated by extracting a fraction $\epsilon = 1 - \mathcal{C}_f/\mathcal{C}_i = 0.15(2)$ of the initially un-decohered atoms, and performing perfect state detection on this sub-ensemble. The loss of signal would be the same as observed in our experiment, but the sub-ensemble's estimate of θ would be $G = -10\log_{10}(\epsilon) + 4.9 = 13.2(9)$ dB noisier than the 4.9(6) dB sub-projection-noise precision demonstrated in this thesis using a collective measurement approach. Conceptually, this reduction in noise can be described as arising from a noiseless amplifier of gain G placed before a 15/85 linear atom beam splitter [185].

This fundamental gain in precision is enabled by the collective interaction of the atomic ensemble and the probe mode.

9.2 Spectroscopic gain in the presence of decoherence

Generating spin squeezed states with phase resolution below the SQL takes us one step closer towards making ever more precise phase and frequency measurements. The natural next step is to apply the generated squeezed states to an actual measurement. The question of how to harness the power of entangled states for metrological gain under different decoherence models is currently a very active field of theoretical research. In this section, I will briefly discuss several situations in which decoherence during the phase evolution can reduce or even eliminate the spectroscopic gain afforded by the intrinsic phase resolution enhancement of the generated squeezed states. The final step in Ramsey spectroscopy is to map the evolved phase onto a change in populations, and then read out the populations. To realize the full potential accorded by the squeezed states, it is therefore necessary to read out the state with sufficiently low noise — a topic already treated in Chapters 3 and 4. More precisely, the readout noise needs to be much lower than the projection noise of the squeezed state. With low noise readout techniques, recent experiments have demonstrated Ramsey interferometry beyond the SQL with spin squeezed states over evolution times of $\lesssim$20 ms [73, 75, 76, 186, 187].

In systems whose Ramsey evolution time is limited by uncorrelated single particle decoherence, Ref. [188] has showed that maximally entangled cat states provide no spectroscopic enhancement in *frequency* measurements over coherent spin states. The reason is because cat states are so sensitive to atomic decoherence such that the optimal Ramsey evolution time is drastically shortened by a factor of N, completely negating the quantum advantage provided by the N times faster rate of phase evolution. However, Refs. [188, 189] showed that improvement of frequency measurements from partially entangled states that have a high degree of permutation symmetry, such as spin squeezed states, can be obtained. Taken together, the gains achievable from modest amounts of spin squeezing and the extreme fragility of maximally entangled states suggest that pursing the

Heisenberg limit in large ensembles could throw off our scent in the pursuit of higher measurement precision. Generating macroscopic cat states is a very worthy scientific goal for understanding quantum superpositions at macroscopic scales, but cat states might not be practical for metrology with large ensembles.

Besides being extremely sensitive to dephasing [66, 190], maximally entangled states are also extremely sensitive to losses. The loss of a single atom effectively collapses the wavefunction into a product state wavefunction into all spin up or all spin down. In the density matrix formalism, tracing over a single particle results in a completely mixed state. The mixed state can be interpreted as a classical mixture of all the atoms in spin up or all spin down with probability 50% each. Spin squeezed states, in contrast, have been shown to be robust against loss [191], uncorrelated single particle dephasing [192], and to a lesser extent, correlated dephasing [37]. The reason for this robustness arises from the permutation symmetry of squeezed state [191]. Unlike a cat state, small losses from a spin squeezed state do not destroy entanglement completely. Losses degrade the amount of squeezing dependent on the relative levels of losses and squeezing. In analogy to squeezed light, the degradation of spin squeezing in atomic systems due to losses is analogous to vacuum noise coupling in through a dark port. As an example, for squeezing levels of 3 dB, one could afford to lose $\sim 50\%$ of the particles before losing the squeezing. Unlike photons, it is easier to trap and hold onto atoms for long periods of times, and one could imagine atomic spin squeezing might be able to surpass even photonic squeezing one day.

It is important to make a distinction between *phase* and *frequency* measurements. Frequency measurements rely on the accumulation of an evolved phase over time, during which decoherence can occur. In contrast, a phase measurement is robust because it can be made, in principle, in an arbitrarily short amount of time so that decoherence is frozen in its tracks. As a result decoherence is not expected to degrade spectroscopic gains for a phase measurement. This does rely on performing the phase measurement immediately after the squeezed state is prepared. Alternatively, squeezing may be stored in the θ-quadrature which is insensitive to dephasing in ϕ while waiting for the phase measurement experiment to be readied. When the phase is ready to be measured, a rotation that aligns the squeezing along ϕ activates the phase measurement.

In optical clocks, where coherence times are limited by the laser local oscillator dephasing[1] (an example of correlated dephasing), the precision of the clock can be enhanced by using squeezed states of large ensembles, with the optimal Allan variance scaling as $N^{-1/3}$ relative to the SQL [37]. This optimal Allan variance scaling is achieved using moderately squeezed states with $\xi_{\rm m}^{-1} \simeq \sqrt{N}$, far from the Heisenberg limit of $\xi_{\rm m}^{-1} = N$ for large N. The favorable scaling with N argues for using large ensembles, as is pursued in this thesis, to obtain more potential improvement. Using an ensemble size of $N = 10^6$ as an example, the optimal amount of squeezing would be $\xi_{\rm m}^{-1} \simeq 10^3 = 30$ dB. So for squeezing less than 30 dB, such as our experiment where $\xi_{\rm m}^{-1} = 3.4$ dB, the full amount of squeezing would be reflected in the clock Allan variance improvement.

Instead of making *more precise* measurements, one can also choose to spend the squeezing on making *more frequent* measurements. Increase in measurement bandwidth with squeezed states can be achieved without loss of sensitivity provided the Ramsey evolution time is shorter than the single particle decoherence time [38]. Atomic magnetometer bandwidth improvement enabled by entanglement has been demonstrated in Ref. [102]. Bandwidth improvement with nondemolition measurements have also been demonstrated in Ref. [125].

9.3 Fundamental Limits on Squeezing via Probing the ^{87}Rb cycling transition

Squeezing via probing an open optical transition, as was the case for the experiment presented in Chap. 5, is fundamentally limited by Raman spin flips as shown in Chap. 4. As an outlook on future experiments, we consider a situation in which Raman spin flips are greatly reduced, namely probing on a cycling transition [130, 193]. Using the framework developed in Chapters 3 and 4, we show that larger amounts of squeezing are possible in this configuration than with probing on an open transition. The key results are that as NC is increased, the spectroscopic enhancement scales as $\xi_{\rm m}^{-1} \sim NC$, as expected in the cycling limit, until it enters a region of saturation of the

---

[1] Nature provides atoms with such long coherence times that the best ultra-narrow linewidth lasers cannot yet match.

spectroscopic enhancement set by the ratio $\omega_{\mathrm{hf}}/\Gamma$ of the hyperfine splitting to the excited state decay linewidth as a result of the Raman spin flips caused off-resonant scattering off other states, i.e. the notion of a cycling transition is an approximate concept.

As a concrete example of how a cycling transition can be used to enhance probing, we consider the cycling transition in ^{87}Rb, $|\uparrow\rangle \equiv |F = 2, m_F = 2\rangle$ to $|e\rangle \equiv |F = 3', m_F = 3\rangle$ at wavelength 780 nm. The spin down state is chosen as $|\downarrow\rangle \equiv |F = 1, m_F = 1\rangle$. For the following, the probing scheme with relevant energy levels, dipole matrix elements, decay branching ratios, dressed mode frequencies, and probe laser detunings are shown and defined in Fig. 9.2. Here we will extend the previous models of the precision of the estimation of J_z and the loss of signal due to wavefunction collapse to capture the essential physics for this system. Key results are that there exists a region of saturation, or universal spectroscopic enhancement, set only by atomic properties and in which varying atom number and cavity finesse can have little impact. The asymmetry in the cavity coupling to $|\uparrow\rangle$ and $|\downarrow\rangle$ allows this saturation region to be surpassed at large values of NC but the scaling then proceeds as $\xi_{\mathrm{m}}^{-1} \sim \sqrt{NC}$.

We must first consider what limits the rate of Raman scattering processes that can lead to diffusion of the spin projection J_z. The probe polarization can be set to pure σ^+ to better than 10^{-4}, so that Raman scattering from $|\uparrow\rangle$ is suppressed to at least this level or greater. The more fundamental Raman scattering limitation arises from the finite hyperfine splitting $\omega_{\mathrm{hf}} = 2\pi \times (6834\ \mathrm{MHz})$. Specifically, atoms in $|\downarrow\rangle$ can non-resonantly Raman scatter probe photons from $|e'\rangle \equiv |F = 2', m_F = 2\rangle$.

In the following discussion, the quantity m_s is importantly defined as the average number of probe photons (normalized to the total atom number) Rayleigh scattered into free space by atoms in $|\uparrow\rangle$. All other scattering processes will be scaled from this quantity using the quantities defined in Fig. 9.2. The key parameters for rescaling are the ratio of the dipole matrix elements $r = M_{\downarrow e'}/M_{\uparrow e} = 1\sqrt{2}$, the decay branching ratio $B_{3e'} = 1/6$ from $|e'\rangle$ to $|3\rangle \equiv |F = 2, m_F = 1\rangle$, and the detunings of the probe light δ_e and $\delta_{e'} = \delta_e - \omega_{\mathrm{hf}} - \omega_{\mathrm{ehf}}$ from resonance with the transitions $|\uparrow\rangle \rightarrow |e\rangle$ and $|\downarrow\rangle \rightarrow |e'\rangle$ respectively. Because $\omega_{\mathrm{hf}} \gg \omega_{\mathrm{ehf}}$, we neglect the excited state hyperfine

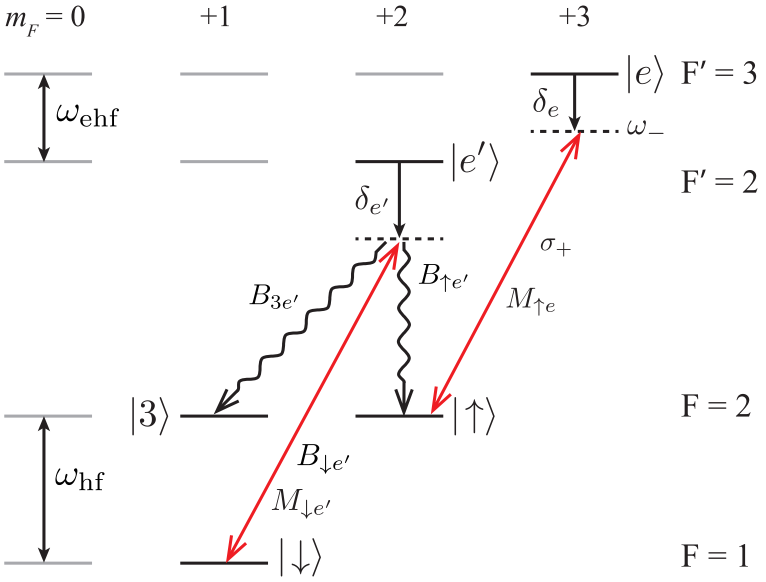

Figure 9.2: Probing scheme using the cycling transition in ^{87}Rb. The ground hyperfine states $F = 2$ and $F = 1$ are split by $\omega_{\text{hf}} = 2\pi \times (6834\text{ MHz})$. The values of m_F are labeled across the top. The relevant $F' = 3$ and $F' = 2$ excited D2 transitions at wavelength 780 nm are also shown with the excited state splitting $\omega_{\text{ehf}} = 2\pi \times (267\text{ MHz})$. The pseudo spin-1/2 system is here composed of $|\uparrow\rangle = |F = 2, m_F = 2\rangle$ and $|\downarrow\rangle = |F = 1, m_F = 1\rangle$. Ideally, the σ^+-polarized probing laser couples only $|\uparrow\rangle$ to the optically excited state $|e\rangle$ with dipole matrix element $M_{\uparrow e}$ at a frequency detuning δ_e that is approximately equal to the dressed-cavity mode frequency ω_-. In this illustration, δ_e is negative. By dipole selection rules, $|e\rangle$ can only decay back to $|\uparrow\rangle$. However, the same probe laser also couples $|\downarrow\rangle$ to the single excited state $|e'\rangle$ with dipole matrix element $M_{\downarrow e'}$ and larger detuning from resonance $\delta_{e'} = \delta_e - \omega_{\text{hf}} + \omega_{\text{ehf}}$. The ratio of matrix elements is $M_{\downarrow e'}/M_{\uparrow e} = 1/\sqrt{2}$. Finally, the state $|e'\rangle$ decays to states $|\downarrow\rangle$, $|\uparrow\rangle$, and $|3\rangle$ with fractional branching ratios $B_{\downarrow e'} = 1/2$, $B_{\uparrow e'} = 1/3$, and $B_{3e'} = 1/6$ respectively.

splittings so that $\delta_{e'} \approx \delta_e - \omega_{\text{hf}}$.

The rms imprecision in the estimate of J_z relative to the projection noise level can be approximately modeled as

$$\left(\frac{\Delta J_z}{\Delta J_{z,\text{CSS}}}\right)^2 = 4p_\uparrow m_s + p_3 m_s + \frac{\widetilde{m}_s^{\text{proj}}}{m_s}\,. \tag{9.1}$$

Any small gains in the imprecision of the estimate of J_z from state preparation or prior knowledge has been neglected. Starting in order of physical significance, the first and second terms arise from diffusion of J_z caused by Raman transitions from $|\downarrow\rangle \to |\uparrow\rangle$ and $|3\rangle$ with effective probabilities $p_\uparrow$

and p_3 given approximately by

$$p_{\uparrow,3} = B_{\uparrow,3\ e'} r^2 \left(\frac{\delta_e}{\delta_{e'}}\right)^2 . \tag{9.2}$$

In this simple treatment, Raman decays to $|3\rangle$ are treated as loss, as reflected in the smaller numerical pre-factor in front of the second term of Eq. (9.1).

The third term in Eq. (9.1) is modified to reflect that both states can interact with the probe at large detunings such that the dressed cavity mode frequency is less sensitive to quantum projection noise in J_z, and thus more probe photons must be used to resolve J_z at the projection noise level, i.e.,

$$\widetilde{m}_s^{\text{proj}} = \frac{m_s^{\text{proj}}}{R_{\text{ray}}} . \tag{9.3}$$

Here, m_s^{proj} is defined by Eqs. (3.19), (3.9), and (3.4). Indistinguishability is accounted for by

$$R_{\text{ray}} = \left(1 - r\left|\frac{\delta_e}{\delta_{e'}}\right|\right)^2 . \tag{9.4}$$

Note that $R_{\text{ray}} \leq 1$ with an asymptotic value of $R_{\text{ray}} \to (1-r)^2$ at large detunings.

There are two effects that are neglected in Eq. (9.3) by first assuming they are small, and then verifying this to be the case after the calculations. First, in applying the dressed cavity linewidth result for κ' from Eq. (3.9), we assume that the cavity mode is negligibly further broadened by atoms in state $|\downarrow\rangle$. By estimating the additional broadening evaluated at the optimal cavity detuning and average number of scattered photons, we find that the optimal spectroscopic enhancements calculated in Fig. 9.3 are reduced by < 0.3 dB due to the neglected mode broadening. Second, we assume that the dressed mode frequency ω_- calculated from Eq. (3.4) is only modified by a small fraction by atoms in state $|\downarrow\rangle$. Again, this assumption is verified to be the case at the optimal cavity detuning and the average number of scattered photons, with the exception of the case where $N > 10^8$ and cavity finesse $F = 100$, as shown in Fig. 9.3 where several dB of deviations are possible due to this effect.

Next, we consider how collapse due to free space scattering reduces the coherence $\mathcal{C}$, specifically

$$\mathcal{C} = e^{-m_s(R_{\text{ray}}+R_{\text{ram}})}\,, \tag{9.5}$$

where the partial cancellation of wavefunction collapse due to indistinguishable Rayleigh scattering off of both $|\uparrow\rangle$ and $|\downarrow\rangle$ (see [139]) is accounted for by R_{ray}.

The term R_{ram} accounts for Raman scattering from $|\downarrow\rangle$ to $|3\rangle$.

$$R_{\text{ram}} = B_{3e'} r^2 \left(\frac{\delta_e}{\delta_{e'}}\right)^2 . \tag{9.6}$$

As before, we assume that Raman scattering to state $|3\rangle$ is equivalent to atom loss. Note also that $R_{\text{ram}} \leq B_{3e'} r^2$.

Equations (9.1) - (9.6) are used to numerically estimate the optimal spectroscopic enhancement $\xi^{-1}_{\text{m, opt}}$ shown versus atom number N in Fig. 9.3 for a range of technologically reasonable cavity finesses assuming our cavity geometry and perfect quantum efficiency $q = 1$. The optimization is done with respect to both m_s and the dressed cavity mode frequency ω_- (tuned by changing the bare cavity frequency). The mode frequency ω_- at the optimum is shown in Fig. 9.4. The loss of signal due to wavefunction collapse and scattering to $|3\rangle$ at the optimum is shown in Fig. 9.5.

At low atom number, the spectroscopic enhancement scales as $\xi^{-1}_{\text{m, opt}} \sim qNC$. At high atom number, the spectroscopic enhancement scales as $\xi^{-1}_{\text{m, opt}} \sim \sqrt{qNC}$. There is an intermediate region of atom number for which the spectroscopic enhancement is relatively flat versus atom number with $\xi^{-1}_{\text{m, opt}} \sim \omega_{\text{hf}}/\Gamma$. The physical origin of this plateau arises from the form of the critical detuning of Eq. (3.24).

In the good cavity limit, the scattering necessary to reach projection noise level sensitivity m_s^{proj} falls as $1/\delta_c^4$ for $\delta_c < \delta_c^\circ$, making it beneficial to operate with $|\omega_-| \sim \delta_c \geq \Gamma\sqrt{NC/q}$. However, the Raman transition probabilities $p_{\uparrow,3}$ continue to grow quadratically with the detuning, while detuning farther no longer rapidly reduces m_s^{proj}.

Assuming the critical detuning δ_c° is optimal for the reasons above, and in the limit of $|\omega_-| < \omega_{\text{hf}}$, the Raman transition probabilities scale as $p_{\uparrow,3} \sim (NC/q)(\Gamma/\omega_{\text{hf}})^2$, while $m_s^{\text{proj}} \sim 1/qNC$.

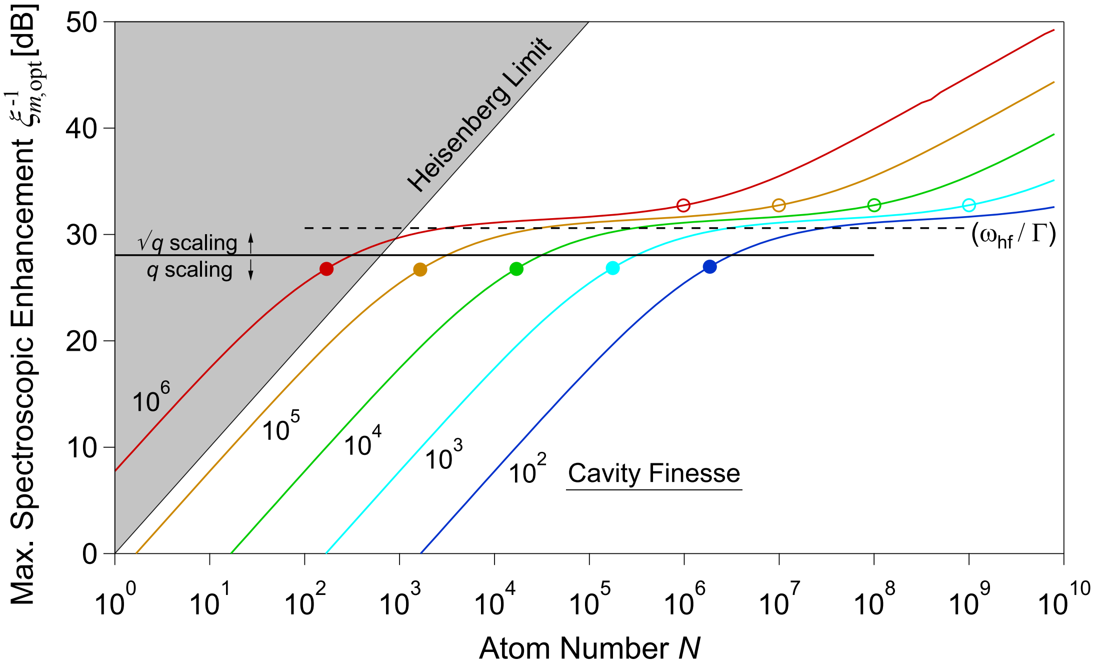

Figure 9.3: Theoretical optimal spectroscopic enhancement $\xi^{-1}_{\mathrm{m,\,opt}}$(solid curves) in dB relative to the SQL versus total ^{87}Rb atom number N for our current cavity geometry and probing near the D2 cycling transition as shown in Fig. 9.2. The optimization is performed for a range of technically realizable cavity finesses $F = 10^2, 10^3, 10^4, 10^5$, and 10^6 (blue, cyan, green, yellow, and red curves respectively) under the assumption of perfect quantum efficiency $q = 1$. Note the unphysical regime below the Heisenberg limit (disallowed grey region). A region of saturation of $\xi^{-1}_{\mathrm{m,\,opt}}$ versus N occurs near $\xi^{-1}_{\mathrm{m,\,opt}} \approx \omega_{\mathrm{hf}}/\Gamma$ shown by the labeled horizontal dashed line. The physical origin for the saturation region arises from competition between the scaling of the off-resonance Raman scattering probabilities and the dressed cavity mode broadening, as described in the text. The points of 3 dB deviation from NC scaling at low atom number (solid circles) and $\sqrt{NC}$ scaling at large atom number (open circles) occur when the solid curves cross $\xi^{-1}_{\mathrm{m,\,opt}} = 27$ dB and 33 dB, respectively. The approximate transition from q to $\sqrt{q}$ scaling occurs when the solid curves cross $\xi^{-1}_{\mathrm{m,\,opt}} = 28$ dB, the point at which the scaling is approximately $q^{3/4}$.

Optimizing the total noise in our estimate of J_z using Eq. (9.1) with respect to m_s reproduces the observed plateau value $\xi^{-1}_{\mathrm{m,\,opt}} \sim \omega_{\mathrm{hf}}/\Gamma \sim 10^3$. The plateau region is exited at low atom number when loss of signal, described by Eq. (9.5), dominates the reduction in spectroscopic enhancement, as illustrated by the loss of signal due to wavefunction collapse shown in Fig. 9.4. At high atom number, the plateau region is exited when the optimum mode frequency becomes large compared to the hyperfine splitting $|\omega_-| > \omega_{\mathrm{hf}}$, as shown in Fig. 9.5.

Importantly, this analysis shows that there is a range in which increasing either finesse or

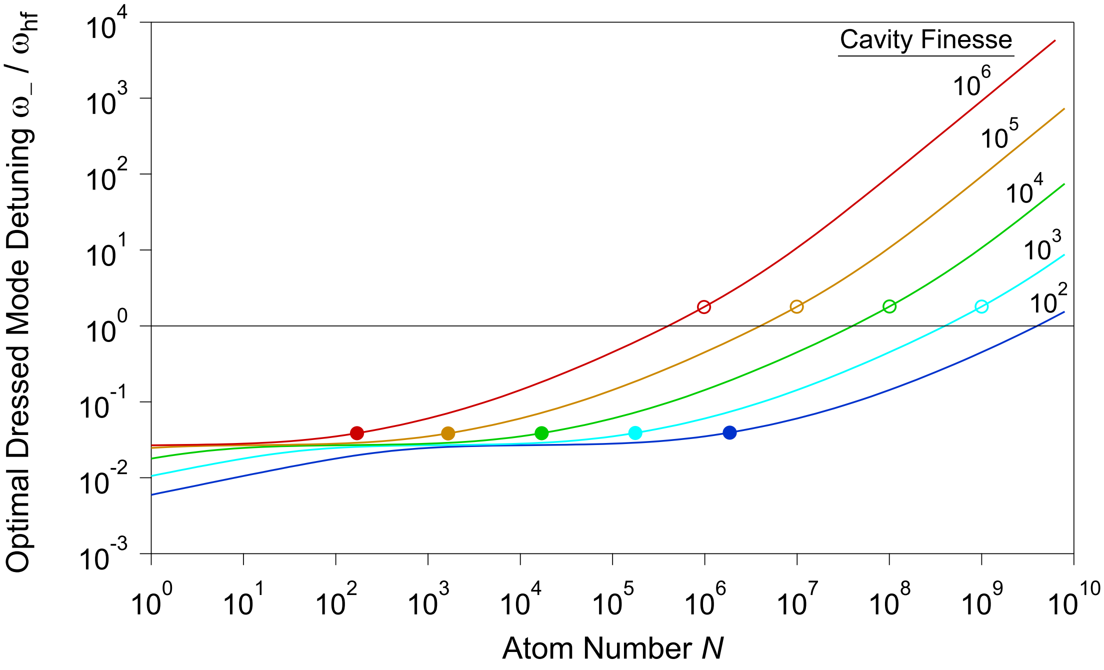

Figure 9.4: The dressed mode frequency ω_- that optimizes the spectroscopic enhancement ξ_{m}^{-1} for the conditions described in Fig. 9.3, where again the cavity finesses $F = 10^2, 10^3, 10^4, 10^5$, and 10^6 correspond to blue, cyan, green, yellow, and red curves, respectively. The open and closed circles indicate the locations of the 3 dB points in Fig. 9.3. The mode frequency is normalized to the hyperfine splitting $\omega_{\mathrm{hf}}/2\pi = 6.834$ GHz. Note that $\omega_- \approx \Gamma$ at $\omega_-/\omega_{\mathrm{hf}} \approx 10^{-3}$. Comparing to Fig. 9.3, one finds that the transition to spectroscopic enhancement scaling as $\xi_{\mathrm{m,\,opt}}^{-1} \propto \sqrt{qNC}$ occurs near $\omega_- \sim 1.8 \times \omega_{\mathrm{hf}}$. Above this point, the spin flip probabilities $p_{\uparrow,3}$ change little with ω_-.

atom number can have little effect on the optimal spectroscopic enhancement achieved. Also, note that the value of the plateau does not depend on the cavity geometry, and therefore represents a universal value that depends only on the atomic properties. One can also show that the range of atom number spanned by the plateau and the position of the first corner scales roughly as $N \sim w_0^2/F$, but does not depend on the cavity length l. Finally, for atom numbers below 10^3, it appears possible to both prepare and readout states near the Heisenberg limit using this approach and technologically feasible cavity finesses. Single atom measurement resolution for $N \lesssim 100$ was recently demonstrated using the approach described here [130].

Looking ahead at how the squeezed state might be of use, we note that the squeezing is generated on a magnetic field sensitive transition desirable for enhancing magnetometer precision

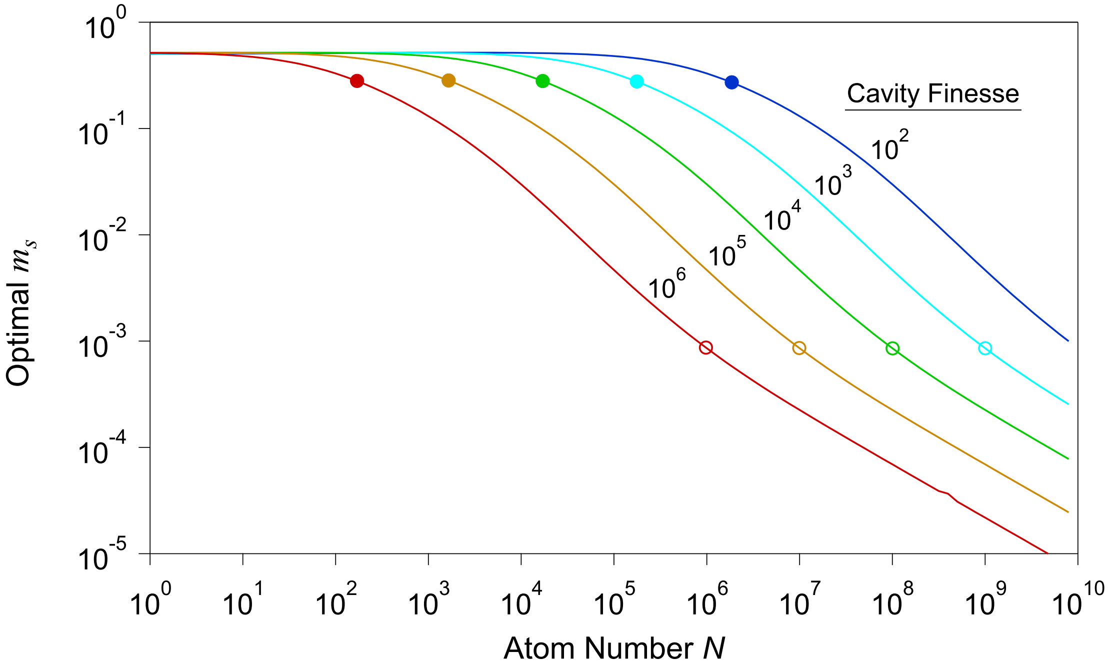

Figure 9.5: The scattering m_s that optimizes the spectroscopic enhancement ξ_{m}^{-1} shown in Fig. 9.3. Again, the cavity finesses $F = 10^2, 10^3, 10^4, 10^5$, and 10^6 correspond to the solid blue, cyan, green, yellow, and red curves, respectively. The open and closed circles indicate the locations of the 3 dB points in Fig. 9.3. Comparing to Fig. 9.3, one finds that the transition to spectroscopic enhancement scaling as $\xi_{\mathrm{m,\,opt}}^{-1} \propto qNC$ occurs when $m_s \approx 0.25$, indicating that at larger N, far off-resonance Raman scattering begins to create significant diffusion of J_z that limits the precision of the estimation of J_z as discussed in the main text.

and/or bandwidth. Looking from a different perspective, the squeezing could be generated using a favorable probing scheme such as the one presented here, and then mapped onto the clock states for precision time keeping via microwave and rf Rabi rotations or rapid adiabatic passage. Ramsey spectroscopy can then be performed on the squeezed clock states, and for low noise readout, the output of the Ramsey interferometer could be mapped back onto the same states squeezing was originally generated on. During the readout, the probe measurement strength can then be increased to provide very high resolution, performing essentially a non-demolition measurement as described in Fig. 2.7. Destroying coherence during the readout step does not affect the precision of the Ramsey interferometer.

9.4 Future Experimental Upgrades

In this section, I consider several improvements in the experimental setup that could be implemented in the next generation Science Cavity.

9.4.1 Improving Cavity Finesse

Having spent a lot of time with the current experimental apparatus whose crucial element — the Science Cavity — has been sealed up in UHV since summer 2008, I can point to many imperfections that have developed since its assembly in a pristine condition. My chief concern is with absorption/scattering losses on the mirrors, costing us a ∼50% loss in detection quantum efficiency. This loss impacts our ability to prepare measurement-induced spin squeezed states with more than 3 dB below the SQL. The squeezing we have generated is not yet limited by Raman spin flip diffusion, but by technical noise. Therefore, at fixed probe photon number and sufficiently far away from the technical noise that behaves almost like a vertical wall, the measurement imprecision would scale inversely to the detection quantum efficiency, just like in the cycling limit. Thus a loss of ∼50% would result in a reduction of ∼ 3 dB of spectroscopic enhancement. I will also mention that the UHV 45° folding mirror presents a 8% loss in detection efficiency in the cavity reflection path. The cause of this loss is unknown, although we hypothesize it could be due to rubidium coating the folding mirror due to its proximity to the rubidium reservoir source.

When the cavity was first assembled, its measured linewidth κ_{2008} was in good agreement with the predicted value $\kappa_0/2\pi = 5.29$ MHz from ATF's mirror transmission measurements. Over time, we noticed a gradual increase in linewidth of ∼1 MHz that can be recovered using 405 nm blue laser diodes to remove adsorbed rubidium on the mirrors surfaces via light-induced desorption. A catastrophic high voltage discharge near the silver epoxy connection between the bottom mirror PZT and the kapton wires in summer 2009 coated the mirrors with material that the blue laser light cannot remove, leading to an almost doubling of the linewidth to $\kappa_{2009}/2\pi = 9.2$ MHz. Since then, the linewidth has gradually crept up to a stable value of $\kappa/2\pi = 11.1(2)$ MHz. After the discharge, we measured a finite resistance between the PZT wires that is not stable, indicative of an intermittent connection or flaky short between the wires. We believe this is due to the kapton coating on the wires soaking up rubidium atoms, leading to a short where the supply and return voltage wires crossed. The short also limits our ability to scan the Science Cavity to a fraction of a FSR currently, although that can be mitigated with laser heating of the PZTs.

For the next generation Science Cavity, we could go up a factor of 10x to 100x in finesse to $F \sim 10^4$ to 10^5 to increase the single particle cooperativity, a key figure-of-merit in cavity-QED experiments. While a higher finesse cavity is more sensitive to losses, we are optimistic that preventive measures can be taken to to avoid degradation of the cavity finesse resulting in reduction in quantum efficiency. Careful assembly of the kapton wires such that they do not cross each other or touch the stainless steel vacuum chamber would prevent shorts. Using kapton dipped wires would also help. We should drive each PZT independently with its own UHV vacuum feedthrough so that in case one goes bad, we have a fallback. A 2D MOT source can be installed to deliver a high flux and collimated beam of cold atoms to the cavity instead of enveloping the whole cavity with rubidium vapor as is currently the case. Heater coils can be installed around the mirrors to drive off rubidium vapor on the mirror surfaces, an approach successfully used in Ref. [194].

9.4.2 Single-ended Cavity to Improve Detection Efficiency

To simplify the detection, a single-ended cavity with the transmissive end 10x to 100x more transmissive than the highly reflective end would be highly desirable so that there is nominally only one detection port (unless we find a good reason to detect the cavity transmission also). We can also perform homodyne detection of the cavity-probe sideband, winning back the 3 dB of signal-to-noise lost in heterodyne detection. We can do so by stabilizing the phase of the interferometer in reflection (described in Chap. 5) with a strong phase-reference sideband ($\sim \mu$W) detected in heterodyne with a very strong reference beam ($\sim$mW to be shot noise limited) that is frequency degenerate with the weak cavity-probe sideband ($\sim$nW). Using the detected phase-reference sideband phase as the error signal, feedback can be applied to the phase of the probe laser beam that carriers both the phase-reference and cavity-probe sidebands. By choosing the carrier phase value to lock to, we can perform homodyne detection of the cavity-probe sideband in the phase quadrature.

9.4.3 Uniform Coupling of Cavity Mode to Atoms

To generate spin squeezed states that can be launched into free space for interferometry such as in a fountain clock or in an atom interferometer requires uniform coupling of the cavity mode to the atoms. There are two ways to obtain uniform coupling — ring cavity or commensurate lattice. In a ring cavity, the cavity mode is a running wave, unlike the standing wave in a Fabry-Perot cavity. By trapping atoms in a small region near the center of the cavity, fairly uniform coupling can be achieved. In a ring cavity, however, the two polarization modes of the cavity typically have different finesses and free spectral ranges due to unequal *s*- and *p*-reflection coefficients (both amplitude and phase). At high finesse, orthogonal polarization modes may be split, impacting one's ability to address both polarization modes simultaneously. In a commensurate lattice, one utilizes a lattice at 2x the probe wavelength such that the antinode of the lattice lines up with every other antinode of the probe mode. Since the atoms are tightly confined in each pancake, good uniform coupling may be achieved. To be consistent with mirror boundary conditions, the commensurate lattice and probe mode starts out in phase in the middle of the cavity and acquires a relative phase slip of $\lambda/2$ by the time they reach the mirrors. Provided the axial extent of the atomic ensemble is much shorter than the cavity length, so the atoms do not see the phase slip, uniform coupling can be achieved.

9.4.4 Removing 17 Hz Vibration Noise Source

An annoying vibration at 17 Hz of the Science Cavity relative to the optics table causes the mode-matching to the cavity to change on timescales of 60 ms. Up and down motion of $\sim 2\lambda_{795}$ peak-to-peak imposes phase noise in the reflected light, which we removed using carrier phase stabilization in Chapter 5. Another effect is the changing of the coupling to the cavity mode due to sideways motion of the cavity at 17 Hz. The effect is mitigated by optimizing the coupling to the cavity mode in the transverse directions so that any offset in the transverse plane affects the transmitted lattice and probe power only to second order. We find a $1-2\%$ peak-to-peak fluctuation in the reflected probe power when mode matching is optimized. The source of the 17 Hz is the AC unit attached to the ceiling of the lab below our lab. Thus our lab floor as well as the non-floating optics table is vibrating at 17 Hz. The cavity, being vibrationally isolated, stays relatively fixed with respect to the local inertial frame defined by the earth. We could float our optical table or modify the vibration isolation. We can replace the viton rubber balls used in the first and lowest frequency stage of vibration isolation with steel ball bearings to transmit the 17 Hz to the cavity while still leaving the second and third stage for high frequency vibration isolation, so there is no differential motion between the optics table and the cavity at low frequencies. While the 17 Hz can affect the cavity resonance frequency via differential acceleration of the top and bottom mirrors, the feedback loop has plenty of gain at the low frequency of 17 Hz compared to the unity gain frequency of ~2 kHz to squash that noise down.

9.5 Summary and Conclusions

We have demonstrated the preparation of conditionally spin squeezed states with 3.4(6) dB spectroscopic enhancement beyond the standard quantum limit. The degree of squeezing achieved in our experiment is currently limited by technical noise associated with the frequency chirping of the Rabi splitting resonances. This technical noise variance, scaling as $\sim M_m^6$ has an extremely unfavorable scaling with the probe photon number M_m.

In the future, our method can be extended to achieve greater violations of the SQL or equivalently obtaining larger amounts of squeezing by reducing the chirping of the resonances via probing on an optical cycling transition. Squeezing via probing on an optical cycling transition with the pseudo spin-1/2 system comprised of the stretched hyperfine ground states of ^{87}Rb is a promising path to achieving more squeezing. By probing on an optical cycling transition, Raman spin-flips that would fundamentally limit squeezing on the clock transition in the scheme presented in this thesis would be greatly suppressed. We also expect that technical noise associated with the frequency chirping of the dressed cavity mode resonance due to probe-induced Raman scattering would be greatly reduced, improving our measurement precision.

Furthermore, many experimental aspects, such as cavity finesse and length, can be easily improved. Running wave cavities or commensurate optical lattices can be employed to create squeezed states appropriate for launching ensembles into free space for matter wave interferometry. It will also be interesting to understand and explore how this system might be applied to probe and manipulate quantum many-body entangled states of large atomic ensembles [195].

Bibliography

[1] A. Einstein, B. Podolsky, and N. Rosen, “Can quantum-mechanical description of physical reality be considered complete?”, Phys. Rev. **47**, 777 (1935) (see p. 1).

[2] N. Gisin, G. Ribordy, W. Tittel, and H. Zbinden, “Quantum cryptography”, Rev. Mod. Phys. **74**, 145 (2002) (see p. 1).

[3] M. A. Nielsen and I. L. Chuang, Quantum computation and quantum information (Cambridge University Press, 2000) (see pp. 1, 123).

[4] J. I. Cirac and P. Zoller, “Goals and opportunities in quantum simulation”, Nature Physics **8**, 264 (2012) (see p. 1).

[5] V. Giovannetti, S. Lloyd, and L. Maccone, “Quantum-enhanced measurements: beating the standard quantum limit.”, Science **306**, 1330 (2004) (see pp. 1, 5).

[6] A. K. Ekert, “Quantum cryptography based on bell’s theorem”, Phys. Rev. Lett. **67**, 661 (1991) (see p. 1).

[7] P. W. Shor, “Polynomial-time algorithms for prime factorization and discrete logarithms on a quantum computer”, SIAM J. on Computing **26**, 1484 (1997) (see p. 1).

[8] I. Bloch, J. Dalibard, and S. Nascimbène, “Quantum simulations with ultracold quantum gases”, Nature Physics **8**, 267 (2012) (see p. 2).

[9] R. Blatt and C. F. Roos, “Quantum simulations with trapped ions”, Nature Physics **8**, 277 (2012) (see p. 2).

[10] J. W. Britton, B. C. Sawyer, A. C. Keith, C.-C. J. Wang, J. K. Freericks, H. Uys, M. J. Biercuk, and J. J. Bollinger, “Engineered two-dimensional Ising interactions in a trapped-ion quantum simulator with hundreds of spins.”, Nature **484**, 489 (2012) (see p. 2).

[11] R Islam, C Senko, W. C. Campbell, S Korenblit, J Smith, A Lee, E. E. Edwards, C.-C. J. Wang, J. K. Freericks, and C Monroe, “Emergence and frustration of magnetism with variable-range interactions in a quantum simulator.”, Science **340**, 583 (2013) (see p. 2).

[12] Z. Chen, J. G. Bohnet, S. R. Sankar, J. Dai, and J. K. Thompson, “Conditional Spin Squeezing of a Large Ensemble via the Vacuum Rabi Splitting”, Phys. Rev. Lett. **106**, 133601 (2011) (see pp. 2, 4, 9, 25, 32, 65).

[13] J. Kitching, S. Knappe, and E. A. Donley, “Atomic Sensors A Review”, IEEE Sensors Journal **11**, 1749 (2011) (see p. 5).

[14] T. P. Heavner, S. R. Jefferts, E. A. Donley, J. H. Shirley, and T. E. Parker, “Nist-F1: recent improvements and accuracy evaluations”, Metrologia **42**, 411 (2005) (see pp. 5, 21, 145).

[15] A. D. Ludlow, T. Zelevinsky, G. K. Campbell, S. Blatt, M. M. Boyd, M. H. G. de Miranda, M. J. Martin, J. W. Thomsen, S. M. Foreman, J. Ye, T. M. Fortier, J. E. Stalnaker, S. A. Diddams, Y. Le Coq, Z. W. Barber, N. Poli, N. D. Lemke, K. M. Beck, and C. W. Oates, "Sr Lattice Clock at 1 x 10^{-16} Fractional Uncertainty by Remote Optical Evaluation with a Ca Clock", Science **319**, 1805 (2008) (see pp. 5, 145).

[16] H. Katori, "Optical lattice clocks and quantum metrology", Nature Photonics **5**, 203 (2011) (see pp. 5, 21, 145).

[17] C. W. Chou, D. B. Hume, J. C. J. Koelemeij, D. J. Wineland, and T. Rosenband, "Frequency Comparison of Two High-Accuracy Al^+ Optical Clocks", Phys. Rev. Lett. **104**, 070802 (2010) (see pp. 5, 21).

[18] T. L. Nicholson, M. J. Martin, J. R. Williams, B. J. Bloom, M. Bishof, M. D. Swallows, S. L. Campbell, and J. Ye, "Comparison of Two Independent Sr Optical Clocks with 1 x 10^{-17} Stability at 10^3 s", Phys. Rev. Lett. **109**, 230801 (2012) (see pp. 5, 21, 145).

[19] T. L. Gustavson, P. Bouyer, and M. A. Kasevich, "Precision rotation measurements with an atom interferometer gyroscope", Phys. Rev. Lett. **78**, 2046 (1997) (see pp. 5, 21, 145).

[20] A Peters, K. Y. Chung, and S Chu, "High-precision gravity measurements using atom interferometry", Metrologia **38**, 25 (2001) (see pp. 5, 21).

[21] J. McGuirk, G. Foster, J. Fixler, M. Snadden, and M. Kasevich, "Sensitive absolute-gravity gradiometry using atom interferometry", Physical Review A **65**, 033608 (2002) (see p. 5).

[22] R Geiger, V Ménoret, G Stern, N Zahzam, P Cheinet, B Battelier, a Villing, F Moron, M Lours, Y Bidel, a Bresson, a Landragin, and P Bouyer, "Detecting inertial effects with airborne matter-wave interferometry.", Nature communications **2**, 474 (2011) (see p. 5).

[23] D. Budker and M. Romalis, "Optical magnetometry", Nature Physics **3**, 227 (2007) (see pp. 5, 21, 145).

[24] G. Lamporesi, A. Bertoldi, L. Cacciapuoti, M. Prevedelli, and G. M. Tino, "Determination of the newtonian gravitational constant using atom interferometry", Phys. Rev. Lett. **100**, 050801 (2008) (see pp. 5, 21).

[25] J. M. Hogan, D. M. S. Johnson, and M. A. Kasevich, "Light-pulse atom interferometry", arXiv:0806.3261, 38 (2008) (see p. 5).

[26] M. A. Hohensee, S. Chu, A. Peters, and H. Müller, "Equivalence principle and gravitational redshift", Phys. Rev. Lett. **106**, 151102 (2011) (see p. 5).

[27] Bouchendira, Rym and Cladé, Pierre and Guellati-Khélifa, Saïda and Nez, François and Biraben, François, "New determination of the fine structure constant and test of the quantum electrodynamics", Phys. Rev. Lett. **106**, 080801 (2011) (see pp. 5, 145).

[28] C. Orzel, "Searching for new physics through atomic, molecular and optical precision measurements", Physica Scripta **86**, 068101 (2012) (see p. 5).

[29] G. Santarelli, P. Laurent, P. Lemonde, A. Clairon, A. G. Mann, S. Chang, A. N. Luiten, and C. Salomon, "Quantum projection noise in an atomic fountain: a high stability cesium frequency standard", Phys. Rev. Lett. **82**, 4619 (1999) (see pp. 5, 21).

[30] C. M. Caves, "Quantum-mechanical noise in an interferometer", Phys. Rev. D **23**, 1693 (1981) (see p. 6).

[31] K. W. Murch, K. L. Moore, S. Gupta, and D. M. Stamper-Kurn, "Observation of quantum-measurement backaction with an ultracold atomic gas", Nature Physics **4**, 561 (2008) (see pp. 6, 54).

[32] T. P. Purdy, R. W. Peterson, and C. a. Regal, "Observation of radiation pressure shot noise on a macroscopic object.", Science **339**, 801 (2013) (see pp. 6, 54).

[33] T. Eberle, S. Steinlechner, J. Bauchrowitz, V. Händchen, H. Vahlbruch, M. Mehmet, H. Müller-Ebhardt, and R. Schnabel, "Quantum Enhancement of the Zero-Area Sagnac Interferometer Topology for Gravitational Wave Detection", Physical Review Letters **104**, 251102 (2010) (see p. 6).

[34] R. Schnabel, N. Mavalvala, D. E. McClelland, and P. K. Lam, "Quantum metrology for gravitational wave astronomy.", Nature communications **1**, 121 (2010) (see p. 6).

[35] J. Abadie et al., "A gravitational wave observatory operating beyond the quantum shot-noise limit", Nature Physics **7**, 962 (2011) (see p. 6).

[36] G. K. Campbell, M. M. Boyd, J. W. Thomsen, M. J. Martin, S Blatt, M. D. Swallows, T. L. Nicholson, T Fortier, C. W. Oates, S. A. Diddams, N. D. Lemke, P Naidon, P Julienne, J. Ye, and A. D. Ludlow, "Probing interactions between ultracold fermions.", Science **324**, 360 (2009) (see p. 6).

[37] A. André, A. S. Sørensen, and M. D. Lukin, "Stability of atomic clocks based on entangled atoms", Phys. Rev. Lett. **92**, 230801 (2004) (see pp. 6, 148, 149).

[38] M. Auzinsh, D. Budker, D. F. Kimball, S. M. Rochester, J. E. Stalnaker, A. O. Sushkov, and V. V. Yashchuk, "Can a quantum nondemolition measurement improve the sensitivity of an atomic magnetometer?", Phys. Rev. Lett. **93**, 173002 (2004) (see pp. 6, 31, 32, 145, 149).

[39] J. S. Bell, "On the problem of hidden variables in quantum mechanics", Rev. Mod. Phys. **38**, 447 (1966) (see p. 6).

[40] J. F. Clauser, M. A. Horne, A. Shimony, and R. A. Holt, "Proposed experiment to test local hidden-variable theories", Phys. Rev. Lett. **23**, 880 (1969) (see p. 6).

[41] S. J. Freedman and J. F. Clauser, "Experimental test of local hidden-variable theories", Phys. Rev. Lett. **28**, 938 (1972) (see p. 6).

[42] M. Arndt, M. Aspelmeyer, and A. Zeilinger, "How to extend quantum experiments", Fortschritte der Physik **57**, 1153 (2009) (see p. 6).

[43] S. Nimmrichter, K. Hornberger, P. Haslinger, and M. Arndt, "Testing spontaneous localization theories with matter-wave interferometry", Phys. Rev. A **83**, 043621 (2011) (see p. 6).

[44] R. Kaltenbaek, G. Hechenblaikner, N. Kiesel, O. Romero-Isart, K. C. Schwab, U. Johann, and M. Aspelmeyer, "Macroscopic quantum resonators (MAQRO)", Experimental Astronomy **34**, 123 (2012) (see p. 6).

[45] L. Diósi, "Models for universal reduction of macroscopic quantum fluctuations", Physical Review A **40**, 1165 (1989) (see p. 6).

[46] R. Penrose, "On Gravity's role in Quantum State Reduction", General Relativity and Gravitation **28**, 581 (1996) (see p. 6).

[47] A. Bassi, K. Lochan, S. Satin, T. P. Singh, and H. Ulbricht, “Models of wave-function collapse, underlying theories, and experimental tests”, Rev. Mod. Phys. **85**, 471 (2013) (see p. 6).

[48] J. G. Bohnet, Z. Chen, J. M. Weiner, D. Meiser, M. J. Holland, and J. K. Thompson, “A steady-state superradiant laser with less than one intracavity photon”, Nature **484**, 78 (2012) (see p. 7).

[49] D. Meiser, J. Ye, D. R. Carlson, and M. J. Holland, “Prospects for a Millihertz-Linewidth Laser”, Physical Review Letters **163601**, 163601 (2009) (see pp. 7, 8).

[50] T. M. Fortier, Y. Le Coq, J. E. Stalnaker, D. Ortega, S. A. Diddams, C. W. Oates, and L. Hollberg, “Kilohertz-resolution spectroscopy of cold atoms with an optical frequency comb”, Phys. Rev. Lett. **97**, 163905 (2006) (see p. 7).

[51] J. G. Bohnet, Z. Chen, J. M. Weiner, K. C. Cox, and J. K. Thompson, “Dynamically controlled superradiant laser for hybrid sensing of collective atomic coherence”, arXiv:1208.1710 (2012) (see p. 8).

[52] J. M. Weiner, K. C. Cox, J. G. Bohnet, Z. Chen, and J. K. Thompson, “Superradiant Raman laser magnetometer”, Applied Physics Letters **101**, 261107 (2012) (see p. 8).

[53] J. G. Bohnet, Z. Chen, J. Weiner, K. Cox, and J. Thompson, “Relaxation Oscillations, Stability, and Cavity Feedback in a Superradiant Raman Laser”, Physical Review Letters **109**, 253602 (2012) (see p. 8).

[54] Z. Chen, J. G. Bohnet, J. M. Weiner, K. C. Cox, and J. K. Thompson, “Cavity-aided non-demolition measurements for atom counting and spin squeezing”, arXiv:1211.0723, 26 (2012) (see pp. 8, 9).

[55] Z. Chen, J. G. Bohnet, J. M. Weiner, and J. K. Thompson, “A low phase noise microwave source for atomic spin squeezing experiments in 87Rb”, Rev. Sci. Instrum. **83**, 044701 (2012) (see pp. 9, 104, 108).

[56] Z. Chen, J. G. Bohnet, J. M. Weiner, and J. K. Thompson, “General formalism for evaluating the impact of phase noise on bloch vector rotations”, Phys. Rev. A **86**, 032313 (2012) (see pp. 9, 123).

[57] D. J. Wineland, J. J. Bollinger, W. M. Itano, F. L. Moore, and D. J. Heinzen, “Spin squeezing and reduced quantum noise in spectroscopy”, Phys. Rev. A **46**, R6797 (1992) (see pp. 10, 18, 111).

[58] D. J. Wineland, J. J. Bollinger, W. M. Itano, and D. J. Heinzen, “Squeezed atomic states and projection noise in spectroscopy”, Phys. Rev. A **50**, 67 (1994) (see pp. 10, 13, 18, 90, 111).

[59] J. Ma, X. Wang, C. P. Sun, and F. Nori, “Quantum spin squeezing”, Physics Reports **509**, 89 (2011) (see pp. 10, 17).

[60] T. J. Kippenberg and K. J. Vahala, “Cavity optomechanics: back-action at the mesoscale.”, Science **321**, 1172 (2008) (see p. 14).

[61] K. Mølmer and A. Sørensen, “Multiparticle entanglement of hot trapped ions”, Phys. Rev. Lett. **82**, 1835 (1999) (see pp. 16, 20, 27).

[62] C. A. Sackett, D Kielpinski, B. E. King, C Langer, V Meyer, C. J. Myatt, M Rowe, Q. A. Turchette, W. M. Itano, D. J. Wineland, and C Monroe, “Experimental entanglement of four particles”, Nature **404**, 256 (2000) (see pp. 16, 27, 145).

[63] V. Meyer, M. A. Rowe, D. Kielpinski, C. A. Sackett, W. M. Itano, C. Monroe, and D. J. Wineland, “Experimental demonstration of entanglement-enhanced rotation angle estimation using trapped ions”, Phys. Rev. Lett. **86**, 5870 (2001) (see pp. 16, 27, 145).

[64] D. Leibfried, M. D. Barrett, T. Schaetz, J. Britton, J. Chiaverini, W. M. Itano, J. D. Jost, C. Langer, and D. J. Wineland, “Toward Heisenberg-limited spectroscopy with multiparticle entangled states”, Science **304**, 1476 (2004) (see pp. 16, 27, 145).

[65] D Leibfried, E Knill, S Seidelin, J Britton, R. B. Blakestad, J Chiaverini, D. B. Hume, W. M. Itano, J. D. Jost, C Langer, R Ozeri, R Reichle, and D. J. Wineland, “Creation of a six-atom ’Schrödinger cat’ state.”, Nature **438**, 639 (2005) (see pp. 16, 27).

[66] T. Monz, P. Schindler, J. T. Barreiro, M. Chwalla, D. Nigg, W. A. Coish, M. Harlander, W. Hänsel, M. Hennrich, and R. Blatt, “14-qubit entanglement: creation and coherence”, Phys. Rev. Lett. **106**, 130506 (2011) (see pp. 16, 27, 145, 148).

[67] A. Noguchi, K. Toyoda, and S. Urabe, “Generation of Dicke States with Phonon-Mediated Multilevel Stimulated Raman Adiabatic Passage”, Physical Review Letters **109**, 260502 (2012) (see pp. 16, 27, 145).

[68] A Sørensen, L. M. Duan, J. I. Cirac, and P. Zoller, “Many-particle entanglement with Bose-Einstein condensates.”, Nature **409**, 63 (2001) (see pp. 18, 19, 90).

[69] M. Kitagawa and M. Ueda, “Squeezed spin states”, Phys. Rev. A **47**, 5138 (1993) (see pp. 18, 19).

[70] R. H. Dicke, “Coherence in spontaneous radiation processes”, Phys. Rev. **93**, 99 (1954) (see pp. 19, 124).

[71] A. Rey, L. Jiang, M. Fleischhauer, E. Demler, and M. Lukin, “Many-body protected entanglement generation in interacting spin systems”, Physical Review A **77**, 052305 (2008) (see p. 20).

[72] J Estève, C Gross, A Weller, S Giovanazzi, and M. K. Oberthaler, “Squeezing and entanglement in a Bose-Einstein condensate.”, Nature **455**, 1216 (2008) (see pp. 20, 145, 146).

[73] C Gross, T Zibold, E Nicklas, J Estève, and M. K. Oberthaler, “Nonlinear atom interferometer surpasses classical precision limit.”, Nature **464**, 1165 (2010) (see pp. 20, 26, 123, 146, 147).

[74] M. F. Riedel, P. Böhi, Y. Li, T. W. Hänsch, A. Sinatra, and P. Treutlein, “Atom-chip-based generation of entanglement for quantum metrology.”, Nature **464**, 1170 (2010) (see pp. 20, 26, 123, 146).

[75] C. F. Ockeloen, R. Schmied, M. F. Riedel, and P. Treutlein, “Quantum metrology with a scanning probe atom interferometer”, arXiv:1303.1313 (2013) (see pp. 20, 146, 147).

[76] T. Berrada, S. van Frank, R. Bücker, T. Schumm, J.-F. Schaff, and J. Schmiedmayer, “Integrated Mach-Zehnder interferometer for Bose-Einstein condensates”, arXiv:1303.1030, 14 (2013) (see pp. 20, 26, 145–147).

[77] M. J. Martin, M. Bishof, M. D. Swallows, X. Zhang, C. Benko, J. von Stecher, A. V. Gorshkov, A. M. Rey, and J. Ye, “A quantum many-body spin system in an optical lattice clock”, Science **341**, 632 (2013) (see p. 20).

[78] M. J. Holland and K. Burnett, “Interferometric detection of optical phase shifts at the heisenberg limit”, Phys. Rev. Lett. **71**, 1355 (1993) (see pp. 20, 60).

[79] T. Kim, O. Pfister, M. J. Holland, J. Noh, and J. L. Hall, "Influence of decorrelation on heisenberg-limited interferometry with quantum correlated photons", Phys. Rev. A **57**, 4004 (1998) (see p. 20).

[80] B Lücke, M Scherer, J Kruse, L Pezzé, F Deuretzbacher, P Hyllus, O Topic, J Peise, W Ertmer, J Arlt, L Santos, A Smerzi, and C Klempt, "Twin matter waves for interferometry beyond the classical limit.", Science **334**, 773 (2011) (see pp. 20, 145, 146).

[81] R. Bücker, J. Grond, S. Manz, T. Berrada, T. Betz, C. Koller, U. Hohenester, T. Schumm, A. Perrin, and J. Schmiedmayer, "Twin-atom beams", Nature Physics **7**, 608 (2011) (see pp. 20, 146).

[82] C. D. Hamley, C. S. Gerving, T. M. Hoang, E. M. Bookjans, and M. S. Chapman, "Spin-nematic squeezed vacuum in a quantum gas", Nature Phys. **8**, 305 (2012) (see pp. 20, 123, 146).

[83] C Gross, H Strobel, E Nicklas, T Zibold, N Bar-Gill, G Kurizki, and M. K. Oberthaler, "Atomic homodyne detection of continuous-variable entangled twin-atom states.", Nature **480**, 219 (2011) (see pp. 20, 145, 146).

[84] J. Fortágh and C. Zimmermann, "Magnetic microtraps for ultracold atoms", Rev. Mod. Phys. **79**, 235 (2007) (see p. 21).

[85] J. Reichel and V. Vuletić, eds., Atom chips (Wiley-VCH, 2011) (see p. 21).

[86] H. Müller, S.-w. Chiow, S. Herrmann, S. Chu, and K.-Y. Chung, "Atom-interferometry tests of the isotropy of post-newtonian gravity", Phys. Rev. Lett. **100**, 031101 (2008) (see p. 21).

[87] A. D. Cronin, J. Schmiedmayer, and D. E. Pritchard, "Optics and interferometry with atoms and molecules", Rev. Mod. Phys. **81**, 1051 (2009) (see pp. 21, 145).

[88] D. Sheng, S. Li, N. Dural, and M. V. Romalis, "Subfemtotesla scalar atomic magnetometry using multipass cells", Phys. Rev. Lett. **110**, 160802 (2013) (see pp. 21, 145).

[89] I. D. Leroux, M. H. Schleier-Smith, and V. Vuletić, "Implementation of cavity squeezing of a collective atomic spin", Phys. Rev. Lett. **104**, 073602 (2010) (see pp. 23, 123).

[90] M. H. Schleier-Smith, I. D. Leroux, and V. Vuletić, "Squeezing the collective spin of a dilute atomic ensemble by cavity feedback", Phys. Rev. A **81**, 021804 (2010) (see p. 23).

[91] I. D. Leroux, M. H. Schleier-Smith, H. Zhang, and V. Vuletić, "Unitary cavity spin squeezing by quantum erasure", Phys. Rev. A **85**, 013803 (2012) (see p. 23).

[92] M. Takeuchi, S. Ichihara, T. Takano, M. Kumakura, T. Yabuzaki, and Y. Takahashi, "Spin squeezing via one-axis twisting with coherent light", Phys. Rev. Lett. **94**, 023003 (2005) (see p. 23).

[93] C. M. Trail, P. S. Jessen, and I. H. Deutsch, "Strongly enhanced spin squeezing via quantum control", Phys. Rev. Lett. **105**, 193602 (2010) (see pp. 23, 32).

[94] S. Chaudhury, S. Merkel, T. Herr, A. Silberfarb, I. H. Deutsch, and P. S. Jessen, "Quantum control of the hyperfine spin of a cs atom ensemble", Phys. Rev. Lett. **99**, 163002 (2007) (see p. 23).

[95] T. Fernholz, H. Krauter, K. Jensen, J. F. Sherson, A. S. Sørensen, and E. S. Polzik, "Spin squeezing of atomic ensembles via nuclear-electronic spin entanglement", Phys. Rev. Lett. **101**, 073601 (2008) (see p. 23).

[96] A. Kuzmich, N. P. Bigelow, and L. Mandel, “Atomic quantum non-demolition measurements and squeezing”, Europhys. Lett. **42**, 481 (1998) (see pp. 23, 32).

[97] L. B. Madsen and K. Mølmer, “Spin squeezing and precision probing with light and samples of atoms in the gaussian description”, Phys. Rev. A **70**, 052324 (2004) (see pp. 23, 32).

[98] A. E. B. Nielsen and K. Mølmer, “Atomic spin squeezing in an optical cavity”, Phys. Rev. A **77**, 063811 (2008) (see pp. 23, 32).

[99] J. Appel, P. J. Windpassinger, D. Oblak, U. B. Hoff, N. Kjrgaard, and E. S. Polzik, “Mesoscopic atomic entanglement for precision measurements beyond the standard quantum limit”, Proc. Nat. Acad. Sci. **106**, 10960 (2009) (see pp. 25, 32).

[100] M. H. Schleier-Smith, I. D. Leroux, and V. Vuletić, “States of an ensemble of two-level atoms with reduced quantum uncertainty”, Phys. Rev. Lett. **104**, 073604 (2010) (see pp. 25, 32, 84, 90, 91, 193, 196).

[101] R. J. Sewell, M. Koschorreck, M. Napolitano, B. Dubost, N. Behbood, and M. W. Mitchell, “Magnetic sensitivity beyond the projection noise limit by spin squeezing”, Phys. Rev. Lett. **109**, 253605 (2012) (see p. 26).

[102] W. Wasilewski, K. Jensen, H. Krauter, J. J. Renema, M. V. Balabas, and E. S. Polzik, “Quantum noise limited and entanglement-assisted magnetometry”, Phys. Rev. Lett. **104**, 133601 (2010) (see pp. 26, 32, 145, 149).

[103] A. Kuzmich, L. Mandel, and N. P. Bigelow, “Generation of spin squeezing via continuous quantum nondemolition measurement”, Phys. Rev. Lett. **85**, 1594 (2000) (see pp. 26, 32).

[104] T. Takano, M. Fuyama, R. Namiki, and Y. Takahashi, “Spin squeezing of a cold atomic ensemble with the nuclear spin of one-half”, Phys. Rev. Lett. **102**, 033601 (2009) (see p. 26).

[105] T. Takano, S.-I.-R. Tanaka, R. Namiki, and Y. Takahashi, “Manipulation of nonclassical atomic spin states”, Phys. Rev. Lett. **104**, 013602 (2010) (see p. 26).

[106] R. Inoue, S.-i.-r. Tanaka, R. Namiki, T. Sagawa, and Y. Takahashi, “Unconditional Quantum-Noise Suppression via Measurement-Based Quantum Feedback”, Phys. Rev. Lett. **110**, 163602 (2013) (see p. 26).

[107] I. Teper, G. Vrijsen, J. Lee, and M. A. Kasevich, “Backaction noise produced via cavity-aided nondemolition measurement of an atomic clock state”, Phys. Rev. A **78**, 051803 (2008) (see pp. 26, 32).

[108] D Meiser, J. Ye, and M. J. Holland, “Spin squeezing in optical lattice clocks via lattice-based qnd measurements”, New Journal of Physics **10**, 073014 (2008) (see p. 26).

[109] G.-B. Jo, J.-H. Choi, C. A. Christensen, T. A. Pasquini, Y.-R. Lee, W. Ketterle, and D. E. Pritchard, “Phase-sensitive recombination of two bose-einstein condensates on an atom chip”, Phys. Rev. Lett. **98**, 180401 (2007) (see p. 26).

[110] L. M. Norris, C. M. Trail, P. S. Jessen, and I. H. Deutsch, “Enhanced squeezing of a collective spin via control of its qudit subsystems”, Phys. Rev. Lett. **109**, 173603 (2012) (see p. 27).

[111] Y. Zhu, D. J. Gauthier, S. E. Morin, Q. Wu, H. J. Carmichael, and T. W. Mossberg, “Vacuum Rabi splitting as a feature of linear-dispersion theory: Analysis and experimental observations”, Phys. Rev. Lett. **64**, 2499 (1990) (see pp. 29, 30, 38, 93).

[112] L. K. Thomsen, S Mancini, and H. M. Wiseman, “Continuous quantum nondemolition feedback and unconditional atomic spin squeezing”, J. Phys. B: At. Mo. Opt. Phys. **35**, 4937 (2002) (see p. 32).

[113] J. Geremia, J. K. Stockton, A. C. Doherty, and H. Mabuchi, “Quantum kalman filtering and the heisenberg limit in atomic magnetometry”, Phys. Rev. Lett. **91**, 250801 (2003) (see p. 32).

[114] K. Mølmer and L. B. Madsen, “Estimation of a classical parameter with gaussian probes: magnetometry with collective atomic spins”, Phys. Rev. A **70**, 052102 (2004) (see p. 32).

[115] A. Kuzmich and T. A. B. Kennedy, “Nonsymmetric entanglement of atomic ensembles”, Phys. Rev. Lett. **92**, 030407 (2004) (see p. 32).

[116] J. J. Hope and J. D. Close, “Limit to minimally destructive optical detection of atoms”, Phys. Rev. Lett. **93**, 180402 (2004) (see p. 32).

[117] J. K. Stockton, R. van Handel, and H. Mabuchi, “Deterministic dicke-state preparation with continuous measurement and control”, Phys. Rev. A **70**, 022106 (2004) (see p. 32).

[118] J. J. Hope and J. D. Close, “General limit to nondestructive optical detection of atoms”, Phys. Rev. A **71**, 043822 (2005) (see p. 32).

[119] S. R. de Echaniz, M. W. Mitchell, M. Kubasik, M. Koschorreck, H. Crepaz, J. Eschner, and E. S. Polzik, “Conditions for spin squeezing in a cold 87 rb ensemble”, J. Opt. B: Quantum Semiclass. Opt. **7**, S548 (2005) (see p. 32).

[120] A. Kuzmich, L. Mandel, J. Janis, Y. E. Young, R. Ejnisman, and N. P. Bigelow, “Quantum nondemolition measurements of collective atomic spin”, Phys. Rev. A **60**, 2346 (1999) (see p. 32).

[121] S. Chaudhury, G. A. Smith, K. Schulz, and P. S. Jessen, “Continuous nondemolition measurement of the cs clock transition pseudospin”, Phys. Rev. Lett. **96**, 043001 (2006) (see p. 32).

[122] P. J. Windpassinger, D. Oblak, U. B. Hoff, J. Appel, N. Kjrgaard, and E. S. Polzik, “Inhomogeneous light shift effects on atomic quantum state evolution in non-destructive measurements”, New J. Phys. **10**, 053032 (2008) (see p. 32).

[123] M. Koschorreck, M. Napolitano, B. Dubost, and M. W. Mitchell, “Sub-projection-noise sensitivity in broadband atomic magnetometry”, Phys. Rev. Lett. **104**, 093602 (2010) (see p. 32).

[124] M. Koschorreck, M. Napolitano, B. Dubost, and M. W. Mitchell, “Quantum nondemolition measurement of large-spin ensembles by dynamical decoupling”, Phys. Rev. Lett. **105**, 093602 (2010) (see pp. 32, 123).

[125] V. Shah, G. Vasilakis, and M. V. Romalis, “High bandwidth atomic magnetometery with continuous quantum nondemolition measurements”, Phys. Rev. Lett. **104**, 013601 (2010) (see pp. 32, 149).

[126] S. Li, P. Vachaspati, D. Sheng, N. Dural, and M. V. Romalis, “Optical rotation in excess of 100 rad generated by rb vapor in a multipass cell”, Phys. Rev. A **84**, 061403 (2011) (see p. 32).

[127] J. Ye, L.-S. Ma, and J. L. Hall, “Ultrasensitive detections in atomic and molecular physics: demonstration in molecular overtone spectroscopy”, J. Opt. Soc. Am. B **15**, 6 (1998) (see p. 32).

[128] I. Teper, Y.-J. Lin, and V. Vuletić, “Resonator-aided single-atom detection on a microfabricated chip”, Phys. Rev. Lett. **97**, 023002 (2006) (see p. 32).

[129] S Bernon, T Vanderbruggen, R Kohlhaas, A Bertoldi, A Landragin, and P Bouyer, "Heterodyne non-demolition measurements on cold atomic samples: towards the preparation of non-classical states for atom interferometry", New J. Phys. **13**, 065021 (2011) (see p. 32).

[130] H. Zhang, R. McConnell, S. Ćuk, Q. Lin, M. H. Schleier-Smith, I. D. Leroux, and V. Vuletić, "Collective state measurement of mesoscopic ensembles with single-atom resolution", Phys. Rev. Lett. **109**, 133603 (2012) (see pp. 32, 60, 149, 155).

[131] H. Tanji-Suzuki, I. D. Leroux, M. H. Schleier-Smith, M. Cetina, A. T. Grier, J. Simon, and V. Vuletic, "Chapter 4 - interaction between atomic ensembles and optical resonators: classical description", in Advances in atomic, molecular, and optical physics, Vol. 60, edited by E. Arimondo, P. R. Berman, and C. C. Lin (Academic Press, 2011), pp. 201 –237 (see p. 33).

[132] J. H. Wesenberg, A. Ardavan, G. A. D. Briggs, J. J. L. Morton, R. J. Schoelkopf, D. I. Schuster, and K. Mølmer, "Quantum computing with an electron spin ensemble", Phys. Rev. Lett. **103**, 070502 (2009) (see p. 33).

[133] I. Diniz, S. Portolan, R. Ferreira, J. M. Gérard, P. Bertet, and A. Auffèves, "Strongly coupling a cavity to inhomogeneous ensembles of emitters: potential for long-lived solid-state quantum memories", Phys. Rev. A **84**, 063810 (2011) (see p. 33).

[134] M. Albert, J. P. Marler, P. F. Herskind, A. Dantan, and M. Drewsen, "Collective strong coupling between ion coulomb crystals and an optical cavity field: theory and experiment", Phys. Rev. A **85**, 023818 (2012) (see p. 33).

[135] T. Holstein and H. Primakoff, "Field dependence of the intrinsic domain magnetization of a ferromagnet", Phys. Rev. **58**, 1098 (1940) (see p. 35).

[136] C. W. Gardiner and M. J. Collett, "Input and output in damped quantum systems: quantum stochastic differential equations and the master equation", Phys. Rev. A **31**, 3761 (1985) (see p. 38).

[137] H. J. Kimble, "Strong interactions of single atoms and photons in cavity qed", Phys. Scr. **1998**, 127 (1998) (see pp. 40, 67).

[138] M. A. Armen, J. K. Au, J. K. Stockton, A. C. Doherty, and H. Mabuchi, "Adaptive homodyne measurement of optical phase", Phys. Rev. Lett. **89**, 133602 (2002) (see p. 43).

[139] H. Uys, M. J. Biercuk, A. P. VanDevender, C. Ospelkaus, D. Meiser, R. Ozeri, and J. J. Bollinger, "Decoherence due to Elastic Rayleigh Scattering", Phys. Rev. Lett. **105**, 200401 (2010) (see pp. 57, 153).

[140] J. J. Bollinger, W. M. Itano, D. J. Wineland, and D. J. Heinzen, "Optimal frequency measurements with maximally correlated states", Phys. Rev. A **54**, R4649 (1996) (see p. 60).

[141] D. A. Steck, Rubidium 87 D Line Data, 2010 (see pp. 67, 70).

[142] G. Santarelli, C. Audoin, A. Makdissi, P. Laurent, G. Dick, and A. Clairon, "Frequency stability degradation of an oscillator slaved to a periodically interrogated atomic resonator", IEEE Trans. Ultrason., Ferroelectr., Freq. Control **45**, 887 (1998) (see pp. 111, 124).

[143] M. Kasevich and S. Chu, "Atomic interferometry using stimulated Raman transitions", Phys. Rev. Lett. **67**, 181 (1991) (see p. 111).

[144] B. Canuel, F. Leduc, D. Holleville, A. Gauguet, J. Fils, A. Virdis, A. Clairon, N. Dimarcq, C. J. Bordé, A. Landragin, and P. Bouyer, "Six-axis inertial sensor using cold-atom interferometry", Phys. Rev. Lett. **97**, 010402 (2006) (see p. 111).

[145] L. Isenhower, E. Urban, X. L. Zhang, A. T. Gill, T. Henage, T. A. Johnson, T. G. Walker, and M. Saffman, "Demonstration of a Neutral Atom Controlled-NOT Quantum Gate", Phys. Rev. Lett. **104**, 8 (2010) (see p. 111).

[146] C. Ospelkaus, U. Warring, Y. Colombe, K. R. Brown, J. M. Amini, D. Leibfried, and D. J. Wineland, "Microwave quantum logic gates for trapped ions", Nature **476**, 181 (2011) (see p. 111).

[147] T. M. Fortier, N. Ashby, J. C. Bergquist, M. J. Delaney, S. A. Diddams, T. P. Heavner, L. Hollberg, W. M. Itano, S. R. Jefferts, K. Kim, F. Levi, L. Lorini, W. H. Oskay, T. E. Parker, J. Shirley, and J. E. Stalnaker, "Precision atomic spectroscopy for improved limits on variation of the fine structure constant and local position invariance", Phys. Rev. Lett. **98**, 070801 (2007) (see p. 111).

[148] N. Ashby, T. P. Heavner, S. R. Jefferts, T. E. Parker, A. G. Radnaev, and Y. O. Dudin, "Testing local position invariance with four cesium-fountain primary frequency standards and four nist hydrogen masers", Phys. Rev. Lett. **98**, 070802 (2007) (see p. 111).

[149] R. Tycko, H. M. Cho, E. Schneider, and A. Pines, "Composite pulses without phase distortion", Journal of Magnetic Resonance (1969) **61**, 90 (1985) (see pp. 111, 123, 125, 138, 139).

[150] S. Wimperis, "Broadband, narrowband, and passband composite pulses for use in advanced nmr experiments", J. Magn. Reson., Ser A **109**, 221 (1994) (see pp. 111, 123, 125, 138, 139).

[151] H. K. Cummins, G. Llewellyn, and J. A. Jones, "Tackling systematic errors in quantum logic gates with composite rotations", Phys. Rev. A **67**, 042308 (2003) (see pp. 111, 123, 125, 138, 139).

[152] D. Chambon, S. Bize, M. Lours, F. Narbonneau, H. Marion, A. Clairon, G. Santarelli, A. Luiten, and M. Tobar, "Design and realization of a flywheel oscillator for advanced time and frequency metrology", Rev. Sci. Instrum. **76**, 094704, 094704 (2005) (see p. 112).

[153] R. Boudot, S. Guerandel, and E. de Clercq, "Simple-design low-noise nltl-based frequency synthesizers for a cpt cs clock", IEEE Trans. Instrum. Meas. **58**, 3659 (2009) (see p. 112).

[154] N. Rossetto, F. Esnault, D. Holleville, J. Delporte, M. Lours, and N. Dimarcq, "Dick effect and cavity pulling on horace compact cold atom clock", in Frequency control and the european frequency and time forum (fcs), 2011 joint conference of the ieee international (2011), pp. 1 –4 (see p. 112).

[155] F. Ramirez-Martinez, M. Lours, P. Rosenbusch, F. Reinhard, and J. Reichel, "Low phase noise frequency synthesiser for the trapped atom clock on a chip", in Frequency control symposium, 2009 joint with the 22nd european frequency and time forum. ieee international (2009), pp. 535 –539 (see p. 112).

[156] P. Wade, "A dual mixer for 5760 Mhz with filter and amplifier", QEX/Communications Quarterly, 9 (1995) (see p. 113).

[157] D. B. Leeson, "A simple model of feedback oscillator noise spectrum", Proc. IEEE **54**, 329 (1966) (see p. 117).

[158] B. Edward and D. Rees, "A broadband printed dipole with integrated balun", Microwave Journal **30**, 339 (1987) (see p. 119).

[159] K. R. Brown, A. W. Harrow, and I. L. Chuang, "Arbitrarily accurate composite pulse sequences", Phys. Rev. A **70**, 052318 (2004) (see pp. 122, 123, 125, 138).

[160] M Bishof, X Zhang, M. J. Martin, and J. Ye, "An optical spectrum analyzer with quantum limited noise floor", arXiv:1303.6741v1 (2013) (see p. 123).

[161] H. Y. Carr and E. M. Purcell, "Effects of diffusion on free precession in nuclear magnetic resonance experiments", Phys. Rev. **94**, 630 (1954) (see pp. 123, 142).

[162] S. Meiboom and D. Gill, "Modified spin-echo method for measuring nuclear relaxation times", Rev. Sci. Instrum. **29**, 688 (1958) (see pp. 123, 142).

[163] L. Viola, E. Knill, and S. Lloyd, "Dynamical decoupling of open quantum systems", Phys. Rev. Lett. **82**, 2417 (1999) (see p. 123).

[164] G. S. Uhrig, "Keeping a Quantum Bit Alive by Optimized π-Pulse Sequences", Phys. Rev. Lett. **98**, 100504 (2007) (see pp. 123, 142).

[165] M. J. Biercuk, H. Uys, A. P. VanDevender, N. Shiga, W. M. Itano, and J. J. Bollinger, "Optimized dynamical decoupling in a model quantum memory", Nature **458**, 996 (2009) (see p. 123).

[166] M. J. Biercuk, H. Uys, A. P. VanDevender, N. Shiga, W. M. Itano, and J. J. Bollinger, "Experimental Uhrig dynamical decoupling using trapped ions", Phys. Rev. A **79**, 062324 (2009) (see p. 123).

[167] Y. C. Liu, Z. F. Xu, G. R. Jin, and L. You, "Spin squeezing: transforming one-axis twisting into two-axis twisting", Phys. Rev. Lett. **107**, 013601 (2011) (see p. 123).

[168] W. Rakreungdet, J. H. Lee, K. F. Lee, B. E. Mischuck, E. Montano, and P. S. Jessen, "Accurate microwave control and real-time diagnostics of neutral-atom qubits", Phys. Rev. A **79**, 022316 (2009) (see pp. 123, 125, 138).

[169] M. Steffen and R. H. Koch, "Shaped pulses for quantum computing", Phys. Rev. A **75**, 062326 (2007) (see p. 123).

[170] B. T. Torosov and N. V. Vitanov, "Smooth composite pulses for high-fidelity quantum information processing", Phys. Rev. A **83**, 053420 (2011) (see p. 123).

[171] N. Khaneja, T. Reiss, C. Kehlet, T. Schulte-Herbrüggen, and S. J. Glaser, "Optimal control of coupled spin dynamics: design of nmr pulse sequences by gradient ascent algorithms", J. Magn. Reson. **172**, 296 (2005) (see p. 123).

[172] J.-S. Li and N. Khaneja, "Control of inhomogeneous quantum ensembles", Phys. Rev. A **73**, 030302 (2006) (see p. 123).

[173] N. Timoney, V. Elman, S. Glaser, C. Weiss, M. Johanning, W. Neuhauser, and C. Wunderlich, "Error-resistant single-qubit gates with trapped ions", Phys. Rev. A **77**, 052334 (2008) (see p. 123).

[174] J. Ye, H. J. Kimble, and H. Katori, "Quantum state engineering and precision metrology using State-Insensitive light traps", Science **320**, 1734 (2008) (see pp. 123, 124).

[175] J. M. Martinis, S. Nam, J. Aumentado, K. M. Lang, and C. Urbina, "Decoherence of a superconducting qubit due to bias noise", Phys. Rev. B **67**, 094510 (2003) (see p. 124).

[176] P Avan and C Cohen-Tannoudji, "Two-level atom saturated by a fluctuating resonant laser beam. calculation of the fluorescence spectrum", J. Phys. B: At., Mol. Opt. Phys. **10**, 155 (1977) (see p. 124).

[177] P Zoller and F Ehlotzky, "Resonance fluorescence in modulated laser fields", J. Phys. B: At., Mol. Opt. Phys. **10**, 3023 (1977) (see p. 124).

[178] J. H. Eberly, K. Wódkiewicz, and B. W. Shore, "Noise in strong laser-atom interactions: phase telegraph noise", Phys. Rev. A **30**, 2381 (1984) (see p. 124).

[179] J. G. Coffer, B. Sickmiller, A. Presser, and J. C. Camparo, "Line shapes of atomic-candle-type Rabi resonances", Phys. Rev. A **66**, 023806 (2002) (see p. 124).

[180] G. J. Dick, "Local oscillator induced instabilities in trapped ion frequency standards", in Proceedings precise time and time interval meeting (1987), pp. 133 –147 (see p. 124).

[181] P. Cheinet, B. Canuel, F. Pereira Dos Santos, A. Gauguet, F. Yver-Leduc, and A. Landragin, "Measurement of the sensitivity function in a time-domain atomic interferometer", IEEE Trans. Instrum. Meas. **57**, 1141 (2008) (see p. 124).

[182] R. Jozsa, "Fidelity for mixed quantum states", J. Mod. Opt. **41**, 2315 (1994) (see p. 138).

[183] A. Wicht, J. M. Hensley, E. Sarajlic, and S. Chu, "A preliminary measurement of the fine structure constant based on atom interferometry", Phys. Scr. **2002**, 82 (2002) (see p. 145).

[184] J. Lodewyck, P. G. Westergaard, and P. Lemonde, "Nondestructive measurement of the transition probability in a Sr optical lattice clock", Phys. Rev. A **79**, 061401 (2009) (see p. 145).

[185] P. Grangier, J. A. Levenson, and J.-P. Poizat, "Quantum non-demolition measurements in optics", Nature **396**, 537 (1998) (see p. 146).

[186] A. Louchet-Chauvet, J. Appel, J. J. Renema, D. Oblak, N. Kjærgaard, and E. S. Polzik, "Entanglement-assisted atomic clock beyond the projection noise limit", New Journal of Physics **12**, 065032 (2010) (see p. 147).

[187] I. D. Leroux, M. H. Schleier-Smith, and V. Vuletić, "Orientation-dependent entanglement lifetime in a squeezed atomic clock", Phys. Rev. Lett. **104**, 250801 (2010) (see p. 147).

[188] S. F. Huelga, C. Macchiavello, T. Pellizzari, A. K. Ekert, M. B. Plenio, and J. I. Cirac, "Improvement of frequency standards with quantum entanglement", Phys. Rev. Lett. **79**, 3865 (1997) (see p. 147).

[189] D. Ulam-Orgikh and M. Kitagawa, "Spin squeezing and decoherence limit in ramsey spectroscopy", Phys. Rev. A **64**, 052106 (2001) (see p. 147).

[190] M Brune, E Hagley, J Dreyer, X Maître, A Maali, C Wunderlich, J. M. Raimond, and S Haroche, "Observing the Progressive Decoherence of the Meter in a Quantum Measurement", Physical Review Letters **77**, 4887 (1996) (see p. 148).

[191] J. K. Stockton, J. M. Geremia, A. C. Doherty, and H. Mabuchi, "Characterizing the entanglement of symmetric many-particle spin-$\frac{1}{2}$ systems", Phys. Rev. A **67**, 022112 (2003) (see p. 148).

[192] C. Simon and J. Kempe, "Robustness of multiparty entanglement", Phys. Rev. A **65**, 052327 (2002) (see p. 148).

[193] M. Saffman, D. Oblak, J. Appel, and E. S. Polzik, "Spin squeezing of atomic ensembles by multicolor quantum nondemolition measurements", Phys. Rev. A **79**, 023831 (2009) (see p. 149).

[194] J. Simon, "Cavity QED with Atomic Ensembles", Thesis (Harvard, 2010), p. 112 (see p. 158).

[195] K. Eckert, O. Romero-Isart, M. Rodriguez, M. Lewenstein, E. S. Polzik, and A. Sanpera, "Quantum non-demolition detection of strongly correlated systems", Nature Physics **4**, 50 (2007) (see p. 161).

Appendix A

Coherent Reinitialization for Reduced Recoil Heating

In this Appendix, we consider whether coherence-preserving QND measurements can also be used to reduce the total photon-recoil heating in a Ramsey spectroscopy measurement cycle. A low number of photon recoils imparted in a complete experimental cycle, not just the readout, would allow neutral atom traps to operate more like ion traps, with their advantages of high duty cycle and high repetition rates. We use the canonical example of Ramsey spectroscopy to show how low photon recoil in a complete experimental cycle can be achieved. Imagine reading out the collective spin projection J_z at the end of a Ramsey sequence with a QND measurement at or below the projection noise limit. If one were to repeat the experimental cycle by optically repumping all the atoms back into $|\downarrow\rangle$, each atom in the ensemble would experience $\approx s/2$ photons worth of recoil heating, where s is the average number of photons scattered by an atom to get from $|\uparrow\rangle$ to $|\downarrow\rangle$ during the repumping process. In Fig. A.1, we show how recoil heating can be reduced by coherently reinitializing most of the atoms into $|\downarrow\rangle$ using a microwave $\pi/2$ pulse before turning on the repumping.

The loss of contrast ϵ due to dephasing during the Ramsey evolution time is assumed to be small for the results presented in this section to be valid. Dephasing causes the off-diagonal elements of the density matrix representing the state of the ensemble to decay, resulting in a mixed state. The mixed state can be regarded as a tensor product of a pure state representing a smaller ensemble of size $N(1-\epsilon)$ atoms in a coherent superposition of $|\uparrow\rangle$ and $|\downarrow\rangle$ [Fig. A.1(a)], with pure states representing the decohered atoms with $\epsilon N/2$ atoms collapsed in $|\uparrow\rangle$ and $|\downarrow\rangle$ on average. The

(a) Atomic spin state after QND measurement:

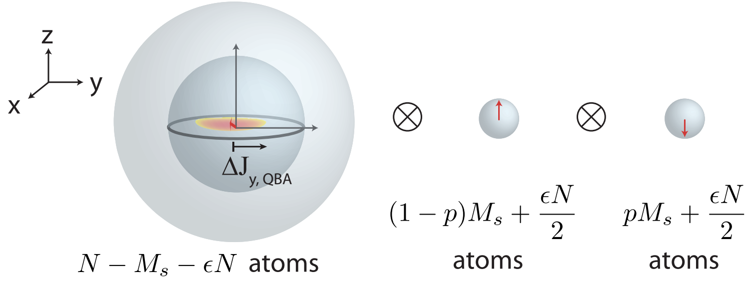

(b) After π/2-rotation about y:

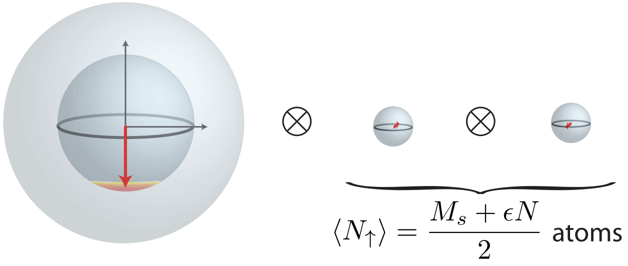

(c) After repumping:

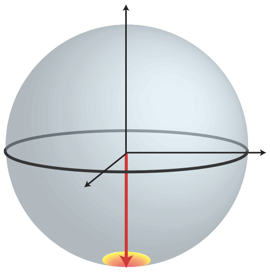

Figure A.1: Coherent reinitialization scheme to reduce photon recoil heating in a complete experimental cycle. (a) Dephasing during the Ramsey evolution can be described as a shrinking of the coherent part of the collective spin from length $N/2$ to length $N(1-\epsilon)/2$, where $\epsilon \ll 1$ characterizes the amount of dephasing. The dephased atoms can be represented as if they had collapsed into $|\uparrow\rangle$ and $|\downarrow\rangle$ with $\epsilon N/2$ atoms in each state. Performing a QND readout with $m_s = M_s/N \ll 1$ results in further shrinkage of the coherent collective spin and additional collapse of the atoms. (b) Performing a microwave $\pi/2$-pulse about $\hat{y}$ rotates the coherent collective spin to the south pole and the collapsed atoms onto the equator of the Bloch sphere. (c) Applying optical repumping beams reinitializes the ensemble to the south pole, with the photon recoil heating arising from repumping the atoms in superposition states into $|\downarrow\rangle$. The contribution arising from the quantum back-action of repumping back into a CSS is negligible provided the spectroscopic enhancement is small compared to the Heisenberg limit.

QND readout causes an additional $(1-p)M_s$ atoms to collapse into $|\uparrow\rangle$ and pM_s atoms to collapse into $|\downarrow\rangle$, provided $m_s = M_s/N \ll 1$. Following a microwave $\pi/2$ pulse that rotates most of the atoms into $|\downarrow\rangle$, we find that approximately $s(m_s + \epsilon)/2$ photon recoils per atom is required to reinitialize the entire ensemble into $|\downarrow\rangle$. The contribution from quantum back-action into J_y is of order $sm_s/Nm_s^{\mathrm{proj}}$ and may be safely ignored for small spectroscopic enhancements.

In summary, we have shown that it is possible to impart only $s(m_s+\epsilon)/2$ optical photon recoils per atom through the coherent reinitialization scheme, as opposed to the much larger $s/2$ recoils per atom without coherent reinitialization. Note the reason why the scheme works is because we have traded optical photon recoils with microwave photon recoils, which impart recoil energy ~ 8 orders of magnitude smaller than that of optical photons. If an optical transition separated $|\uparrow\rangle$ from $|\downarrow\rangle$, such as in optical lattice clocks, the scheme presented would not reduce recoil heating substantially.

Appendix B

Heterodyne PDH Detection Scheme

This appendix describes a heterodyne Pound-Drever-Hall (PDH) detection method in our early attempts at squeezing. Initial attempts using this method provided nearly projection-noise-limited resolution. We chose not to optimize the sensitivity as we realized the IQ detection method, described in Chap. 5 would give fundamentally 3 dB higher signal-to-noise for a symmetric cavity because both transmission and reflection are detected for the IQ demodulation method while information in transmission is not used in the heterodyne PDH method. It is then simple to see that both methods fundamentally have the same signal-to-noise when applied to a single-ended cavity (and driving the more transmissive mirror) as all the information comes out from the reflection port only. However, this technique can be relatively simple to implement and produces a dispersive error signal in real time (without computer processing) appropriate for real-time feedback. A technical advantage of this detection scheme over the heterodyne IQ-demodulation scheme (in reflection) presented in Chap. 5 is that the heterodyne PDH method is insensitive to optical path length fluctuations because the phase reference sidebands and the probe sidebands travel along the same exact optical path.

Here I briefly describe the experiment since the concepts are already laid down in Chapter. 5, and instead focus on the methodology more. We prepare a CSS along $\hat{x}$ using optical pumping all the atoms into $|\downarrow\rangle$ followed by a microwave $\pi/2$-pulse. A vacuum Rabi splitting $\Omega_\uparrow = \sqrt{N_\uparrow}2g$ develops from the strong resonant coupling between the atoms and the cavity mode. The goal then is to measure $N_\uparrow$ very precisely by measuring size of the vacuum Rabi splitting precisely. The

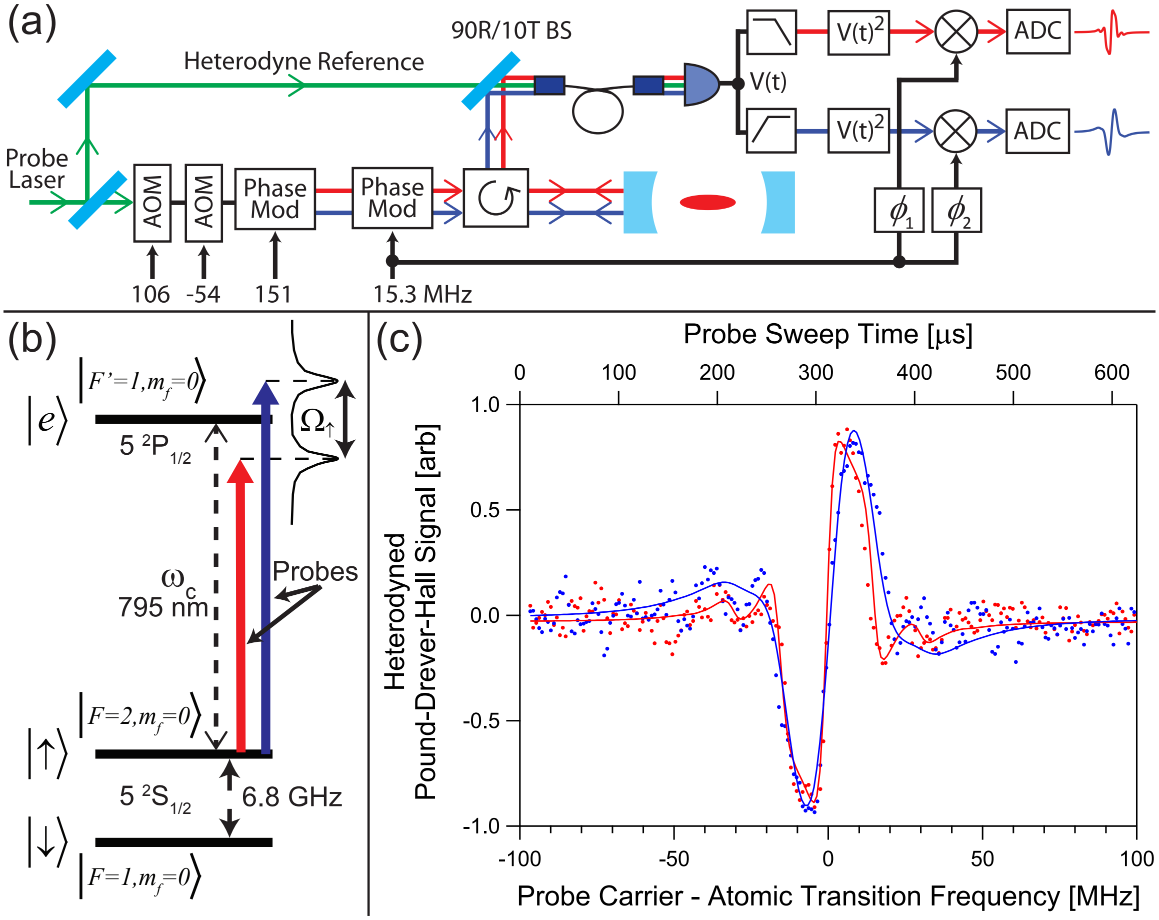

Figure B.1: (a) Experimental setup of the heterodyne PDH scheme used to probe the vacuum Rabi splitting. Both components of the vacuum Rabi splitting are simultaneously probed using the first order phase modulation sidebands generated by the first electro-optic modulator (EOM) and spaced ±151 MHz from the carrier. Additional ±15.3 MHz PDH phase reference sidebands are imposed by the second EOM. (b) Relevant energy level structure of ^{87}Rb. The bare cavity is made resonant with the $|\uparrow\rangle$ to $|e\rangle$ transition, and π-polarized probe light is used. (c) Simultaneous probing of the vacuum Rabi splitting. The blue and red points are the individual PDH error signals simultaneously measured by sweeping the phase-modulated probe laser frequency across the higher and lower frequency modes of the vacuum Rabi splitting respectively. The blue and red solid lines are curve fits to the data using an analytic model of the PDH error signal that includes contributions up to the 5th order sidebands.

vacuum Rabi splitting $\Omega_\uparrow$ is measured by sweeping the probe laser frequency and detecting the light reflected from the cavity input mirror. The resonance signals are extracted using a modified PDH detection scheme, which I call heterodyne PDH, that employs optical heterodyne detection to achieve near photon-shot-noise-limited detection at probe powers of < 100 pW to several nW (see Fig. B.1). To reduce sensitivity to laser and cavity noise, we measure both resonances ω_+ and ω_- simultaneously as discussed in Sec. 6.2. The two probe components are generated by phase modulating the probe light to create sidebands at ±151 MHz from the carrier, chosen to match the vacuum Rabi splitting of 302 MHz. The PDH phase reference sidebands at ±15.3 MHz are then imposed around the probe components by a second phase modulator. To avoid degeneracy of the two probe components in the rf spectrum generated at the photodiode, the probe carrier is blue-shifted 52 MHz with respect to the heterodyne reference beam derived from the same laser as the probe.

In principle, a single 52 MHz AOM on the probe or heterodyne reference beam would suffice. However, we observed spurious signals when using a single 52 MHz AOM that is due to rf pick-up on the probe laser, generating undesired sidebands at our signal frequency. To mitigate pickup, we used doubly shielded BNC cables on all high power rf ($\sim$ 30 dBm) signals in our lab. Because we use a heterodyne beam power of $\sim$1 mW and probe powers at the nW level, spurious modulation of the heterodyne beam at the 10^{-5} to 10^{-6} level would produce heterodyne beatnote powers of the same magnitude as the actual probe signal. From our experience, spurious modulation at this level can occur if attention is not paid to shielding rf signals carefully. The problem was finally eliminated by using two AOMs, one that blueshifts by 106 MHz and another that redshifts by 54 MHz, resulting in a net blueshift of the probe beam by 52 MHz. Any spurious sidebands at 52 MHz would now be second order in the pickup. The probe power is controlled via the rf drive power delivered to the 54 MHz AOM. I note here that these AOMs were tuned from its nominal operating frequency of 80 MHz to 106 MHz and 54 MHz via tuning the LC-resonant circuit inside the AOM. No significant loss of diffraction efficiency was observed. The 106 MHz AOM crystal [1] has a chip near the transducer, which we believe is the cause of its long thermal time constant – a slow relaxation of the beam deflection when the rf power is pulsed fully-on.

The light reflected from the cavity is overlapped with the heterodyne light on a 90/10 beam

---

[1] This AOM is current being used in the 823 nm Lattice Laser setup to provide additional isolation from the Transfer Cavity, and fiber tip reflections.

splitter. Both beams are coupled into a single mode polarization-maintaining (PM) fiber to ensure high spatial mode matching. The heterodyne laser power delivered to the photodiode is typically 0.8 to 1.2 mW. Working at low heterodyne powers provides additional immunity to classical intensity noise, as well as increased probe detection efficiency. The photodetector consists of a Hamamatsu S5973 photodiode, ac-coupled to an Analog Devices AD8015 240 MHz transimpedance amplifier described in Appendix C.

The phase shift of the probe carrier E_0 relative to the phase reference sidebands $E_{\pm 1}$ may be generated via the PDH method, which relies on a square law detector to generate the cross terms $E_0 E_{+1} + E_0 E_{-1}$ resulting in a rf beatnote at the sideband modulation frequency. Demodulating the beatnote into the quadrature component yields the phase shift of the carrier. For good SNR, the carrier photon shot noise needs to dominate over the photodiode electronic noise. Normally this is not a problem when probing an empty cavity; one can simply increase the carrier power. The situation is different when probing atoms in a cavity because atoms can be saturated at high intensities, collapsing the Rabi splitting we wish to probe. Furthermore, to minimize decoherence caused by free space scattering, we could not probe with high powers. The standard methods to achieve (close to) shot noise limited detection is to use a avalanche photodiode (APD) or homodyne/heterodyne detection. We opted for heterodyne detection. Because the heterodyne rf beatnote $E_{\mathrm{LO}}(E_{-1} + E_0 + E_{+1})$ does not contain the desired cross terms between the carrier and the sideband electric fields, we generated the cross terms by electronically squaring the rf beatnote.

The two probe components are separated in the heterodyne rf spectrum using high and low pass filters, and notch filters at 99 MHz and 203 MHz. Each time-domain signal is squared using an Analog Devices AD835 250 MHz voltage multiplier. This step essentially mimics the square law detection of the photodiode that occurs in the usual PDH detection scheme. The resulting 15.3 MHz signals are then demodulated to dc. Figure B.1(c) shows the resulting nearly simultaneously measured PDH error signals when the probe laser frequency is swept across a vacuum Rabi splitting. Linear fits to the central 15 μs of each probe component sweeping through resonance were used to extract the vacuum Rabi splitting $\Omega_{\uparrow}$.

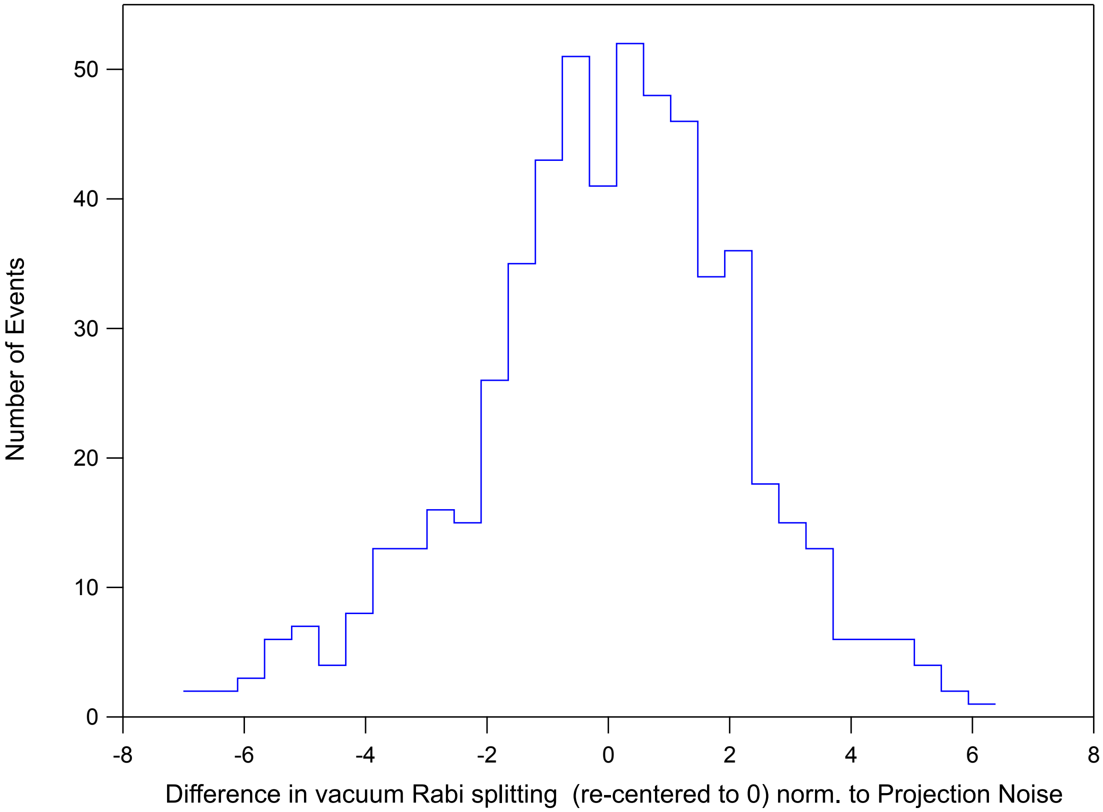

Figure B.2: Histogram of the difference $\Omega_{\uparrow}^{(1)} - \Omega_{\uparrow}^{(0)}$ between two successive measurements $\Omega_{\uparrow}^{(0)}$, $\Omega_{\uparrow}^{(1)}$ of the Rabi splitting showing nearly projection-noise-limited measurement precision. A small horizontal offset has been applied to center the distribution about zero. The rms fluctuation $\Delta\left(\Omega_{\uparrow}^{(1)} - \Omega_{\uparrow}^{(0)}\right)$ is 2.1(1) times the projection noise level in standard deviation for an ensemble of $N = 7.1(3) \times 10^5$ effective atoms. Taking the measurement precision of both measurements to be the same, we infer the precision of a single Rabi splitting is 3.5(4) dB above the quantum projection noise level.

Using this technique at nano-Watt probe powers, we were able to measure the collective spin at a precision of 3.5(4) dB above the quantum projection noise level for an ensemble of $7.1(3) \times 10^5$ effective atoms (see Fig. B.2). At this measurement precision, we calculate $m_s = 0.16$ photons/atom worth of free space scattering, directly proportional to photon recoil heating and loss of contrast as described in Sec. 6.1. Simple extrapolation implies that with $\approx 2.2\times$ more probe photons, the measurement precision would reach the projection noise level while causing ≈ 0.35 photon/atom worth of free space scattering.

Appendix C

AD8015 Photodiode Characteristics

In this Appendix, I include characterizations of the photodiode used in squeezing experiment described in Chap. 5. We used a Hamamatsu S5973 photodiode (1 GHz intrinsic bandwidth) whose uncoated glass cover has been removed to recover about 8% in quantum efficiency. Its sensitivity without glass is 0.54 A/W at 795 nm corresponding to internal photodiode quantum efficiency of 84%.

The photocurrent generated at the photodiode is converted to electric voltage with a 240 MHz transimpedance amplifier (Analog Devices AD8015). The transfer function, noise and transimpedance gain of our AD8015 #2 photodiode used in reflection detection are shown in Figs. C.1, C.2, C.3 respectively. The AD8015 #5 photodiode used in transmission detection has similar characteristics as the AD8015 #2 photodiode.

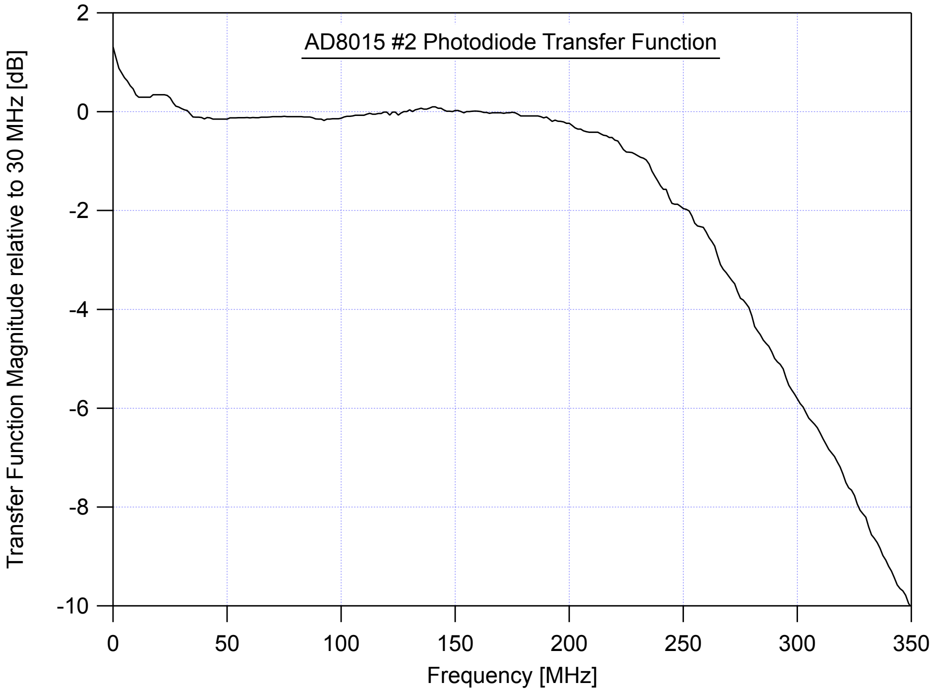

Figure C.1: Transfer Function of AD8015 #2 Photodiode

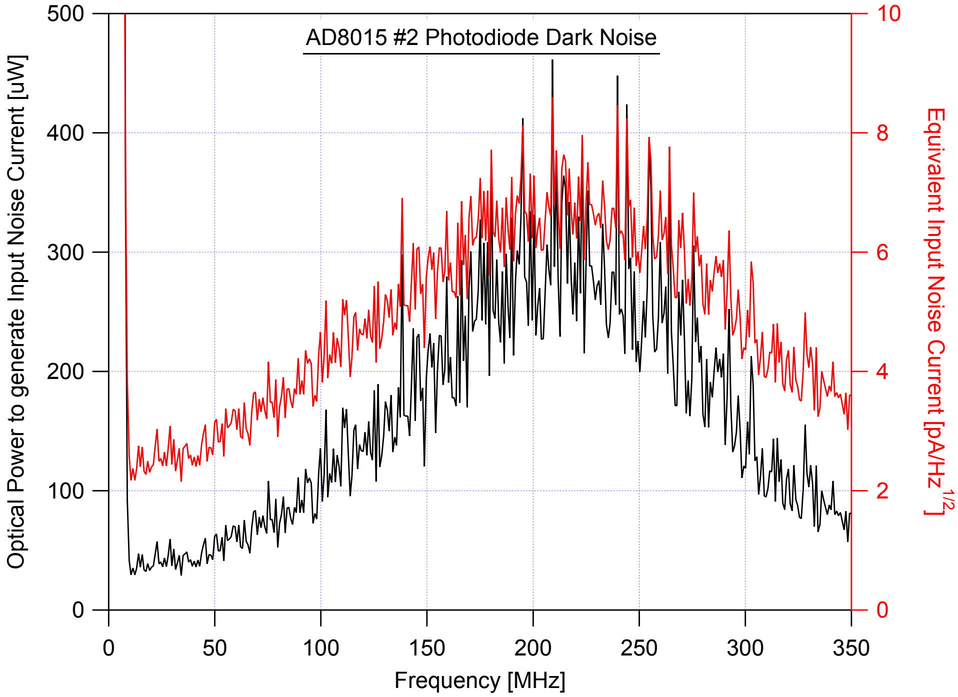

Figure C.2: Noise properties of AD8015 #2 photodiode. Shot-noise-limited detection may be achieved with 0.2 mW and 0.35 mW optical power at detection frequencies of 100 MHz and 200 MHz respectively.

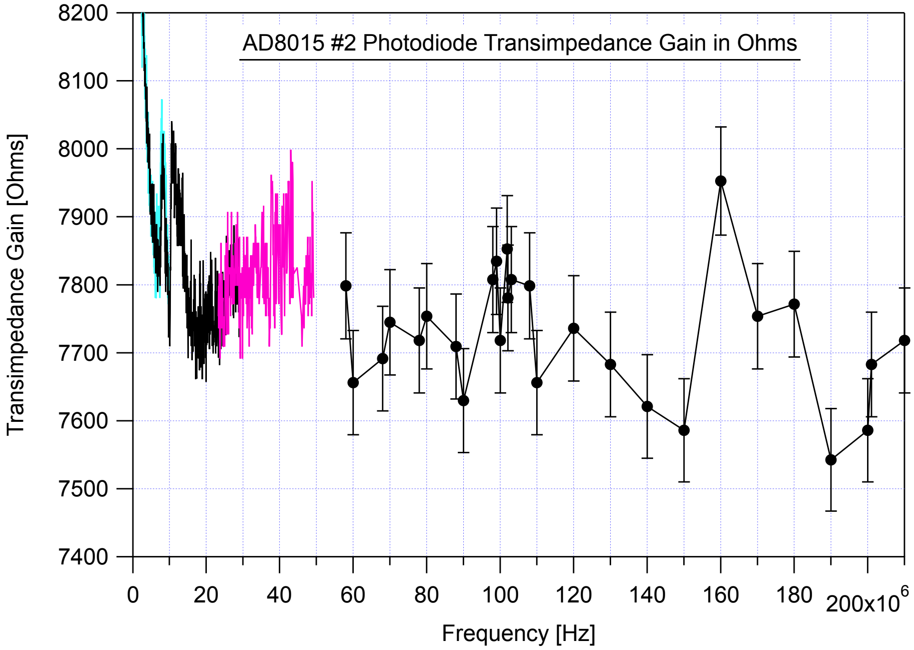

Figure C.3: Measured Transimpedance Gain of AD8015 #2 photodiode. While the AD8015 chip is spec for 10 kOhm transimpedance gain (nominal) in the data sheet, we measured a transimpedance gain of 9 kOhm near DC (at 100 kHz).

Appendix D

Phase Noise Definitions

The power spectral density of phase fluctuations $S_\phi(f_m)$ of an oscillator is the mean squared phase fluctuations $(\Delta\phi(f_m))^2$ at frequency offset f_m from the carrier in a 1 Hz measurement bandwidth

$$S_\phi(f_m) \equiv \Delta\phi(f_m)^2/\mathrm{Hz}\,. \tag{D.1}$$

The phase noise $S_\phi(f_m)$ has units of rad^2/Hz, and includes contributions from both upper and lower noise sidebands at $\pm f_m$.

One can measure $S_\phi(f_m)$ by mixing the oscillator-under-test with a reference oscillator at the same frequency, and with much lower phase noise. The phase of the reference oscillator is chosen so that the mixer output $v(t)$ is proportional to the relative phase difference $\phi(t)$ between the oscillator-under-test and the reference oscillator. The power spectral density $S_\phi(f_m)$ is computed from the autocorrelation function of $\phi(t)$ via the Wiener-Khinchin theorem as

$$S_\phi(f_m) = 2\int_{-\infty}^{\infty} \langle \phi(t)\phi(t+\tau)\rangle_t \, e^{-i2\pi f_m \tau}\, d\tau\,, \tag{D.2}$$

where f_m lies in the range $(0, \infty)$.

The definition of the single sideband (SSB) phase noise $\mathcal{L}(f_m)$ is

$$\mathcal{L}(f_m) \equiv \frac{1}{2} S_\phi(f_m)\,. \tag{D.3}$$

The units for $\mathcal{L}(f_m)$ are rad^2/Hz. It is also commonly expressed in the form $10\log_{10}\mathcal{L}(f_m)$, which has units of dB below the carrier in a 1 Hz bandwidth (dBc/Hz). The mean squared phase fluctuations observed in a Fourier frequency range from f_l to f_h is given by

$$(\Delta\phi)^2 = 2\int_{f_l}^{f_h} \mathcal{L}(f_m)\, df_m\,. \tag{D.4}$$

For an oscillator whose amplitude noise is much lower than its phase noise, the SSB phase noise $\mathcal{L}(f_m)$ is equivalent to the ratio of the power of a noise sideband $P_{\mathrm{SSB}}(f_m)$ at frequency offset f_m in a 1 Hz measurement bandwidth to the power in the carrier P_{car} as measured on a radio/microwave/optical frequency spectrum analyzer

$$\mathcal{L}(f_m) = \frac{P_{\mathrm{SSB}}(f_m)}{P_{\mathrm{car}}}\,. \tag{D.5}$$

Appendix E

Relation between Mean Squared Modulation Amplitude and Single Sideband Phase Noise

In this short note, we establish the connection between the mean squared phase modulation amplitude $\langle \beta^2 \rangle$, used to normalize the covariance noise matrix T in Sec. 8.4.1, and the SSB phase noise $\mathcal{L}(f_m)$. We model the phase modulation $\phi(t) = \beta \sin(2\pi f_0 t + \alpha_m)$, at fixed modulation frequency f_0, as being drawn from a random distribution of α_m and β. The modulation phase α_m is uniformly distributed from 0 to 2π, and the modulation amplitude β is Gaussian distributed with zero mean and variance $\langle \beta^2 \rangle$. The time-averaged squared phase modulation should be further averaged over the distribution for α_m and β to yield the statistical phase fluctuations as

$$\langle \langle \phi(t)^2 \rangle_t \rangle_{\alpha_m,\beta} = \langle \phi(t)^2 \rangle_{\alpha_m,\beta} = \frac{\langle \beta^2 \rangle}{2} \,, \tag{E.1}$$

where we made use of the fact that averaging over time t has the same effect as averaging over phase α_m. Using Eq. D.1, D.3 and E.1, we obtain the relation between the SSB phase noise $\mathcal{L}(f_m)$ and mean squared modulation amplitude $\langle \beta^2 \rangle$ as

$$\mathcal{L}(f_m) = \frac{\langle \beta^2 \rangle}{4} \delta(f_m - f_0) \,. \tag{E.2}$$

Appendix F

Composite and Plain π-pulse Covariance Noise Matrix and Infidelity

Table F.1: Rotation sequence for commonly used composite π-pulses.

Pulse Name	Pulse Sequence
Plain π	$R_{0^\circ}\,[\pi]$
CORPSE π	$R_{0^\circ}\left[\frac{\pi}{3}\right]\,R_{180^\circ}\left[\frac{5\pi}{3}\right]\,R_{0^\circ}\left[\frac{7\pi}{3}\right]$
SCROFULOUS π	$R_{60^\circ}\,[\pi]\,R_{300^\circ}\,[\pi]\,R_{60^\circ}\,[\pi]$
BB1 π	$R_{0^\circ}\,[\pi]\,R_{104.5^\circ}\,[\pi]\,R_{313.4^\circ}\,[2\pi]\,R_{104.5^\circ}\,[\pi]$

The covariance noise matrix W and infidelity $1-F$ for the CORPSE π-pulse, SCROFULOUS π-pulse, BB1 π-pulse and a single π-pulse, which all effectively implement a π-pulse about $\hat{\mathbf{x}}$, are given below. The results assume a white LO phase noise spectrum $\mathcal{L}(f_m) = \mathcal{L}_\circ$. Here we specify the initial Bloch vector $\mathbf{J}_i$ by its polar angle θ_i, measured from the $x-y$ plane, and its azimuthal angle ϕ_i measured from $\hat{\mathbf{x}}$ so that $\mathbf{J}_i = (\cos\theta_i \cos\phi_i, \cos\theta_i \sin\phi_i, \sin\theta_i)$.

F.1 CORPSE π-pulse

For the CORPSE π-pulse sequence $R\left(0,\frac{\pi}{3}\right)R\left(\pi,\frac{5\pi}{3}\right)R\left(0,\frac{7\pi}{3}\right)$ (time ordering right to left), used to suppress static detuning error, we have:

$$W_{xx}=\frac{1}{3}\pi f_R\mathcal{L}_\circ\left(\left(13\pi-3\sqrt{3}\right)\cos^2\theta_i\sin^2\phi_i+\left(13\pi+3\sqrt{3}\right)\sin^2\theta_i\right) \tag{F.1a}$$

$$W_{yy}=\frac{1}{3}\pi f_R\mathcal{L}_\circ\left(13\pi-3\sqrt{3}\right)\cos^2\theta_i\cos^2\phi_i \tag{F.1b}$$

$$W_{zz}=\frac{1}{3}\pi f_R\mathcal{L}_\circ\left(13\pi+3\sqrt{3}\right)\cos^2\theta_i\cos^2\phi_i \tag{F.1c}$$

$$W_{xy}=W_{yx}=\frac{1}{6}\pi f_R\mathcal{L}_\circ\left(13\pi-3\sqrt{3}\right)\cos^2\theta_i\sin 2\phi_i \tag{F.1d}$$

$$W_{yz}=W_{yz}=0 \tag{F.1e}$$

$$W_{xz}=W_{zx}=\frac{1}{6}\pi f_R\mathcal{L}_\circ\left(13\pi+3\sqrt{3}\right)\sin 2\theta_i\cos\phi_i \tag{F.1f}$$

$$1-F=\frac{1}{12}\pi f_R\mathcal{L}_\circ\left(13\pi-3\sqrt{3}\cos 2\theta_i+\left(13\pi+3\sqrt{3}\right)\cos^2\theta_i\cos^2\phi_i\right) \tag{F.1g}$$

F.2 SCROFULOUS π-pulse

For the SCROFULOUS π-pulse sequence $R\left(\frac{\pi}{3},\pi\right)R\left(\frac{5\pi}{3},\pi\right)R\left(\frac{\pi}{3},\pi\right)$ (time ordering right to left), used to suppress static amplitude error, we have:

$$W_{xx}=\frac{3}{2}\pi^2 f_R\mathcal{L}_\circ\left(2\cos^2\theta_i\sin^2\phi_i+\sin^2\theta_i\right) \tag{F.2a}$$

$$W_{yy}=\frac{3}{2}\pi^2 f_R\mathcal{L}_\circ\left(2\cos^2\theta_i\cos^2\phi_i+\sin^2\theta_i\right) \tag{F.2b}$$

$$W_{zz}=\frac{3}{2}\pi^2 f_R\mathcal{L}_\circ\cos^2\theta_i \tag{F.2c}$$

$$W_{xy}=W_{yx}=\frac{3}{2}\pi^2 f_R\mathcal{L}_\circ\cos^2\theta_i\sin 2\phi_i \tag{F.2d}$$

$$W_{yz}=W_{zy}=-\frac{3}{4}\pi^2 f_R\mathcal{L}_\circ\sin 2\theta_i\sin\phi_i \tag{F.2e}$$

$$W_{xz}=W_{zx}=\frac{3}{4}\pi^2 f_R\mathcal{L}_\circ\sin 2\theta_i\cos\phi_i \tag{F.2f}$$

$$1-F=\frac{3}{16}\pi^2 f_R\mathcal{L}_\circ(5+\cos 2\theta_i) \tag{F.2g}$$

F.3 BB1 π-pulse

The BB1 π-pulse sequence $R(0,\pi)\,R(\phi_R,\pi)\,R(3\phi_R,2\pi)\,R(\phi_R,\pi)$ (time ordering right to left), where $\phi_R = \arccos\left(-\frac{1}{4}\right) \approx 104.5°$, is used to compensate for amplitude error with little to no cost in the sensitivty to detuning error. The covariance noise matrix W and infidelity $1-F$ for the BB1 π-pulse are:

$$W_{xx} = \frac{5}{4}\pi^2 f_R \mathcal{L}_\circ \left(4\cos^2\theta_i \sin^2\phi_i + \sin^2\theta_i\right) \tag{F.3a}$$

$$W_{yy} = \frac{5}{4}\pi^2 f_R \mathcal{L}_\circ \left(4\cos^2\theta_i \cos^2\phi_i + 3\sin^2\theta_i\right) \tag{F.3b}$$

$$W_{zz} = \frac{5}{4}\pi^2 f_R \mathcal{L}_\circ \cos^2\theta_i \left(2 - \cos 2\phi_i\right) \tag{F.3c}$$

$$W_{xy} = W_{yx} = \frac{5}{2}\pi^2 f_R \mathcal{L}_\circ \cos^2\theta_i \sin 2\phi_i \tag{F.3d}$$

$$W_{yz} = W_{zy} = -\frac{15}{8}\pi^2 f_R \mathcal{L}_\circ \sin 2\theta_i \sin\phi_i \tag{F.3e}$$

$$W_{xz} = W_{zx} = \frac{5}{8}\pi^2 f_R \mathcal{L}_\circ \sin 2\theta_i \cos\phi_i \tag{F.3f}$$

$$1 - F = \frac{5}{16}\pi^2 f_R \mathcal{L}_\circ \left(4 + 2\cos^2\theta_i - \cos^2\theta_i \cos 2\phi_i\right) \tag{F.3g}$$

F.4 Plain π-pulse

Finally, we provide expressions for the covariance noise matrix and infidelity for a plain π-pulse $R(0,\pi)$ as a useful benchmark to compare against composite π-pulses. The noise covariance matrix W and infidelity $1-F$ for a plain π-pulse are:

$$W_{xx} = \pi^2 f_R \mathcal{L}_\circ \left(1 - \cos^2\theta_i \cos^2\phi_i\right) \tag{F.4a}$$

$$W_{yy} = \pi^2 f_R \mathcal{L}_\circ \cos^2\theta_i \cos^2\phi_i \tag{F.4b}$$

$$W_{zz} = \pi^2 f_R \mathcal{L}_\circ \cos^2\theta_i \cos^2\phi_i \tag{F.4c}$$

$$W_{xy} = W_{yx} = \frac{1}{2}\pi^2 f_R \mathcal{L}_\circ \cos^2\theta_i \sin 2\phi_i \tag{F.4d}$$

$$W_{yz} = W_{yz} = 0 \tag{F.4e}$$

$$W_{xz} = W_{zx} = \frac{1}{2}\pi^2 f_R \mathcal{L}_\circ \sin 2\theta_i \cos\phi_i \tag{F.4f}$$

$$1 - F = \frac{1}{4}\pi^2 f_R \mathcal{L}_\circ \left(1 + \cos^2\theta_i \cos^2\phi_i\right) \tag{F.4g}$$

F.5 Composite Pulse Static Error Cancellation

Table. F.2 shows the lowest order static error cancellation for commonly used composite π-pulses, and also the plain π-pulse as a benchmark for comparison. The following parameters are used: static fractional amplitude error as $\epsilon = \Delta f_R / f_R$ and the static fractional detuning error of the local oscillator as $\delta = (f_{\mathrm{LO}} - f_a)/f_a$.

Table F.2: Comparison of strengths and weaknesses of composite pulse sequences for performing a π-pulse with the rotation axis parallel or perpendicular to the Bloch vector.

Pulse Name	Phase Noise Sensitivity $(\Delta\theta)^2$	Static Error $\Delta\theta_{\text{static}}$	Static Infidelity $\Delta\mathbf{J}^2/4 = 1 - F$
Plain $\parallel$	$\pi^2 f_R \mathcal{L}_\circ$	-2δ	δ^2
Plain $\perp$	$O(\mathcal{L}_\circ^2)$	$-\frac{\pi\delta^2}{2} - \pi\epsilon$	$\frac{\pi^2\delta^2}{16} + \frac{1}{4}\pi^2\delta\varepsilon + \frac{\pi^2\varepsilon^2}{4}$
CORPSE $\parallel$	$\frac{1}{3}\pi\left(3\sqrt{3} + 13\pi\right) f_R \mathcal{L}_\circ$	$\left(-1 - \frac{5\pi}{2\sqrt{3}}\right)\delta^3 - \frac{5\pi\delta\epsilon}{\sqrt{3}}$	$\left(\frac{1}{4} + \frac{5\pi}{4\sqrt{3}} + \frac{37\pi^2}{48}\right)\delta^6 - \frac{1}{12}\left(-10\sqrt{3} - 37\pi\right)\pi\delta^4\epsilon + \frac{37}{12}\pi^2\delta^2\epsilon^2$
CORPSE $\perp$	$O(\mathcal{L}_\circ^2)$	$\left(\sqrt{3} - \frac{\pi}{2}\right)\delta^2 - \pi\epsilon$	$\left(\frac{3}{4} - \frac{\sqrt{3}\pi}{4} + \frac{\pi^2}{16}\right)\delta^4 + \frac{1}{4}\pi\left(\pi - 2\sqrt{3}\right)\delta^2\epsilon + \frac{\pi^2\epsilon^2}{4}$
SCROFULOUS $\parallel$	$\frac{3\pi^2}{2} f_R \mathcal{L}_\circ$	$\frac{1}{32}\sqrt{3}\pi^5\epsilon^5 - 4\delta$	$4\delta^2 + \frac{3\pi^4\epsilon^4}{64}$
SCROFULOUS $\perp$	$\frac{3\pi^2}{2} f_R \mathcal{L}_\circ$	$6\sqrt{3}\delta^3 + 3\pi\delta^2\epsilon - \frac{1}{2}\sqrt{3}\pi^2\delta\epsilon^2 - \frac{\pi^3\epsilon^3}{4}$	$\frac{27\delta^4}{4} - \frac{9}{8}\pi^2\delta^2\epsilon^2 + \frac{3\pi^4\epsilon^4}{64}$
BB1 $\parallel$	$\frac{5\pi^2}{4} f_R \mathcal{L}_\circ$	$\frac{1}{32}\sqrt{15}\pi^3\epsilon^3 - 2\delta$	$\delta^2 - \frac{1}{32}\sqrt{15}\pi^3\delta\epsilon^3 + \frac{15\pi^6\epsilon^6}{4096}$
BB1 $\perp$	$\frac{15\pi^2}{4} f_R \mathcal{L}_\circ$	$\frac{15\pi\delta^4}{16} + \frac{15}{8}\pi\delta^2\epsilon - \frac{5\pi^3\epsilon^3}{32}$	$\frac{25\pi^2\delta^6}{64} + \frac{25}{16}\pi^2\delta^2\epsilon^2 + \frac{25\pi^6\epsilon^6}{4096}$

Appendix G

Fundamental Limits on Squeezing via Differential Measurement of $^{87}\mathrm{Rb}$ clock transition

Using the framework developed in Chapters 3 and 4, we now analyze the fundamental limits on squeezing on a clock transition comprised of two hyperfine ground states, taking into account Raman spin flips and decoherence.

From Sec. 3.3, we have shown that the measurement resolution at fixed free space scattering improves with cavity detuning δ_c, but ultimately saturates to a value set by the collective cooperativity parameter NC. For squeezing on a clock transition comprised of two hyperfine ground states, the maximal detuning is approximately half of the ground state hyperfine splitting $\delta_c = \omega_{\mathrm{hf}}/2$. We find that the squeezing is fundamentally limit by the ratio $\omega_{\mathrm{hf}}/\Gamma$ of the hyperfine splitting to the excited state decay linewidth.

To be specific, we analyze the measurement scheme demonstrated by the MIT group [100] in which they used the same pseudospin states presented in this thesis, namely the clock states of $^{87}\mathrm{Rb}$ $|\uparrow\rangle \equiv |5^2S_{1/2}, F=2, m_F=0\rangle$ and $|\downarrow\rangle \equiv |5^2S_{1/2}, F=1, m_F=0\rangle$. For differential probing of the hyperfine clock transition, the bare cavity frequency is tuned to the average of the two ground states to optically excited state transitions near 780 nm. This tuning ensures that an atom in $|\downarrow\rangle$ shifts the dressed cavity resonance frequency by an equal, but opposite amount as an atom in $|\uparrow\rangle$. The excited state hyperfine splitting ~ 500 MHz is much less than the ground hyperfine splitting and is taken to be zero for the following analysis.

The problem is analyzed by extending the linearized two-mode model of Eq. (3.6) to a linearized three-mode model in which the atomic operator $\hat{a}$ is generalized to operators $\hat{a}_\downarrow$ and $\hat{a}_\uparrow$ to yield three coupled differential equations, along with the same input-output relations given by Eq. (3.8):

$$\begin{aligned}\frac{d\langle\hat{c}\rangle}{dt} &= -\frac{1}{2}\kappa\langle\hat{c}\rangle - \imath g\left(\sqrt{N_\uparrow}\langle\hat{a}_\uparrow\rangle - \sqrt{N_\downarrow}\langle\hat{a}_\downarrow\rangle\right) + \sqrt{\kappa_1}c_i\,,\\ \frac{d\langle\hat{a}_\uparrow\rangle}{dt} &= -\frac{1}{2}\left(\Gamma + \imath\,\omega_{\mathrm{hf}}\right)\langle\hat{a}_\uparrow\rangle - \imath\sqrt{N_\uparrow}g\langle\hat{c}\rangle\,,\\ \frac{d\langle\hat{a}_\downarrow\rangle}{dt} &= -\frac{1}{2}\left(\Gamma - \imath\,\omega_{\mathrm{hf}}\right)\langle\hat{a}_\downarrow\rangle - \imath\sqrt{N_\downarrow}g\langle\hat{c}\rangle\,. \end{aligned} \tag{G.1}$$

The equations are now written in a rotating frame at the bare cavity resonance frequency that is chosen such that the two optical atomic transitions are detuned by $\pm\omega_{\mathrm{hf}}/2$. The rate of scattering into free space is described by the two field amplitudes $a_{s,\uparrow,\downarrow} = \sqrt{\Gamma}\langle\hat{a}_{\uparrow,\downarrow}\rangle$ and normalized such that the rate of photons scattered into free space is simply $\dot{M}_s = |a_{s,\uparrow}|^2 + |a_{s,\downarrow}|^2$.

From the coupled set of Eq. (G.1), we find that the rms phase shift of the transmitted light field caused by the rms projection noise level fluctuation in the population difference is:

$$\Delta\phi^{\mathrm{proj}} = \sqrt{N}C\left(\frac{\Gamma}{\omega_{\mathrm{hf}}}\right)\left(\frac{1}{1+NC\Gamma^2/\omega_{\mathrm{hf}}^2}\right)\,. \tag{G.2}$$

This expression assumes the damping rates are small $\kappa, \Gamma \ll \omega_{\mathrm{hf}}, \sqrt{N/2}\,2g$. The phase shift initially climbs with increasing atom number as $\sqrt{N}$, but saturates to a maximum value $\Delta\phi^{\mathrm{proj}} = \sqrt{C}/2$ at a critical atom number given by $NC = (\omega_{\mathrm{hf}}/\Gamma)^2$, after which the phase shift decreases as $1/\sqrt{N}$. The physical interpretation for this decrease is that above the critical atom number, the dressed cavity mode linewidth κ' rapidly starts to broaden with increasing atom number. The number of free-space-scattered photons required to resolve the projection noise level phase shift of the probe is

$$m_s^{\mathrm{proj}} = \frac{1}{4qNC}\left(1 + NC\left(\frac{\Gamma}{\omega_{\mathrm{hf}}}\right)^2\right)\,. \tag{G.3}$$

The diffusion of the difference between the estimate of J_z and the actual value of J_z is driven by Raman transitions that move atoms from $|\uparrow\rangle$ to $|F=1\rangle$ or $|\downarrow\rangle$ to $|F=2\rangle$. Raman transitions between states of the same F (i.e., $\Delta F = 0$) lead to loss of coherence, but do not change the coupling of the atom to the cavity mode in the limit where the excited state hyperfine splitting is neglected, as we do here. Hyperfine changing transitions $\Delta F \neq 0$ cause the detuning to change sign, but not magnitude, making such a process equivalent to a spin flip. Accounting for transition branching ratios, we find that to a good approximation, we can apply Eq. (4.4), with an effective spin flip probability $p = 1/6$. Assuming the loss of coherence is small, then the optimal spectroscopic enhancement with respect to average probe photon number is

$$\xi^{-1}_{\mathrm{m,\,opt}} = \frac{\sqrt{6qNC}}{1 + 4NC\Gamma^2/\omega^2_{\mathrm{hf}}} \,. \tag{G.4}$$

At small N, the spectroscopic enhancement scales as $\sqrt{6qNC}$, reaching a peak value of $\xi^{-1}_{\mathrm{m,\,opt}} = \sqrt{3q/8}\,\omega_{\mathrm{hf}}\,/\Gamma$ at a value $NC = \frac{1}{4}(\omega_{\mathrm{hf}}/\Gamma)^2$, slightly before the maximum phase shift is reached. At larger NC, the spectroscopic enhancement scales as $\xi^{-1}_{\mathrm{m,\,opt}} = \sqrt{3q/8NC}(\omega_{\mathrm{hf}}/\Gamma)^2$.

Taking the quantum efficiency to be $q = 1$, the maximum spectroscopic enhancement for ^{87}Rb is quite large at 28 dB. The exact details of the full measurement sequence (i.e., whether rotations such as π-pulses are used to cancel sources of technical noise) are needed to construct an optimal estimator of J_z, but, at best, a 3 dB further improvement may result.

Because C does not depend on the cavity length, the optimum N for peak spectroscopic enhancement scales as $(w_0^2/F)(\omega_{\mathrm{hf}}/\Gamma)^2$, where w_0 is the cavity mode waist, and F is the cavity finesse. More fundamentally, no change in the cavity geometry (w_0 and l) or finesse F changes the maximum obtainable enhancement in spectroscopic sensitivity. This enhancement is determined solely by the atomic properties. Figure. G.1 shows the spectroscopic enhancement versus atom number for a range of technologically feasible cavity finesses.

Resolving very small phase deviations or small frequency shifts imposes technical challenges that are modified with cavity geometry or finesse, as shown by the probe frequency (Fig. G.2) and probe phase shift (Fig. G.3) resolutions required to obtain the spectroscopic sensitivities shown in Fig. G.1. All three figures assume the same cavity geometry as ours, $l = 1.91$ cm and $w_0 = 71$ μm. Finally, we note that Fig. G.2 shows the technical requirement on probe frequency resolution is more relaxed above the optimum N compared to achieving the same spectroscopic enhancement at a value below the optimum N.

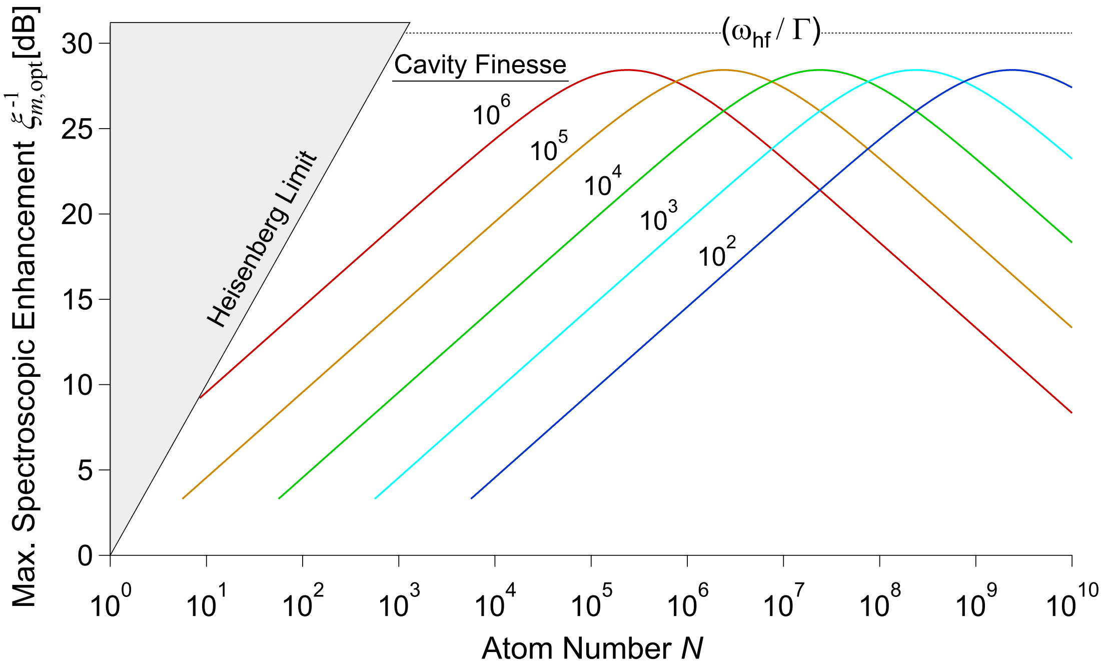

Figure G.1: The fundamental optimum spectroscopic enhancement for differential probing of the ^{87}Rb clock transition, as performed in Ref. [100]. The calculations are performed for our current cavity geometry and assume a net quantum efficiency of $q = 1$. The purple, light blue, green, orange, and red curves correspond to cavity finesses of $F = 10^2, 10^3, 10^4, 10^5$, and 10^6, respectively. All these finesses are experimentally feasible. The atom number N at which the spectroscopic enhancement is maximized scales with the cavity mode waist w_0 and cavity finesse F as w_0^2/F.

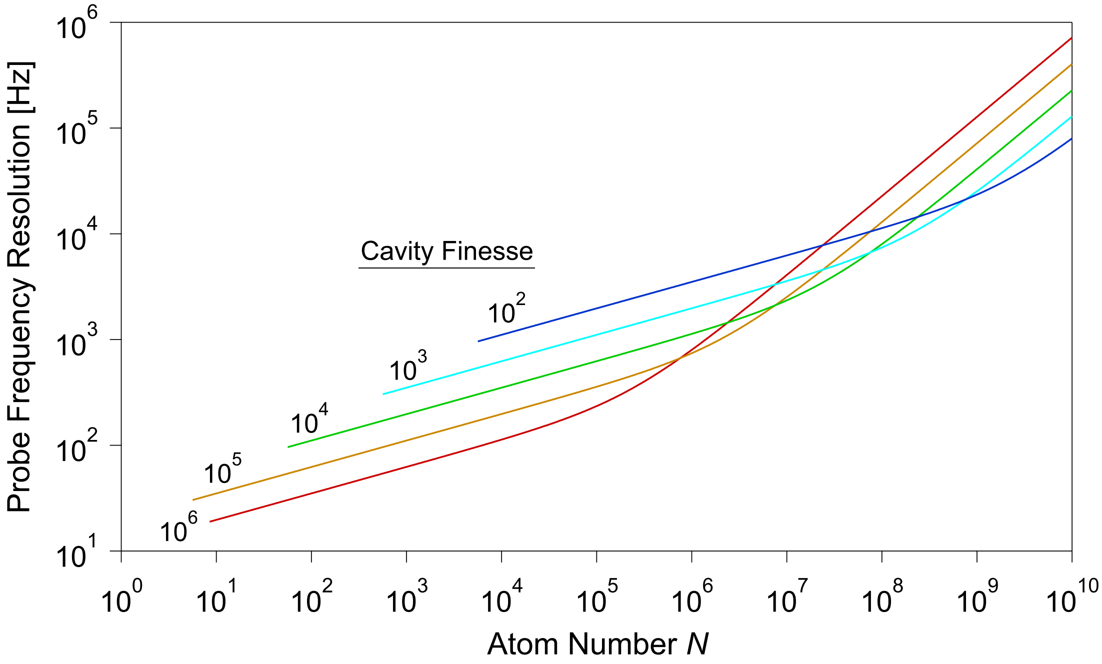

Figure G.2: Frequency resolution with which the relative frequency of the probe and dressed cavity mode must be measured to obtain the spectroscopic enhancements shown in (and under the same conditions as) Fig. G.1 . The purple, light blue, green, orange, and red curves correspond to cavity finesses of $F = 10^2, 10^3, 10^4, 10^5$, and 10^6, respectively.

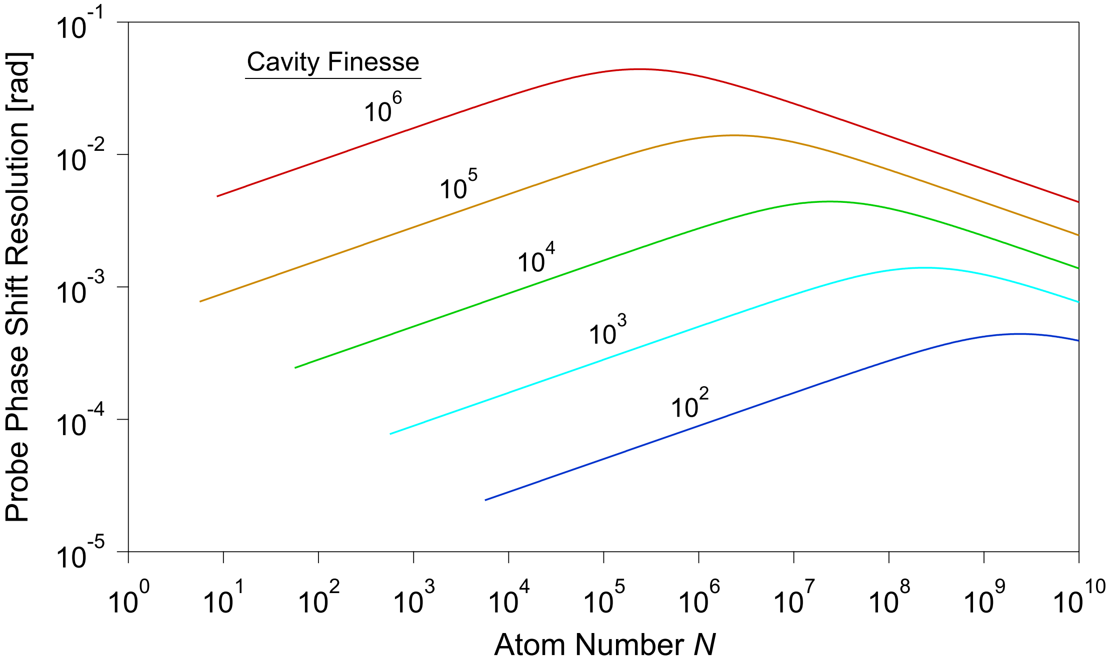

Figure G.3: Phase resolution with which the transmitted probe light must be measured to obtain the spectroscopic enhancements shown in (and under the same conditions as) Fig. G.1. The purple, light blue, green, orange, and red curves correspond to cavity finesses of $F = 10^2, 10^3, 10^4, 10^5$, and 10^6, respectively.